Partial Neutron Capture Cross Sections of Actinides using Cold Neutron Prompt Gamma Activation Analysis

Christoph Genreith

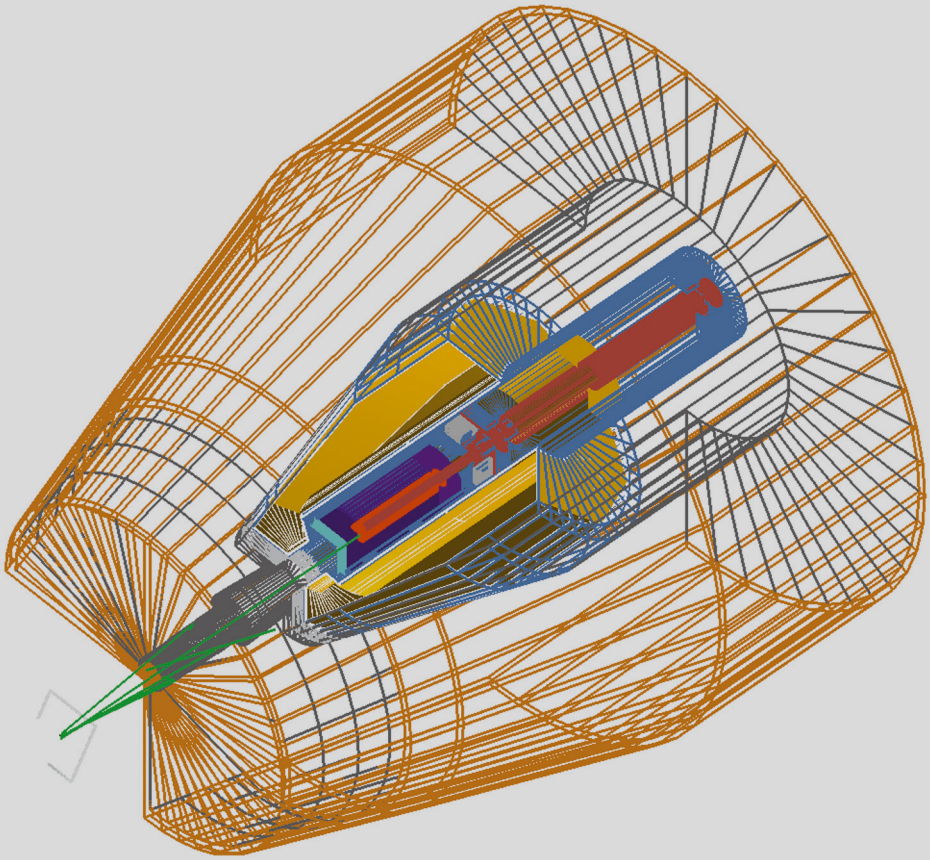

Energie & Umwelt / Energy & Environment
Band / Volume 250
ISBN 978-3-95806-036-4

JÜLICH
FORSCHUNGSZENTRUM

Schriften des Forschungszentrums Jülich
Reihe Energie & Umwelt / Energy & Environment Band / Volume 250

Forschungszentrum Jülich GmbH
Institut für Energie- und Klimaforschung
Nukleare Entsorgung und Reaktorsicherheit (IEK-6)

Partial Neutron Capture Cross Sections of Actinides using Cold Neutron Prompt Gamma Activation Analysis

Christoph Genreith

Schriften des Forschungszentrums Jülich
Reihe Energie & Umwelt / Energy & Environment Band / Volume 250

ISSN 1866-1793 ISBN 978-3-95806-036-4

Bibliographic information published by the Deutsche Nationalbibliothek.
The Deutsche Nationalbibliothek lists this publication in the Deutsche Nationalbibliografie; detailed bibliographic data are available in the Internet at http://dnb.d-nb.de.

Publisher and Distributor: Forschungszentrum Jülich GmbH
Zentralbibliothek
52425 Jülich
Tel: +49 2461 61-5368
Fax: +49 2461 61-6103
Email: zb-publikation@fz-juelich.de
www.fz-juelich.de/zb

Cover Design: Grafische Medien, Forschungszentrum Jülich GmbH

Printer: Grafische Medien, Forschungszentrum Jülich GmbH

Schriften des Forschungszentrums Jülich
Reihe Energie & Umwelt / Energy & Environment, Band / Volume 250

D 82 (Diss. RWTH Aachen University, 2015)

ISSN 1866-1793
ISBN 978-3-95806-036-4

The complete volume is freely available on the Internet on the Jülicher Open Access Server (JuSER) at www.fz-juelich.de/zb/openaccess.

Abstract

Nuclear waste needs to be characterized for its safe handling and storage. In particular long-lived actinides render the waste characterization challenging. The results described in this thesis demonstrate that Prompt Gamma Neutron Activation Analysis (PGAA) with cold neutrons is a reliable tool for the non-destructive analysis of actinides.

Nuclear data required for an accurate identification and quantification of actinides was acquired. Therefore, a sample design suitable for accurate and precise measurements of prompt γ-ray energies and partial cross sections of long-lived actinides at existing PGAA facilities was presented. Using the developed sample design the fundamental prompt γ-ray data on ^{237}Np, ^{241}Am and ^{242}Pu were measured. The data were validated by repetitive analysis of different samples at two individual irradiation and counting facilities – the BRR in Budapest and the FRM II in Garching near Munich. Employing cold neutrons, resonance neutron capture by low energetic resonances was avoided during the experiments. This is an improvement over older neutron activation based works at thermal reactor neutron energies. 152 prompt γ-rays of ^{237}Np were identified, as well as 19 of ^{241}Am, and 127 prompt γ-rays of ^{242}Pu. In all cases, both high and lower energetic prompt γ-rays were identified. The most intense line of ^{237}Np was observed at an energy of $E_\gamma = 182.82(10)$ keV associated with a partial capture cross section of $\sigma_\gamma = 22.06(39)$ b. The most intense prompt γ-ray lines of ^{241}Am and of ^{242}Pu were observed at $E_\gamma = 154.72(7)$ keV with $\sigma_\gamma = 72.80(252)$ b and $E_\gamma = 287.69(8)$ keV with $\sigma_\gamma = 7.07(12)$ b, respectively. The measurements described in this thesis provide the first reported quantifications on partial radiative capture cross sections for ^{237}Np, ^{241}Am and ^{242}Pu measured simultaneously over the large energy range from 45 keV to 12 MeV. Detailed uncertainty assessments were performed and the validity of the given uncertainties was demonstrated. Compared to existing literature data on prompt γ-ray energies and emission probabilities the uncertainties of the data were improved.

In addition to the basic nuclear data necessary for PGAA, the thermal radiative neutron capture cross sections of ^{237}Np and of ^{241}Am were determined from decay measurements after neutron irradiation. The thermal radiative neutron capture cross section of ^{237}Np was determined as $\sigma_c^0 = 176.3(47)$ b . The thermal radiative neutron capture cross section of ^{241}Am was determined as $\sigma_c^0 = 667.7(312)$ b. The thermal radiative neutron capture cross section of ^{242}Pu was calculated as $\sigma_c^0 = 21.9(15)$ b using nuclear structure simulations with the statistical decay code DICEBOX, constraint by the measured prompt γ-ray data. In the corresponding simulation the total radiative width of the capture state was found to be 28(1) meV. Also, the neutron separation energies of ^{238}Np and of ^{243}Pu were derived. The neutron separation energy of ^{238}Np was calculated as $S_\mathrm{n} = 5488.02(17)$ keV. The neutron separation energy of ^{243}Pu was calculated as $S_\mathrm{n} = 5036.33(59)$ keV. Detection limits for PGAA at FRM II were calculated for ^{237}Np as 0.056 µg, for ^{241}Am as 0.017 µg and for ^{242}Pu as 0.20 µg.

Zusammenfassung

Die Behandlung und Lagerung von nuklearen Abfällen, erfordert die Charakterisierung des Radionuklidinventars. In diesem Kontext ist die Charakterisierung von langlebigen Actinoiden besonders herausfordernd. Die in dieser Arbeit beschriebenen Resultate zeigen, dass sich die Prompt Gamma Neutronen Aktivierungsanalyse (PGAA) an kalten Neutronenstrahlen für die zuverlässige zerstörungsfreie Analytik von Actinoiden eignet.
Im Rahmen dieser Arbeit wurden die für die Identifikation und Quantifizierung mittels PGAA notwendigen grundlegenden nuklearen Daten einiger Actinoide untersucht. Es wurde ein Probendesign entwickelt, um die Energien und die partiellen Wirkungsquerschnitte von Actinoiden unter Nutzung existierender PGAA-Einrichtungen präzise bestimmen zu können. Mit dem entwickelten Probendesign wurden diese Daten für die Nuklide ^{237}Np, ^{241}Am und^{242}Pu gemessen. Messungen wurden sowohl am BRR in Budapest als auch am FRM II, in Garching bei München durchgeführt. Die erhaltenen Datensätze wurden dabei in jeweils mindestens zwei Messungen validiert. Für diese Messungen wurden kalte Neutronen verwendet, so dass resonanter Neutroneneinfang während der Bestrahlungen vermieden wurde. Dies stellt eine Verbesserung gegenüber älteren Messungen an thermischen Neutronenstrahlen da. 152 prompte γ-Linien vom Neutroneneinfang an ^{237}Np konnten in den Messungen identifiziert werden, wie auch 19 Linien vom Neutroneneinfang an ^{241}Am und 127 Linien vom Neutroneneinfang an ^{242}Pu. In allen Fällen wurden sowohl hoch-, als auch niederenergetische Linien identifiziert. Die intensivste prompte γ-Linie für ^{237}Np wurde mit einer Energie von $E_\gamma = 182.82(10)$ keV und einem partiellen Einfangquerschnitt von $\sigma_\gamma = 22.06(39)$ b bestimmt. Für ^{241}Am und für ^{242}Pu wurden die jeweiligen intensivsten Linien zu $E_\gamma = 154.72(7)$ keV mit $\sigma_\gamma = 72.80(252)$ b, sowie zu $E_\gamma = 287.69(8)$ keV mit $\sigma_\gamma = 7.07(12)$ b gemessen. Für alle gewonnenen Daten wurde eine detaillierte Bestimmung der jeweiligen Unsicherheiten durchgeführt und deren Gültigkeit validiert. Im Vergleich zu älteren Messungen der Energien und Emissionswahrscheinlichkeiten der untersuchten prompten γ-Strahlung konnten die Unsicherheiten reduziert werden.
Zusätzlich zu den für PGAA notwendigen Daten wurden die thermischen Neutroneneinfangquerschnitte von ^{237}Np und von ^{241}Am an Hand von nach den Bestrahlungen aufgenommenen Zerfallsspektren bestimmt. Der thermische Neutroneneinfangquerschnitt von ^{237}Np wurde zu $\sigma_c^0 = 176.3(47)$ b und der von ^{241}Am wurde zu $\sigma_c^0 = 667.7(312)$ b bestimmt. Der Einfangquerschnitt von ^{242}Pu wurde auf Basis von Kernsimulationen mittels des nuklearen Zerfallscodes DICEBOX unter Berücksichtigung der gemessenen prompten γ-Strahlung zu $\sigma_c^0 = 21.9(15)$ b ermittelt. Die zugehörige Simulation ergab eine totale Zerfallsbreite für ^{243}Pu von 28(1) meV. Des Weiteren wurden die Neutronen-Separationsenergien von ^{238}Np und von ^{243}Pu bestimmt. Die Neutronen-Separationsenergie von ^{238}Np wurde zu $S_\mathrm{n} = 5488.02(17)$ keV und die von ^{243}Pu wurde zu $S_\mathrm{n} = 5036.33(59)$ keV berechnet. Für die PGAA Einrichtung am FRM II wurden zudem Nachweisgrenzen von 0.056 µg für ^{237}Np, 0.017 µg für ^{241}Am und 0.20 µg für ^{242}Pu errechnet.

Contents

Abstract ii

Zusammenfassung iii

1 Introduction 1

2 Physical and Technical Background 5
2.1 Atomic Structure . . . 8
2.2 Nuclear Structure . . . 13
2.2.1 Backshifted Fermi Gas Model . . . 17
2.2.2 Constant Temperature Model . . . 18
2.3 Neutron Reactions with Nuclei . . . 18
2.4 Radiation Emitted in Nuclear Reactions . . . 21
2.4.1 α-Radiation . . . 21
2.4.2 β-Radiation and Electron Capture . . . 22
2.4.3 X- and γ-Radiation . . . 23
2.4.4 Internal Conversion . . . 25
2.4.5 Photon Strength Function . . . 26
2.5 Photon Interactions with Matter . . . 28
2.5.1 Photoelectric Effect . . . 28
2.5.2 Photon Scattering . . . 29
2.5.3 Photo Pair Production . . . 31
2.5.4 Mass Attenuation Coefficient . . . 31
2.6 Radiation Detection . . . 33
2.6.1 Curved Crystal Spectrometers . . . 33
2.6.2 Solid State Detectors . . . 34
2.6.2.1 Scintillation Detectors . . . 34
2.6.2.2 Germanium Detectors . . . 34
2.7 Neutron Activation Analysis . . . 39
2.7.1 Instrumental Neutron Activation Analysis . . . 43
2.7.2 Prompt Gamma Neutron Activation Analysis . . . 44
2.8 Monte Carlo Simulation Tools . . . 46
2.8.1 Geant4 and MCNP5 . . . 46
2.8.2 DICEBOX . . . 47

3 Experimental Details 51
3.1 Irradiation Facilities . . . 51
3.1.1 The PGAA Facility at BRR . . . 51

3.1.1.1 Simulation of the Budapest Research Reactor (BRR) facility employing Geant4 . . . 54
3.1.2 The PGAA Facility at FRM II . . . 55
3.1.2.1 Optimization of the FRM II PGAA Facility using Geant4 58
3.2 Spectrum Evaluation . . . 60
3.2.1 HYPERMET-PC . . . 60
3.2.2 Calibration of the Instruments . . . 62
3.2.3 Evaluation Procedure . . . 66
3.3 Design and Validation of Actinide Samples for PGAA . . . 68
3.3.1 Actinide Starting Materials . . . 69
3.3.2 Aluminum Encapsulation . . . 70
3.3.3 Quartz Glass Vials . . . 73
3.3.4 Quartz Glass Sheets . . . 78
3.4 Characterization of Actinide Samples for Irradiation . . . 83
3.4.1 Monte-Carlo Simulations of Samples in the Cold Neutron Beam . . 85

4 Results and Discussion 93
4.1 Neptunium-237 . . . 93
4.1.1 Partial Neutron Capture Cross Sections of ^{237}Np . . . 94
4.1.2 Neutron Separation Energy . . . 106
4.1.3 Thermal Neutron Capture Cross Section of ^{237}Np . . . 107
4.2 Americium-241 . . . 110
4.2.1 Partial Neutron Capture Cross Sections σ_γ of ^{241}Am . . . 111
4.2.2 Thermal Neutron Capture Cross Section of ^{241}Am . . . 114
4.3 Plutonium-242 . . . 119
4.3.1 Partial Neutron Capture Cross Sections σ_γ of ^{242}Pu . . . 120
4.3.2 ^{243}Pu Decay Radiation and Half-Life . . . 130
4.3.3 Neutron Separation Energy . . . 131
4.3.4 Nuclear Structure Calculations . . . 132
4.3.4.1 PSF and LD Models . . . 132
4.3.4.2 The Level Scheme of ^{243}Pu . . . 134
4.3.4.3 Thermal Neutron Capture Cross Section of ^{242}Pu . . . 136
4.4 Detection Limits . . . 140

5 Conclusion 143

List of References 147

List of Abbreviations 161

List of Figures 163

A Data from Measurements **I**
A.1 Data sets from ^{242}Pu neutron irradiations I
A.2 Data sets from ^{237}Np neutron irradiations VII

B Level Scheme of ^{243}Pu **XV**

C Population-Depopulation Plots **XXI**

D Addtional Plots for the ^{237}Np Evaluation **XXV**

E Plots of Actinide Spectra **XXVII**

F Values of Physical Quantities used in this Work **XXXIII**

Acknowledgement **XXXV**

CHAPTER I

Introduction

Nuclear waste has to meet the requirements defined by appropriate authorities for intermediate storage or final disposal. Thus, the characterization of nuclear waste is crucial to verify that these requirements are fulfilled. Actinides are one of the possible components of nuclear waste, that need to be declared. Long-lived actinides responsible for the long-term radio-toxicity of nuclear waste emit only low energetic decay γ-rays (e.g. ^{241}Am). This renders an exact quantification in complex and dense matrices very complicated. If no decay γ-rays of suitable energies and intensities exist, destructive analytical techniques have to be applied to characterize actinide content. Representative samples of a matrix have to be dissolved and actinides have to be separated prior to spectroscopy using the short-ranged α- and β-radiation or prior to mass spectrometry for the identification and quantification. The sample preparation is very time consuming, personnel is exposed to radiation and the samples are destroyed in the process, rendering further investigation of the sample impossible. Thus, a non-destructive analytical method for the identification and quantification of actinide contents is desirable [1].

Prompt Gamma Neutron Activation Analysis (PGAA) is a non-destructive analytical method and offers an alternative for characterization besides standard passive γ-ray spectrometry and other non-destructive methods. PGAA is based on the emission of prompt γ-radiation after radiative neutron capture by nuclei. This reaction takes place for every nuclide (except ^{4}He) and thus, in principle, allows the simultaneous analysis of all nuclei in a given sample. The emitted prompt γ-rays have energies of up to several MeV and hence have a much higher penetration power compared to the decay radiation of long-lived actinides, allowing the assay of high density samples. Due to its dependence on the neutron capture reaction the intensity of the emitted γ-radiation is controllable through an externally applied neutron radiation. In this way even traces of actinides for which the intensity of the decay radiation is too low can be determined. In addition, PGAA also allows the simultaneous multi-element analysis of inactive components in a matrix.

The application of PGAA, however, crucially depends on accurate and reliable nuclear data related to the energy and partial radiative neutron capture cross sections of emitted prompt γ-radiation. The most precise and extensive data on prompt γ-ray energies and partial radiative neutron capture cross sections are reported in the PGAA-database developed at the BRR [2] and evaluated by the International Atomic Energy Agency (IAEA) [3]. The evaluated data are published in the Evaluated Gamma-ray Activation File (EGAF) [4].

This database, however, only provides prompt γ-ray data for the stable nuclei, for ^{232}Th and natural uranium.
Current publications on prompt γ-radiation are sparse and their interest is mainly focused on nuclear structure analysis. Thus, data on prompt γ-ray energies and, at most, emission probabilities with uncertainties in the order of 10 % are provided, if any. More accurate prompt γ-ray energies for the lower energetic region of prompt γ-radiation were determined using curved crystal spectrometers. However, these detectors are not practicable for standard analytical procedures due to their low detection efficiencies, while the prompt γ-rays identified in these experiments often have an energy spacing too close to be resolved with a more practicable High-Purity-Germanium (HPGe) spectrometer. In the previous works, measurements of low and high energetic prompt γ-radiation were performed separately, also due to technical limitations at the time the measurements were made. This gives rise to uncertain normalizations. Furthermore, samples of insufficiently defined dimensions or with large amounts of material were often used, giving rise to large uncertainties in the corrections of photon and neutron absorption effects. Practically no reliable data on partial capture cross sections of actinides are provided and no measurements of prompt γ-ray energies and partial capture cross sections including both the high and low energy regions are present in the current literature. The available data are therefore unreliable for PGAA applications.

In the framework of the development of non-destructive assay techniques for the determination of actinide inventory in complex matrices this work aims at providing the basic prompt γ-ray data of actinides. A sample design will be presented which is suitable for accurate PGAA measurement and meets the safety requirements for handling radioactive actinides. Am, after Pu, is the second most important actinide contributing to the long-term heat load and radioactivity of nuclear waste. The prompt γ-rays of ^{241}Am ($T_{1/2} = 432.6\,\mathrm{yr}$) and its decay product ^{237}Np ($T_{1/2} = 2.144 \cdot 10^6\,\mathrm{yr}$) have been measured, as well as ^{242}Pu ($T_{1/2} = 3.73 \cdot 10^5\,\mathrm{yr}$) produced by neutron capture of ^{241}Pu or ^{241}Am (with subsequent decay of the short-lived $^{242\mathrm{g}}$Am ($T_{1/2} = 16.01\,\mathrm{h}$)). The long-lived ^{242}Pu is not a major contributor to the long-term radioactivity of nuclear waste, but it is of interest in this work as it has a relatively small thermal neutron capture cross section compared to other actinides. If the method presented can be applied to ^{242}Pu, it can be assumed to be successful for other actinides having larger cross sections, too.

Additionally, thermal capture cross section data are fundamental for reactor burnup calculations and thus for the determination of radioactive inventory in spent nuclear fuel. However, the thermal capture cross section data of actinides are often not measured well and disagree with each other in different evaluated data tables, such as the Evaluated Nuclear Data File (ENDF) (USA)[5], the Joint Evaluated Fission and Fusion File (JEFF) (OECD)[6] or the Japanese Evaluated Nuclear Data Library (JENDL) (Japan)[7]. It is therefore the objective of this work, besides measuring the PGAA-data, to determine the thermal radiative neutron capture cross sections of the investigated nuclides. These measurements are possible by measuring the decay radiation after the neutron irradiation

– for the PGAA measurements – terminated.

To summarize, the objective of this work is to present a method for the accurate and precise measurement of the prompt γ-ray energies and partial thermal radiative neutron capture cross sections of actinides and to provide experimental data with realistic uncertainties for the selected actinides (^{237}Np, ^{241}Am and ^{242}Pu). It is also the objective of this work to measure the thermal radiative capture cross sections of the investigated actinides and to investigate the potential of PGAA for quantifying actinide residues in complex matrices originating from nuclear installations and activities (e.g. in nuclear waste matrices or safeguard swipe samples). In the future, these improved nuclear data can be used to develop innovative analytical methods for identification and quantification of such actinides using PGAA as a non-destructive and reliable tool.

CHAPTER II

Physical and Technical Background

In this section the necessary background information underlying this thesis will be provided. For more detailed information beyond the scope of this section please refer to textbooks such as [2, 8, 9, 10] on which also the contents of this section is based. In this preface, a brief description will be given of units, dimensions and, the basic particles and forces from the standard model of particle physics. Then the atomic structure will be discussed in the first section. After that the structure of the atomic nucleus and its constituents – the nucleons – is discussed. The next section gives an overview of nuclear reactions, focusing especially on the (n,γ) reaction which is the fundamental reaction underlying the method presented in this work. Then the radiation following a nuclear reaction will be discussed before the principles of γ-ray detection will be explained. Combining these principles, a section describing the method of PGAA employed in this work will follow. At the end of this section a short description of Monte Carlo methods will be given, which utilize experimental and theoretical results for the simulation of particle movement in environments too complex to calculate.

Due to their comparable small quantity the units used in this work are usually not given in the International System of Units (SI) [11]. A brief description of the used non-SI units is tabulated in Table 2.1. Of these the connection between mass and energy is given by Einstein's energy-mass-equivalence [12]

$$E = mc^2, \tag{2.1}$$

with E being the energy, m the mass of a particle, and c the speed of light in vacuum.

Dimension	unit	unit name	SI unit equivalent
Length	Å	Angstrom	$1 \cdot 10^{-10}$ m
Cross section	b	Barn	$1 \cdot 10^{-28}$ m^2
Energy	eV	Electronvolt	$1.602\,176\,565 \cdot 10^{-19}$ J
Mass	u	Atomic mass unit	$1.660\,538\,921 \cdot 10^{-27}$ kg
Mass	eV/c^2	–	$1.782\,662 \cdot 10^{-36}$ kg
Charge	e	Elementary charge	$1.602\,176\,565 \cdot 10^{-19}$ C

Table 2.1: Non-SI units used in this thesis.

Of the vast number of elementary particles known in particle physics, matter is basically built up of the stable electron (e^-), the up- and the down-Quark (u,d). In this work the anti-electron called "positron" (e^+) is also important as well as the uncharged electron neutrino (ν_e) and respective anti-neutrino ($\bar{\nu_e}$). These particles are all proxies of the so-called "fermions", which are particles with an intrinsic angular momentum called "spin", of $\frac{\hbar}{2}$. For the sake of simplicity it is usually given as $\frac{1}{2}$ omitting $\hbar$ ($\hbar = \frac{h}{2\pi} \approx 1.054\,572 \cdot 10^{-34}$ Js) $= 6.582\,119 \cdot 10^{-16}$ eV s is the reduced Planck constant). The electron possesses the smallest indivisible free charge in nature -e. Its antiparticle, the positron, carries its negation which is a charge of $+e = e$.

The fundamental forces or interactions between particles are the strong, the electromagnetic, the weak and the gravitational force. The latter is not relevant for processes discussed in this work as it is several orders of magnitude weaker than the other forces. While the electromagnetic and gravitational interaction basically have an infinite range with their potential following a $1/r$-law with the distance r between the interacting particles, the strong and weak force only have a finite range. In particle physics these forces are quantized. An interaction between two particles is therefore described by the exchange of virtual particles created within the limits of the uncertainty principle [13]. This principle is formulated as:

$$s_E \cdot s_t \geq \frac{\hbar}{2}, \tag{2.2}$$

with s_E, s_t being the standard deviations of the energy E and the life time t of a particle state in a measurement [13, 14]. For these forces, basically the rule is that the more energy is needed to "create" such a particle the shorter the time it can exist. The particles mediating the fundamental forces are called "bosons". They have an integer spin. For the strong interaction these bosons are the six gluons (g), for the electromagnetic interaction it is the photon (γ) and for the weak interaction there are the charged W^+-,W^-- and uncharged Z^0-bosons. The particles and their properties are listed in Table 2.2.

According to the quantum mechanical principle of wave-particle duality, a wave (like the classical electromagnetic radiation), besides its wave character, also has particle character and particles also exhibit wave characteristics. This is true of compound particles as well as elementary particles. A matter wave can thus be assigned to each particle. For particle velocities $v \ll c$ (the non-relativistic case) the wavelength of the assigned matter wave is given by the de'Broglie wavelength [16]:

$$\lambda = \frac{h}{m \cdot v} = \frac{h}{\sqrt{2m \cdot E_{kin}}}, \tag{2.3}$$

with m being the mass and E_{kin} the kinetic energy of the particle. The higher the mass

Class	Particle	Mass [MeV]	Charge [e]	Spin [$\hbar$]	Interacting
Leptons	e^-	0.510 998 928	-1	1/2	EM,W
	e^+	0.510 998 928	1	1/2	EM,W
	ν_e	$< 2 \cdot 10^{-6}$	0	1/2	EM,W
	$\bar{\nu_e}$	$< 2 \cdot 10^{-6}$	0	1/2	EM,W
	u	$\approx$2.3	2/3	1/2	S,EM,W
	d	$\approx$4.8	$-1/3$	1/2	S,EM,W
Bosons	γ	0	0	1	EM
	g	0	0	1	S
	$W^{+/-}$	80.385	0	1	W
	Z^0	91.1876	0	1	W

Table 2.2: Table of particles relevant for this work together with key properties [15]. The type of interaction that the particles participate in is denoted by EM (elecrotmagnetic), S (strong) and W (weak).

or velocity of a particle, the smaller the wavelength will be. Thus, the wave nature of the particle in this case becomes less important for measurements. Due to the wave nature of a particle it can basically be described in terms of a wave function. Through superposition wave functions of singular particles add up, so that even complex systems can be described by a single wave function.

The evolution of such a wave function is given by the Schrödinger equation. For stable (time independent) particle systems at non-relativistic velocities the general Schrödinger equation for a particle with wave function $\Psi(\mathbf{r})$ in a potential $V(\mathbf{r})$ is

$$E\Psi(\mathbf{r}) = \left[\frac{-\hbar^2}{2m}\Delta' + V(\mathbf{r})\right]\Psi(\mathbf{r}), \tag{2.4}$$

here $\mathbf{r}$ being the vector to a position in space and Δ' the Laplace operator. In one dimension the Laplace operator is simply the second derivative. Note that, in this case, the energy of the system is constant and equivalent to the eigenvalue of the Schrödinger equation E. Also note that a solution with an energy E lower than the maximal potential $V(\mathbf{r})$ is called a bound state, as opposed to an unbound state where the particle can move freely. The Schrödinger equation has only in a number of special cases an analytical solution, but it is very useful for the description of the bound states of atoms and atomic nuclei. These will be discussed in the following.

2.1 Atomic Structure

During the early development of Chemistry John Dalton explained the observation of stoichiometry in chemical reactions with the concept that all matter is composed of small units called "atoms". With Joseph John Thomson's discovery of the negatively charged electron e^- which could be extracted by ionizing an atom (that is removal of an electron from an atomic shell) it was established that atoms had to be composed of electrons and an equal amount of positively charged matter, as atoms themselves were known to be uncharged. In the beginning of the 20th century Ernest Rutherford *et al.* performed scattering experiments with positively charged $^2He^+$, so-called α-particles, emitted in the radioactive decay of radium on gold atoms. They found that the atom consisted of a small positively charged core the so-called "atomic nucleus" (or simply "nucleus") holding practically all of the mass of the atom, and a number of electrons [17], somehow distributed around the nucleus. Due to these observations and the similarity of the potential of the electromagnetic force to that of the gravitational force with its $1/r$-dependence an atomic model with electrons orbiting the nucleus like planets orbiting the sun was developed. It was established that the nucleus carries a charge of Ze, where Z corresponds to the atomic number which uniquely identifies a chemical element, and that the nucleus is orbited b s Bohr to include c ation that electrons lustration of the Bo

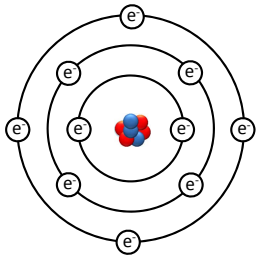

Figure 2.1: Bohr/Rutherford model of the atom, with electrons e^- orbiting the atomic nucleus on discrete orbits.

When several years later Erwin Schrödinger formulated an equation (described in the preface) the current form of the atomic model was developed [19, 20], which will now be discussed in more detail.

The model of the atom involves a nearly spherical symmetric potential only dependent on the distance from the center of the atomic nucleus r. For such problems it is convenient to use spherical coordinates and determine separable solutions of the Schrödinger equation of the form $\Psi(r, \theta, \phi) = R(r)Y(\theta, \phi)$. To explain the basic features of the solution of the

Schrödinger equation, a single particle in a central potential is assumed. The angular part of this form of the Schrödinger equation can hence be solved using the eigenfunctions of the angular part of the Laplace operator. These eigenfunctions are the so-called Laplace spherical harmonic functions $Y_\ell^{m_l}(\theta, \phi)$, with l being a non-negative integer number and m_l being an integer number with

$$-l \leq m_l \leq l. \tag{2.5}$$

This means there are $(2l + 1)$ spherical harmonic functions for each value of l. When there is more than one possible solution for the wave function of a particle in a potential for the same energy eigenvalue, the level described by this energy eigenvalue is called "degenerate". So all spherical symmetric potentials have a $(2l+1)$ level degeneracy. Since the angular part of the Laplace operator is proportional to the square of the angular momentum operator $\hat{\mathbf{L}}$, the angular momentum vector $\mathbf{L}$ is also quantized with its length being $\sqrt{l(l+1)} \cdot \hbar$. Therefore, the quantum number l is called "angular quantum number". The quantum number m_l corresponds to the z-component of $\mathbf{L}$ and thus also follows that $-l \leq m_l \leq l$. It is called the "magnetic quantum number" and specifies the exact wave function that applies to a particle in a level. Wave functions having an angular quantum number $l = 0$ are called "s-orbitals", those with $l = 1$ are "p-orbitals" and those with $l = 2$ are called "d-orbitals" etc.

The radial part of the Schrödinger equation is

$$E_n \cdot R(r) = \frac{\hbar^2}{2m} \left(\frac{\partial^2 R(r)}{\partial r^2} + \frac{2}{r} \frac{\partial R(r)}{\partial r} \right) + \left[V(r) + \frac{l(l+1)\hbar^2}{2 \cdot m \cdot r^2} \right] \cdot R(r). \tag{2.6}$$

Note that an angular momentum dependent part is added to the central potential. The term $\frac{l(l+1)\hbar^2}{2 \cdot m \cdot r^2}$ is called the "centrifugal potential". Thus, the effective potential depends on the angular momentum state. As the centrifugal potential is positive for $l \neq 0$, thus repellent, and added to the original central potential the effective potential becomes positive eventually creating the so-called "centrifugal barrier".
An electron in a central potential alike the potential of an atomic nucleus with charge Ze yields the potential

$$V(r) = -\frac{Ze^2}{2\pi\epsilon_0 \cdot r}, \tag{2.7}$$

with the vacuum permittivity ϵ_0.

This problem described by equation 2.6 with the potential of equation 2.7 can be solved employing Laguerre polynomials multiplied by exponential functions. The energy eigenvalues and thus the level energies then are

$$E_n = -\frac{mZ^2e^4}{32\pi^2{\epsilon_0}^2\hbar^2 \cdot n^2}, \tag{2.8}$$

with n being the principal quantum number. The energy of a solution corresponds to an energy level, because it is a possible state of a particle bound in the system. A bound state solution of any Schrödinger equation for the principal quantum number $n = 1$ is called "ground state", as it is the lowest possible state in the potential. All other solutions for $n > 1$ are called excited states. All bound state solutions with a different energy eigenvalue are called levels and can be uniquely identified by the principal quantum number. It holds that $0 \leq l < n$, such that the total degeneracy of each level is $\sum_{l=0}^{n-1}(2l+1) = n^2$. Note that the distance between two energy levels defined by equation 2.8 decreases with higher energy ($n \propto 1/\sqrt{E_n}$), that is the spacing gets smaller and practically gives rise to an infinite number of possible levels, a quasi-continuum of levels, up to the point where the electron has enough energy to reach the continuum and is treated as a free particle.
In reality even the simplest atom like the ^{1}H is a two particle system, but for ^{1}H or ions like $^2He^+$, with only one electron, the system can still be solved analytically by a calculation in their center of mass system. The results follow the same $E_n \propto Z^2/n^2$ dependence of the energy levels as the single-particle discussion above.

Due to the fact that s-orbitals are always spherical symmetric and the nucleus is not point-like, the electron has a non-zero probability of being inside the nucleus. The average distance of an electron in the $n = 1$ s-orbital from the nucleus is $3/2 \cdot a_0$, with $a_0 \approx 0.529\,\text{Å}$ being the Bohr atomic radius, which is the smallest orbit an electron can have according to Bohr's atomic model. The probability of finding an electron within a_0 is $\approx 32\,\%$ for an $n = 1$ s-orbital and decreases for the higher s-orbitals, for instance to $\approx 3.4\,\%$ for the $n = 2$ s-orbital. With higher angular momentum the probability of finding the electron within a_0 decreases, for instance for the $n = 2$ p-orbital this probability is $\approx 0.4\,\%$. This means that for higher n and $l = n - 1$ the spacial probability distribution becomes more and more like a classical orbit [21]. Note that with higher n the electron has on average a larger distance from the nucleus, so it becomes more and more "free". See Figure 2.2 for a schematic of an s- and p-orbital for illustration. Summing up all possible orbitals for a given n yields the total probability distribution for an electron for that level. Note that this sum is always spherical symmetric and therefore the levels in an atom are called "shells" giving rise to the name "shell model".

There are some effects that decrease the above discussed degeneracy of energy levels that will be reviewed briefly. In quantum theory a particle possesses a kind of intrinsic angular momentum, called the "spin" $\mathbf{S}$. The length of $|\mathbf{S}| = \sqrt{s(s+1)}\hbar$. So its associated quantum number is s and its projection on the z-axis is $\hbar m_s$ with the the spin projection quantum number m_s. For fermions $s = 1/2$ and thus $m_s = \pm 1/2$. The angular momentum vector $\mathbf{L}$ adds up with the spin $\mathbf{S}$ to the total angular momentum $\mathbf{J}$:

$$\mathbf{J} = \mathbf{L} + \mathbf{S} \tag{2.9}$$

$$|\mathbf{J}| = \sqrt{j(j+1)}\hbar \tag{2.10}$$

$$\tag{2.11}$$

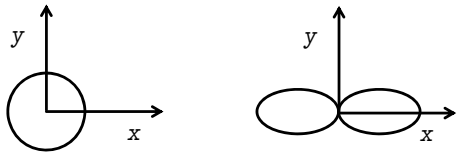

s-orbital p-orbital

Figure 2.2: Schematic illustrations of s- and p-orbital solutions of the Schrödinger equation in a central potential.

and its z-component $|\mathbf{J}_z|$

$$|\mathbf{J}_z| = \hbar m_j, \text{with} \tag{2.12}$$

$$m_j = m_l + m_s = m_l \pm \frac{1}{2}. \tag{2.13}$$

Since m_l is an integer and m_s for fermions is half of an integer, m_j must also be half of an integer value. For an electron in an atomic orbital with angular momentum l this yields two possible values for j. Due to effects such as the so-called the "spin-orbit-interaction" resulting from electrodynamics, the "Darwin term" resulting from special relativity, and "Lamb Shift" resulting from the quantization of the electromagnetic field the l degeneracy of the levels is lifted creating a so-called "fine structure".
By treating the nucleus not as a point-like static object also the m_l degeneracy is lifted creating the "hyperfine structure". For further information please refer to a text book such as in reference [22].
These effects create a very complex level structure even in these comparably simple cases.

Another important property of the angular solutions of the Schrödinger equation is the behavior of $Y_\ell^{m_l}(\theta, \phi)$ under a parity operation, which is the inversion of coordinates through the origin, yielding for spherical coordinates

$$\theta \to \pi - \theta \tag{2.14}$$

$$\phi \to \pi + \phi \tag{2.15}$$

which is a reflection in θ and a rotation in ϕ. A parity operation $\hat{\mathbf{P}}$ applied two times to the same system will result in the original system state. Thus, $\hat{\mathbf{P}}(\hat{\mathbf{P}}\Psi(r, \theta, \phi)) = \Psi(r, \theta, \phi)$ and therefore $\hat{\mathbf{P}}$ has eigenvalues of $P = \pm 1$. If $P = +1$ the system has even parity, if $P = -1$ the system has odd parity. The Hamiltonian of this problem is invariant under the parity operation $\hat{\mathbf{P}}$, because its potential is radial symmetric. Thus, the energy levels

and any observable property of the system remain unchanged when the system is reflected. This yields $|\Psi(r,\theta,\phi)|^2 = |\Psi(-r,\pi-\theta,\pi+\phi)|^2$ and thus $\Psi(r,\theta,\phi) = \pm\Psi(-r,\pi-\theta,\pi+\phi)$. It can be shown that the parity operator maps the spherical harmonic functions as

$$\hat{\mathbf{P}}Y_\ell^{m_l}(\theta,\phi) = (-1)^l \cdot Y_\ell^{m_l}(\theta,\phi). \tag{2.16}$$

So a wave function can have either odd or even parity.

For systems with more than one electron (the typical case in atoms aside hydrogen), an analytical solution of the Schrödinger equation is not possible. Nevertheless in such systems basically all the mentioned principles remain valid, so that every atom has a unique shell structure. The major problem is the interaction of the electrons with one another. An electron in the ground state will dampen the potential for any electron that is further away from the nucleus. The simplest theoretical approach is to neglect the interaction of electrons within a shell and to solve the Schrödinger equation of an electron with the Coulomb potential of the nucleus dampened by the inner shell electrons. A few qualitative descriptions of multi-electron systems will now be given.
According to the Pauli exclusion principle [23] two fermions cannot have the same quantum numbers, that is the same wave functions. Since a fermion has a spin which can be either positive or negative, the ground state of an atom can be occupied by at most two fermions at once in the s-orbital. The first excited level can be occupied by up to four fermions in both s- and p-orbitals and so on.
The fundamental rule that physical systems approach a state of minimal energy applies and suggests that the inner shells will be filled first. The order in which orbitals in the shells and subshells are filled is given by Hund's rules. The first of which is the result of the Pauli exclusion principle that shells and subshells are closed if all possible states (defined by all quantum numbers) are occupied by an electron. It follows that the total angular momentum of a closed shell is 0. The second of Hund's rules is that the energy of the electrons is minimal if the sum of the electron spins is maximal. Thus, if an orbital is occupied by one electron, other orbitals (of the same energy) will be occupied with spins of the same direction as the spin of the first electron, before a second electron of opposite spin occupies the same orbital.
The third rule concerns the ordering in which states with different m_l are occupied. Since higher m_l states have a greater average distance from the nucleus they also have a higher average distance from one another. Thus, states with higher value of m_l will be occupied first.
Electrons occupying the outermost orbitals are called "valence electrons". These are not necessarily electrons of the highest energetic shell, because the distance of levels becomes very small. In heavier atoms the number of electrons is larger and subshells can have a spacing so that electrons in higher l states can have a larger distance from the nucleus than electrons occupying the next higher energetic shell (e.g. lanthanides and actinides).

This discussion gives a reasonable understanding of how the atom is built up, of the

electron structure and the Schrödinger equation, which will be useful in the next sections. Further details can be found in text books like [22, 21]. In the following section the structure of the nucleus will be discussed in analogy to the discussion of the electron structure in this section.

2.2 Nuclear Structure

The atomic nucleus itself consists of Z positively charged protons (p), with charge $+e$, and N uncharged neutrons (n). As they are constituents of the nucleus these particles are called nucleons and their total number corresponds to the atomic mass number $A = Z+N$. The proton is identical with $^1\mathrm{H}^+$, the fully ionized hydrogen atom that is the hydrogen nucleus, which is the smallest nucleus of all elements. The proton has a mass of $1.007\,\mathrm{u} = 938.27\,\mathrm{MeV/c^2}$ and the neutron has a slightly higher mass of $1.008\,\mathrm{u} = 939.57\,\mathrm{MeV/c^2}$. Thus, a nucleus can be uniquely identified with its mass number A and atomic number Z and the corresponding atom is called a nuclide. Nuclides with the same Z but different A, that is different number of neutrons, are called isotopes. Nuclides with identical A but different Z, that is different number of protons, are isobars. Nuclides with both identical Z and A but different energy states of the nucleons are called isomers.

The mean nuclear radius can be approximated by

$$R \approx R_0 \cdot \sqrt[3]{A}, \qquad R_0 = 1.2\text{–}1.25\,\mathrm{fm}, \tag{2.17}$$

based on experimental scattering results yielding a constant nuclear density (see reference [10]). Thus, the nucleus has a dimension in the fm-range, being roughly five orders of magnitude smaller than the electron shell of an atom.

A nucleon can be separated from a nucleus if at least its binding energy is transferred to it, alike the ionization of an atom. Within the scope of this work, the neutron separation energy S_n is of most interest. It is the minimum energy needed to remove a neutron from a nuclide ${}^{\mathrm{Z}}_{\mathrm{A}}\mathrm{X}$, which correspond to the difference in binding energies E_B between a nucleus $(A,\, Z)$ and its next lighter isotope $(A-1,\, Z)$ as described in equation 2.18.

$$S_\mathrm{n} = m({}^{\mathrm{A}}_{\mathrm{Z}}\mathrm{X}) + m_n - m({}^{\mathrm{A-1}}_{\mathrm{Z}}\mathrm{X}), \qquad \text{masses } m \text{ in eV}. \tag{2.18}$$

The nucleons themselves are not structureless particles but are composed of quarks and bound together by the strong force. The differences in charge and mass between a neutron and a proton are direct effects of their different valence quarks. A proton consists of two u- and one d-Quark and thus has a charge of $1\,e$ and the neutron consisting of two d- and one u-Quark is thus not charged but has a higher mass.

The strong force is based on the exchange of gluons (g). The interaction between nucleons is weaker and is based on a secondary interaction between their constituent quarks, which is a meson exchange as depicted in Figure 2.3. Quarks are fermions and thus due to the Pauli exclusion principle they cannot occupy the same quantum state. This prevents the quarks of different nucleons from direct exchange, effectively causing a kind of repulsive force at small distances. Thus the potential of the force between nucleons is much more complicated than that of the gluon exchange and is usually given in terms of an effective potential.

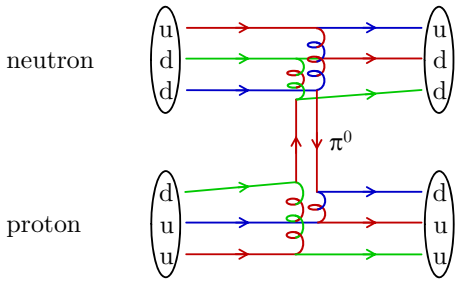

Figure 2.3: A Feynman graph depicting the exchange of a π^0-meson between two nucleons. The colors correspond to the color charge of the quarks (lines) and gluons (spirals).

A nucleus can in principle be described as a quantum system using the Schrödinger equation, but since the nucleons interact via both the strong and the Coulomb force and each nucleon interacts with all the others there would be $A \cdot Z!$ interactions involved. This is even far more complex than the problem with multiple electrons in the atomic shells. With the assumption of the nuclear potential being approximately spherical in analogy to the atomic shell model, a quantum state in a nucleus is also described by the principal quantum number n, an angular momentum with quantum numbers l and m_l and the spin s with m_s, thus the total angular momentum quantum number is again j with m_j. A possible quantum state for a nucleon also has a parity associated with it. It is often feasible to approximate the nucleus as a single object with a nuclear spin $\mathbf{I}$, which is the vector sum of all A nucleons' angular momenta j, and a parity P. If a single nucleon with $\mathbf{j}_{\text{nucleon}}$ determines all the properties of the nucleus, the nucleus has a nuclear spin of $\mathbf{J} = \mathbf{I}_{\text{g.s.}} + \mathbf{j}_{\text{nucleon}}$ in which $\mathbf{I}_{\text{g.s.}}$ is the nuclear spin of the rest nucleus with its nucleons in ground state. $\mathbf{J}$ corresponds to the total angular momentum of the nucleus with its length being J, but is determined by the angular momentum state of a single nucleon ($\mathbf{j}_{\text{nucleon}}$). Thus, J is usually assigned to a level in the nuclear level scheme. The parity of a nucleon in that state is denoted in a superscript to the nuclear spin as $J^{\pm}$, with $+$ denoting even and $-$ odd parity, even though there is no theoretical connection of J and P. Since nucleons have half integer values of j, J has an integer value for nuclei with even A and half integer values for nuclei with odd A.

The nuclear shell model treats nucleons as a non-interacting Fermi-gas [24, 25], corresponding to the treatment of electrons in the atomic shell model, approximating the forces between the nucleons with an effective central potential. An approximation of this potential is given by the Woods-Saxon potential [26]

$$V(r) = -\frac{V_0}{1 + \exp(\frac{r-R}{a})}, \tag{2.19}$$

with R being the nuclear radius from equation 2.17. The empirical constant V_0 is in the order of 50 MeV and depends on the measured nucleon separation energy. a is also deduced from measurements and in the order of 0.5 fm to 0.7 fm [27]. An interaction similar to the electron spin-orbit interaction, giving rise to the atomic fine structure, is much stronger for nucleons. Thus, the degeneracy of subshells is lifted and the shells and levels from the Woods-Saxon potential are altered. This model is capable of describing several measured nuclear properties, but is still a major simplification, as it assumes that all but one nucleons are paired, thus basing all nuclear properties on this unpaired valence nucleon [10].
Since the effective potentials for neutrons and protons are different due to the Coulomb force, the energy levels are also different. More precisely, the repellent Coulomb force between protons decreases the depth of the potential. This results in there being, in principle, more bound states (levels) for neutrons in a nucleus than for protons, as the neutron separation energy is generally higher than the proton separation energy. This observation is reflected well in the chart of nuclides.
A problem of this model is that unlike the electrons in the atomic shell model, the nucleons' dimensions are in the same order of magnitude as the dimension of the entire nucleus. Thus, collisions are likely. But if all levels are filled to an extent that no nucleon is able to gain enough energy in a single collision to be excited into a free level, no energy will be transferred because the collision cannot occur. Thus, the nucleons can be regarded as independent and thus they can be assigned to a kind of orbital. The number of nucleons in a closed shell corresponds to the so-called "magic numbers", which mark especially well-bound nuclei. The nuclear shell model is able to reproduce and predict new magic numbers, but it also predicts and most importantly explains the ground state spins and parities of nuclei reasonably well. It comes to its limits, though, with excited states in more complex nuclei. A schematic view of the levels of protons and neutrons in the Woods-Saxon potential can be seen in Figure 2.4.

Note that due to the uncertainty principle (equation 2.2) a level cannot have a certain energy but has to cover an energy region. The more stable, that is the longer-lived, a state with a nucleon in that level is, the sharper is the energy distribution. This can be described with a Breit-Wigner distribution

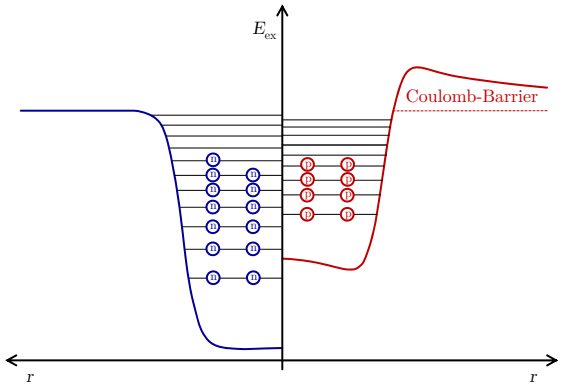

Figure 2.4: Effective potential for nucleons in an atomic nucleus of Woods-Saxon and Coulomb type for angular momentum $l = 0$, the red line corresponds to the effective potential for protons (red circles) and the blue line to the potential of neutrons (blue circles). The spacing between energy levels decreases with the square root in excitation energy E_{ex} due to the idealized Fermi-gas phase space. Each level is filled with up to two nucleons with opposite spins according to the Fermi-Dirac statistics.

$$p(E) = \frac{1}{2\pi} \frac{\Gamma}{(E - M)^2 + \Gamma^2/4}, \tag{2.20}$$

with the natural line width $\Gamma = \hbar/\tau$ and the lifetime of the state τ. The natural width for typical levels is smaller than 10^{-4} eV and thus usually negligible, as typical level spacings are in the range of keV for low energetic nuclear levels. This also means that the levels can still be separated, as the spacing between levels is usually higher than the width of the individual levels. As the level spacing becomes smaller with higher energy due to their width the levels overlap forming a quasi-continuum of levels. This is the case especially for states above the nucleon separation energy.

In reality these assumptions are not met and even the approach of introducing a multi-particle shell model, accounting for collective effects of the nucleons, does not account for effects like the deformation of larger nuclei. So especially in large nuclei the level schemes are very complicated and cannot be calculated from theory to a good approximation. Thus, the specific levels have to be determined experimentally. By the theory, however, a good model on the statistical property of these levels is provided. A quantity called the level density $\rho(E_{ex}, J)$, which is the number of levels per unit energy, can be predicted [28, 29, 30].
The specific models that are used in this work are the constant temperature formula (CTF)

and the Backshifted Fermi-gas (BSFG) level density (LD) models. Both models are based on the number of nucleons A, the nuclear angular momentum J and excitation energy E_{ex}.

2.2.1 Backshifted Fermi Gas Model

For the BSFG model the nucleons of a nucleus are considered to be a non-interacting Fermi-gas [31, 32]. This is the same assumption as for the deduction of the shell structure in the nuclear shell model. The Fermi-gas model is altered to account for non-equidistant states near the Fermi-energy due to the shell structure and nucleon-nucleon pairings. It is "back-shifted" in excitation energy by an energy parameter E_1, which accounts for the extra amount of energy necessary to break-up nucleon-nucleon pairs. It can be written as

$$\rho_{\mathrm{BSFG}}(E_{\mathrm{ex}}, J) = f(J) \cdot \pi(E_{\mathrm{ex}}) \cdot \frac{\exp(2\sqrt{a(E_{\mathrm{ex}} - E_1)})}{12\sqrt{2}S_{\mathrm{cut}}\sqrt[4]{a}(E_{\mathrm{ex}} - E_1)^{5/4}}, \tag{2.21}$$

with the spin distribution factor

$$f(J) = \frac{2J+1}{2S_{\mathrm{cut}}^2} \cdot \exp\left(-\frac{(J+\frac{1}{2})^2}{2S_{\mathrm{cut}}^2}\right), \tag{2.22}$$

describing the distribution of J for a given excitation energy E_{ex} and the spin cut-off factor

$$S_{\mathrm{cut}} = \sqrt{\left(0.0146 \cdot A^{\frac{5}{3}} \cdot \frac{1+\sqrt{1+4a(E_{\mathrm{ex}} - E_1)}}{2a}\right)} \tag{2.23}$$

a is the level density parameter deduced from the shell model, which is slightly energy dependent, approximately following $a \propto 0.21 \cdot A^{0.87}\mathrm{MeV}^{-1}$ [33]. This parameter is taken from the parameterization by von Egidy and Bucurescu [34].
The parity dependence $\pi(E_{\mathrm{ex}})$ accounts for the observation that one specific parity is more likely than the other for low energetic levels, whereas for higher energetic levels the parities are equally distributed among the levels. The parity dependence is assumed to follow a Fermi-Dirac distribution and is based on the semi-empirical mass formula as described in reference [35].

$$\pi(E_{\mathrm{ex}}) = \frac{1}{2} \cdot \left(1 \pm \frac{1}{1+\exp(c(E_{\mathrm{ex}} + \delta_p))}\right), \tag{2.24}$$

where "+" is used for the parity dominant for the lower energetic levels (either positive or negative parity) and "-" for the other parity. The factors $c = 3\,\mathrm{MeV}^{-1}$ and $\delta = a_0 + a_1/A^{a_2}$ are empirically determined from fitting this function to experimental data in the nuclear mass region $10 \leq A \leq 110$ [35]. In this work it is used to describe the level density of the nucleus ^{243}Pu with an even atomic number and odd mass number and thus $a_0 = -0.08$, $a_1 = 75.22$ and $a_2 = 0.89$ according to reference [35].

2.2.2 Constant Temperature Model

The CTF describes the nucleons as a classical ideal gas at a definite temperature resulting in a simpler level density of

$$\rho_{\mathrm{CTF}}(E_{\mathrm{ex}}, J) = \frac{f(J) \cdot \pi(E_{\mathrm{ex}})}{\theta} \cdot \exp\left(\frac{E_{\mathrm{ex}} - E_0}{\theta}\right), \tag{2.25}$$

$f(J)$ being the spin distribution factor and $\pi(E_{\mathrm{ex}})$ the parity dependence. $E_0 = E_1 - 821\,\mathrm{keV}$ is the back-shift parameter [36] and $\theta = a^{-0.733}$ is the critical temperature to break-up nucleon-nucleon pairs.

The results of both models differ primarily at low excitation energies. This is the region were the level spacings are often large enough for the levels to be directly deducible from experiment. Parameterizations of these models based on experimental data can be found in [34], showing good agreement with measured levels, for instance, for the heavy nucleus ^{242}Am. Both models reproduce the known levels well, starting from an excitation energy of about 150 keV.

2.3 Neutron Reactions with Nuclei

Free neutrons that can be created for instance in nuclear fission inside a reactor can interact with nuclei on their path. A neutron of a given kinetic energy E_{n} is not affected by the Coulomb force of a nucleus and can therefore reach the attracting strong potential of a nucleus even with low kinetic energies. In the following, the kinetic energy of a neutron is simply referred to as the neutron energy, since the rest energy is constant. Because interactions between an incident neutron and a nucleus depend on the neutron energy it is useful to partition neutrons into categories. Thermal neutrons have an energy of $E_{\mathrm{th}} = 0.0253\,\mathrm{eV}$, corresponding to their average energy at room temperature. Cold neutrons have an energy below that value $E_{\mathrm{n}} < E_{\mathrm{th}}$ and fast neutrons have an energy $E_{\mathrm{n}} > 1\,\mathrm{MeV}$. Epithermal neutrons have energies in the range between thermal and fast neutron energies.

A neutron, depending on its energy, can interact with a nucleus by several mechanisms. It can undergo elastic or inelastic scattering where the neutron exchanges energy with the nucleus. In the case of elastic scattering the total kinetic energy of the system stays constant and is divided between the neutron and the nucleus depending on the scattering angle and masses of the involved nucleus and neutron. In the case of inelastic scattering the neutron is absorbed by the nucleus but a neutron is re-emitted shortly after, which can be depicted as an $(\mathrm{n}, \mathrm{n}')$ reaction. In this process the energy transfer to the nucleons in the scattering nucleus can lead for instance to nucleons being transferred to higher energy levels (leaving the nucleus in an excited state). Other processes occurring after the neutron absorption, that do not lead to a re-emission of a neutron are for instance the radiative capture process (n, γ) in which a new nucleus the so-called "compound nucleus" is formed with the original nucleons and the incident neutron of energy E_n occupying the so-called "capture state". In this process an excited compound nucleus with excitation energy

$$E_\mathrm{c.s.} = S_\mathrm{n} + E_\mathrm{n}, \tag{2.26}$$

is formed. For thermal and cold neutrons the neutron's kinetic energy is negligible and hence $E_\mathrm{c.s.}$ is only slightly higher than the neutron separation energy S_n. Due to the centrifugal barrier (see equation 2.6) at these energies neutron capture with a neutron angular momentum $l = 0$ relative to the nucleus is dominant – so-called "s-wave capture". The angular momentum of the capture state is given by

$$J_\mathrm{c.s.} = I_\mathrm{nucleus} \pm \frac{1}{2} \qquad \text{if } I_\mathrm{nucleus} \neq 0 \tag{2.27}$$

or

$$J_\mathrm{c.s.} = \frac{1}{2} \qquad \text{if } I_\mathrm{nucleus} = 0 \tag{2.28}$$

where I_nucleus is the nuclear spin of the capturing nucleus. Due to parity conservation the parity of the capture state is identical to the parity of the capturing, that is the target, nucleus.

At higher neutron energies other reactions including the (n, α) reaction, with the emission of an α-particle, (n, p) or $(\mathrm{n}, 2\,\mathrm{n})$ may occur. With the exception of radiative neutron capture (the (n, γ) reaction) the cross sections for these processes usually are small or zero for cold and thermal neutrons, since not enough energy is transferred into the compound nucleus by the incident neutron, as can be seen exemplary for ^{197}Au in Figure 2.5. An important exception is the $^{6}\mathrm{Li}(\mathrm{n}, \alpha)^{3}\mathrm{H}$ reaction, which has a thermal cross section of 940 b[37] compared to a thermal capture cross section of 39 mb [5], as well as

the $^{10}B(n,\alpha)^{7}Li$, with a thermal (n,α)[5] cross section of 3842 b and a thermal capture cross section of 0.5 b[5]. The high cross sections for these nuclei can be utilized to absorb neutrons and thus for neutron radiation shielding.

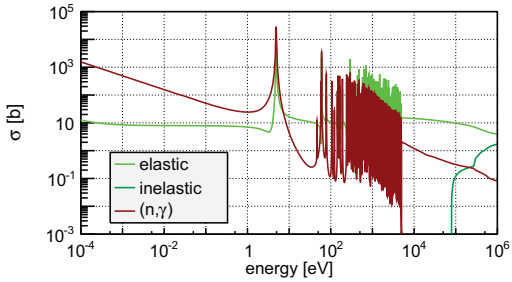

Figure 2.5: Cross section for radiative capture, elastic and inelastic scattering of ^{197}Au.

For thermal and cold neutrons the probability of being absorbed and thus the cross section $\sigma_{abs}(E_n)$ is basically dependent on the time the neutron is in the range of the nuclear force. Thus it can be understood that the capture cross section is anti-proportional to the velocity of the neutron or in terms of energy of the neutron E_n

$$\sigma_{abs}(E_n) \propto \frac{1}{\sqrt{E_n}}. \tag{2.29}$$

Thus the cross section can be described by a single known cross section value, usually the thermal cross section $\sigma_{0,abs}$ for the whole region with

$$\sigma_{abs}(E_n) = \sigma_{0,abs}\sqrt{\frac{E_0}{E_n}}. \tag{2.30}$$

The relation of equation 2.30 holds for low neutron energies below the first resonance (if any) in the cross section, that is a possible quasi-bound level above the neutron separation energy. The formation of these resonances can be understood by taking into account the phase of the neutron wave function inside and outside the nuclear potential. Due to the continuity condition for the Schrödinger equation for specific energies both functions will match in their maximum amplitudes, strongly increasing the probability of the compound nucleus formation in these cases. For details please refer to reference [10]. As this is a resonant reaction it can be described also in terms of a Lorentzian function like the Breit-Wigner function (equation 2.20), but it can be distorted by direct scattering of the neutron at the nuclear potential, causing over and under fluctuations before and after the resonance. From the Lorentzian equation the $1/\sqrt{E_n}$-law can also be deduced for energies much smaller than the resonance energy [38]. A resonance causes a distortion from the

$1/\sqrt{E_\mathrm{n}}$-law as can be seen in Figure 2.6 exemplary for the ^{241}Am radiative capture cross section, with its especially low energetic resonance at 0.307 eV. It can be seen that the distortion is not strictly positive but can lead to a decrease of the cross section below the expected $1/\sqrt{E_\mathrm{n}}$ behavior in front of the resonance. Note that all processes that can occur after the neutron absorption show the same behavior exhibiting the same resonances. In particular the radiative neutron capture cross section exhibits these resonances. The lowest energy at which resonances occur for the nuclides used in this work is that of ^{241}Am at 0.307 eV [39]. In order to ensure formation of the compound nucleus in the capture state instead of a resonance state, cold neutrons are used in this work.

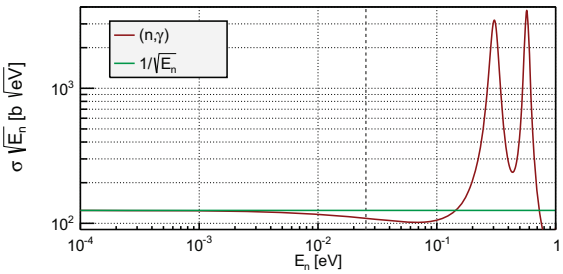

Figure 2.6: Cross section for the radiative neutron capture of ^{241}Am and a corresponding $1/\sqrt{E_\mathrm{n}}$-dependence. The cross section has been weighted with $\sqrt{E_\mathrm{n}}$ to stress the divergence from the simple shape. The thermal energy of 0.0253 eV is marked by the vertical dashed gray line.

2.4 Radiation Emitted in Nuclear Reactions

An excited nucleus, such as a compound nucleus after a neutron absorption, or an unstable nucleus will emit radiation and decay into a stable ground state nucleus. The radiation emitted after the formation of compound nuclei was briefly described in section 2.3 and will now be discussed in more detail. Radioactive – that is unstable – nuclei typically decay by emission of ionizing α-radiation or β-radiation followed by photon emission. Most important for this work is the photon emission.

2.4.1 α-Radiation

An unstable nucleus can decay by the emission of an α-particle, that is $^4\mathrm{He}^{2+}$. In this process the original nucleus' mass number is reduced by 4 and its atomic number by 2.

$$^{\mathrm{A}}_{\mathrm{Z}}\mathrm{X} \rightarrow {}^{\mathrm{A}-4}_{\mathrm{Z}-2}\mathrm{X} + \alpha \tag{2.31}$$

This effect is possible due to the quantum mechanical tunnel effect, that is the α-particle having a non-zero probability to appear outside of the nuclear potential. Due to their high mass and charge, α-particles are highly ionizing and thus have a relatively small range in matter. The most probable α-particle emitted by α-decay of ^{242}Pu has an energy of 4.9005(12) MeV, which is a typical α-energy. In SiO_2 with a molar mass of $60.0843\,\mathrm{g\,mol^{-1}}$ and a density of $2.2\,\mathrm{g\,cm^{-3}}$ its range is only about 0.04 mm. As α-decay is a two-body decay the energy of the α-particle is discrete and characteristic for the decaying nucleus.

2.4.2 β-Radiation and Electron Capture

An unstable nucleus in which energy can be gained by converting a nucleon into another nucleon type (n $\rightarrow$ p or p $\rightarrow$ n) can decay via β-decay or electron capture. As a neutron has a slightly higher mass than a proton, a free neutron decays with a lifetime of 887.7 s [40] into a proto cted in the Feynman graph in Fig

(2.32)

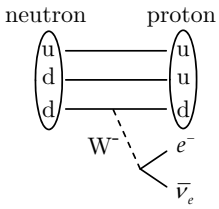

Figure 2.7: A Feynman graph depicting the decay of a free neutron.

This can also happen to a bound neutron in a nucleus ${}^{A}_{Z}X$ if in the nucleus ${}^{A}_{Z+1}X$ a free level exists, with an excitation energy large enough to create the electron and the neutrino minus the energy difference between a u- and a d-quark. The electron emitted in this type of nuclear decay is called "β^--particle", to distinguish it from electrons of other origin than nuclear decay. The most probable β^--particle emitted in the decay of ^{242}Am has a maximum energy of 622.67 keV. In SiO_2 with the properties described in section 2.4.1, the said β^--particle has a range of about 1 mm.

The opposite process, a proton of a nucleus ${}^{A}_{Z}X$ decaying into a neutron in nucleus ${}^{A}_{Z-1}X$ is also possible suitable level energies presupposed. As mentioned in section 2.1 especially the electrons in s-orbitals have a probability of being located inside the nucleus. This can

lead to a process called electron capture ϵ, in which a quark in the proton exchanges charge with the electron thus "merging" electron and proton into a neutron. In this process only an electron neutrino is emitted conserving energy and momentum. But since usually the capture of an electron in a low lying shell is more likely, other electrons in higher shells will transit to the free level, emitting X-rays.

$$\mathrm{p} + \mathrm{e}^- \rightarrow \mathrm{n} + \nu_e \tag{2.33}$$

If the energy difference between the proton level in ${}^{\mathrm{A}}_{\mathrm{Z}}\mathrm{X}$ and the neutron level in ${}^{\mathrm{A}}_{\mathrm{Z\text{-}1}}\mathrm{X}$ becomes higher than $2 \cdot m_\mathrm{e} \approx 1022\,\mathrm{keV}$, instead of capturing an electron the proton is able to emit a positron, which is then called a "β^+-particle".

$$\mathrm{p} \rightarrow \mathrm{n} + \mathrm{e}^+ + \nu_e \tag{2.34}$$

This process, if allowed, competes with electron capture and creates the same nucleus. A positron will be slowed down like an electron in the surrounding matter, but the slower it becomes the more likely it will annihilate with another electron, creating two 511 keV photons emitted in opposite directions to conserve momentum and energy.
As the β-decay processes involve a neutrino due to conservation of energy and momentum (and of Lepton number) these decay modes are three-body decays. Thus, the energy is distributed among the nucleus, the β-particle and neutrino, so that an emitted β-particle does not have a discrete energy. A large number of emitted β-particles exhibit a continuous energy spectrum with a characteristic maximum possible energy.

2.4.3 X- and γ-Radiation

Electrons in an atomic shell or nucleons in a nuclear shell that do not fill the lowest available levels will eventually transit to an available level with lower energy. In this process either internal conversion electrons are emitted or, if allowed and the energy-difference between the levels is high, more likely a photon carrying the energy-difference will be created. If this process occurs in the electron shells of an atom the emitted photons are called "X-rays", typically having energies in the low keV-regime up to a few hundred keV. In the case of photons being emitted from a nucleon transition in the nucleus, the photons are called "γ-rays" and have typically higher energies than X-rays ranging from tens of keV to several MeV.
Usually a state with a nucleon in a higher energy level than necessary decays within 10^{-9} s, but sometimes the lifetime of such a state is significantly longer. These states are called "isomeric" or "metastable" states.
Since a photon has a spin of 1, a transition by photon emission is only possible if the angular momentum changes between the two levels by at least 1. The photons can carry

a larger angular momentum. The higher the angular momentum the photon carries, the less likely is its creation. The additional angular momentum gives the photon radiation a multipolarity moment much like the classical electrodynamic multipolarities. The type of multipolarity moment is not determined by the difference in angular momentum between the levels alone, but also by their respective parities. In classical electrodynamics it can be shown, that electric multipoles of order L, denoted as EL, have a parity of $P = (-1)^L$ and magnetic multipoles of order L, denoted as ML, have a parity of $P = (-1)^{L+1}$. The order of the multipole corresponds to the angular momentum L in quantum theory. Considering that the initial level has an angular momentum of J_i and the final level has an angular momentum of J_f, by application of the conservation of angular momentum this yields the following selection rules for possible transitions:

$$|J_i - J_f| \leq L \leq J_i + J_f \quad \text{and } L \neq 0 \tag{2.35}$$

Parity stays the same: even electric, odd magnetic ($M1$,$E2$,$M3$,...) (2.36)

Parity changes: odd electric, even magnetic ($E1$,$M2$,$E3$,...) (2.37)

The lowest possible multipole moment generally dominates, as the emission of γ-rays with these angular momenta usually happens faster. Also usually an electric multipole moment is more likely than a magnetic one of the same order. Thus, a mixture of a higher magnetic with a relevant amount of a lower electric moment, such as $M1$ and $E2$ often occurs. If the γ-ray emission for a transition is not allowed, this transition is called "forbidden".
The γ-radiation with higher multipolarities is no longer isotropically emitted but has preferred directions. However, since in this work reactions with a large number of nuclei with random orientations are studied, the anisotropic emission is not measurable because it is statistically smoothed.

An excited nucleus with an excitation energy E_{ex} usually de-excites in a series of transitions each producing a γ-ray until the nucleus reaches its ground-state, which in turn may be a stable nucleus or not. The energy of each γ-ray is basically the difference in energy between the two levels E_T minus a recoil correction E_R, which is the energy transferred to the nucleus due to the γ-ray emission.

$$E_\gamma = E_T - E_R, \tag{2.38}$$

$$E_R = \frac{E_\gamma^2}{2m_A c^2}, \tag{2.39}$$

with m_A being the mass of the emitting nucleus of mass number A. Note that E_R is

small for heavy nuclei. For actinides it is mostly below 1 % of E_γ, thus $E_\gamma \approx E_T$. An initial level de-excited by a γ-ray or conversion electron is so-called "depopulated" (as the nucleon leaves the state) by γ-ray emission and the final level is "populated" (as the nucleon arrives in that state). Thus, the ground state of the nucleus is the only state that is only populated and not depopulated. Each neutron eventually reaches the ground state, as long as no other process changing the nucleus is more likely (such as a direct *alpha*- or β-decay of an isomer). Thus, the sum of the emission probabilities of γ-rays and conversion electrons emerging from a level population has to be identical with the sum of the emission probabilities from the level depopulation. This is, a level has to be so-called "balanced". So the γ-ray energies in a single γ-ray cascade de-exciting a nucleus add up to the original excitation energy. In the case of cold neutron capture it holds

$$S_\mathrm{n} \approx E_\mathrm{ex} \approx \sum_{\gamma \in \mathrm{cascade}} E_\gamma. \tag{2.40}$$

In the case of neutron capture the first γ-ray that de-excites the capture state is called a "primary" γ-ray, whereas all γ-rays following subsequently in the γ-ray cascade de-exciting the intermediate levels are called "secondary" γ-rays.

If one wants to relate the activity of a radioactive source to the emission probability of a particular γ-ray, this can be done by multiplying the decay probability of the nuclide with the emission probability of the γ-ray and is usually referred to as p_γ.

2.4.4 Internal Conversion

Internal Conversion is a process in which the energy of a transition between levels in the nucleus is transferred to an electron from the atomic shell. The electron is then emitted carrying the transferred energy minus its binding energy. Since the now free level in the atomic shell is filled by another electron, X-ray radiation is emitted.
The probability that internal conversion occurs increases with Z^3, making it very important for heavier nuclei. At the same time the probability decreases rapidly with the transition energy.
Usually internal conversion competes with the decay through γ-ray emission. Slower magnetic transitions are more likely to decay by internal conversion than electric transitions. Also it holds that the higher the multipole order the more likely becomes the internal conversion. A forbidden transition can only decay through internal conversion.
If the total decay rate of a particular state needs to be known the effect of internal conversion has to be corrected for (i.e to calculate the level balance). This can be done by using the internal conversion coefficient

$$\alpha = \frac{N_\mathrm{e}}{N_\gamma}, \tag{2.41}$$

with N_e being the number of emitted conversion electrons and N_γ the number of emitted γ-rays. These coefficients can be calculated, which in this work is done using the BRICC tool [41]. Note that a similar process can occur for X-ray transitions in the atomic shell. In that case the emitted electron is called an "Auger-electron" instead of a conversion electron.

2.4.5 Photon Strength Function

The photon strength function (PSF) is a statistical description of the average electromagnetic properties of a given nucleus [42, 43, 44]. Thus, the PSF is essential for the calculation of transitions in an excited nucleus, especially when these transitions are unobserved. This is the case for most γ-rays being emitted directly after a neutron capture process in the quasi-continuum of levels. Considering the selection rules in equation 2.37 the most likely transitions have $E1$ multipolarity. This is only possible with a change in parity, but given enough free levels beneath the capture state it is likely that appropriate levels exist.

Due to a lack of corresponding measurements a PSF $S^{XL}(E_\gamma)$ often has to be assumed. To start with, in most cases a so-called "single particle strength" is used, corresponding to $S^{XL}(E_\gamma) = \text{const.}$, which is predicted by the simplified extreme compound nucleus model [45]. For the $E1$ PSF the giant dipole resonance, observed in nuclear reactions with γ-emission, can be utilized to parameterize more sophisticated theoretical models. The dipole resonance is characterized by two peaks each of which are described in the typical Lorentzian form of equation 2.20 with some nuclide specific parameters. Using measured photo-absorption cross sections σ_{p-abs} (in units of mb) for photons of energy E_γ (in units of MeV) according to the formula

$$S^{E1}(E_\gamma) = \frac{1}{3(\pi\hbar c)^2} \cdot \frac{\sigma_{p-abs}}{E_\gamma} \tag{2.42}$$

an empirical $S^{E1}(E_\gamma)$ can be fitted or a theoretical one can be tested [44, 46].

A theoretical approach consistent with the experimental data for most nuclei is given by the Brink-Axel model (BA). The model assumes the Brink hypothesis [42, 43] that the giant dipole resonance is built up from all levels with the same shape. The BA can be parameterized by the shape of the giant dipole resonance as

$$S_{BA}^{E1}(E_\gamma) = \frac{1}{3(\pi\hbar c)^2} \cdot \sum_{i=1}^{2} \frac{\sigma_{GR,i} E_\gamma \Gamma_{GR,i}^2}{(E_\gamma^2 - E_{GR,i}^2) + E_\gamma^2 \Gamma_{GR,i}^2}, \tag{2.43}$$

with E_{GR} being the centroid of the resonance, Γ_{GR} being the width of the resonance and σ_{GR} its cross section. The summation is with regard to two vibrational modes of the nucleus resulting in the double peak. A model which allows a violation of the Brink hypothesis and usually is in good agreement with experimental data after fitting of the empirical parameter k_0 is the enhanced generalized Lorentzian (EGLO) model of the form

$$S_{EGLO}^{E1}(E_\gamma) = \sum_{i=1}^{2} \frac{\sigma_{GR,i} \Gamma'_{GR,i}}{3(\pi\hbar c)^2} \left[F_K \frac{4\pi^2 \Theta^2 \Gamma'^2_{GR,i}}{E_{GR}^5} + \frac{E_{GR,i} \Gamma'_{GR,i}}{(E_\gamma^2 - E_{GR,i}^2) + E_\gamma^2 \Gamma_{GR,i}^2} \right] \tag{2.44}$$

with the Fermi-liquid parameter $F_K = 0.7$ [46, 47]. The enhanced width is given by

$$\Gamma'_{GR} = \frac{\Gamma_{GR}}{E_{GR}^2} (E_\gamma^2 + 4\pi^2 \Theta^2) \cdot \left[k_0 + (1 - k_0) \frac{E_\gamma - E_0}{E_{GR} - E_0} \right], \tag{2.45}$$

with a reference energy $E_0 = 4.5\,\mathrm{MeV}$ and the nuclear temperature

$$\Theta = \sqrt{(E_{\mathrm{ex}} - \Pi)/a} \tag{2.46}$$

for a given excitation energy E_{ex} and the pairing energy

$$\Pi = \begin{cases} 0.5 \cdot |E_{\mathrm{pair,d}}| & \text{even-even nucleus} \\ 0 & \text{odd } A \text{ nucleus} \\ -0.5 \cdot |E_{\mathrm{pair,d}}| & \text{even-even nucleus} \end{cases} \tag{2.47}$$

using the pairing energy of the deuteron $E_{\mathrm{pair,d}}$ [44].

For the $M1$ PSF a parameterization exists for some heavy nuclei like several U isotopes [48]. The $E2$ PSF is parameterized by a single Lorentzian following a giant quadrupole electric resonance (GQER).

Concerning the statistical properties of the nuclear levels, it is important to note that the partial radiative width Γ^{XL}, and thus the probability for allowed transitions from level i with E_i to a level f with E_f, follows a Porter-Thomas distribution [49] with a mean value of

$$\left\langle \Gamma^{XL}_{\gamma,i,f} \right\rangle = \frac{S^{XL}(E_\gamma) E_\gamma^{2L+1}}{\rho(E_i, J_i^{P_i})}, \tag{2.48}$$

with XL denoting the type of multipolarity (EL or ML) and $\rho(E_i, J_i^{P_i})$ the level density (LD).

2.5 Photon Interactions with Matter

Photons are able to interact with matter in several ways. Like neutrons, they cannot directly interact with the Coulomb-potential and are thus indirect ionizing particles. This allows photons to have a higher range in matter than ionizing particles such as electrons or α-particles. Photons can, like neutrons, undergo elastic and inelastic scattering, they can be absorbed resulting in excitation and possibly ionization of an atom or nucleus or they can produce particle-antiparticle pairs, provided they have enough energy and are in the Coulomb-potential of an atomic nucleus.

2.5.

The ı being
absc

(2.49)

and

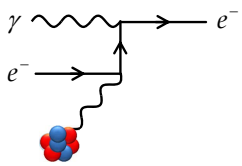

Figure 2.8: Feynman graph of the photoelectric effect with a bound electron.

The energy of the incident photon is totally absorbed by the electron in the atomic shell. Due to energy and momentum conservation a small part of the energy also has to be transferred to the nucleus. Thus, the photoelectric effect is not possible with unbound electrons. It is possible for de-localized electrons in a lattice structure by creating quantized lattice vibrations called "phonons".

If the incident photon's energy E_γ is higher than the electron binding energy E_B, the electron will be freed from the nuclear Coulomb-potential having an energy of

$$E_\mathrm{e} = E_\gamma - E_A - E_B, \tag{2.50}$$

where $E_A = 2m_\mathrm{e}^2/m_A$ (m_A being the nuclear mass) is the recoil energy transferred to the nucleus. The electron binding energy increases with Z^2 but also is higher for lower energetic shells. Thus, if the photon has enough energy to overcome the electron binding energy of a lower lying shell new electrons become available for the photoelectric effect, thus drastically increasing its probability. So the cross section for this process is noncontinuous at these energies. At energies above the binding energy of the innermost electron it was found to follow

$$\sigma_\mathrm{ph} \propto Z^5 \cdot E_\gamma^\delta \tag{2.51}$$

with

$$\delta = 3.5 \qquad \text{for } E_\gamma \leq m_\mathrm{e} \cdot c^2 \tag{2.52}$$

$$\delta = 1 \qquad \text{for } E_\gamma > m_\mathrm{e} \cdot c^2. \tag{2.53}$$

After the electron is emitted, the leftover vacancy in the shell will be occupied by another electron from a higher lying level, thus the photoelectric effect is usually accompanied by X-ray emission.

2.5.2 Photon Scattering

In elastic scattering – namely Rayleigh-, Thomson- and Raman-scattering – incident photons excite an atom or molecule into a vibrational or rotational movement, which finally leads to the isotropic emission of photons of the same energy, when the atom or molecule is de-excited. Thus, these processes do not lead to an energy loss of the photons but only to a change of direction. Elastic scattering is typically only dominant for low energy photons. For an isotropic source of photons the effect of photons being scattered out of a certain direction is to some extent compensated by photons being scattered into that direction.

At higher energies the inelastic Compton scattering is more important. In this scattering process an incident photon transfers only a part of its energy to a free or quasi-free electron that can be for instance a valence electron. Thus, this reaction reads:

(2.54)

angle θ
betv iatic of
this

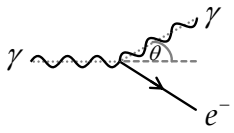

Figure 2.9: Compton scattering of an incident photon with a quasi-free electron.

The energy of the outgoing photon can be derived quasi-classically from the conservation of momentum and energy as

$$E'_{\gamma}(\theta) = \frac{E_{\gamma}}{1 + \frac{E_{\gamma}}{m_{\mathrm{e}}c^2}(1 - \cos\theta)} \tag{2.55}$$

and the energy of the electron is hence $E'_{\mathrm{e}^-} = E_{\gamma} - E'_{\gamma}$. So, the energy transfer in this process is a continuous function of the scattering angle θ. A photon scattered in forward direction ($\theta = 0°$) thus does not transfer energy to the scattering electron. A backscattered photon ($\theta = 180°$) will transfer a maximum amount of energy to the electron, so that the minimal possible photon energy and corresponding maximal electron energy after the scattering event are given by:

$$E'_{\gamma,\mathrm{min}} = \frac{E_{\gamma}}{1 + \frac{E_{\gamma}}{m_{\mathrm{e}}c^2}} \tag{2.56}$$

$$E'_{\mathrm{e}^-,\mathrm{max}} = \frac{2E_{\gamma}^2}{m_{\mathrm{e}}c^2 + E_{\gamma}} \tag{2.57}$$

For $E_{\gamma} \gg m_{\mathrm{e}}c^2$ the differential Compton scattering cross section as a function of θ and E can be described by the Klein-Nishina formula [50]. The general properties of the total Compton scattering cross section then can be described by

$$\sigma_{\mathrm{com}} \propto \frac{Z}{E_{\gamma}}. \tag{2.58}$$

2.5.3 Photo Pair Production

Photo pair production describes the process of a photon being converted into an e^--e^+ pair in the Coulomb-potential of a nucleus. Due to the conservation of energy and momentum a pl vithout
mor ı boson
of t So the
reac

(2.59)

The

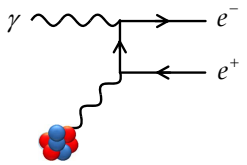

Figure 2.10: Feynman-graph of the pair production effect at a bound electron.

Any excess energy of E_γ over the minimum to create the e^--e^+ pair will be shared among the created particles. The cross section of the pair-production can be described by the Bethe-Heitler model [51] giving the relation

$$\sigma_{\mathrm{pp}} \propto Z^2 \ln(E_\gamma) \tag{2.60}$$

2.5.4 Mass Attenuation Coefficient

The mass attenuation coefficient relates the cross sections of the above mentioned photon interactions to a macroscopic ensemble of photons, a photon beam, interacting with large quantities of matter.

All the effects described above can occur in matter and will lead to a decrease of the incident photon energy. Considering a beam of photons this will lead to a statistical decrease in photon number, that is a dampening of the beam intensity. Considering the photons and their reactions as independent of one another, the dampening corresponds to a Poisson-process and leads to an exponential decrease of beam intensity I_0 with the

thickness d of the material.

$$I(E_\gamma, d) = I_0 \cdot \exp(-\frac{N_A \cdot \rho}{M} \cdot \sigma_{\mathrm{pr}}(E_\gamma) \cdot d), \tag{2.61}$$

here M is the molar mass and ρ the density of the material, $N_A \approx 6.022 \cdot 10^{23}\,\mathrm{mol}^{-1}$ the Avogadro constant and $\sigma_{\mathrm{pr}} = \sigma_{ph} + \sigma_{com} + \sigma_{pp} + ...$ the total cross section. It is convenient to cumulate all material specific constants into the mass attenuation coefficient

$$\mu(E_\gamma) = \frac{N_A \cdot \rho}{M} \cdot \sigma_{\mathrm{pr}}(E_\gamma). \tag{2.62}$$

As the density is not necessarily a material constant $\mu(E_\gamma)/\rho$ is usually used and tabulated for instance in the XCom database [52]. With this, equation 2.61 becomes

$$I(E_\gamma, d) = I_0 \cdot \exp(-\frac{\mu(E_\gamma)}{\rho} \cdot \rho(E_\gamma) \cdot d), \tag{2.63}$$

The proportionalities given by equations 2.51, 2.58 and 2.60 show that the corresponding effect will be dominant in different photon energy regimes and that these regimes will drastically change with Z. In general it can be concluded that for low γ-ray energies the photoelectric effect dominates, for intermediate γ-ray energies Compton scattering is most likely and for high energetic γ-rays the photo pair production becomes the most likely effect.
For germanium the mass attenuation coefficient is shown in Figure 2.11, along with the mass attenuation coefficients for the single processes, clearly demonstrating the general dominance of any one effect in a given energy region.

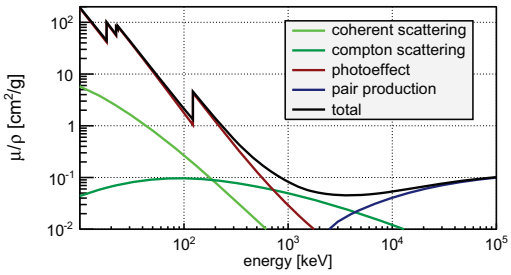

Figure 2.11: Mass attenuation coefficients for germanium for the different interaction types of photons with matter.

A similar simplification can also be made for the absorption of neutrons in matter, by

introducing the macroscopic cross section $\Sigma(E_\gamma) = \frac{N_A \cdot \rho}{M} \cdot \sigma_{\mathrm{pr}}$.

2.6 Radiation Detection

For the purpose of this work radiation has to be detected with regard to its energy. Thus, an energetically resolved spectrum has to be measured. Therefore, a suitable detector system needs to provide a correlation between the incident particle energy and the energy that is deposited in the detector via the various processes described in section 2.5. In this work two detector principles are used, the semiconductor spectrometer and the scintillation spectrometer. For both the basic detector response function will be discussed. In addition, the curved crystal spectrometer will be mentioned as it was used for several measurements in the literature.

2.6.1 Curved Crystal Spectrometers

Curved crystal spectrometers are based on the deflection of photons in a crystal lattice, called "Bragg deflection". Photons with a wavelength λ incident to a crystal lattice are deflected if they fulfil the condition

$$n\lambda = 2d\,\sin(\theta), \tag{2.64}$$

with d being the distance between parallel lattice planes, θ the angle between the incident photon direction and the lattice plane and n an integer number (the order of deflection). For these kinds of detectors basically a crystal is placed in front of a photon source and a simple counter is placed at an angle to this crystal, such that it detects the radiation deflected in the crystal. Either the crystal or the counter is rotated and so the wavelength of the incident photons can be determined. The wavelength resolution and thus the energy resolution basically only depends on the distance between crystal and the counter. A higher distance yields a higher angular resolution during the rotation. A corresponding energy resolution in the order of a few eV is achieved in the applications discussed in this work. Note that a higher distance also reduces the efficiency of the system limiting the method. As the energy of a photon is anti-proportional to its wavelength, the distance between the lattice planes needs to be smaller for the detection of higher energetic photons adding another limitation for this method for high energy γ-rays. Details can be found for instance in [53].

2.6.2 Solid State Detectors

Solid state detectors used in scintillation or semiconductor spectrometers are able to cover a range of a few keV to several MeV of incident photon energies. With regard to a neutron separation energy in the MeV-range this is a significant advantage over curved crystal spectrometers.

2.6.2.1 Scintillation Detectors

Scintillation detectors are based on the excitation of electrons by incident photons into higher energy levels in certain types of materials which are luminescent when excited by radiation. An excited state decays in a cascade emitting smaller energetic photons in the optical range. This process is called a "scintillation". Thus, the scintillation material needs to be transparent for optical photons to be effective. For the emission of one scintillation photon an incident photon energy in the order of tens to above hundred eV is needed. So the total number of optical photons created is rather small. For Bismuth germanium oxide (BGO) the yield is only about 8200 optical photons per MeV deposited energy (more than 100 eV per optical photon). Thus, the energy resolution of scintillators is rather limited due to the involved Poisson like statistics. However, for practical reasons they are still widely used for spectroscopy. Similarly to other types of detectors the number of created optical photons is proportional to the incident photon energy.

The created optical photons traverse the scintillator material and are reflected at any surface of the material by a sheet of mirroring material except where a photomultiplier is positioned. The latter collects the optical photons which produce electrons on a photocathode via the photoelectric effect. The created electrons are multiplied, thus increasing signal strength and converting it to a detectable current. These signals can be converted into an energy resolved spectrum by an multi-channel analyzer (MCA).

In this work BGO, an inorganic crystal, is used. Its advantage over other scintillators is its high density of $\rho = 7.13\,\mathrm{g\,cm^{-3}}$ and the large atomic number of Bismuth ($Z = 83$). As the photon interaction processes with matter described by relations 2.51, 2.58 and 2.60 indicate, these properties favor a fast energy deposition in the BGO. Thus, smaller detectors reach a good efficiency for high energy photons. Their mechanical and chemical properties also allow the fabrication of complicated detector structures. Another advantage is the BGO's insensibility to radiation damage.

2.6.2.2 Germanium Detectors

A Germanium detector is based on the semiconductivity of the germanium crystal.
In semiconductors the outer electron shells of atoms in the lattice structure merge, forming electron bands in the material. In these bands the electrons are shared between all atoms

in the material and, in principle, can move freely within the crystal as long as there are available free states. The original valence electrons occupy the valence band, which, in the ground state, is completely filled, so that no free states for electrons exist and restricting the electrons from movement. Former higher levels form additional bands, the energetically next higher band is the so-called "conduction band", as electrons that gain enough energy (for instance through photon absorption), have available free states all over the material and thus can move quasi-free through the material. Given an outer electric field these free charge carriers can be collected and transformed into a current. In addition, the now free electron state – called a "hole" – in the valence band can also move like a positive charged particle, as other electrons can now occupy this free state. The energy necessary to create such an electron-hole pair is 2.96 eV at liquid nitrogen temperature, thus more than 300 000 of these pairs are formed per MeV deposited energy. The creation is almost a Poisson process, only almost because the e^--hole pairs are all created on the same particle track and hence are not independent. Thus, their creation is not independent. Therefore, the uncertainty of the number of pairs i that are created is $s_i = \sqrt{F \cdot i}$, corrected by the Fano factor F ($F \approx 0.1$ of germanium). Note that the Fano factor decreases the uncertainty by a factor of three compared to the Poisson uncertainty. It follows for the uncertainty s and thus roughly for the peak width in the detector response that $s \propto \sqrt{E}$ for a given energy E of an incident photon [9]. As there are no possible states for electrons in between the valence and the conduction band this energy region is called the "band gap".

These properties of the germanium crystal can be changed for a detector system by bringing atoms with one additional valence electron or one valence electron less into the lattice structure, thus creating additional states inside the band gap. This process is called "doping". If one additional valence electron is introduced it can more easily be lifted to the conduction band. An introduced element with an additional valence electron is called a "donor", as a quasi-free e^- is introduced, and a crystal doped with a donor element is called "n-type".
The opposite process is called "p-type" doping and the introduced element is an acceptor as a state is created that can easily be occupied by an electron from the valence band, thus creating a movable hole in the valence band. The band structure of p- and n-type doped Ge is depicted in Figure 2.12.

If materials with different types of doping are in contact, an electric current will emerge that depletes a zone around the contact from all movable charges. By application of a high voltage this depletion zone can be extended over the whole crystal. Radiation traversing this depletion zone will create pairs of movable electrons and holes, which – by the external high voltage – are drawn to the electrical contacts. The amperage of the short electric current pulse that is generated by this process is proportional to the energy deposited in the crystal. Then the electric current is amplified and further processed by a MCA. After analogue-to-digital conversion the MCA basically converts the amperage of the electric current pulse to separate channels, thus a histogram of the pulse counts versus the channel

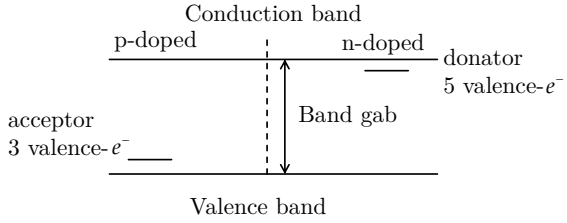

Figure 2.12: Sketch of the band structure in a Ge crystal with additional states from n- and p-doping.

number, the so-called "gamma spectrum", can be created.

A germanium detector is produced from a single crystal of Ge with a purity of at least 99.999 %, and thus being called a HPGe crystal. The crystal lattice has to be as perfect as possible, otherwise electrons or holes could be trapped by the imperfect band structure and thus not collected, losing some of the signal. To create a HPGe detector one surface of a germanium crystal is p-doped and the opposite surface is n-doped. The p-doped layer is a few µm thick and is achieved by implementing B-ions into the lattice structure. The n-doping is achieved by drifting Li into the germanium surface. Thus, the thickness of this layer can reach several mm. These layers called "p-" and "n-contact", as they also serve to collect the electric signal from the movable electron and holes, can be brought to any two opposing surfaces of the detector. Since by thermal energy it is possible to create unwanted electron-hole pairs in the depletion layer, the HPGe detector is operated at liquid nitrogen temperature (77 K).

A sketch of a detector response function of a HPGe detector is depicted in Figure 2.13. The full energy peak marks the upper end of the spectrum, with its energy corresponding to the energy of the detected photons. For historical reasons these peaks in a spectrum are also called "lines". The so-called "Compton plateau" is a direct result of the energy loss due to Compton scattering according to equation 2.55 and corresponds to the case when the scattered photon leaves the detector material and thus the deposited energy is reduced. The Compton edge corresponds to scattering under 180° (back-scattering) of the incident photon at a loosely bound electron, with the scattered photon escaping the detector volume so that only the energy transferred to the electron is deposited. Thus, the energy of the Compton edge with respect to the energy of the full energy peak can be derived from the electron energy in equation 2.57. The region between the Compton edge and the full energy peak is filled with events in which a photon escapes after depositing energy in several Compton scattering processes (and events where the detected photon did undergo low-angle Compton scattering near the detector prior to detection). This region thus is called "multiple Compton" scattering region. The single and double escape peaks result

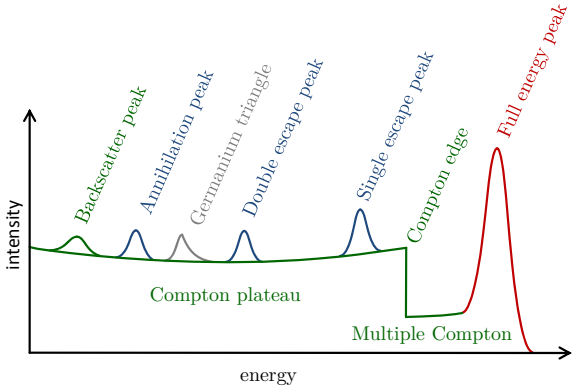

Figure 2.13: Sketch of a detector response function of a Ge semiconductor detector in a gamma and neutron radiation field. Features arising from the photoelectric effect are marked red, features from the Compton effect are marked green, features arising from pair production are marked blue. A germanium triangle arising from fast neutron interactions with Ge atoms in the detector material is marked gray.

from pair production and one or both of the annihilation photons leaving the detector material. They are thus 511 keV and 1022 keV lower in energy than the corresponding full energy peak. The annihilation peak at 511 keV results from the same effect in the surrounding material. In this case, however, one of the 511 keV photons escaping from the material surrounding the detector deposits all of its energy in the detector material. This peak is typically relatively broad as the annihilation occurs at finite momentum states. There is no 1022 keV annihilation peak, as the photons created in the e^--e^+ annihilation have opposite directions and cannot both be detected, unless the detector surrounds the annihilation-point.
The backscatter peak is in a similar manner the remaining energy of a Compton scattered photon after a heads-on scattering in the material opposite of the detector, so it is an inverse Compton edge. Since usually lots of photons with different energies are scattered in the surrounding material and the energy difference between the Compton edge and the full energy peak is not as sensitive to the incident photon energy, this feature is actually rather broad in the region of 230–250 keV including many inverse Compton edges.
A feature introduced due to fast neutron inelastic scattering is the so-called "germanium triangle". In a (n, n') reaction a germanium atom is displaced from its lattice position and is excited at the same time. The de-excitation energy plus the recoil energy transferred to the germanium atom form a broadened peak, with its lower edge corresponding to the de-excitation energy. The triangular shape comes from the fact that the recoil energy is badly transformed into electron-hole pairs and thus generally only a small amount of it is detected.

At energies higher than the full energy peak so-called "coincidence peaks" can occur, if two photons deposit their energy in the detector within the time interval the detector needs to process the signal. The coincident detection can occur due to two random photons being detected in the same time interval in which case it is a so-called "random coincidence". This effect is kept low by measuring at low count rates. Another type of coincident photon detection is when two photons from the same decay cascade are detected. As these photons are created with random directions these so-called "real coincidence" events are reduced by decreasing the solid angle covered by the detector with respect to the radiation source, i.e. by increasing the sample to detector distance or introducing a collimator.
Other features that occur in the spectrum are X-ray peaks in the energy range up to 150 keV, resulting from the processes described in section 2.4.3. Due to their origin in the atomic shell they are broader than γ-ray peaks. Also X-rays produced by the photoelectric effect in the HPGe crystal may leave the detector volume, thus creating X-ray escape peaks. Their energy is lower than the energy of the full energy peak by the energy of the escaped X-ray. As the X-ray energies are relatively low a contribution to this peak will occur only if the photoelectric effect occurs in the outer parts of the HPGe crystal. It occurs most likely by the K-shell X-rays at around 10 keV escaping from the detector volume. The resulting X-ray escape peaks are usually several orders of magnitude smaller than the full energy peaks and thus mostly have a lower count rate than the background especially for large volume HPGe-detectors. Note that the effect increases for lower incident photon energies, as for these photons the photoelectric effect will more likely occur near the surface of the crystal.

Detection Efficiency

These intrinsic finite volume effects and the geometry of a sample-detector arrangement make it necessary to define the detection efficiency ϵ in order to normalize a measured full energy peak area to the total number of the photons emitted from a source with that energy. The detection efficiency is usually measured by determining the full energy peak area A_P for lines at different energies with known emission probabilities per decay p_γ of radioisotope sources with known activities A. If the sample to detector distance is far larger than the sample dimensions, i.e. the sample is point-like, the efficiency can be regarded as independent of the sample dimensions and can be calculated using calibrated point sources. Otherwise the calibration sources need to have the same dimensions as the sample. The efficiency becomes

$$\epsilon(E_\gamma) = \frac{A_P}{A \cdot p_\gamma \cdot t_{\text{live}}}, \tag{2.65}$$

with the live time t_{live} of the measurement $\ll T_{1/2}$ of the used radioisotopes. The detector needs time to collect events and is thus only sensitive after the depletion layer is sufficiently

clear of charges again, thus $t_{\text{live}} < t_{\text{real}} = t_M$, with t_M being the actual measurement time or real time t_{real}. The difference between the live time and the real time is the dead time $t_D = t_{\text{real}} - t_{\text{live}}$. Note that t_D increases with the count rate, as does the occurrence of pile-up events, which should be avoided.

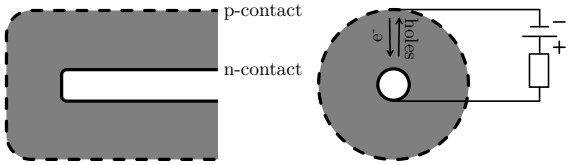

Figure 2.14: Sketch of an n-type coaxial HPGe detector, with the thinner p-contact layer (dashed black line) and the n-contact layer (thick black line). The direction of the movement of electrons and holes to the electric contacts is indicated by the black arrows.

In this work, closed-ended coaxial n-type HPGe-detectors are used with the thicker n-doped layer on the inner surface, as depicted in Figure 2.14. This choice is made primarily because n-type detectors prove to be less sensitive to lattice defects – occurring after fast neutron collisions with Ge-atoms – and thus to an incomplete collection of movable charges [9]. Also, as the outer contact layer is thinner for n-type detectors, thus providing a thinner insensitive so-called "dead layer". Thus, they are more sensitive to lower energetic photons and it is less likely for a scattered photon to be absorbed in the insensitive volume and thus lost.
This is important because a BGO scintillation detector is placed around the HPGe detector which should be able to detect any radiation escaping from the HPGe-volume. If a particle is detected both in the BGO and the HPGe detector within a given time frame, it most likely originates from an escaping photon after scattering or pair production. Thus, this event can be electronically discriminated so that it is not processed further to the MCA and thus not acquired in the gamma spectrum. Using both detectors in this configuration, which is called an "anticoincidence mode" allowing the suppression of the unwanted background from Compton scattering and of escape peaks. With this so-called "Compton suppression" the peak-to-background ratio is, hence, improved and the sensitivity of the detector system is enhanced.

2.7 Neutron Activation Analysis

The purpose of neutron activation analysis (NAA) is to qualitatively and quantitatively determine the elemental composition of a given sample of material. Radiative neutron capture (see section 2.3) with cold or thermal neutrons is utilized as depicted in Figure

2.15. The compound nucleus is highly excited and de-excites through a cascade of one primary and usually several secondary prompt γ-rays into its ground-state. If the ground state is radioactive it will eventually decay often under emission of γ-rays, these are called "delayed" γ-rays, because the half-lives of these created ground state nuclei are much longer than that of the compound nucleus decay. As both the prompt and delayed γ-radiation is induced by the neutron irradiation, the investigated nuclides are so-called "activated", hence the name of the analysis.

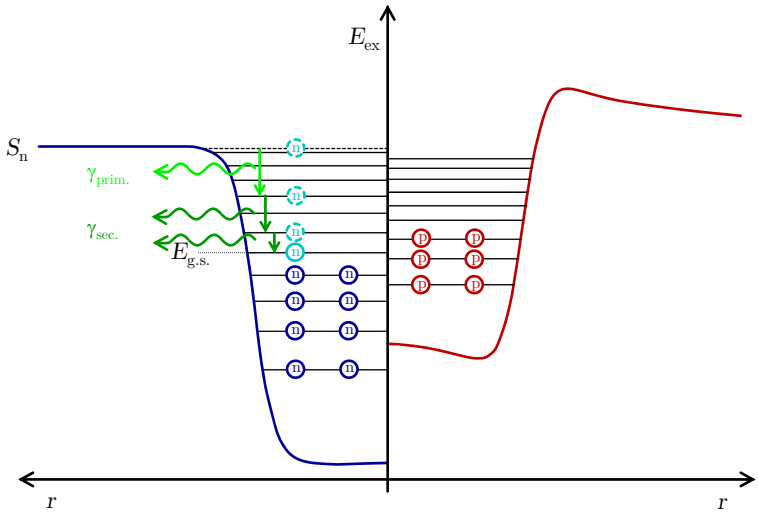

Figure 2.15: Radiative neutron capture of a nucleus. The captured neutron (turquoise) in the capture state transits through free levels until it reaches the ground state $E_{g.s.}$ emitting a primary ($\gamma_{prim.}$) and (several) secondary ($\gamma_{sec.}$) prompt γ-rays. S_n is the neutron separation energy.

For a qualitative analysis of the components in a sample it is sufficient to know the emitted γ-ray energies and the emission intensities relative to one another. For a quantitative analysis it is also necessary to have precise knowledge on the neutron flux incident on the sample and on the (n, γ) cross section. The neutron flux is defined – similar to a photon flux – as the number of neutrons N crossing a unit surface S. In the case of a neutron beam this surface is perpendicular to the neutron beam axis. During a time interval Δt the average neutron flux is defined as

$$\Phi(t) = \frac{N}{S \cdot \Delta t} = \frac{\int_S dS \int_E dE_n \Phi(E_n, \mathbf{r}, t)}{S}. \tag{2.66}$$

Its unit is $\mathrm{cm}^{-2}\,\mathrm{s}^{-1}$. As the cross section dependents on the incident neutron energy the differential neutron flux $\Phi(E_\mathrm{n}, t) \coloneqq d\Phi/dE_\mathrm{n}$ can be defined likewise, as the flux of neutrons of a specific energy. The differential neutron flux $\Phi(E_\mathrm{n}, \mathbf{r}, t)$ corresponds to the number of neutrons traversing an infinitesimal volume at position $\mathbf{r}$ weighted with their track-length in that volume. The neutrons having a specific energy E_n and their number can vary over a time t.

In activation analysis usually neutrons from fission processes in nuclear reactors are used, which are moderated through elastic scattering with light nuclei (e.g. ^{1}H,^{2}H) to thermal or cold energies, depending on the temperature of this so-called "moderator". Thus, these neutrons are not mono-energetic, but have certain energy distributions. In the reactor this is usually a Maxwellian distribution. For a thermal neutron distribution, that is neutrons at room temperature, the most probable value is $E_\mathrm{th} = 0.0253\,\mathrm{eV}$, but the distribution extends well to the 0.1 eV range.
Cold neutron beams extracted from a reactor are usually guided through straight or curved neutron guides consisting of so-called "super-mirrors". In these the neutrons undergo total reflection at the walls of the beam guide, if their energies are in a specific range. Thus, it is possible to filter out neutrons of unwanted higher energies and to create a beam of neutrons with energies well below neutron absorption resonances.

Through the decay radiation from the created compound nuclei the reaction rate $R(t)$ can be determined (as given in equation 2.67).

$$R(t) = n \int_V dV \int_E dE_\mathrm{n} \sigma_c(E_\mathrm{n}) \Phi(E_\mathrm{n}, \mathbf{r}, t), \tag{2.67}$$

here $\sigma_c(E_\mathrm{n})$ is the radiative capture cross section, $\Phi(E_\mathrm{n}, \mathbf{r}, t)$ the differential neutron flux, E_n the neutron energy, $\mathbf{r}$ a position vector in three dimensional space and V the sample material volume. In this formula it is assumed that the mass distribution in the sample material is homogeneous and that the sample to detector distance is far larger than the sample dimensions, so that the sample can be regarded as point like.
If $\sigma_c(E_\mathrm{n})$ is known and the flux has been determined by other means, the total number of the capturing nuclei in the sample can be calculated.

What is measured with a γ-detector is a full energy peak area A_P. It is related to the reaction rate using the detection efficiency $\epsilon(E_\gamma)$ (see equation 2.65) to

$$A_P = p_\gamma \cdot \frac{\epsilon(E_\gamma)}{\eta_0(E_\gamma)} \cdot \int_{t=0}^{t_\mathrm{live}} dt' R(t'), \tag{2.68}$$

with the γ-ray emission probability per capture event p_γ and a correction factor η_0, accounting for different properties between the efficiency measurement and the sample measurement. η_0 includes basically corrections for photon absorption in the sample, that are

not present in the sources used for efficiency calibration.

Cross sections are measured relative to a comparator isotope with a precisely known thermal neutron capture cross section $\sigma^0_{c,\mathrm{comp}} = \sigma_{c,\mathrm{comp}}(E_{\mathrm{th}})$. The comparator is irradiated for a time $t_{\mathrm{Irr.}}$ in the same neutron flux as the isotopes of which the cross sections should be determined. From the activation of the comparator a thermal equivalent flux Φ_0 is calculated, which is the hypothetical flux of thermal neutrons resulting in the same reaction rate as the one measured. Using Φ_0 equation 2.67 becomes

$$R = \eta_1^{-1} \cdot n\sigma_c^0\Phi_0, \tag{2.69}$$

η_1 includes deviations of $\sigma_c(E_{\mathrm{n}})$ and $\sigma_{c,\mathrm{comp}}(E_{\mathrm{n}})$ from the $1/\sqrt{E_{\mathrm{n}}}$ dependence and neutron flux differences between the comparator and the sample (e.g. due to differences in the geometrical position or time). Neutron flux differences between the comparator and the sample are avoided by having the comparator and the investigated isotope in a homogeneous mixture, if possible. As η_1 is not simply a correction of the neutron absorption in the sample, but corrects for different reaction rates in the comparator and the sample, it is called the "reaction rate correction".
Generally it holds

$$\eta_1 = \frac{\int_V dV \int_E dE_{\mathrm{n}} \frac{\sigma_{c,\mathrm{comp}}(E_{\mathrm{n}})}{\sigma^0_{c,\mathrm{comp}}} \Phi_{\mathrm{comp}}(E_{\mathrm{n}}, \mathbf{r}, t)}{\int_V dV \int_E dE_{\mathrm{n}} \frac{\sigma_c(E_{\mathrm{n}})}{\sigma^0_c} \Phi(E_{\mathrm{n}}, \mathbf{r}, t)}, \tag{2.70}$$

with Φ_{comp} being the neutron flux in the comparator. In this way the correction factor

$$\eta(E_\gamma) = \eta_0(E_\gamma) \cdot \eta_1, \tag{2.71}$$

is defined, so that equation 2.68 with equation 2.69 becomes

$$A_P = p_\gamma \cdot \frac{\epsilon(E_\gamma)}{\eta(E_\gamma)} \cdot n\sigma_{c,0}\Phi_0. \tag{2.72}$$

Under the assumption that $\sigma_c(E_{\mathrm{n}})$ of the comparator and of the investigated isotope have the same shape (in particular $1/\sqrt{E_{\mathrm{n}}}$), which is usually true for cold neutrons, and the assumption that both are in a homogeneous mixture, it holds $\eta_1 = 1$.

For the purposes of NAA it is convenient to define the convolution of the capture cross section and the emission probability of a certain γ-ray as the partial radiative neutron capture cross section

$$\sigma_\gamma = p_\gamma \cdot \sigma_c, \tag{2.73}$$

with p_γ being the emission probability per decay or neutron capture event of a γ-ray and σ_c the radiative neutron capture cross section. As p_γ is basically constant as long as only the capture state is populated in the neutron capture event (no resonance neutron capture), $\sigma_\gamma(E_\mathrm{n})$ follows the same systematics as the capture cross section.

2.7.1 Instrumental Neutron Activation Analysis

The instrumental neutron activation analysis (INAA) is the conventional neutron activation analysis making use of the activity determination of isotopes with longer half-lives. The sample material containing nuclide $^{\mathrm{A}}\mathrm{X}$ is activated in the thermal column of a nuclear reactor or with a lower neutron flux at an external neutron beam. After a period of time t_A the sample material is removed from the neutron radiation and measured with a gamma spectrometer. The time between the removal of the sample material and the beginning of the measurement is the cooling time t_C, after which the measurement time t_real starts. If the ground state of a created compound nucleus $^{\mathrm{A+1}}\mathrm{X}$ is unstable and has a sufficiently long half-life it will decay in its usual radioactive decay mode. In many cases this involves the creation of γ-rays producing full energy peaks in the measured γ-ray spectrum. Thus, the compound nucleus – created in neutron capture reactions – can be identified. If the intensity of a γ-ray line is known the total number of compound nuclei created and thus the reaction rate can be calculated. The number M of ground state compound nuclei $^{\mathrm{A+1}}\mathrm{X}$ in the sample material at a given time t, which corresponds to the activity of the sample during the process, can be described by the differential equation

$$\frac{dM(t)}{dt} = R - \lambda M(t), \tag{2.74}$$

with $\lambda = \ln(2)/T_{1/2}$ being the decay constant of the exponentially decaying $^{\mathrm{A+1}}\mathrm{X}$ nuclei with a half-life $T_{1/2}$. As the decay of the created nuclei is usually much slower than their creation during neutron irradiation, the number of ground state compound nuclei $^{\mathrm{A+1}}\mathrm{X}$ in the sample material increases until the numbers of the decaying and of the created nuclei are equal, which is when both processes are in equilibrium. In this case $M(t)$ reached its so-called "saturation-activity". After the end of irradiation the number of nuclei will follow the usual exponential decay, as depicted in Figure 2.16.
In order to determine the number of atoms N_X of the investigated nuclide $^{\mathrm{A}}\mathrm{X}$ in the sample material, a measured peak area A_P resulting from the compound nuclei activity has to be corrected for the described effects. Therefore, following from the activation (equation 2.74) and reaction rate (equation 2.69) it holds

N_X =

for a given
absorption i
be divided l

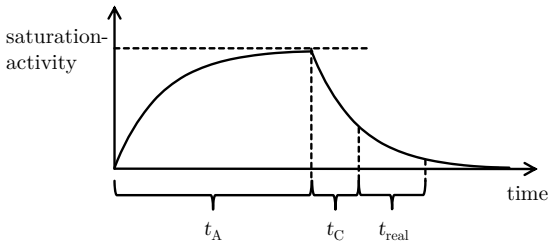

Figure 2.16: Build-up and decay of activity produced in neutron activation.

Equation 2.75 can also be used to determine σ_γ for a given line and thus σ_c or p_γ if the respective other quantity is known. It can also be used to determine the thermal equivalent neutron flux Φ_0 from the measurement of an irradiated comparator, for which $\sigma_{\gamma,\mathrm{comp}}$ and the number of atoms are known.

2.7.2

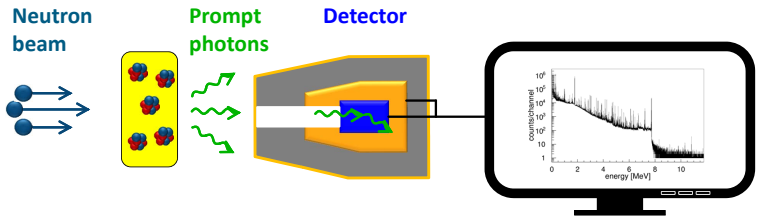

Figure 2.17: Sketch of the PGAA principle. A sample (yellow) is activated by irradiation with a neutron beam and simultaneously counted.

In Prompt Gamma Neutron Activation Analysis (PGAA) unlike in INAA the measurement is performed during neutron irradiation (as depicted in Figure 2.17). Thus, the

γ-rays from the de-excitation of the compound nucleus can be measured directly. As the de-exciting levels have half-lives in the order of 10^{-12} s to 10^{-9} s which is usually below the time resolution of the detector system these γ-rays are called "prompt". The primary γ-rays from the de-excitation of the capture state and the lower energetic secondary γ-rays can be measured all at once and from their occurrence the number of original atoms ^{A}X can be deduced similar to the method used in INAA. As the half-lives corresponding to the prompt γ-ray emissions are small, the saturation-activity is practically immediately reached, thus equation 2.75 reduces to

$$N_X = \frac{A_P \cdot \eta(E_\gamma)}{\epsilon(E_\gamma) \cdot \Phi_0 \cdot \sigma_\gamma \cdot t_{\text{live}}}. \tag{2.76}$$

Similar to the INAA approach also the decay of the created nuclei can be used to determine N_X. If the half-lives of the created nuclei are not far smaller than the irradiation time, the build-up of their activity has to be corrected for in the same way as corrections are deduced for INAA. It holds

$$N_X = \frac{\lambda t_{\text{real}}}{\lambda t_{\text{real}} - 1 - \exp(-\lambda t_{\text{real}})} \frac{A_P \cdot \eta(E_\gamma)}{\epsilon(E_\gamma) \cdot \Phi_0 \cdot \sigma_\gamma \cdot t_{\text{live}}}, \tag{2.77}$$

where the measurement time of the measurement t_{real} equals the irradiation time t_A. A detailed description of PGAA and its application can be found in [2].

Note that resonances would influence the emission probabilities p_γ of the primary γ-rays drastically as the initial state is not always the capture state. For the secondary γ-rays this effect is not as important because the higher levels are statistically filled. Further, for higher neutron energies γ-rays originating from other reactions are observed. All these effects would produce additional lines in the already very dense spectrum. Thus, in order to minimize unwanted lines, in this work strictly cold neutrons with kinetic energies far below the first neutron resonances are used. In this region the radiative neutron capture usually predominates over other reactions and the neutrons do not carry enough kinetic energy for any threshold reaction. In contrast to stable isotopes thermal neutrons can also induce fission in irradiation of actinides, as nuclei such as ^{235}U and ^{239}Pu have so much excess energy that fission is possible without additional energy. Thus, the fission is predominant for some nuclides even in the cold neutron regime. For all nuclides used in this work, however, the (n, γ) reaction predominates in the cold neutron regime.

2.8 Monte Carlo Simulation Tools

Through the simulation of complex physical systems it is possible to study parameters that cannot or can hardly be studied by direct measurement. In this work two particle tracking Monte Carlo codes are used to study, both, the neutron flux inside the samples and the detection of γ-rays from these samples in the detector system, to calculate precise correction factors for the cross sections derived from PGAA measurements.
Monte Carlo methods are based on random number generation and the correlation of these random numbers to probabilities for physical process to occur.

2.8.1 Geant4 and MCNP5

Monte-Carlo N-Particle code version 5 (MCNP5) [54] is a simulation code for neutron, photon and electron transport using the Monte Carlo method. In an input file the user has to provide basic properties of the system to be simulated, including the physical geometry, source specifications and the particle detection mechanism.
Each simulated trajectory is started by choosing a random position and momentum of a primary particle according to the specified source properties. Then a small step is performed by moving the particle along its momentum direction with a step size not larger than the mean free path of the particle in the traversed material. After this step it is determined by random number creation correlated with the reaction cross sections if the particle undergoes an interaction. If for instance an elastic scattering event is found to occur the momentum direction is changed and another step is performed. If in the process particles are created or set into motion (like an electron in Compton scattering) these particles are assigned a momentum fit to the physical process and are hence simulated in the same way as the primary particle. An event with all its particle trajectories is finished after all particles have stopped, either due to their energy being below a threshold energy, or due to the particle leaving the simulation volume.

In this work MCNP5 is used for simulations of the neutron transport through the used samples, to access the neutron flux distribution inside the samples and to calculate reaction rates. Thus, it can be accounted for the decrease of the neutron flux in the sample and for different reaction rates in the sample and the comparator used for the flux determination, including effects due to deviations from the capture cross sections' $1/\sqrt{E_\mathrm{n}}$ dependence. For this purpose MCNP5 provides several flux measurement tallies of which the F2 surface flux tally and the F4 average volume flux tally are used. Although MCNP5 is a well tested and fast code for the simulation of neutron transport with typical applications being reactor criticality calculations, its use is somewhat limited for transport simulations of other particles including photons.

Thus, for photon transport simulations Geometry And Tracking 4 (Geant4) [55, 56] is used. It is basically a transport code for any defined particle and physical processes are

simulated similarly to the simulations in MCNP5. Geant4 is a framework written in C++ and is freely available. Its major advantage over MCNP5 is the object-oriented programming. The user can influence all basic aspects of the simulation by writing user-defined classes that are used instead of the standard ones. It is obligatory to provide a DetectorConstruction class, including the complete geometry of the modeled system, a PhysicsList class, specifying the physics that are used in the simulation, and a PrimaryGeneratorAction class, in which the particle source properties are described. Additionally the analysis of the simulated events is processed in the Analysis class and an altered SteppingAction class. For the simulations performed in this work the G4LivermorePhysics-class was used. The Livermore-model parameters are derived from the EPDL97-database [57] and generally show very good agreement with data provided in the NIST-database [52] for photon energies above 10 keV [58].

2.8.2 DICEBOX

DICEBOX [59] is a Monte Carlo code to simulate nuclear de-excitation γ-ray cascades after neutron capture using *a priori* assumed nuclear models. The code is based on Bohr's extreme statistical model of the formation and decay of compound nuclei [60]. Prior to simulation, the user specifies the photon strength function (PSF) (see equations 2.43 and 2.44) and the level density (LD) models (see equations 2.21 and 2.25) to use and can alter their initial parameters, if adjustable. In addition the user has to specify the capture state and provide all available measured data on the primary γ-radiation. Also, DICEBOX uses a user-provided file containing an *a priori* built-up level scheme up to a critical energy $E_{\text{crit.}}$, with measured transition energies and corresponding σ_γ values. For levels with energy below $E_{\text{crit.}}$ it is assumed that the level scheme is completely known including level energies, spins J, parities P, transition probabilities (in form of σ_γ values) and transition multipolarities XL.

The simulation of de-excitation γ-ray cascades is then performed by first creating a so-called "realization" of the level scheme above $E_{\text{crit.}}$.
This means that levels are randomly created according to the given level density between $E_{\text{crit.}}$ and the measured neutron separation energy S_{n}. The parities of the created levels are assumed to follow a Fermi-Dirac distribution according to the semi-empirical mass formula (see section 2.2.1 and reference [35]).
Transition probabilities and multipolarities are assigned to the modeled levels according to the Porter-Thomas distribution (see equation 2.48) based on the assumed PSF and LD. This means that the radiative width $\Gamma^{XL}_{\gamma_{i,f}}$ for allowed transition (according to the selection rules in equation 2.37) between an initial level i with energy E_i and a final level f with energy E_f is created following a Porter-Thomas distribution. By normalizing the simulated widths to the also simulated total radiative capture state width Γ_0, the modeled emission probabilities per neutron capture event $p^{\text{sim}}_{\gamma,i,f}$ of a transition are obtained as

$$p^{\mathrm{sim}}_{\gamma,i,f} = \frac{\Gamma^{XL}_{\gamma_{i,f}}}{\Gamma_0}. \tag{2.78}$$

Internal conversion coefficients for these transitions are calculated with the BRICC code [41]. Within this modeled level scheme a large number of individual γ-ray cascades so-called "events" are simulated. This process is typically repeated several times for different realizations of the level scheme, to avoid any bias arising from a specific realization and to assess the fluctuation range, that is the uncertainty, of the simulation.

From the simulation aside from the radiative widths also the thermal radiative capture cross section can be extracted. The sum of the experimentally determined $\sigma^{\mathrm{exp}}_{\gamma_{i,\mathrm{GS}}}$ and the simulated $\sigma^{\mathrm{sim}}_{\gamma_{i,\mathrm{GS}}}$ γ-ray transitions directly populating the ground state corresponds to the thermal radiative neutron capture cross section σ^0_c, as given in the following equation 2.79.

$$\sigma^0_c = \sum \sigma^{\mathrm{exp}}_{\gamma_{i,\mathrm{GS}}}(1+\alpha_{\gamma_{i,\mathrm{GS}}}) + \sum \sigma^{\mathrm{sim}}_{\gamma_{i,\mathrm{GS}}}(1+\alpha_{\gamma_{i,\mathrm{GS}}}) = \frac{\sum_i \sigma^{\mathrm{exp}}_{\gamma_{i,\mathrm{GS}}}(1+\alpha_{\gamma_{i,\mathrm{GS}}})}{1-P^{\mathrm{sim}}_{\mathrm{GS}}}, \tag{2.79}$$

where $P^{\mathrm{sim}}_{\mathrm{GS}}$ is the simulated ground state population and $\alpha_{\gamma_{i,\mathrm{GS}}}$ are the internal conversion coefficients. $P^{\mathrm{sim}}_{\mathrm{GS}}$ is obtained like any simulated level population from the simulated $\Gamma^{XL}_{\gamma_{i,f}}$'s. As in the extreme statistical model the $\Gamma^{XL}_{\gamma_{i,f}}$'s are treated as uncorrelated and independent, they sum up to the total decay width $\Gamma_{\gamma,i}$ of a given level as shown in equation 2.80.

$$\Gamma_{\gamma,i} = \sum \Gamma^{XL}_{\gamma_{i,f}} \tag{2.80}$$

Using equation 2.80 and equation 2.78 the modeled population of a level is calculated as

$$P^{\mathrm{sim}}_i = \frac{\Gamma_{\gamma,i}}{\Gamma_0} \tag{2.81}$$

The simulated average total radiative capture state width Γ_0 can be compared to measured data to assess the validity of the model. Also, the simulated population of the levels below $E_{\mathrm{crit.}}$ that are depopulated under the emission of measured γ-radiation can be used to assess the model's validity. From the measurements of the σ_γ values the experimental level depopulation can be calculated as

$$P^{\mathrm{exp}}_i = \frac{\sum^{<i}_{f=\mathrm{GS}} \sigma^{\mathrm{exp}}_{\gamma_{i,f}}(1+\alpha_{\gamma_{i,f}})}{\sigma^0_c}, \tag{2.82}$$

where $\alpha_{\gamma_{i,f}}$ are the internal conversion coefficients corresponding to the transition. This calculation can be performed for all levels up to $E_{\text{crit.}}$ that have measured de-excitation γ-rays. As the population and depopulation of a level has to be the same, so that the level is balanced, it should hold that $P_i^{\text{exp}} = P_i^{\text{sim}}$. The agreement between both values is generally shown in a so-called "population-depopulation plot", in which the simulated population of level i P_i^{sim} is plotted against the experimental depopulation P_i^{exp} of that level. A perfect agreement is visualized in these plots by a bisecting line corresponding to $P_i^{\text{exp}} = P_i^{\text{sim}}$. Thus, the consistency of simulation and experimental results can be checked.

All the Monte Carlo simulations discussed above use experimentally evaluated data. Using particle transport simulation codes like MCNP5 and Geant4 (and others) new installations, including transmutation plants or non-destructive nuclear waste characterization facilities like the MEDINA project [61], can in principle be planned. These codes, however, can only produce reliable results if the provided cross section data for all simulated processes are accurate and precise enough. Especially cross section data of actinides are rarely known well enough and are in disagreement with each other between different evaluated data tables, e.g. ENDF (USA)[5], JEFF (OECD)[6] or JENDL (Japan)[7].

It is one aim of this work to describe a method for the accurate and precise measurement of partial thermal radiative capture cross sections, as well as thermal radiative capture cross sections of actinides. This is the scope of chapter 3. In chapter 4 data for some selected actinides (^{237}Np, ^{241}Am and ^{242}Pu) will be provided along with a detailed uncertainty assessment. In combination with e.g. Monte Carlo based simulation tools these improved data can be used to develop non-destructive assays for the quantification of actinide residues from nuclear activities in complex matrices using PGAA.

CHAPTER III

Experimental Details

In this section the measurement facilities and evaluation tools employed in this work will be discussed. A description of the evolution of the sample designs made between 2011 and 2013 will then be given before the finalized sample design will be discussed as well as the specific details of the samples with which the results in this work are measured. Also the results of a validation experiment for the final sample type will be discussed. The section will conclude with a discussion of the photon absorption and reaction rate corrections of the final samples.

3.1 Irradiation Facilities

The neutron irradiations carried out in this work were performed at the external cold neutron beams in Garching and Budapest using the equipment at the local PGAA facilities. A short description of these facilities will now follow.

3.1.1 The PGAA Facility at BRR

The Budapest Research Reactor (BRR) is a water-cooled and water-moderated 10-MW reactor built in 1959 [62]. Its thermal neutron flux in the core is $2 \cdot 10^{14}\,\mathrm{cm^{-2}\,s^{-1}}$, while a thermal equivalent neutron flux of around $1 \cdot 10^{8}\,\mathrm{cm^{-2}\,s^{-1}}$ is provided for a PGAA facility. The PGAA facility of the Budapest Neutron Center [2, 63, 64, 65, 66] is located at the end of a curved super-mirror neutron guide of the BRR. This PGAA facility was in operation from 1996 to 2000 [67] using thermal neutrons. In 2001 a liquid hydrogen cold neutron source was installed at the BRR and the neutron guide was reconstructed and the PGAA station has operated at cold neutron energies since then [63]. The neutron spectrum at the PGAA-station has been measured in a time-of-flight experiment [66] exhibiting an average neutron energy of 0.012 eV. The neutron spectrum is shown in Figure 3.1(a).

The neutron guide is split into an upper and a lower part to provide two cold neutron beams. Both can be closed separately with a shutter of borated rubber and a sheet of cadmium. The upper beam is used for the PGAA station while the lower one is used for the neutron radiography instrument. Thus, at both stations similar neutron spectra are provided. The beam tubes for both instruments are covered with an enriched ^{6}Li-plastic (with the isotopic abundance of ^{6}Li being enriched to 86.6 %), which acts as an

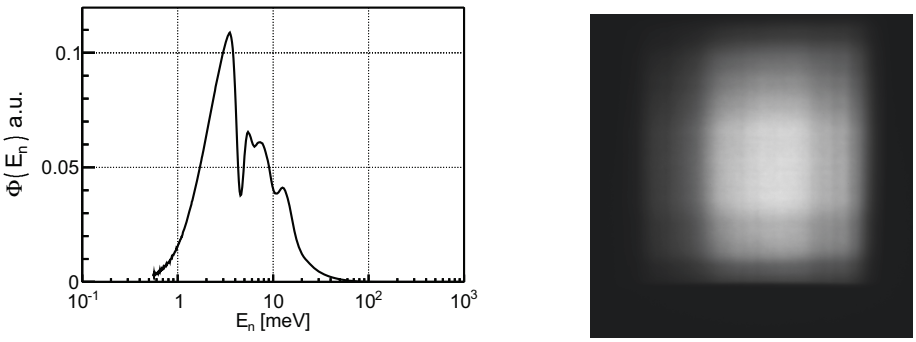

(a) (b)

Figure 3.1: (a) Cold neutron spectrum at the PGAA station of the Budapest Neutron Center. (b) Image of the beam profile at the neutron radiography station.

radiation protection and prevents scattered neutrons from influencing the measurement at the PGAA station. The beam guide of the PGAA station ends 1.5 m behind the sample chamber in a ^{6}Li-containing beam stop surrounded by lead bricks.
The neutron beam homogeneity was tested with the neutron radiography station at the end of the lower part of the beam guide. A CCD camera is used to register the photons from a scintillator/converter screen, irradiated by neutrons. With the CCD camera ten images were taken with open beam and their average was determined. Then another set of ten images was taken with closed beam and again the average was calculated. The images were subtracted from one another, resulting in a picture of the beam profile. This image presented in Figure 3.1(b) shows a rather homogeneous beam profile with some vertical lines from the reflections on the guide walls and some much slighter horizontal lines. The neutron beam dimensions are roughly 3.3 by 3.5 cm. The side length of a pixel in the image corresponds to 46 µm. As the neutron guide is basically identical to the one for the PGAA station, a similar beam profile can be expected there. Thus, it can be concluded that the neutron beam is homogeneous over distances of the order of mm especially at the center of the beam profile.
During any irradiation the stability of the neutron flux is monitored and recorded with an ORDELA Model 4511 N neutron gas-detector placed behind the beam shutters, so that a constant irradiation can be ensured [65].

A picture of the setup at the PGAA station is shown in Figure 3.2(a). The neutron beam enters through the lead-covered beam shutters on the left-hand side passes through the aluminum sample chamber (in the middle of the image) and leaves the image on the right-hand side towards the beam stop. The detector is placed perpendicular to the neutron beam axis and covered with a 2.4 mm thick sheet of enriched ^{6}Li-plastic.

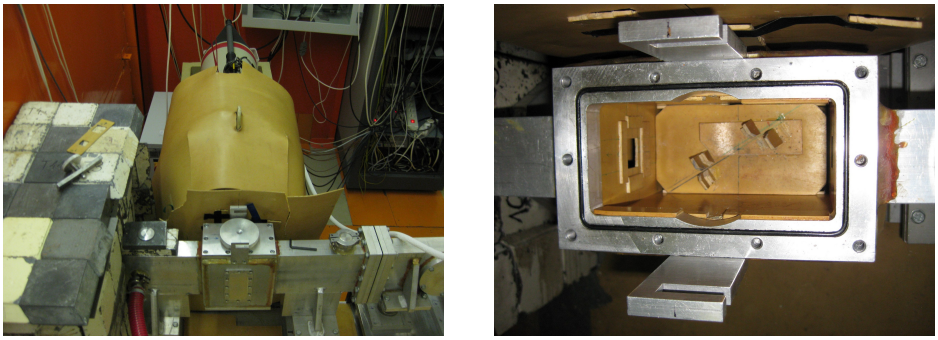

(a) (b)

Figure 3.2: (a) A view of the PGAA station at the Budapest Neutron Center with the neutron beam entering from the left, with the aluminum sample chamber in front of the detector system and the second beam guide towards the neutron radiography station to the right. (b) Top-down view on the inside of the sample chamber.

In Figure 3.2(b) the aluminum sample chamber is shown. It is lined with a 2.4 mm thick sheet of enriched ^{6}Li-plastic on the inside. A 2×2 cm opening can be seen in front the sample chamber on the left-hand side. Next to this opening mounts for an additional ^{6}Li-plastic collimator can be seen, e.g. for the 24 mm^2 pinhole collimator usually used in this work. On the bottom of the sample chamber supports from ^{6}Li-plastic for the positioning of samples can be seen. Samples are typically fastened onto an aluminum sample-holder frame with Teflon® strings. The frame is introduced into the sample chamber through the round cap visible on the image in Figure 3.2(a) and placed between the supports. The samples can be placed parallel to the neutron beam axis, perpendicular to it or at an angle of 30°, which corresponds to 60° to the central axis of the detector. By tilting the sample the aluminum frame is prevented from being irradiated, causing a decrease and deformation of the neutron flux, and from decreasing the detection efficiency by absorbing photons that otherwise would reach the detector. The sample chamber has a window facing the detector which consists of a 0.5 mm thick aluminum foil. The sample chamber is thus completely closed and can be evacuated in order to decrease the activation of air.

The basic detector arrangement is shown in Figure 3.3. The spectrometer consists of a coaxial n-type HPGe detector with 27-% relative efficiency manufactured by Canberra. It is surrounded by an approximately 48 mm thick, eight segment, coaxial BGO scintillation detector that acts as a Compton suppressor as described in section 2.6.2.1. In addition a 65 mm thick BGO scintillation detector, the so-called "back-catcher", is placed in the opening behind the HPGe detector, closing the distance between the cooper cold finger and the aluminum holder of the HPGe crystal. Spectra are acquired using a Canberra

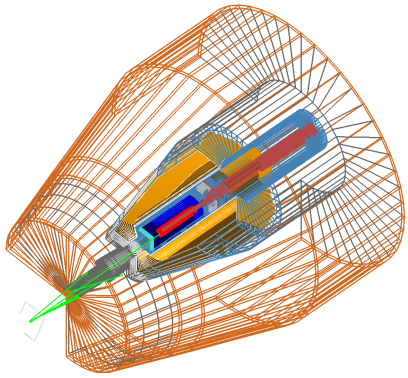

Figure 3.3: Geant4 representation of the detector used at the PGAA station of the Budapest Neutron Center and a sample in a tilted position. The green lines emerging from the sample represent simulated photon tracks, red lines represent electron tracks. The non-wire-frame parts are the HPGe detector (blue) and the BGO Compton shield (orange) surrounding it. The shielding, sample and supporting parts are all drawn as wire-frame models, with the color corresponding to a material type.

AIM 556 MCA.
The detector is shielded against scattered neutrons with a 2.4 mm thick sheet of enriched ^{6}Li-plastic. The detector system is also shielded against photon radiation from outside the sample chamber with a 11 cm thick lead shield with a circular collimator opening of 22 mm and an additional 10 mm thick tungsten collimator right in front of the BGO. The overall distance between the center of the sample chamber and the HPGe detector surface is 235 mm. In addition to the PGAA station a low background counting chamber called "DÖME" is provided at the BRR site. The 155 mm thick chamber walls consist of pre-World War 2 steel and thus free from man-made radioactivity. Either a Canberra GR1319 HPGe detector or a Canberra Low Energy planar HPGe detector (Low Energy Germanium Detector (LEGe)) with their respective cryostats can be placed inside the low-background chamber allowing for a sample-to-detector distance of up to 250 mm [65]. A precise distance from the detector is kept by using a special aluminum frame and aluminum distance pieces. For the decay measurements carried out in this work a sample-to-detector distance of 167 mm is used.

3.1.1.1 Simulation of the BRR facility employing Geant4

For the purpose of determining precise self-absorption corrections for the evaluation of cross section data, the whole detector setup was modeled within the Geant4 framework (see section 2.8.1). A neutron radiographic image of the HPGe-detector as well as the technical details given by the manufacturer were used.

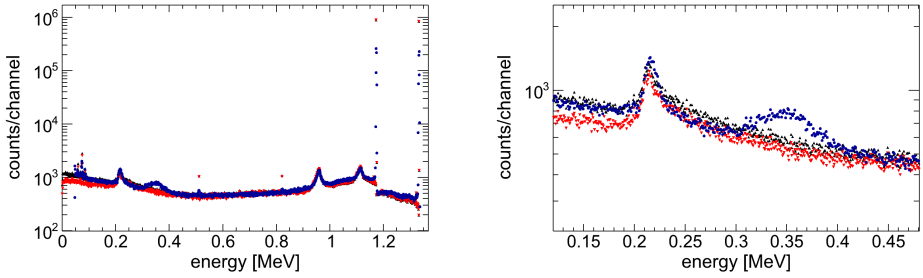

(a) (b)

Figure 3.4: (a) A spectrum measured for ^{60}Co at the Budapest PGAA station (blue points), along with a simulated spectrum with complete Compton suppressor (red downward triangles) and with deactivated back-catcher (black upward triangles). (b) Close-up near the lower end of the spectra.

In Figure 3.4 a measured spectrum of a ^{60}Co source is shown along with two simulated spectra. The form of the measured spectrum is reproduced very well by the Geant4 simulation, but at the low-energy end of the spectrum a slight difference can be seen. The backscatter peak is well reproduced and the bump at 350 keV seems to be a feature introduced by the used source, as it is not present in other measurements. The simulation implies that for energies below the backscatter peak the Compton suppression is expected to be stronger than observed in the measurement. In this region mainly forward-scattered photons contribute to the Compton plateau and in fact turning off the back-catcher in the simulation leads to a good reproduction of the measured spectrum shape in that region. Indicating the signal of the back-catcher not being processed correctly, it did not contribute to the Compton suppression, which has recently been confirmed by the Budapest PGAA group [68].

3.1.2 The PGAA Facility at FRM II

The Forschungs-Neutronenquelle Heinz Maier-Leibnitz (FRM II) is a light-water-cooled and heavy-water-moderated pool-type reactor with a power of 20 MW. It went into operation in 2004 and is operated with only one element of nuclear fuel using highly enriched uranium (95 % ^{235}U).
A liquid deuterium moderator around the fuel element serves as a cold neutron source, producing neutrons with their energies following a Maxwellian distribution with an average energy of 5 meV. From the cold source neutrons are extracted with several curved neutron guides. Due to different curvatures and positions relative to the cold source, the neutron energy spectra at the end of the neutron guides differ significantly. The PGAA

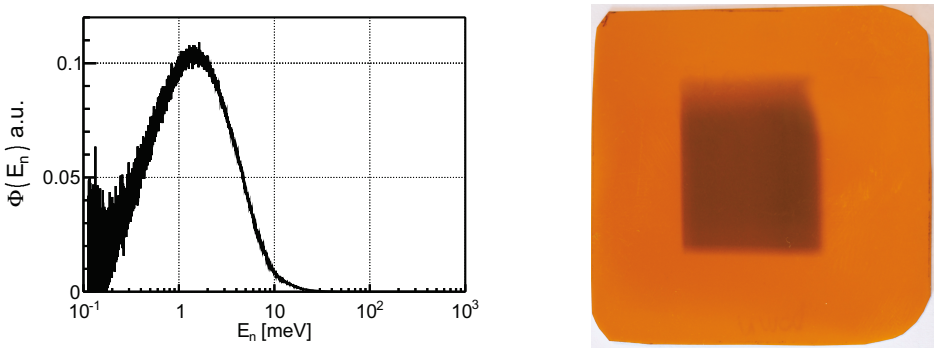

(a) (b)

Figure 3.5: (a) Cold neutron spectrum at the PGAA station of the FRM II. (b) Image of the neutron beam profile taken with a special Li-containing film. The film was fit in the sample Teflon® holder, thus its dimensions are 5×5 cm.

facility is located at the end of a 51 m long curved neutron guide with the last 5.8 m having an elliptical shape that serves to focus the neutron beam and thus increases the neutron flux at the sample position to a thermal equivalent neutron flux of the order of $1 \cdot 10^{10}\,\mathrm{cm}^{-2}\,\mathrm{s}^{-1}$. The elliptical shape of the guide can be extended with a removable 1.1 m long neutron guide (elliptical beam extension) up to the sample chamber. This increases the flux yet by a factor of two at the cost of additional background radiation resulting from the irradiation of the removable extension. Also, the beam extension increases the divergence of the neutron beam. The neutron wavelength spectrum at the sample position was measured with a compact time-of-flight setup [69]. The neutron spectrum shown in Figure 3.5 (a) was derived by converting the neutron wavelength λ_n to the neutron energy E_n via the de'Broglie relationship (equation 2.3), thus the measured flux distribution $d\Phi/d\lambda_\mathrm{n}$ is converted by

$$\frac{d\Phi}{d\lambda_\mathrm{n}} = \frac{d\Phi}{dE_\mathrm{n}}\frac{dE_\mathrm{n}}{d\lambda_\mathrm{n}} \tag{3.1}$$

$$\Rightarrow \frac{d\Phi}{dE_\mathrm{n}} = \frac{m_\mathrm{n}\lambda_\mathrm{n}^3}{h^2}\frac{d\Phi}{d\lambda_\mathrm{n}}, \tag{3.2}$$

with m_n being the neutron mass and h the Planck constant. With an average energy of 1.6 meV the neutron beam is significantly colder than the neutron beam provided at the PGAA station of the BRR. The beam profile of the neutron beam is shown in Figure 3.5 (b). For this image the optional elliptical beam extension was not used.

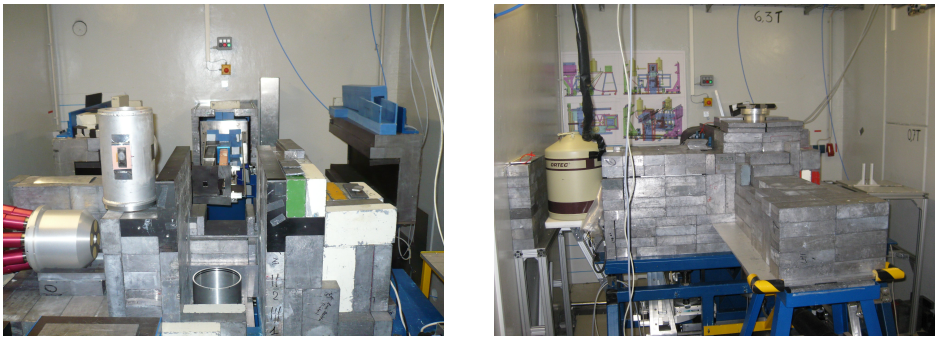

(a) (b)

Figure 3.6: (a) A picture taken during the installation of the PGAA facility at FRM II, with the sample chamber in the middle lower part, the interchangeable ends of the beam guide on the middle upper part and a BGO detector at the detector position to the right [70]. (b) A picture of the completed setup.

The sample chamber is a cylindrical tube placed vertically of 15 cm inner diameter manufactured from aluminum with zirconium windows in the directions of the incoming neutron beam and the detector. Thus, the chamber can be evacuated. Up to six samples can be placed on a sample holder. The latter is made from Teflon® and is slid into the sample chamber onto a moving mechanism. Due to the moving mechanism the samples can be changed automatically from a PC workstation.
Similarly to the PGAA facility at the BRR, the detector system at FRM II consists of a HPGe detector surrounded by BGO scintillation detector acting as a Compton suppressor, however without an additional back-catcher. The HPGe detector used is an Ortec n-type Poptop detector with a relative efficiency of 60 %. For the collection of the spectra a DSPEC-50 digital spectrometer is used. The detector system is encased with a 20 cm thick wall of lead bricks shielding against external γ radiation with a cylindrical collimator of 2 cm diameter facing the sample chamber. The entrance of the collimator is covered by a 2.4 mm thick piece of ^{6}Li-plastic and an additional lithium-containing ceramic with a thickness of 5 mm. The total distance between the sample and the detector is 29.5 cm.

The whole detector system including the sample chamber and the cryostat is placed on a heavy load table that can be moved on rails. This is done in order to access the interchangeable ends of the neutron guide and to place an additional collimator at the end of the neutron guide. In this work a self-made collimator is used made from a 5 mm thick sheet of borated rubber with a circular hole of 5 mm in diameter. The γ-rays produced in the $^{10}\mathrm{B}(\mathrm{n},\alpha)^{7}\mathrm{Li}$ reactions are prevented from entering the sample chamber by a 32 mm thick lead block with a 5 mm hole, with the block being directly attached to the borated rubber. The position of this self-made collimator is adjusted so that the collimated beam

is centered on the middle of the samples. This is checked by irradiating a special Li-containing film that is placed in the sample holder. When the beam is opened the film quickly blackens where the neutron beam traverses it. Pictures from the installation phase and of the final PGAA facility can be seen in Figure 3.6.

3.1.2.1 Optimization of the FRM II PGAA Facility using Geant4

As the PGAA facility in Garching is still relatively new it is constantly being improved. In assisting these attempts, a model of the system was implemented in Geant4, which later was also used for calculating photon self-absorption corrections. The model was created using a technical drawing of the BGO, a detailed drawing of the HPGe detector provided by Ortec and the measured dimensions of the shielding and sample chamber. The model is shown in Figure 3.7.

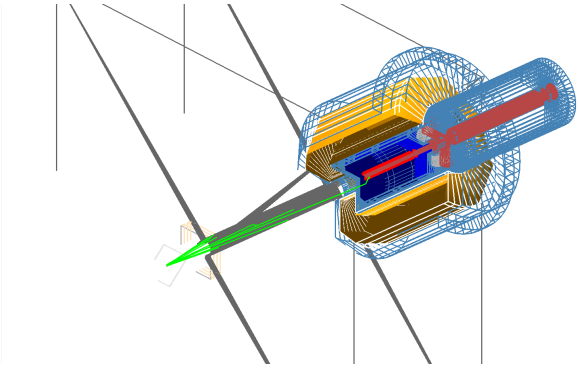

Figure 3.7: A Geant4 representation of the detector used at the PGAA station at FRM II and a sample in tilted position. The green lines emerging from the sample represent simulated photon tracks, the red lines represent electron tracks.

The model was helpful in the process of choosing a new BGO Compton shield for the PGAA spectrometer.
It was found that the BGO crystal should be at least 1 cm thick at the front and at least 4 cm thick at the perimeter. The model was used to predict if a specially manufactured 95 mm long but therefore thinner HPGe crystal would be better suited for a planed position-sensitive detection setup compared to a standard size HPGe crystal. In contrast to the expectation, it was found that the use of this crystal would decrease the efficiency at 400 keV by about 20 % and at 2 MeV almost by 30 %. Thus, it was decided against a specially manufactured HPGe crystal.

Additionally, the Geant4 model was used for optimizing the position of the HPGe detector inside the BGO detector. The BGO has a front opening with a diameter of 3 cm

and an opening of 8.4 cm at the back, where the HPGe detector is inserted. It contains no back-catcher. The shape of the remaining Compton-plateau drastically changes depending on the position of the HPGe detector. If the detector is placed close to the frontal opening of the BGO, the Compton edges become wider, as fewer of the escaping photons can be detected, but at the same time improves the Compton suppression at the lower end of the spectrum. The simulations showed that a relatively flat Compton plateau could be achieved by placing the HPGe detector at a distance of 4 cm from the frontal part of the BGO, as shown in Figure 3.8. Because of this result, the placement of the HPGe detector inside the BGO was adjusted accordingly at the PGAA-station.

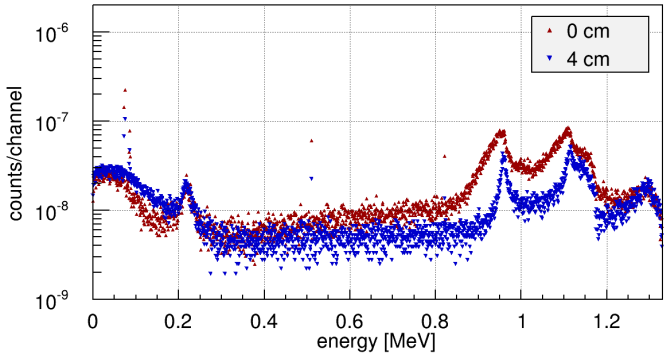

Figure 3.8: Optimization of the position of the HPGe detector inside the BGO detector at the PGAA-facility of FRM II. The simulated background of a ^{60}Co with the HPGe detector as close as possible to the frontal opening of the BGO (red triangles) and the result of a simulation where the HPGe detector is placed 4 cm from the frontal part of the BGO (blue triangles).

The positioning of the HPGe detector in vertical direction was also investigated. Elevating the HPGe detector by 5 mm and thus moving it off the central axis of the collimator influences the efficiency, as the volume of the HPGe detector directly behind the collimation window changes (because the void of the cold finger is moved out of the plane).
It was found that a 5 mm elevation can increase the efficiency by almost 45 % for the ^{60}Co lines at around 1 MeV but the elevation may be not favorable as it would break the radial symmetry of the system. Moving the HPGe detector off the central axis was not yet tested.

Also, it was investigated how the cut-off energy of the BGO detector, that is the lowest energy deposited in the BGO crystal to be regarded as a veto-signal, influences the suppression at the Compton-edge. As a result the cut-off energy should be below 10 keV up to where the suppression is basically constant. A publication on the current setup of the PGAA facility at FRM II including these simulation results is in preparation.

3.2 Spectrum Evaluation

The acquired PGAA gamma spectra are very complex with several hundred peaks in each spectrum as exemplary shown in Figure reffig:PGAASpectrum. The analysis of these spectra was carried out with a series of computer programs, which will be described in this section.

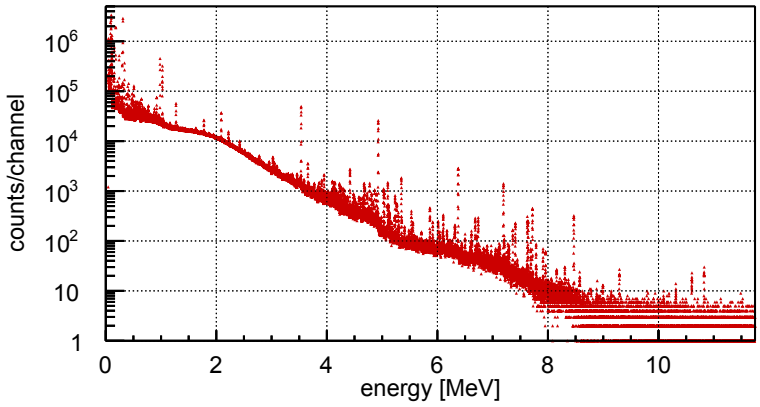

Figure 3.9: A PGAA spectrum obtained at the Budapest PGAA facility from the irradiation of a ^{237}Np containing sample.

3.2.1 HYPERMET-PC

A reliable peak-fitting procedure is crucial for accurate gamma spectra analysis. The determined peak area has to be independent of the shape of the background, particularly as a detection efficiency measured separately and thus at very different background should be used. In the case of multiple overlapping peaks it is important that the evaluated peak areas are resolved correctly.

PGAA spectra with typically 800 identifiable peaks were acquired in the energy range from 40 keV/50 keV to 12 MeV. Within this range, the peak density, peak areas and the background upon which the peaks are being evaluated changes drastically. In the low-energy region up to 1.5 MeV the density of peaks is extremely high, as a large number of secondary γ-rays from the neutron capture process are found in this region, accompanied by the decay γ-rays of the created nuclei as well as the decay γ-rays from the samples themselves, if they contain any radioisotopes. Additionally, intense X-rays created for instance in internal conversion processes are present in the energy range up to about 120 keV. Further complications arise from the fact that peaks may have different shapes

depending on the γ-ray energy and the peak count rate. Whereas small peaks can usually be fitted with a simple Gaussian function, peaks with typically more than 10 000 counts are so precisely outlined that a skewness to lower energies is observed. This originates from incomplete charge collection in the detector crystal (see section 2.6.2.2). Also, as multiple Compton scattering events in the detector volume and low-angle Compton scattering at the collimator walls result in a small loss of energy, the baseline below these peaks increases proportional to the peak area. Additionally, due to effects such as electron or low-energy X-ray escape from the sensitive volume of the detector, which are basically surface effects, another tailing effect may occur leading to a tailed over-fluctuation of the baseline at the peak position [8, 9].

A tool specially designed to meet the evaluation needs of these complicated spectra is HYPERMET-PC [71, 72]. HYPERMET-PC is based on the HYPERMET code written in FORTRAN and developed at the Naval Research Laboratory in Washington D.C. [73]. It was specifically designed for the analysis of γ-ray spectra obtained with germanium detectors. It features a semi-empirical peak-shape function very much suited for fitting peaks in these kinds of spectra, along with an algorithm for finding and fitting these peaks automatically. Based on these features HYPERMET-PC was developed at the Institute of Isotopes and Surface Chemistry in Budapest from 1992 to 1999. The HYPERMET code was translated into the MS-DOS compatible C++ programming environment Borland C++ and additional features were added to help evaluating PGAA and INAA spectra. Among these features was the implementation of tools to handle the efficiency and non-linearity calibration of the detector system and apply these corrections directly to measured spectra if wanted. A more detailed description of the features added to the original HYPERMET code can be found in [74]. The code today can be used within the freely available DOS emulator DOSBox.

For peak fitting a skewed Gaussian is available, which is a Gaussian modified by an exponential function on its low-energy side. The skew term is modeled by an exponential function, because the incomplete charge collection causing the skew term happens due to lattice defects. These defects can be assumed to be homogeneously distributed within the crystal rendering charge trapping basically to being a Poisson process with an unknown mean free path. Thus, the skew term parameters are mainly fixed for the detector system so that the skew term depends on the total height of the peak. For very intense peaks it is sometimes necessary to allow HYPERMET-PC to vary the skew term parameters by up to $\pm 30\,\%$ in order to get good fitting results. The peak shape can further be deformed by other effects such as pile-up on the high-energy side of the peak caused by the spectrometer randomly detecting a low-energy photon of the background together with the photon belonging to the peak, a so-called "random coincidence".
The baseline is fit together with the peaks.Aside a linear and a second order polynomial function, two peak-specific baseline functions are available. The second order polynomial is used as a description of the baseline to approximate complex background shapes such as the slope of a germanium triangle.

The step function below a peak describing the effect of the rising of the baseline by multiple Compton scattering events, is described by an error function with its height depending on the peak area. For the fit of the aforementioned skew term at the peak position an exponential function is implemented, basically modifying the step and is called a "tail". The parameters of both functions depend on the parameters of the associated peak.
HYPERMET-PC is able to fit up to ten peaks simultaneously together with their background in regions of 20 to 100 channels. An example of a fitted region is shown in Figure 3.10.

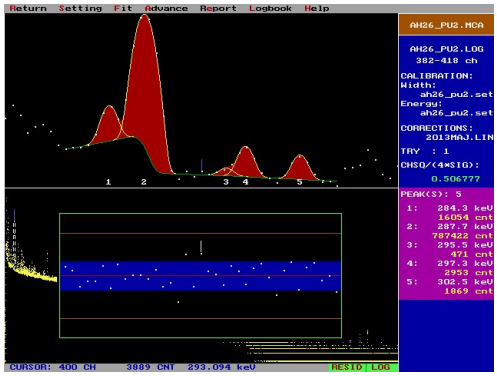

Figure 3.10: A region of a PGAA spectrum obtained at the Budapest PGAA facility from the irradiation of a ^{242}Pu containing sample fitted in HYPERMET-PC.

The width of the peaks depends on the number of electron-hole pairs created and thus on the energy of the incident photon, following a square-root function as described in section 2.6.2.2. Thus, prior to an evaluation, the peak width is calibrated by finding and fitting suitably large resolved peaks in the high and low-energy region of the spectrum. For this the Gaussian width can be fitted freely in HYPERMET-PC. The width of these two peaks is then used to fit the parameters a and b of the function $\sqrt{a + bE}$, where E is the energy. Then in a fit of a region the peak width of the included peaks is determined in a constrained fit of these two parameters, where they are only allowed to vary by $\pm 20\,\%$. Using this constraint HYPERMET-PC is capable of resolving peaks that overlap, which otherwise, especially in the case of peaks with similar heights, might only result in one Gaussian with a higher width. Note that X-ray peaks are typically broader then γ-ray peaks, due to their original line widths. If the information is needed their fits thus have to be performed separately.

3.2.2 Calibration of the Instruments

To determine the energy and intensity of radiation from a measured spectrum, the channels of the MCA need to be assigned to the corresponding energies and the peak areas have to

be converted into the activities of the radiation. The energy conversion is accomplished by a two-point energy calibration within each measured spectrum, applying a previously determined non-linearity function. The intensity mapping is achieved by determining the efficiency function of the detector.

The non-linearity and efficiency functions of the detector systems were determined using sources containing radioisotopes with certified activities as well as prompt γ-ray sources. These sources were placed at the same position as the samples measured later. The certified radioisotope sources emit γ-rays up to the low MeV-range. For PGAA measurements the energy region is therefore extended to above 10 MeV by using prompt γ-ray sources that are irradiated at the sample position. A list of the sources used for the calibrations at the PGAA facilities in Budapest and Garching are listed in Table 3.1. For the extension into the high energy regime PGAA measurements of a deuterated urea sample utilizing the prompt γ-rays of the ^{14}N(n,γ)^{15}N reaction and of a PVC sheet utilizing the prompt γ-rays of the ^{35}Cl(n,γ)^{36}Cl reaction were performed at both facilities.

Table 3.1: List of the certified standard sources used for the non-linearity (NL) and the efficiency (EFF) calibration at the specified PGAA facility along with their certified activities with relative uncertainties (one standard deviation) and the reference date (ISO8601 formatted).

	Source	Activity [kBq]	Reference Date	Calibration
BRR	^{60}Co	201.0(0.7 %)	2009-01-05	EFF
	^{133}Ba	213.4(0.5 %)	2012-06-01	EFF, NL
	^{152}Eu	203.9(0.7 %)	1978-07-01	EFF, NL
	^{207}Bi	392.2(2.0 %)	1981-06-17	EFF
	^{226}Ra	159.0(1.25 %)	2012-06-01	EFF, NL
	^{241}Am	112.4(0.5 %)	2012-06-01	EFF
FRM II	^{60}Co	102.6(0.5 %)	2011-07-01	EFF
	^{109}Cd	84.1(0.9 %)	2011-07-01	EFF
	^{137}Cs	56.7(0.5 %)	2011-07-01	EFF
	^{133}Ba	None given		EFF(relative), NL
	^{152}Eu	39.0(0.7 %)	2011-07-01	EFF, NL
	^{152}Eu	393.0(1.5 %)	2008-03-01	EFF, NL

Non-linearity

The energy deposited in the detector is represented by the channel number provided by the MCA. As the electronic processes of the signal treatment, such as the conversion from analog to digital signal, are not completely linear the conversion from channel to energy is not completely linear, either. This deviation from a linear calibration, which would result

from a linear fit between two channels of known energies, is called the "non-linearity" of the detector system. To assign the correct energies to all peaks a correction needs to be applied. This non-linearity reaches up to 1 keV at the Budapest PGAA station, which is below 0.01 % over the whole energy range and up to 2 keV at the Garching PGAA-station, which still is below 0.02 % over the whole energy range.

HYPERMET-PC offers a tool for determining this non-linearity and for applying the corresponding corrections to a measured spectrum [75, 76]. For the correction the peak positions of the well known γ-ray energies of the calibration sources are utilized.
The non-linearity values are determined between pairs of peaks with corresponding tabulated energy. Then an empirical polynomial function with up to an order of 8, created from a base of orthogonal polynomials, is fitted with a least squares method. The order of the polynomial is increased as long as the added parameters are significant. Note that the fitted function is only a valid approximations for the real non-linearity function for energies between the outermost γ-ray peaks used for the fit.
For the extension of the energy calibration above the highest energy of the certified calibration sources, the prompt γ-rays of Cl and N are used, because very precise data on the prompt γ-radiation of Cl is available and N has a number of prompt γ lines above 8.5 MeV, allowing an extension of the calibration to the 10 MeV-range.

The non-linearity function for the Budapest PGAA facility is shown in Figure 3.11. In the case of the PGAA facility in Garching it was not possible to fit a suitable polynomial over the whole energy range, thus two non-linearity functions were used, one for energies up to 1408 keV (^{152}Eu) and one starting from 1213 keV (^{152}Eu) with a slight overlap. Both are shown in Figure 3.12. Note that the high reduced χ^2 of the first fit is caused primarily by the two lines of ^{133}Ba below the 122 keV line of ^{152}Eu. This may indicate that the non-linearity of the system below this energy is slightly unstable over time.

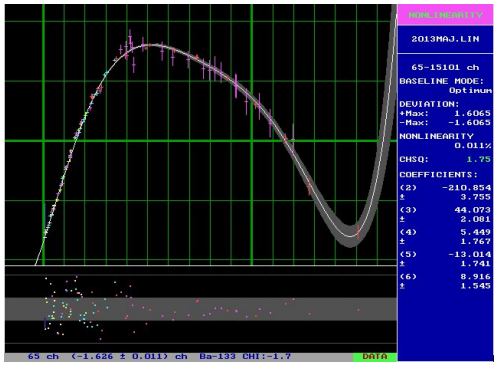

Figure 3.11: Non-linearity function for the PGAA facility of the BRR.

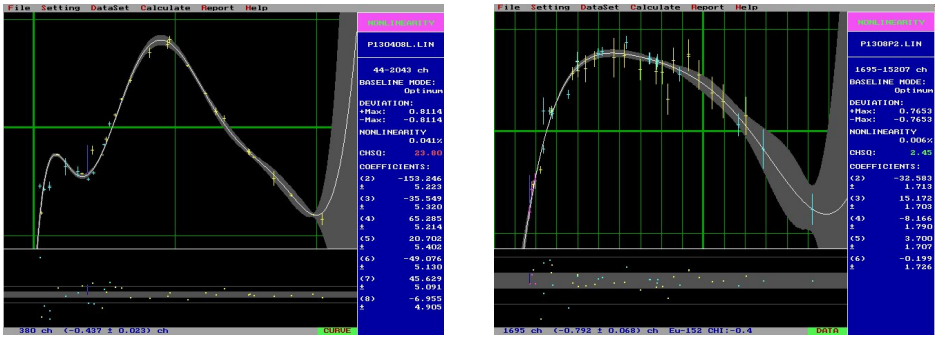

(a) (b)

Figure 3.12: Non-linearity functions of the PGAA facility at the FRM II.(a) Non-linearity function in the low-energy regime up to 1408 keV. (b) Non-linearity function in the high energy regime starting from 1213 keV.

Detection Efficiency

As explained in section 2.6 it is necessary to correct the peak areas in a spectrum for the energy-dependent detector efficiency. The probability of the detector registering a photon of a given energy originating from the sample position is influenced by the geometrical setup. It is for instance influenced by the source-to-detector distance, the detector collimation, the size of the HPGe crystal and the absorption in material between the source and the detector (e.g. in the neutron shielding or in the detector casing).
The absolute efficiency for the detection of photons with a given energy from a source with a known activity A (or known reaction rate for (n,γ) reactions) is given by equation 2.65. The activity A_0 of certified calibration sources on a given reference date is usually known with an uncertainty in the percent range, rendering these sources an excellent choice for calculating the absolute efficiency. During a measurement the activity of the sources can be regarded as constant as the half-lives $T_{1/2}$ of the used radioisotopes are far larger than the measurement time t_{real}. The activity can then be calculated using the exponential decay law (see equation 3.3) and the known time that has passed since the reference date Δt.

$$A = A_0 \exp\left(-\frac{\ln(2)}{T_{1/2}} \cdot \Delta t\right) \tag{3.3}$$

This however only allows a point-wise definition of the detection efficiency. Therefore, an empirical function has to be fitted to these points in order to determine an efficiency valid for the whole energy range investigated. HYPERMET-PC offers a tool for determining this efficiency function [75]. An empirical polynomial like the one used in the

previous section is least squares fitted through the points on a log-log scale [77, 78], thus the resulting function is of the form

$$\epsilon(E_\gamma) = \exp\left(\sum_{i=0}^{n} (\ln E_\gamma)^i\right). \tag{3.4}$$

To extend the energy range up to the 10 MeV-region sources with well-known partial radiative capture cross sections are used. For a calculation of the absolute efficiency exact knowledge of the neutron flux is needed to calculate the reaction rates. Therefore, instead of calculating the absolute efficiency, the efficiency relative to the strongest line is calculated via the known γ-ray emission intensities relative to the strongest line. As several of the lines including the strongest line are in the energy region covered by the calibration sources, where the absolute efficiency is easily determined, this relative efficiency can be normalized accordingly.
The efficiency functions for both PGAA facilities are shown in Figure 3.13, as calculated in HYPERMET-PC. Note that the efficiency of the PGAA station at the BRR is approximately an order of magnitude higher than that at the FRM II, caused by the larger source-to-detector distance and the sharper collimation. For comparison, both efficiency functions are plotted together in Figure 3.14.

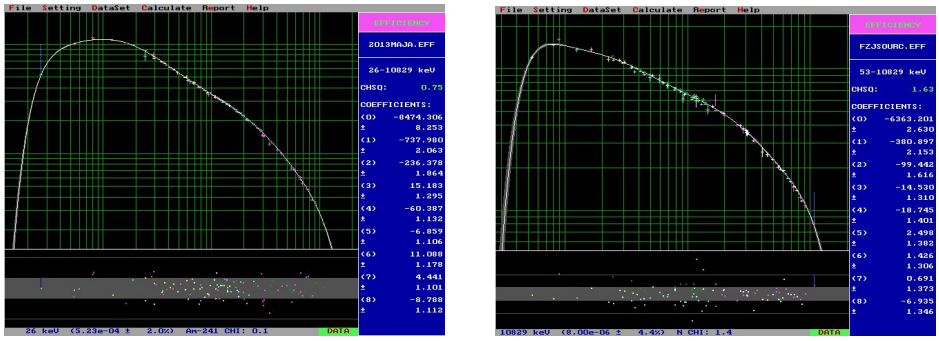

(a) (b)

Figure 3.13: Efficiency functions of the PGAA facilities at (a) the BRR and (b) the FRM II calculated in HYPERMET-PC.

3.2.3 Evaluation Procedure

A spectrum is evaluated in HYPERMET-PC by first calibrating the peak width. Then a two-point energy calibration is made using two separate peaks of known energies preferably one in the high and one in the low-energy region. Subsequently the corresponding

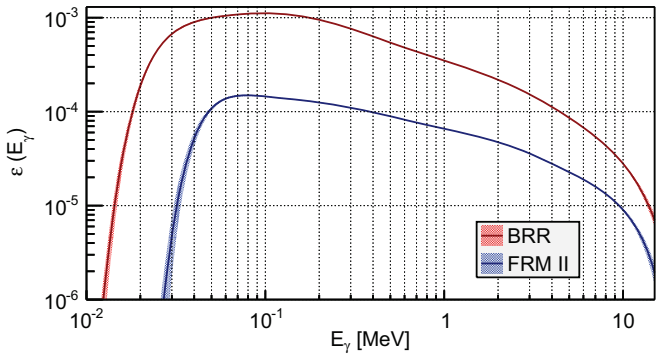

Figure 3.14: Comparison of the detection efficiency functions of the PGAA detectors at the BRR and the FRM II.

non-linearity correction is applied. Then the automatic peak finder is used to determine peaks. For this step only the linear background is allowed. Afterwards each region is inspected and it is checked whether the peaks and the background are described well by the fitted functions. The choice of functions used to describe the background is to some degree a decision of the experimenter. Within the scope of this work, the reduced χ^2 and the residuals of a fit, both provided by HYPERMET-PC, are used as an indication of the quality of the fit. The reduced χ^2 is generally sought to be reduced. More complex background functions leave fewer degrees of freedom for the fit, wherefore it is generally attempted to use the linear background whenever possible.
In a good fit the residuals between the data and the fit should follow a normal distribution and no systematic trends should be visible in the channel-dependent residual plot (see the lower part of Figure 3.10 for an example of this plot). This is used as an additional indication to decide if a fit is good or whether further changes have to be applied. Another indicator of a good description of the background is a visual check of whether the background would be described well by the fitted background function also beyond the borders of the fitted region.

After each region is examined, a so-called "peaklist" is exported from HYPERMET-PC and transferred into Microsoft Excel, where the peaks are identified according to their emitters, as far as possible. This is done by using the EGAF PGAA database [4, 79], created from PGAA measurements of all naturally occurring elements. Decay radiation is identified using the Evaluated Nuclear Structure Data File (ENSDF) [80, 81] and, if available, the Decay Data Evaluation Project (DDEP) [82] data, evaluated by the Laboratoire National Henri Becquerel, France. Single and double escape peaks are checked for. So are Compton edges of very intense peaks that could influence the baseline below a peak, in which case the peak fitting is to be rechecked in HYPERMET-PC. Each peak is tagged according to its emitter. Corrections are applied for peaks that should have a

contribution from prompt or decay γ-rays of previously identified sources, by means of the emission probabilities or partial radiative capture cross sections of the sources.
The obtained data are then further analyzed using the ROOT [83] framework developed at Cern and the computing environment provided by the Scipy package [84] within the Python programming language.

3.3 Design and Validation of Actinide Samples for PGAA

Samples containing actinides have to meet several requirements in order to be suitable for PGAA measurements. Not only should they be thin in order to reduce both, neutron and photon absorption within the sample (thereby introducing unnecessary uncertainties), they should also be no bigger than the scale on which the used neutron beam is homogeneous in order to ensure a uniform irradiation.
At the same time there has to be enough material to actually detect γ-ray peaks over the background of the measurement. This background is mostly produced by the sample casing which is necessary for radioactive samples. PGAA measurements are typically carried out by putting the sample material into a bag of 0.025 mm thick FEP (fluorinated ethylene-propylene polymer) foil, as carbon with a thermal capture cross section of 3.5 mb and fluorine with a thermal capture cross section of 9.6 mb produce little background radiation during irradiation.
This procedure is not ideal, first for experimental reasons. The geometry of powdery material (like the material used in this work) inside a bag is badly defined introducing unaccessible, thus uncorrectable, systematic uncertainties into the measurement. Second the procedure is not ideal for safety reasons as the FEP foil does not offer a good protection against α-radiation. The thickness of the foil is of the same order of magnitude as the range of the emitted α-particles, so it cannot be guaranteed that no α-radiation penetrates the bag. Also a bag this thin could crumble eventually due to radiation damage after being exposed to α-radiation for some time.

Thus, a more massive casing is needed for actinide materials, while still keeping the background radiation as low as possible. As prompt γ-rays are characteristic for the nucleus that captured a neutron, each type of nuclide present in the irradiated part of the sample casing contributes a different set of prompt γ-lines to a PGAA spectrum. Since every added peak might overlap or even obscure one of the peaks of the actinide, it is desirable to keep the number of different nuclides in the casing to a minimum.

In the following a description of sample material and sample designs that were made within the scope of this work will be given. In addition, some results will be given that were obtained from the PGAA measurements of the first two generations of the sample design. Then the finalized sample design and the procedure to manufacture samples of this design will be presented in detail. Finally results of experiments will be presented that were performed to investigate the expected accuracy in PGAA measurements with

this kind of samples.

3.3.1 Actinide Starting Materials

In this section the actinide starting materials used for the measurements are described. $^{242}PuO_2$ in powdery form was obtained in 2009 from Oak Ridge National Laboratory (ORNL) by the Sektion Physik of Technische Universität München (TUM). This material was transferred to Institut für Energie und Klimaforschung: Nukleare Entsorgung und Reaktorsicherheit (Institute for Energy and Climate Research: Nuclear Waste Management and Reactor Safety) (IEK-6) of Forschunsgzentrum Jülich GmbH (FZJ) in 2010. On request ORNL provided a detailed elemental and isotopic characterization of the $^{242}PuO_2$ batch from which the delivered material was taken. From this analysis it can be seen that the $^{242}PuO_2$ has an isotopic purity of 99.932 % ^{242}Pu and is chemically practically pure with contaminants from other elements summing up to less than 250.6 µg/g which is less than 0.03 %. The isotopic composition found in this analysis is summarized in Table 3.2. In PGAA measurements a Cl content of 0.03 wt% could be determined. Other impurities were below the detection limits. In decay measurements γ-ray peaks resulting from the decay of ^{241}Am, ^{243}Am and ^{239}Np were found. The measured 31 kBq mg^{-1} (2.3 µg mg^{-1}) of ^{241}Am ($T_{1/2}$ = 432.6(6) yr) in the material results from the decay of ^{241}Pu ($T_{1/2}$ = 14.33(4) yr), which has basically decayed since the ORNL measurement. ^{243}Pu ($T_{1/2}$ = 4.956(3) h) decays via β-emission to ^{243}Am ($T_{1/2}$ = 7367(23) yr) and this decays via α-emission to ^{239}Np ($T_{1/2}$ = 2.356(3) d). ^{243}Pu is created by neutron capture of ^{242}Pu and is not listed in the isotopic composition given by ORNL. An ^{243}Am activity of 39 Bq mg^{-1} in the material was found and an equal activity of ^{239}Np, showing that both isotopes, as would be expected, are in equilibrium.

Table 3.2: Isotopic composition of powdery $^{242}PuO_2$ used for the sample preparation, as measured by ORNL in 1980. The half-lives of the isotopes are taken from [82, 85, 86, 80].

Pu Isotope	Half-Life [yr]	Abundance [%]
^{238}Pu	87.74(3)	0.004
^{239}Pu	24 100(11)	0.005
^{240}Pu	6561(7)	0.022
^{241}Pu	14.33(4)	0.035
^{242}Pu	373 000(3000)	99.932
^{244}Pu	$8.12(3) \cdot 10^7$	0.002

$^{237}NpO_2$ in powdery form was obtained by IEK-6 at FZJ most likely in 1979 from Amersham-Buchler (today: Eckert & Ziegler Nuclitec GmbH)[87]. They obtained the material from the British Atomic Energy Authority and it is likely to have been taken from a batch produced in 1977 at ORNL. Unfortunately, neither FZJ, nor Eckert &

Ziegler Nuclitec GmbH or ORNL had still analysis details in their archives. However, the material was at some point chemically purified from spent nuclear fuel, in which ^{237}Np is produced by ^{235}U capturing two neutrons in succession with the intermediate rather stable ^{236}U which in turn only decays by α-emission. As the starting material of nuclear fuel is naturally occurring uranium containing basically only ^{235}U and ^{238}U, no ^{236}Np is produced. Also, as the known Np isotopes have half-lives in the order of days, aside from ^{236}Np, while ^{237}Np has a half-life of $2.144(7) \cdot 10^6$ yr, it is unlikely that significant amounts of other Np isotopes can be found in the sample material.
However, aside from ^{237}Np and ^{238}Np produced in the irradiation no traces of other Np-isotopes could be detected in a 23 h decay measurement at the "DÖME" low background counting facility at the BRR or in the PGAA spectra. A negligible amount of ^{241}Am was found in α- and also in γ-spectroscopic measurements. From PGAA measurements of the samples encapsulated in quartz glass sheets a 0.23 wt% chlorine contribution was found. In addition, a pellet pressed from 3.37 mg of the material was dissolved inside a container made of PFA by successively adding 1 mL 7 M HNO_3, 10 µL 40 %-HF and 200 µL 3 M HCL. A part of the solution than was measured via inductively coupled plasma mass spectrometry (ICP-MS) by Institut für Kernchemie, Johannes Gutenberg-Universität, Mainz [88]. Less than 0.1 % of other nuclide contamination was observed. In an experiment published in 1979 a target of 600 mg of $^{237}NpO_2$ powder also obtained from ORNL with a purity of 99.52 % was used [89]. Given the time and the source of the material it is very likely from the same stock batch as the material used in this work. The purity of the target material in the publication is basically consistent with the ICP-MS, PGAA and α measurements. Thus, in the following a purity of 99.52(10) % is assumed for the $^{237}NpO_2$, with an arbitrary uncertainty based on the uncertainty of the new measurements.

In addition, ^{241}Am dissolved in nitric acid was purchased from Eckert & Ziegler Nuclitec GmbH in 2012. The obtained activity of 185 MBq was delivered to Physikalisch-Technische Bundesanstalt (PTB) in Braunschweig, the German National Metrology Institute. The PTB prepared samples of ^{241}Am activity of about 4 MBq each and certified this activity as well as the purity with regard to other radio-isotopes.

3.3.2 Aluminum Encapsulation

The first generation of samples for actinide irradiation were prepared by pressing small amounts (several mg) of actinide powder into pellets mounted between two thin aluminum foils. Aluminum was chosen as a casing as it can be obtained in thin and pure foils and it produces only short-lived activity after irradiation (^{28}Al with a half-life of 2.25 min). The thermal capture cross section $\sigma_\gamma^0 = 0.231(3)$ b is relatively low. Hence, it does not produce much background, if the sample is irradiated with a sufficiently collimated neutron beam.

Within a glove box at FZJ the actinide powder was filled into a pressing die specially

designed for pressing pellets of 3 mm diameter, as shown in Figure 3.15(a). This die was sealed and carried to a pellet press. After pressing, the die was opened again within the glove box and the pellet was mounted between two 0.25 mm thick circular foils of 99.99 % aluminum (Alfa Aeser®) with a diameter of 5 cm, as can be seen in Figure 3.15(b). The foils themselves were screwed together tightly in a screw cap frame made from industrial aluminum. The concept is shown in Figure 3.16 which demonstrates that the aluminum screw caps are not irradiated, even if the neutron beam at the Budapest PGAA station is not collimated further than by the 2×2 cm beam opening of the sample chamber. The mass of this type of casing is around 17 g.

(a) (b)

Figure 3.15: Preparation of aluminum encapsulated samples. (a) $^{237}NpO_2$ powder mixed with gold powder as a comparator is transfered from an Eppendorf vial to the pressing die. (b) A pressed pellet of $^{237}NpO_2$ was placed in a deepening of an aluminum foil and closed with a second aluminum foil.

In this way two pellets of $^{237}NpO_2$ powder and two pellets of a mixture with 99.96 % pure gold powder were prepared. The mass of the pellets was determined by difference weighing of the empty casing and the filled casing on a balance next to the glove box. The gold powder was placed in an Eppendorf vial outside the glove box and weighted, than some $^{237}NpO_2$ powder was added in the glove box and the Eppendorf vial was weighted again. After mixing both powders inside the Eppendorf vial with an anti-static spatula, the vials content was filled into the pressing die. Assuming a homogeneous mixture the amount of gold and actinide in the pellet was calculated according to their mass ratio in the Eppendorf vial. However, it was found that the balance was not stable on the mg-level producing a rather high uncertainty on the measured content mass. Furthermore the aluminum casing with a total weight of the order of 15 g made the difference weighing of pellet masses of the order of 8 mg unreliable.

Four samples were produced which along with a blank sample casing were shipped

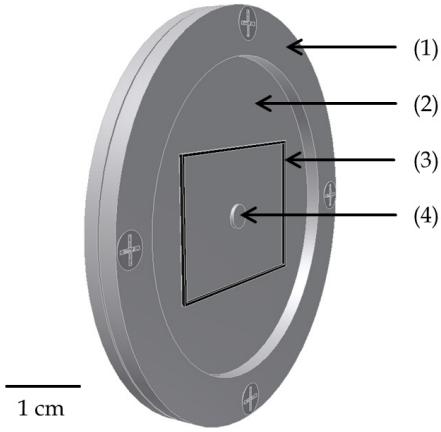

Figure 3.16: CAD drawing of the aluminum sample casing. (1) screwing cap, (2) aluminum foils, (3) projection of the maximal beam dimensions (black line) at the PGAA station at the BRR and (4) deepening in which the sample is mounted.

to the PGAA facility at the BRR. PGAA measurements were carried out in the 30° tilting position. During first irradiation attempts it was found that the pellets were not completely irradiated with the collimated beam. The sample casing was moved around within the sample holder frame in order to find the sample via an increase in count rate. With only one of the samples (containing 8.6 mg of $^{237}NpO_2$) a decent count rate of the expected most intense peak could be achieved without irradiating the screw caps. It was decided to use the fully opened neutron beam of 2 × 2 cm. The sample wa irradiated for 20 h and a blank sample casing was irradiated for 40 h in order to get a good assessment of the background radiation.

In this experiment 97 prompt γ-ray lines of ^{237}Np could be identified and their relative intensities could be determined. Self-absorption of photons in the sample was corrected for by approximating the pellet seen from the side as a parallelogram, as depicted in Figure 3.17. The self-absorption correction factor η_0 for a pellet tilted by an angle θ together with the photon absorption in the aluminum casing can then be calculated according to

$$\eta_0 = \exp\left(-\mu_{\mathrm{Al}}(E_\gamma)x\right) \cdot \frac{1 - \exp\left(-\mu_{\mathrm{NpO_2}}(E_\gamma)y\right)}{\mu_{\mathrm{NpO_2}}(E_\gamma)y}, \tag{3.5}$$

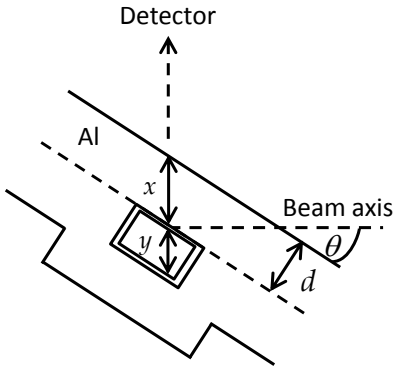

Figure 3.17: Sketch illustrating the self-absorption correction for a pellet tilted at angle θ against the neutron beam axis.

with $\mu_{\mathrm{Al}}(E_\gamma)$ denoting the linear attenuation coefficient in aluminum at an energy E_γ and $\mu_{\mathrm{NpO_2}}(E_\gamma)$ being the linear attenuation coefficient in NpO_2. The values of $\mu_{\mathrm{Al}}(E_\gamma)$ and $\mu_{\mathrm{NpO_2}}(E_\gamma)$ where obtained from the NIST XCom database [52]. The effective thickness y of the pellet is calculated with its known diameter, assuming that the density of the pellet equals the nominal density of NpO_2 of $\rho_{\mathrm{NpO_2}} = 11.1\,\mathrm{g\,cm^{-3}}$ [90]. As the processes involved in photon absorption are all basically interactions with single nuclei, the actual distance which the photon propagates through the material is far less important than the number of nuclei it encounters. The latter is kept constant by the above described calculation.

A comparison of the resulting relative intensities with the relative intensities tabulated in ENSDF showed a significant statistical disagreement for the lines below 1 MeV and a systematical disagreement for the higher energetic lines. As the data tabulated in the ENSDF is merged from two separate experiments in different regimes it was concluded that the renormalization between these experiments is not correct. This result was published in [91].

After the measurements the samples were brought back to FZJ and opened in the glove box. It was found that the pellets containing gold powder where crumbled (for instance see Figure 3.18), whereas the pure $^{237}NpO_2$ pellets proved to be more stable (for instance the sample used for the published results, shown in Figure 3.18(a)). It was also confirmed that none of the pellets stayed in the central deepening of the aluminum foils.

3.3.3 Quartz Glass Vials

In order to be able to inspect the samples visually it was decided to construct a transparent casing. The new casing should also allow to omit the difference weighing of the high mass

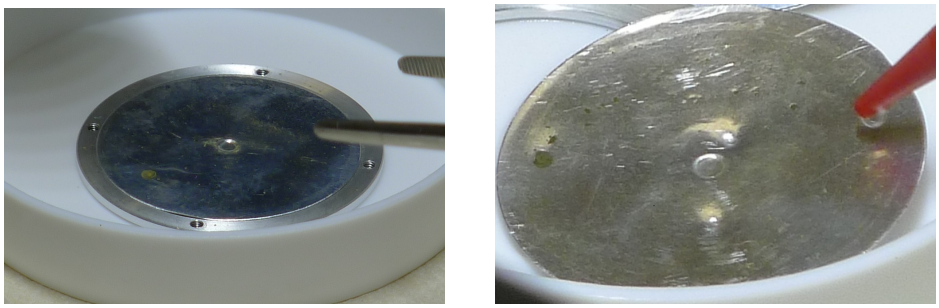

(a) (b)

Figure 3.18: After the PGAA measurement at the BRR the aluminum-encapsulated samples are opened within the glove box at FZJ. (a) This pellet, pressed from $^{237}NpO_2$, has stayed almost intact. (b) This pellet, pressed from $^{237}NpO_2$ mixed with gold powder, has crumbled.

aluminum cases. A simpler approach was made by placing the actinide powder directly into quartz glass vials.
Vials of Suprasil® quartz glass with a height of 4 cm, an outer diameter of 3 mm and an inner diameter of 1.5 mm with a slight funnel at the top and a semi-spheric end were obtained. Their mass being in the range of 0.5 g, this constituted a significant improvement for difference-weighing. As the balance stood outside of the glove box, mass measurements were carried out with the glass vial fixed inside an Eppendorf vial. After the measurement of the component masses the Eppendorf vials were opened in the glove box and the glass vials were placed inside a specially designed vial holder. Using a piece of quartz wool any material sticking to the sides of the glass vial was pushed down to the top of the bulk powder. Then a quartz sphere slightly bigger than the inner diameter of the glass vials was introduced in the funnel and the vial was sealed with epoxide glue. Due to the risk of breaking, the vials were afterwards sealed in bags of 0.025 mm thick FEP foil.
In this way six samples were produced: one containing $^{237}NpO_2$ powder, one containing $^{242}PuO_2$ powder and two samples containing gold powder and the actinide for each of the actinides. In addition, a blank sample casing was produced.
Completed samples can be seen in Figure 3.19(a).

The samples were transported to the PGAA station at the BRR. For the PGAA measurements a 44 mm^2 pinhole collimator made from enriched ^{6}Li-plastic was introduced to the supports at the chamber opening. The samples were mounted on the aluminum sample holder frame and placed right at the center of the neutron beam spot with the help of a previously prepared drawing on plotting paper. The actinide samples without gold powder and the blank sample were irradiated for about 24 h each. The samples containing gold were irradiated for 9 h to 18 h. After PGAA measurement each sample was moved

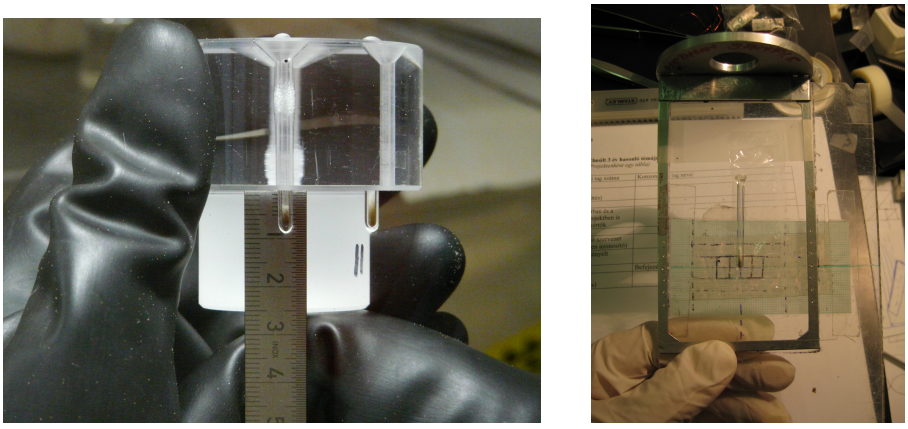

(a) (b)

Figure 3.19: (a) Vials filled with $^{242}PuO_2$ powder (left vial) and with $^{242}PuO_2$ and gold powder (right vial). (b) A prepared sample in a quartz vial casing is placed in the center of the aluminum sample holder frame at the Budapest PGAA station.

into the "DÖME" chamber and a decay spectrum was collected.

In addition neutron radiographic images of the samples were taken at the neutron radiography station. As the neutron beam there is similar to the neutron beam at the PGAA station, these images were used to check how transparent the samples are for neutrons and thus how big the suppression of the neutron flux inside the samples was, as the brightness of the pixels roughly corresponds to the neutron beam intensity. The neutron radiographic images of the samples are presented in Figure 3.20. A comparison of the average pixel brightness in the center of the vials with an empty part of the vial yielded a neutron absorption of about 10 % in the $^{242}PuO_2$, 25 % in the gold and almost 40 % in the $^{237}NpO_2$. The images are further used to determine the actual filling height, used to calculate the density of the actinide powder.

The necessary correction for the photon absorption in the samples can hardly be calculated analytically in this geometry. It can, however, be estimated with the help of simulation tools. The photon absorption correction factor was estimated using Geant4 simulations. It was assumed that the vials are cylinders with a semi-spheric bottom part. The gold was assumed to fill the whole semi-sphere and the actinide powder to be strictly on top of the gold powder, as depicted in Figure 3.21. The reaction rate in the sample decreases with a decrease of the neutron flux. It was assumed that, starting at the surface facing the neutron beam the flux decreases exponentially down to the value obtained from the neutron radiographic images. This is a rough approximation, but as the maximum flux depression is below 40 % it is still reasonable.

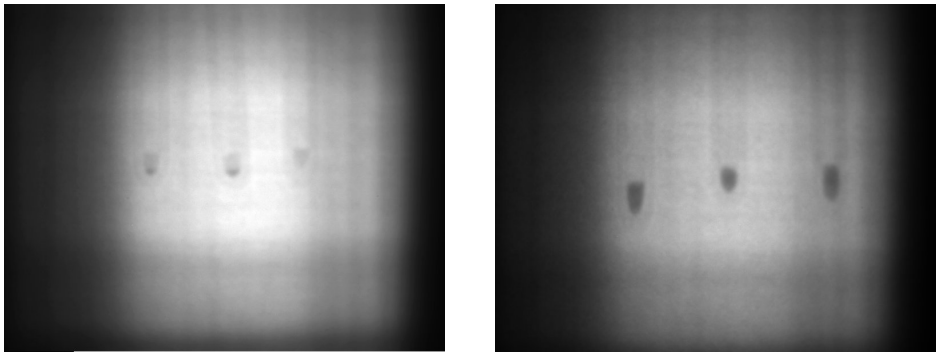

(a) (b)

Figure 3.20: Neutron radiographic images of the actinide samples encapsulated in quartz glass vials. (a) Vials filled with $^{242}PuO_2$ and gold powder (left and middle vial) and $^{242}PuO_2$ powder (right vial). (b) Vials filled with $^{237}NpO_2$ and gold powder (left and middle vial) and with $^{237}NpO_2$ powder (right vial).

For each line two simulations were carried out, one with the geometry and the flux depression activated and one without the geometry and flux depression. In this second one the same amount of photons was simulated starting from random homogeneously distributed points within the sample volume.
The ratio of the simulated peak areas from both simulations yields the photon absorption correction factor η_0. At 84 keV, the energy of the major decay line of ^{243}Pu, this yielded a correction of 47 %. For the major decay peak of ^{198}Au at 411.80 keV the correction was calculated to be 5 %.

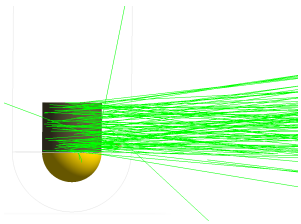

Figure 3.21: Geant4 simulation of 100 photons (green lines) originating from the actinide powder in the sample.

Partial and thermal capture cross section results from this experiment were published in [92]. After the irradiation at the BRR the samples were transported to the PGAA station at the FRM II where the experiment was repeated. Decay spectra were obtained at the PGAA station by measuring with the beam shutter closed.

A comparison of the thermal capture cross sections obtained in the two experiments are shown in Figure 3.22. The thermal capture cross sections for ^{242}Pu were obtained from the measured peak area of the most intense prompt γ-ray by using the tabulated emission probability per neutron capture event [93]. Unfortunately, this probability is associated with a large uncertainty of about 20 %, making it the dominant factor to the total uncertainty of the obtained thermal capture cross section values.
The results for the thermal capture cross section of ^{237}Np were obtained from the peak of the 1028.54 keV γ-ray from the decaying ^{238}Np. In this case the uncertainty of the result is dominated by the uncertainty of the mass measurement.

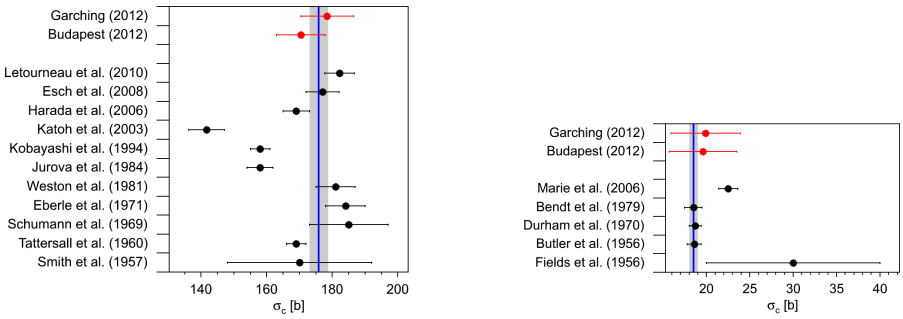

(a) (b)

Figure 3.22: Comparison of the thermal capture cross sections derived from experiments with powdery samples at the Budapest and Garching PGAA-facility for (a) ^{237}Np (b) ^{242}Pu. References can be found in the publication [92].

The determined thermal capture cross sections compare well with literature data. There are, however, a few experimental aspects that could be improved. As the flux monitor was not irradiated by the same part of the neutron beam as the actinide the major issue in these experiments is the unknown effect of flux inhomogeneity on the measurement. Further, the distribution of the gold powder and the actinide powder inside the vial is not completely known adding unknown uncertainties to the calculation of neutron and photon absorption. Also the vials do not have the idealized shape assumed for the photon absorption correction. A better defined geometry is thus desirable. And finally the uncertainty of the mass determination, which was of the order of 4 % for the low gold amounts and of the order of 2 % for the actinide powder, should be decreased, as it limits both the uncertainty of the found cross section values and also the calculation of absorption effects.

3.3.4 Quartz Glass Sheets

To provide a well-defined and stable geometry and to allow for an optical examination of the sample, successful aspects from both previous methods were combined. As it had proved difficult to control a homogeneous mixing of the gold powder with the actinide powder and the pellets pressed from this mixture had proved unstable, it was decided to split the flux monitor and the actinide into two separate units. A gold foil and a pellet pressed from the actinide powder were combined in one sample. The pellet was fixed in place inside a sandwich of three thin sheets of quartz glass, the middle one of which having a hole for mounting the pellet. To keep the background radiation of the sample casing to a minimum Suprasil® quartz sheets with a nominal thickness of only 0.20(2) mm and a density of 2.2 g cm^{-3} were purchased from Heraeus Quarzschmelze Hanau, Germany [94].

Sample Preparation

A sample casing consisted of three 4 × 4 cm Suprasil® quartz sheets, with one having a centered hole of 3 mm in diameter. The latter will serve as the middle sheet in a sandwich of the three sheets. The thickness at the center of each quartz sheet was measured with a micrometer screw. As the division of the micrometer screw was in the order of 10 µm an uncertainty for the thickness determination of 5 µm was assumed. The measurement of the thickness was repeated three times for each sheet. Afterwards, the sheets were cleaned with acetone and distilled water, so that no optical traces of contaminants such as reams remained. After drying the sheets were put into coated paper bags and transported into the glove box.

To omit unnecessary transportation of the fragile pellets in and out of the glove box a hydraulic mini-pellet press from Specac® Ltd was installed in the glove box. Specac® dies were altered to produce pellets with 2.82 mm diameter. For each material that should be pressed into a pellet (e.g. $^{237}NpO_2$ powder, $^{242}PuO_2$ powder or NaCl powder) a separate die was manufactured to avoid cross-contamination. The diameter of the dies were measured three times with a caliper at different positions and all dies were found to produce pellets with 2.82(3) mm, where the uncertainty corresponds to that given in the data sheet of the caliper.

Within the glove box, a pellet was pressed from the powdery starting material by applying a pressure of roughly 9 kN for about 10 s as depicted in Figure 3.23. In order to obtain a precise measurement of the masses of both the actinide pellet and the flux monitor a XP6 micro balance was obtained from Mettler-Toledo® and installed in the glove box. In addition an anti-static unit was obtained to remove any charge from a sample before its measurement, as at these small masses electrostatic effects could significantly alter the measurement results. The whole setup in the glove box is shown in Figure 3.24.

As the pellets are too fragile for weighing them directly on the scale and moving

them around, even with plastic tweezers, a small supporting structure for weighing was manufactured. A small shovel-like cylinder of 5 mm in diameter with a 0.1 mm thick bottom was found to provide practicability, while keeping the extra mass to a minimum. The aluminum weighing support itself had a mass in the order of 30 mg to 40 mg. It is shown in Figure 3.25(b) with a gold foil placed in it. Before weighing the aluminum supports were thoroughly cleaned with acetone and distilled water and then dried. For each pellet a new weighing support was used to avoid any contamination between the pellets.

A mass measurement of a pellet was carried out by first weighing the aluminum support itself ten times and checking if the result was stable. Then the pressed pellet was removed from the die and cautiously placed on the aluminum weighing support. The weighing support with the pellet was then measured for another ten times. While in the weighing chamber for the last time, the lower and the middle quartz sheets for the sample casing were unpacked and placed on a special support made from aluminum to align the sheets. After that the pellet was cautiously placed in the hole of the middle glass sheet. To check if any residues from the pellet remained on the weighing support the latter was directly weighted again for ten times. If any residues were found the measured residue mass was subtracted from the pellet mass.

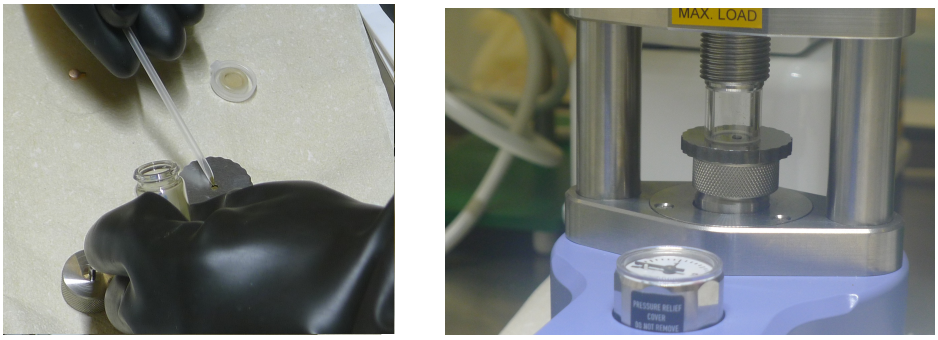

(a) (b)

Figure 3.23: (a) A pellet press die is filled with powdery starting material with the help of an anti-static spatula. (b) After pressing, the pellet was removed from the die.

If a gold flux monitor was to be included in the sample, a circular gold foil was cut from a nominally 3 µm thick gold foil obtained from Alfa Aesar® with a purity of 99.9 %. The foil was cut with a specially manufactured hollow punch matching the pellet radius. Mass weighing was carried out in a similar manner as for the pellet, also using one of the aluminum weighing supports. After weighing, the measured mass of the gold foil was used to calculate the thickness of the foil. A spare gold foil was measured and later remeasured on a Sartorius® micro-balance recently installed at the PGAA facility at FRM II. The

results agreed well within their uncertainties.
The weighted gold foil was then placed on top of the pellet in the hole of the middle glass sheet. Afterwards the last of the glass sheets was put on top. The sheets were carefully pressed together and the alignment was fixed. Then the outer edges of the glass sheet sandwich were covered with epoxide glue and rested to dry. After the glue hardened, the quartz glass sandwich was removed from the glove box, tested for outer radioactive contamination and sealed inside a previously prepared bag of 0.025 mm thick FEP foil. Some stations of the manufacturing process are shown in Figure 3.25.

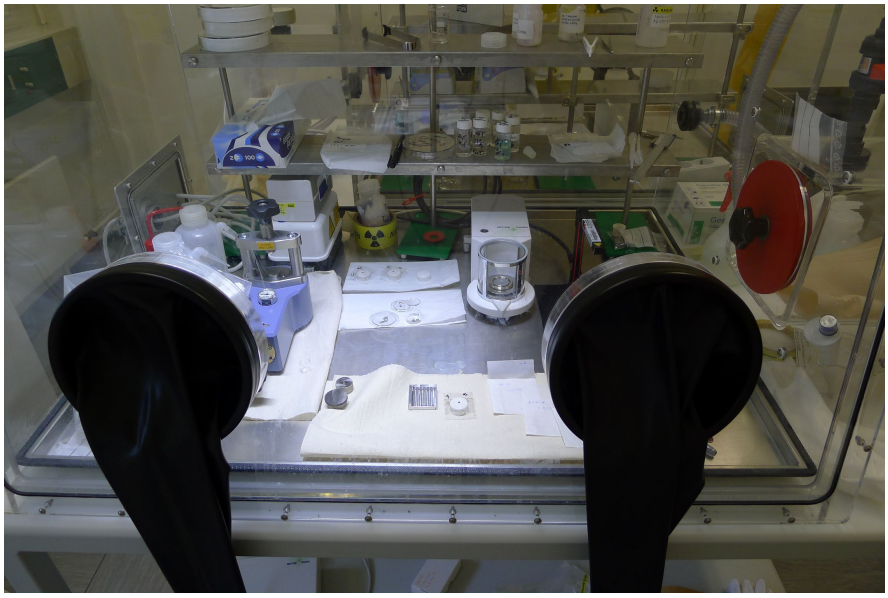

Figure 3.24: Glove box setup with mini-pellet press together with an opened pressing die (left), micro-balance together with anti-static unit (to the right of the press) (right) and completed sample together with an aluminum support for gluing (middle,front).

Mass Measurement Uncertainty

The manufacturer of the micro-balance certifies a mass measurement uncertainty of 0.4 µg under ideal conditions. However, the surroundings of the glove box are not ideal for the operation of a micro balance. Thus, the real uncertainty of the mass measurement on the installed balance was measured. In order to determine the uncertainty of a mass measurement with the micro-balance, a test pellet was produced from NaCl, which can be pressed into very stable pellets. This test pellet was weighted 120 times. After each ten weighings the test pellet was removed from the aluminum support and it was checked if the balance was still correctly tarred. 20 measurements were carried out with a different

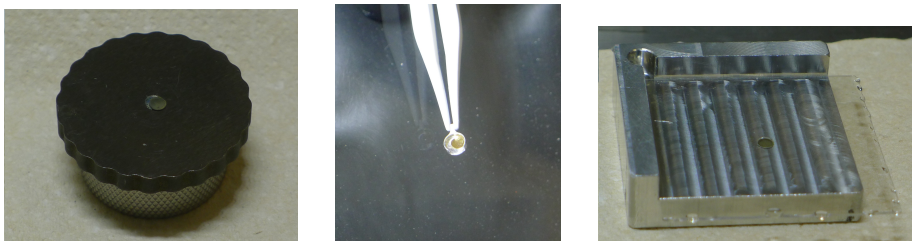

(a) (b) (c)

Figure 3.25: Assembly of a quartz glass sheet encapsulated sample. (a) The pellet is removed from the pressing position and moved towards the edge of the side support of the pellet press die. (b) A circular piece of gold foil on an aluminum weighing support. (c) The pellet is placed inside the quartz glass sandwich, which is mounted on a support frame for alignment. One side of the sandwich is already glued with epoxide glue.

aluminum weighing support for the same pellet. No significant shift of the weighing result was observed after the change of the support, though it seemed that the ten measurements carried out in a row tended to exhibit a slightly correlated behavior. The overall results are shown in Figure 3.26 together with a Gaussian fit. The fit has a reduced χ^2 of 0.3, supporting the assumption of a Gaussian distribution of the mass measurement results.

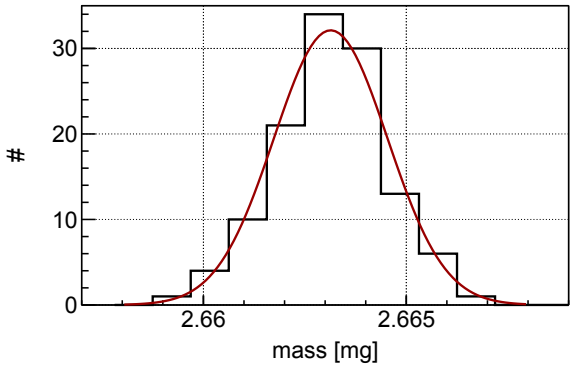

Figure 3.26: Histogram of 120 mass measurements of a single NaCl pellet and a Gaussian fit (red curve) with a reduced χ^2 of 0.3.

For the uncertainty of a single measurement, an unbiased estimator of the standard deviation of these 120 mass measurements was calculated. At first the unbiased variance with one degree of freedom lower than the sample size was calculated (the bias from using the mean of the distribution instead of the real value of the mass was thus accounted for).

The square root of the unbiased variance is not an unbiased standard deviation. Thus, the square root of the unbiased variance was divided by

$$\sqrt{\frac{2}{n-1}}\,\frac{\Gamma\left(\frac{n}{2}\right)}{\Gamma\left(\frac{n-1}{2}\right)}, \tag{3.6}$$

with Γ being the Gamma function and n the number of entries, which was 120 in this case. This factor did not increase the standard deviation much. All in all the standard deviation of the measurements was calculated to be 1.485 µg, which corresponds to a relative uncertainty of 0.056 %. The absolute value of 1.485 µg was used as a lower limit of the uncertainty on a single measurement and the relative uncertainty was applied to higher masses. This demonstrates that the actual uncertainty of the mass measurement in the glove box environment is almost a factor of four higher than the uncertainty specified by the manufacturer.

Validation of the experimental procedure using NaCl pellets

For a validation of the sample preparation and the spectrum evaluation it was decided to prepare samples containing isotopes with well-known cross section data. A material suited well for this purpose is NaCl. ^{35}Cl has a thermal capture cross section of 44 b [5], which is in the range of the thermal capture cross sections of actinides such as ^{242}Pu. Also, its prompt γ-radiation is well studied, rendering it ideal for comparing the obtained results with the tabulated data [4]. And furthermore, as mentioned above, NaCl can be pressed to very stable pellets.

Thus, within the scope of a Bachelor thesis [95], samples from NaCl were manufactured in the same way as described above.
Pure NaCl obtained from Goodfellow was used for these pellets. Three samples were produced, two of which contained a gold foil to determine the average neutron flux during irradiation. The PGAA measurements were carried out at the PGAA facility at the BRR as well as at the FRM II. During these measurements the samples were placed at the sample position with the gold foil facing the neutron beam.
The measured peak areas were corrected for photon self-absorption. Following a similar approach as the one described by equation 3.5 in section 3.3.2 for the evaluation of the aluminum encapsulated samples. The depression of the neutron flux was calculated using the macroscopic thermal capture cross section of gold (see section 2.5.4). This approach yielded a depression of approximately 0.25 % of the neutron flux in the gold foil and thus was regarded es negligible.

As NaCl is hygroscopic, the water content of the sample was estimated based on the PGAA measurement. From the strong prompt γ line of hydrogen at 2223 keV the

number of hydrogen atoms in the sample was determined after subtracting the hydrogen background found in the PGAA measurement of the blank sample. From the number of hydrogen atoms the mass of incorporated H_2O was determined, assuming that no other hydrogen containing contaminants were present in the sample. It was found to constitute 4 % to nearly 6 % of the total sample mass, which is a significant amount. For this reason the determination of the H_2O mass turned out to be the central source of systematic uncertainty.

The partial thermal radiative capture cross sections for chlorine and sodium were determined. The results from the measurements at the different facilities showed agreement within their uncertainties. Over all observed prompt γ-rays, however, a systematic shift between the tabulated and the measured partial capture cross sections was observed. On average the measured partial capture cross sections determined at the BRR PGAA facility were lower than the tabulated partial capture cross sections by almost 0.5 times the combined standard deviation of experiment and tabulated data. The partial capture cross sections determined from the measurements at the PGAA facility at FRM II were found to be lower than the tabulated values on average almost 1.5 or 1 times the combined standard deviation. Differences between the FRM II and BRR measurements were explained by the distorted peak shape of large peaks in the FRM II spectra. Tha latter could also explain the different shifts observed for these measurements. The peaks in the FRM II spectra tended to have a very pronounced low-energy tail. Also, they tended to exhibit an additional tail on the higher energy side of a peak. However, the systematic deviation might also be explained by the used correction for the neutron absorption. As cold neutrons exhibit a higher macroscopic cross section than thermal neutrons, the applied correction for neutron absorption is probably too low. Especially the absorption correction for the colder neutron beam at FRM II should be higher than that for the neutron beam at BRR, which also might explain the observed differences between the measurements.

Still, as the systematic difference was found to be rather small in absolute terms, the sample design can be regarded suitable for PGAA measurements.

3.4 Characterization of Actinide Samples for Irradiation

Ten samples were manufactured in the way described in section 3.3.4, five from $^{242}PuO_2$ powder and five from $^{237}NpO_2$. The characteristics of these samples can be found in Tables 3.3 and 3.4, respectively. The front of the sample corresponds to that side of the sample which faces the neutron beam and the detector during the PGAA measurements. Thus corresponds to the side with the gold foil in the case of the samples with flux monitor.

From PGAA measurements of the samples containing gold and corresponding measurements of blank sample casings, it was consistently found that the pellets pressed from

Table 3.3: List of ^{242}Pu samples made for irradiation. The measured pellet and gold foil masses are given and the corresponding calculated number of ^{242}Pu and ^{197}Au atoms (# ^{242}Pu/# ^{197}Au).

Sample No.	Quartz glass thickness [mm] front	middle	back	Pellet mass [mg]	# ^{242}Pu [10^{17}]	Gold mass [mg]	# ^{197}Au [10^{17}]
1	0.185(5)	0.220(5)	0.189(5)	3.1828(18)	69.02(13)	0.4045(15)	12.36(5)
2	0.208(5)	0.231(5)	0.211(5)	9.3034(52)	201.70(39)		
3	0.180(5)	0.211(5)	0.187(5)	5.1192(29)	110.98(22)	0.4092(15)	12.50(5)
4	0.205(5)	0.223(5)	0.203(5)	2.6368(15)	57.19(10)		
10	0.190(5)	0.210(5)	0.190(5)	6.1568(34)	133.48(26)	0.4117(15)	12.57(5)

Table 3.4: List of ^{237}Np samples made for irradiation. The measured pellet and gold foil masses are given and the corresponding calculated number of ^{237}Np and ^{197}Au atoms (# ^{237}Np/# ^{197}Au).

Sample No.	Quartz glass thickness [mm] front	middle	back	Pellet mass [mg]	# ^{237}Np [10^{17}]	Gold mass [mg]	# ^{197}Au [10^{17}]
5	0.189(5)	0.235(5)	0.189(5)	3.3399(18)	73.93(15)		
6	0.179(5)	0.230(5)	0.188(5)	4.8212(27)	106.78(22)	0.4080(15)	12.46(5)
7	0.218(5)	0.232(5)	0.239(5)	3.1581(18)	69.95(14)	0.4081(15)	12.48(5)
8	0.208(5)	0.208(5)	0.207(5)	5.2045(93)	115.28(23)		
9	0.201(5)	0.206(5)	0.203(5)	4.9288(28)	109.17(21)		

$^{242}PuO_2$ powder contained 0.37(5) atoms of hydrogen per atom of ^{242}Pu. This corresponds to a water content of 1.2(2) wt%. As all pellets were pressed from the same powder and under similar conditions it was assumed that the relative water content was the same for all $^{242}PuO_2$ pellets. For the pellets pressed from $^{237}NpO_2$ powder the water content was found to be 0.6(2) wt%. In Figure 3.27(a) a neutron radiographic image is shown taken at the neutron radiography station at BRR using the cold neutron beam. From this it can be estimated that the overall neutron absorption in the sample is below 20 %.

In addition, samples from ^{241}Am dissolved in nitric acid were prepared and calibrated against certified standards by PTB. Droplets of around 12 µL of the solution were dried onto the center of one of the quartz sheets each and covered with another quartz sheet. The thicknesses of the quartz sheets were not measured and thus were taken from the manufacturer's information as 0.20(5) mm. Two samples were prepared by drying the droplet on top of small circular gold foils of 3 mm diameter. The gold foils were from the same batch as the ones used for the pellet samples. The gold foils with the dried ^{241}Am solution were also sealed between two quartz glass sheets each (see Figure 3.27(b)). The specifications, as measured by PTB, are given in Table 3.5. The activity of the ^{241}Am in the samples was certified with an uncertainty of 0.75 %. Hence, the number of ^{241}Am

atoms and the ^{241}Am mass can be calculated with a similar accuracy.

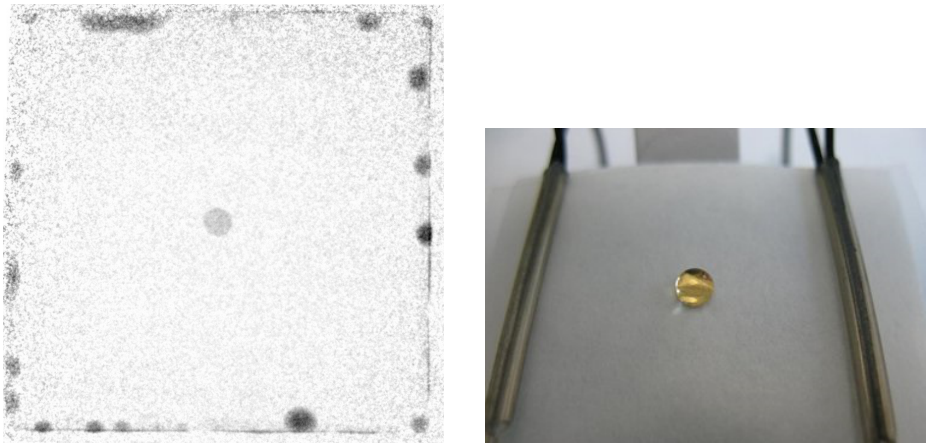

(a) (b)

Figure 3.27: (a) A neutron radiographic image of sample 6, taken at the neutron radiography station at BRR. (b) A droplet of 12 µL ^{241}Am-nitrate solution on top of a circular gold foil of 3 mm diameter (courtesy of PTB).

Table 3.5: Specifications of the ^{241}Am targets. The thickness of the quartz glass sheets was not measured. The manufacturer states it to be 0.20(5) mm. The gold masses and ^{241}Am activities were measured and the activities were certified by PTB.

Sample No.	Activity [MBq]	# ^{241}Am [10^{17}]	Mass ^{241}Am [µg]	Gold mass [mg]	# ^{197}Au [10^{17}]
1503	4.67(4)	0.9191(69)	36.80(28)		
1506	3.87(3)	0.7617(59)	30.50(24)	0.432(5)	13.19(16)
1507	4.66(4)	0.9172(69)	36.72(28)	0.434(5)	13.26(16)

3.4.1 Monte-Carlo Simulations of Samples in the Cold Neutron Beam

In order to calculate the necessary correction factors for the neutron and photon absorption in the samples and their casings, appropriate representations of the measurement setups were modeled in MCNP5 and Geant4.

Reaction Rate Correction

The reaction rate correction factors η_1 were calculated by means of MCNP5 simulations. A circular neutron beam of 3.2 mm diameter was introduced with the distribution of the neutron energies taken from the measured neutron flux at the respective facilities. According to the real setup at the corresponding PGAA facilities the sample was tilted against the neutron beam. For a simulation $1 \cdot 10^{10}$ neutrons were simulated. The statistical uncertainties from the simulation are thus negligible. For the simulations the gold foil was assumed to be 100 % pure ^{197}Au, with a density of 19.32 g cm^{-3} [96]. The thickness of the foil was deduced from the known density and the measured mass multiplied by the purity of the gold foil. The composition of the actinide pellets was modeled according to the description of the starting material in section 3.3.1. For the $^{242}PuO_2$ pellets the ORNL mass spectrometry results were adjusted for the decay of radioisotopes since the given date. For the $^{242}PuO_2$ and $^{237}NpO_2$ pellets the measured water content was also implemented into the model.
The Suprasil® quartz sheets were assumed to consist of pure SiO_2 with a density of 2.2 g cm^{-3} [94] using the natural isotopic abundance of both oxygen and silicon. The FEP foil was modeled as pure FEP with a density of 2.15 g cm^{-3} [97].
F4 tallies were used to calculate the average neutron flux in the pellet and in the gold foil. In addition, F2 tallies were used to calculate the neutron flux at the gold foil surface, corresponding to the front surface of the sample, at the surface in between the gold foil and the pellet and at the back surface of the pellet. For samples where no gold foil was present only the flux through the surfaces of the pellet and the average flux in the pellet were calculated. This was done in order to determine the source distribution for the required later simulation of photons originating from within the pellet. Results for the simulated neutron fluxes in the pellet and the gold foil are plotted in Figure 3.28, along with results for the different surfaces.

The calculated average fluxes in the gold foil and in the pellet were used to determine the reaction rate correction factors η_1 (please refer to equation 2.70). For that purpose, the simulated fluxes were convoluted with the capture cross sections of the corresponding nuclides normalized at thermal energy. The resulting relative reaction rates in the gold foil and in the pellet were hence divided to calculate η_1.
The real thickness of the sample is unknown but limited by both the maximum thickness of the middle quartz sheet and by the maximum density of the material. As all involved neutron reactions are independent of the distance between two nuclei, only depending on the properties of the nuclei, the actual thickness is not crucial. As the sample is tilted, however, different thicknesses produce a slightly different projection of the sample with regard to the neutron beam profile. This causes slightly different irradiations and thus different reaction rate correction factors. For each sample therefore one simulation was performed assuming the maximum possible thickness (i.e. the thickness of the middle glass sheet) and one assuming the maximum density of the actinide oxides. The mean of both values was defined as η_1 and half of the difference between the two simulations was

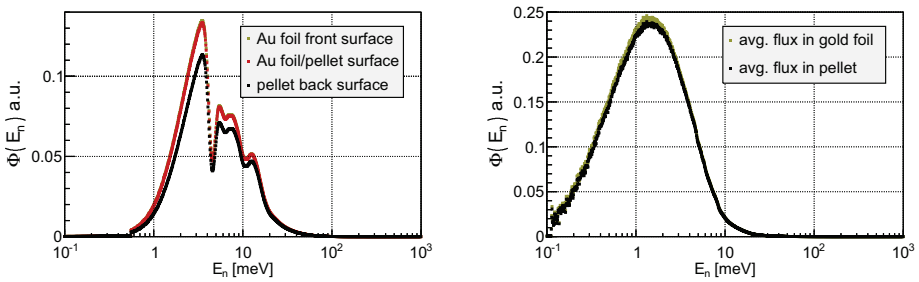

(a) (b)

Figure 3.28: (a) Simulated neutron fluxes at the front surface of the gold foil, the surface between the gold foil and the NpO_2 pellet and the back surface of the pellet for sample 6 and the cold neutron energy distribution at the BRR PGAA station. (b) Simulated average neutron flux in the gold foil and the PuO_2 pellet volume for sample 10 and the cold neutron beam at FRM II.

added to the overall uncertainty of η_1.
To asses the uncertainty arising from the uncertainties of the used capture cross section databases, the macroscopic cross section in the simulations was varied by plus and minus one standard deviation. Their mean yielded the same value as the simulated η_1. Half of the difference between the two simulations was added to the total uncertainty.
Similar simulation sets were made for the mass and radius uncertainties. In each case half of the difference was added to the overall uncertainty on η_1. Finally, the statistical uncertainty of the simulation was added to the overall uncertainty, which was of the same order of magnitude as the propagated mass uncertainty and more than an order of magnitude lower than the predominant uncertainty contributions from the variations of cross section, sample thickness and radius. The calculated uncertainty can thus be regarded as a conservative estimate.
The different values for η_1 along with their calculated uncertainties are tabulated in Table 3.6 for all samples.

The correction factors for the ^{242}Pu samples agree within their uncertainties. In this case, the choice of database is not important for the end results. In the case of the ^{237}Np samples the correction factors based on the two evaluated databases differ by about 2.5 times their uncertainties. This might be explained by the occurrence of the first neutron resonance at a neutron energy of 0.489 eV (for comparison the first resonance of ^{242}Pu occurs at 2.676 eV) [39]. The closer the resonance is to the thermal neutron energy, the more the shape of the capture cross section is deviated from a simple $1/\sqrt{E_n}$ dependency at thermal energy. Thus, the shape of the resonance influences the calculated correction factors strongly. The basic deviations of the capture cross section from $1/\sqrt{E_n}$ are illustrated in Figure 3.29.

Table 3.6: Reaction rate correction factors η_1 for the neutron fluxes at the different PGAA measurement setups at the BRR and the FRM II. The factors and their uncertainties were calculated using MCNP5 simulations with the measured neutron energy distributions and sample properties. The databases used for the simulation and for the convolution with the simulated neutron fluxes are indicated in parentheses at the top [5, 98]. The $1/\sqrt{E_n}$ values were derived by assuming the gold and actinide cross sections to follow a $1/\sqrt{E_n}$-law up to the thermal point and by using the flux simulated with the ENDF/B-VII.1 database [5]. The actinide contained in the sample is given in parentheses next to the sample number for convenience.

	Sample No.	η_1 (ENDF/B-VII.1) [5]	η_1 (JEFF 3.2) [98]	η_1 ($1/\sqrt{E_n}$)
BRR	3 (^{242}Pu)	1.0214(9)	1.0230(9)	1.0180(9)
	6 (^{237}Np)	1.0369(43)	1.0530(45)	1.0785(44)
FRM II	3 (^{242}Pu)	1.0259(10)	1.0282(9)	1.0215(10)
	10 (^{242}Pu)	1.0291(11)	1.0312(11)	1.0247(11)
	6 (^{237}Np)	1.0424(40)	1.0636(42)	1.0967(41)
	7 (^{237}Np)	1.0120(31)	1.0323(33)	1.0651(32)
	1506 (^{241}Am)	0.8914(40)	0.9515(41)	1.0076(41)
	1507 (^{241}Am)	0.8918(42)	0.9520(42)	1.0081(41)

For the ^{241}Am samples the reaction rate corrections are even smaller than 1 because of two strong low-energetic resonances at 0.307 eV and at 0.574 eV [39]. These cause a huge drop in the cross sections at thermal neutron energy compared to a simple $1/\sqrt{E_n}$ dependency. In this case the difference in the resonance shape between the JEFF and ENDF evaluations is also very strong, as illustrated in Figure 3.30.

Nevertheless, in the end result it turned out that the results were compatible regardless of the chosen database, as the uncertainty contributed by other influences were much higher than the uncertainties of η_1. For comparison cross section results are usually given with the JEFF and also with the ENDF based reaction rate correction factors applied.

Photon Absorption Correction

To calculate the necessary correction for photon absorption within the sample material and casing the measurement setups were modeled in Geant4. These models were already described in section 3.1.1.1 for the BRR setup and in section 3.1.2.1 for the FRM II setup. The samples were modeled in Geant4 in a similar way as they were modeled in MCNP5, albeit using the predefined Geant4 material database when possible. The modeled samples were then situated at the sample position with the appropriate tilting angle.

As mentioned earlier, the calculated reaction rates at the pellet and gold foil surfaces were used to model the source distribution of photons originating from the neutron ac-

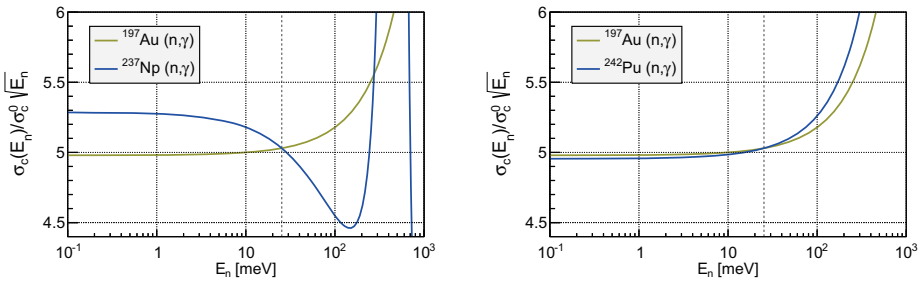

Figure 3.29: Deviations from $1/\sqrt{E_\mathrm{n}}$ of the capture cross sections of (a) ^{237}Np and (b) ^{242}Pu. The cross sections are multiplied with $\sqrt{E_\mathrm{n}}$ and the capture cross section of the ^{197}Au comparator element is plotted for convenience. The thermal neutron energy of 0.0253 eV is indicated by the thick gray dashed line. The cross sections were normalized at thermal neutron energy.

tivation. It was assumed that the neutron flux and thereby the reaction rate decreased exponentially between the front and the back surface of the pellet (or the gold foil respectively). This corresponds to a Lambert-Beer absorption law (see section 2.5.4). The decrease in the reaction rate from the front to the back surface in principle leads to a decrease of the photon absorption correction factor with regard to the situation where a homogeneous irradiation is assumed. This is because photons produced in the front part of the sample which faces the detector propagate a shorter distance through the material before reaching the detector than photons produced in the back part of the sample.

To obtain the photon absorption correction factor η_0 for a given photon energy two simulations were performed. In one simulation the sample geometry and the source distribution mentioned above was used, while in the second instead of the sample a homogeneous source distribution with the dimensions and position of the sample was implemented. This basically means that in the second simulation all absorption effects were turned off. Thus, the ratio of the simulated full energy peak areas from the two simulations corresponds to the photon absorption correction factor η_0.

At high photon energies the photon absorption becomes negligible and the simulated peak areas become compatible within their uncertainties. Thus, the uncertainty resulting from the Poisson process in the simulation becomes dominant. This is an artificial increase of the uncertainties, hence for photon energies $\geq$ 400 keV the correction was calculated similar to equation 3.5. Assuming a homogeneous source distribution and treating the photons as being emitted straight at the detector the photon absorption in the pellet was calculated according to

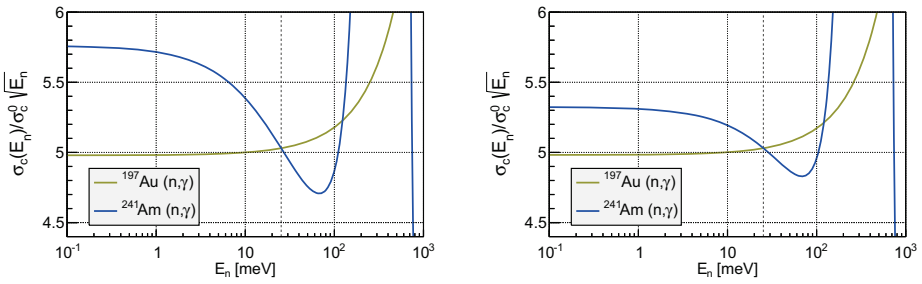

Figure 3.30: Deviations of the capture cross sections at thermal neutron energy in the (a) ENDF/B-VII.1 and (b) JEFF-3.2 evaluated data libraries for ^{241}Am. The cross sections are multiplied by $\sqrt{E_\mathrm{n}}$ and the capture cross section of the ^{197}Au comparator element is plotted for convenience. The thermal neutron energy of 0.0253 eV is indicated by the thick gray dashed line. The cross sections were normalized at thermal neutron energy.

$$\eta_0 = \exp\left(-\mu_{\mathrm{FEP}}(E_\gamma)x\right) \cdot \exp\left(-\mu_{\mathrm{SiO_2}}(E_\gamma)y\right) \cdot \frac{1-\exp\left(-\mu_{\rho,\mathrm{Pel}}\delta\right)}{\mu_{\rho,\mathrm{Pel}}\delta}, \tag{3.7}$$

via integration of the Lambert-Beer law. Here, $\mu_{\rho,\mathrm{Pel}}$ is the mass attenuation coefficient of the pellet material, $\mu_{\mathrm{SiO_2}}$ and μ_{FEP} are the respective mass attenuation coefficients of quartz and FEP, E_γ is the photon energy and θ the tilting angle of the sample. The term x represents the thickness of the FEP divided by $\cos(\theta)$ and y the same value with the thickness of the front quartz sheet. The exponent of the last term was calculated from the measured sample properties according to

$$\delta = \rho \cdot \frac{d}{\cos(\theta)} = \frac{m}{\pi r^2 d} \cdot \frac{d}{\cos(\theta)} = \frac{m}{\pi r^2 \cos(\theta)}, \tag{3.8}$$

with m being the measured mass of the pellet, r being the radius of the sample and d being the thickness of the sample. The values of the mass attenuation coefficients without coherent scattering were taken from National Institute for Science and Technology (NIST) XCom [52]. NIST estimates the uncertainties of the mass attenuation coefficients to below 3 % for photon energies relevant to this work. The only relevant exceptions are uncertainties near the K absorption edges, which for the actinides are at around 120 keV. Within a 10 % interval around this absorption edge the uncertainty is estimated to be 10 % [99, 100].

Uncertainties are propagated through equation 3.7. The uncertainty of the measured photon energy was propagated by calculating η_0 for the energy plus and minus one standard deviation. Half of the difference between these two values was quadratically added to the overall uncertainty. This uncertainty calculation was performed for the simulation results too, in which case the statistical uncertainty from the simulation was added quadratically to the propagated uncertainty. In Figure 3.31 the simulated and the calculated values of η_0 are plotted for comparison. It can be seen that above 400 keV the approximation using equation 3.7 is consistent with the simulation. Thus, above this value η_0 deduced from equation 3.7 was used to calculate the photon absorption correction. The small systematic shift observed below 400 keV increases with lower photon energies and might well be the result of the decrease of the reaction rate within the sample, as explained above. The single values still remain compatible within their uncertainties over the whole energy range from 30 keV to 10 MeV, as for lower photon energies the uncertainties also increase. Due to the small sample size the effect of the different source distributions is relatively small. The small systematic effect was nevertheless corrected by using the simulated results at lower photon energies.

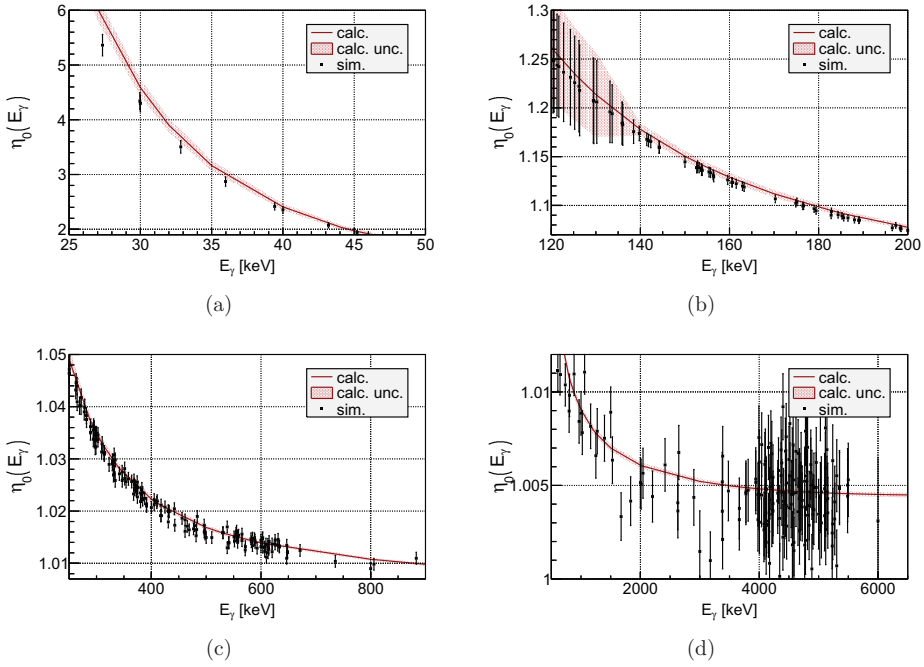

Figure 3.31: Exemplary comparison of the photon absorption correction factors from a Geant4 simulation of sample 8 (NpO_2) with values calculated with the approximate formula using NIST XCOM attenuation coefficients. The simulations were performed for the FRM II PGAA detector. (a) Low energy regime, where the difference between simulated an analytical is significant. (b) In the mid energy regime the systematic deviations are within the given uncertainties. (c) In this region the systematic difference becomes negligible. (d) At high energies the simulation results have a high relative uncertainty, as the simulated peak areas become compatible within their uncertainties.

CHAPTER IV

Results and Discussion

In this section, the results of the PGAA and decay measurements of the actinide samples described in section 3.4 will be presented.
First, the results for ^{237}Np will be shown, followed by the results obtained for ^{241}Am and the results for ^{242}Pu. In the last part, detection limits will be calculated for the investigated actinides at the different measuring facilities.

4.1 Neptunium-237

The samples made of $^{237}NpO_2$ powder and a blank sample casing were irradiated and counted at the PGAA facilities at BRR and FRM II sites. Prior to irradiation, the pellets' integrity was visually checked. Due to the limited neutron beam time not all of the intact samples could be irradiated at both facilities. All irradiations were carried out at very low count rates to decrease the probability of random-coincidence events and to keep the dead time as low as possible. The dead time was usually a few percent even for the PGAA measurements. Information on the measurement times is tabulated in Table 4.1. The beam-to-sample angles were 30° and 45° at BRR and at FRM II, respectively. At both facilities the sample front faced the neutron beam. The decay measurements were usually carried out with the coaxial HPGe-detector in the "DÖME" low background counting chamber at BRR and at the PGAA station at FRM II with the neutron beam closed. The long decay measurement of sample 8 at BRR was carried out at the PGAA station after closing the neutron beam. The spectra of samples 8 and 9 measured at BRR and FRM II are shown in the appendix (Figures E.3, E.4 and E.5).

At FRM II the neutron beam was collimated with the self-made 5-mm collimator of boron containing rubber and lead. The collimator was placed at the end of the neutron beam guide as described in section 3.1.2. The neutron-beam position was determined using a Li-containing radiography film, and the sample was placed in the center of the beam spot, as shown in Figure 4.1. After irradiation the position was checked again prior to the removal of the sample from the sample holder.

Table 4.1: Details on the measurements of ^{237}Np samples performed at the different sites. The front of the samples (e.g. defined by the gold foil) was facing the detector. The type of measurement is indicated as (p)rompt (during irradiation) and (d)elayed (after irradiation). All measurements were carried out with coaxial HPGe-detectors. The decay measurement of sample 8 at BRR was carried out at the PGAA-station and is marked by (*).

	Sample No.	t_{real} [s]	t_{live} [s]	Rate [cps]	type
BRR	6	64 945.9	63 170.8	668.76	p
	6	20 002.0	19 890.4	743.21	d
	8	234 580.8	227 869.1	668.26	p
	8	252 888.4	252 093.5	133.27	d*
	9	72 719.2	71 637.9	396.54	p
	9	82 846.0	82 399.8	697.91	d
	Blank	20 280.5	20 216.4	44.21	p
FRM II	6	27 261.2	26 291.8	1092.02	p
	6	36 660.5	36 610.4	39.78	d
	7	21 639.1	20 464.1	1468.79	p
	7	38 901.2	38 859.4	29.09	d
	8	45 065.6	43 557.8	1025.26	p
	8	4848.2	4839.8	14.12	d
	Blank	36 000.0	35 947.4	25.52	p

4.1.1 Partial Neutron Capture Cross Sections of ^{237}Np

The absolute energy calibration of the system was made using clearly identified background lines in addition to the non-linearity function determined with the standard sources. For the spectra from the irradiation of samples 8 and 9 at BRR the decay γ-line at 311.904(5) keV [82, 86] of ^{233}Pa and the prompt γ-line of ^{28}Si at 4933.89 keV [101] were used for the two-point energy calibration. A comparison of the energies of identified background lines from the irradiation of sample 8 with the corresponding literature data is shown in Figure 4.2(a). A similar plot for sample 9 can be found in the appendix (Figure D.1). It can be seen that the energy calibration reproduces the literature values very well over the whole energy range, with respect to the given uncertainties. As no single non-linearity function consistent over the whole energy range could be created for the spectrometer at the PGAA station at FRM II, the energy calibration was made piecewise with closer lying supporting points. For this the 300.129(5) keV [82, 86] decay γ-line of ^{233}Pa and the prompt γ-lines of ^{28}Si neutron capture at 1273.35 keV, at 4933.89 keV and at 7199.199(23) keV [101] were used. The validity of this calibration is demonstrated in Figure 4.2(b).

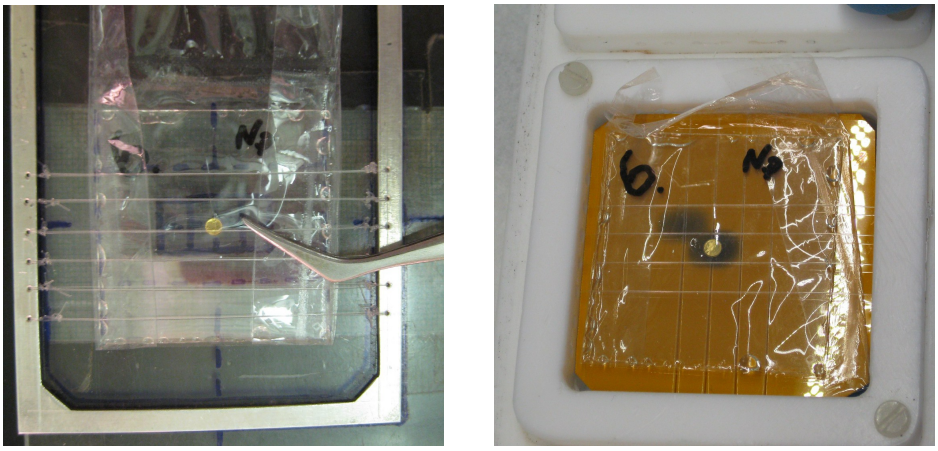

(a) (b)

Figure 4.1: Pictures of sample 6 in the sample holder frames at (a) BRR and (b) FRM II. In (b) two darkend areas are visible on the Li-containing film, the one left of the actual beam spot is due to a prior trial of the placement of the self-made collimator.

The prompt γ-rays of the neutron capture of ^{237}Np were identified in gamma spectra collected during the irradiation of sample 8 at the PGAA stations at BRR and FRM II and of sample 9 at BRR. The spectra measured during the irradiation of a blank sample casing and the decay spectra after irradiation were used to identify background lines (discussed above) and also for quantifying any background contribution to peaks produced by identified ^{237}Np prompt γ-rays. Using the EGAF [4] library it was thoroughly checked for the presence of any stable element in the measurement, and using the ENSDF [80] database it was checked for the presence of other actinides, as far as data exist. It was further checked for decay radiation of any radioisotopes and for X-rays using the ENSDF [80], DDEP [82] and NuDat 2.6 [102] databases, as well as the Table of Isotopes [103]. The identification of prompt neutron capture γ-rays of ^{237}Np was then undertaken using the adopted level scheme of ^{238}Np tabulated in the ENSDF [80] database.

In this way, 171 prompt γ-rays of the ^{237}Np neutron capture were identified in the long 2.7-d irradiation of sample 8 at BRR, 125 of which were also measured in the shorter irradiation of sample 9. The irradiation of sample 9 was carried out using a newly installed automatic neutron collimator located upstream of the neutron beam further away from the sample position. Thus, besides the shorter irradiation, the neutron flux also turned out to be lower compared to the irradiation of sample 8 where the collimator was positioned in the mounts at the neutron beam opening of the sample chamber. With the higher neutron flux at FRM II 152 of the prompt γ-rays were confirmed. In Figure 4.3(a) the consistency between the γ-ray energies measured using samples 8 and 9 at BRR is shown

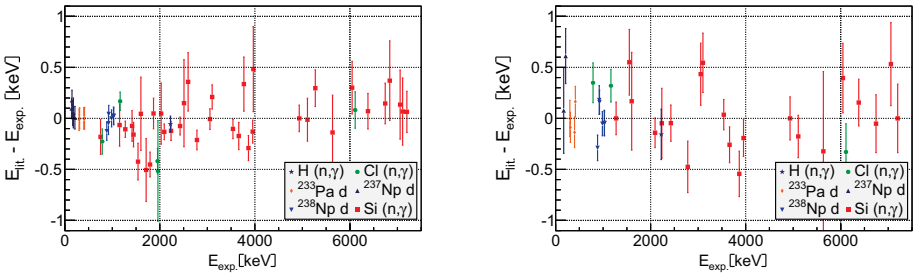

(a) (b)

Figure 4.2: Comparison of the energies of identified background lines measured during the irradiation of sample 8 at (a) BRR and (b) FRM II with tabulated values.

in the form of a histogram of the residuals divided by the uncertainty of the residuals, a so-called "pull plot". Explicitly, the pull of a quantity x (e.g. a γ-ray energy) from two measurements of this quantity x_1 and x_2 with associated measurement uncertainties s_1 and s_2 is given by

$$\text{pull} = \frac{x_1 - x_2}{\sqrt{s_1^2 + s_2^2}}. \tag{4.1}$$

The mean of the distribution corresponds to the average difference between the measured values in terms of standard deviations. An excellent agreement between two measurements would result in a pull plot with Gaussian shape centered at 0 with a root-mean-square (RMS) of 1. If the center of the distribution is not compatible with 0 a systematic effect is likely. An RMS significantly higher than 1 could indicate that the uncertainties are underestimated. The pull plot of the γ-ray energies in Figure 4.3(a) has a mean of -0.022 ± 0.075, perfectly compatible with 0, and an RMS of 0.84 ± 0.05. The pull plot of the relative intensities measured in the irradiation of sample 8 compared to those measured in the irradiation of sample 9 at BRR is shown in Figure 4.4(a). It has a mean of 0.024 ± 0.085 and an RMS of 0.95 ± 0.06. So the two measurements at BRR show a very good agreement with each other.
The agreement between the weighted averages of the BRR measurement and the FRM II measurement is shown in Figure 4.3(a) for the energies and in Figure 4.4(a) for the relative intensities. Whereas the pull plot for the γ-ray energies shows good agreement of the measurements with a mean of 0.077 ± 0.076 and an RMS of 0.94 ± 0.05, the agreement is not as good for the relative intensities with a mean of -0.204 ± 0.087 and an RMS of 1.078 ± 0.062. This is still a fair agreement, as the mean is compatible with 0 within 2.3 standard deviations which can be explained by the distorted peak shapes in the FRM II measurements for peaks with high count rates, as is the case for the most intense peak

with respect to which all other intensities are normalized. This uncertainty creates a systematic shift of the whole pull plot, as all relative intensities are relative to the most intense peak. A decrease of the peak area by 0.45 times its uncertainty could already account for the observed shift. In absolute terms the shift corresponds to an average of -0.00080 ± 0.00048 between the BRR and FRM II measurements. In Figure 4.5(b) the differences between the measured relative intensities are plotted as a function of the measured energies, to show that no significant systematic effect is present over the measured energy range. A similar plot for the measured energies can be found in the appendix Figure D.2 and one comparing the data measured for samples 8 and 9 at BRR in Figure D.3.

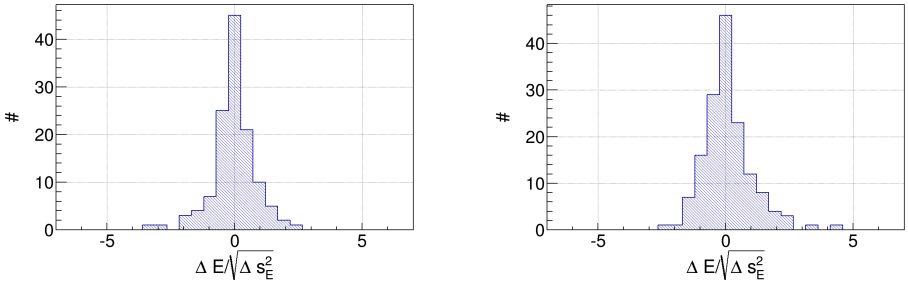

(a) (b)

Figure 4.3: Pull plots of measured ^{237}Np prompt γ-ray energies. (a) from the measurement of samples 8 and 9 at BRR. (b) from the weighted average of the energies measured at BRR and at FRM II. ΔE denotes the residual of both γ-ray energy measurements and $\sqrt{\Delta s_E^2}$ the uncertainty of the residual.

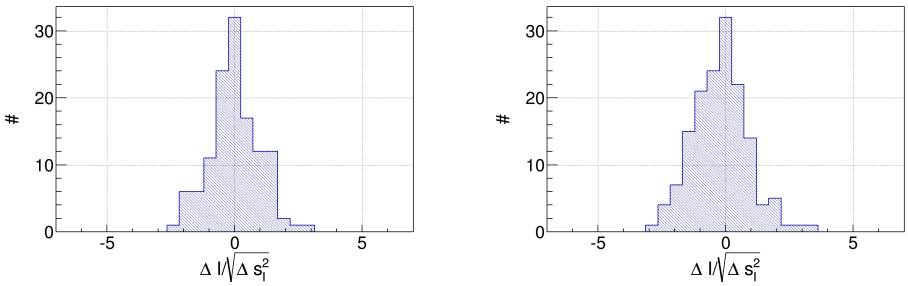

(a) (b)

Figure 4.4: Pull plots of ^{237}Np prompt γ-ray intensities (a) from the measurement of samples 8 and 9 at BRR. (b) from the weighted average of the intensities measured at BRR and at FRM II.

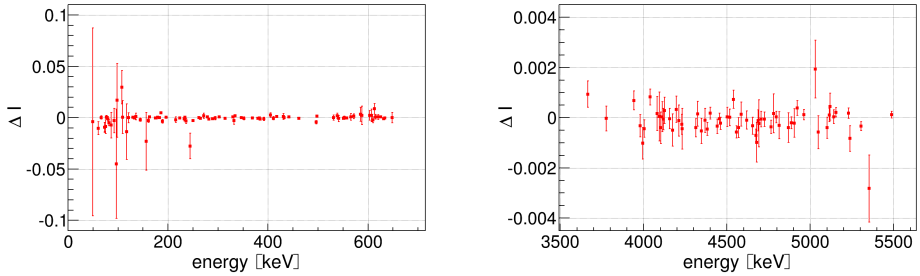

(a) (b)

Figure 4.5: Comparison of the relative intensities of ^{237}Np prompt γ-rays measured at BRR with the ones measured at FRM II as a function of the measured energy. (a) Close up on the lower energy regime. (b) Close up on the high energy regime.

The full data sets of the measurements can be found in the appendix Table A.4, A.5 and A.6 also including the lines which are not yet confirmed by other measurements. 52 γ-rays found consistently in all three measurements listed in Table A.7 could not be clearly identified to originate from ^{237}Np(n, γ)^{238}Np based on the existing level scheme. The energies of the listed γ-rays and their emission intensities relative to the 182.82(10) keV line are in very good agreement (at most 1.6 standard deviations between the different measurements). As the existence of these lines is confirmed regardless of the sample or the facility used, they, too, are likely to be prompt γ-rays of ^{237}Np.

For the 152 prompt γ-rays from ^{237}Np neutron capture which were consistently identified in the measurements of sample 8 at BRR and FRM II, weighted averages of the measured energies and the relative intensities were calculated and are listed in Table 4.2. 125 of these prompt γ-lines were found consistently in all three measurements. For the combination of the measured values at first the weighted averages of the two measurements at BRR were calculated and associated with the smaller of the two uncertainties. Lines identified in the long irradiation of sample 8 but not in the irradiation of sample 9 were kept. Then the weighted averages of these combined values with the measured values at FRM II were calculated and again associated with the smaller of the two uncertainties. The average is formed in two steps because the correlations between the measurements are different.
Intensities marked with asterisks in Table 4.2 were corrected for interferences with other peaks seen in the blank sample irradiation or in the decay counting for small expected interferences from observed radioisotopes. Corrections were applied by weighting the peak area measured in the blank sample irradiation spectrum or the decay counting spectrum by the corresponding live times and subtracting that value from the peak area. In the case of expected interferences from other radioisotopes or sources of prompt γ-rays – clearly identified – the expected contribution to the peak area was subtracted using a clearly

identified line of the same source in the same spectrum and the respective emission probabilities. These corrections were usually relatively small, in or below the percent range. In the following some more special cases will be described.

Prompt γ-ray line at 60.30(10) keV
A 10-% contribution from the strongest decay γ-line of the ^{241}Am at 59.59 keV was taken into account in the prompt measurements at BRR based on the decay measurements. For sample 9, this was not necessary as the peaks could be separated. In the FRM II measurement this contribution was only 0.5 % due to the higher induced activity.

Prompt γ-ray lines at 72.83(10) keV and at 73.14(10) keV
This doublet was not resolvable in the FRM II measurement due to the distorted peak shapes. Thus, the total intensity of both lines was determined and then divided by the ratio determined in the BRR measurements. In all cases a small background interference from a $K_{\alpha,2}$ X-ray of Pb at 72.8 keV was corrected for based on the blank sample irradiation measurements.

Prompt γ-ray line at 75.01(10) keV
In the BRR measurements the strong $K_{\alpha,1}$ X-ray line of Pb at 75.0 keV contributed 5 % to the measured peak area and was corrected for by using the blank sample irradiation measurement. At the FRM II this contribution was slightly higher with about 8 %, probably due to the larger amount of Pb in the shielding. A stronger contribution stemming from a ^{233}Pa decay γ-ray at 75.27 keV and a ^{237}Np decay γ-ray at 74.54 keV was corrected for using the respective decay measurements. This contribution was found to be 60 % in the measurement of sample 8 and 69 % in the measurement of sample 9 at the BRR. This difference can be explained by the lower neutron flux in the measurement of sample 9, caused by the use of a different collimator, as discussed earlier. In the measurement of sample 8 at FRM II this contribution reduced to only 16 % due to the higher neutron flux and thus the increased reaction rate. The measured relative intensities agree between all three measurements, with the measured values being 0.0533(61) for the measurement of sample 9 at BRR, 0.0495(132) for the measurement of sample 8 at BRR and 0.0440(25) for the measurement of sample 8 at FRM II.

Prompt γ-ray line at 86.64(17) keV
This is a special case, as two strong background lines interfere with this prompt γ-ray peak. The strongest ^{237}Np decay line at 86.477 keV with an intensity of 12.26(12) [82, 104] per 100 decay events and a decay line of its short-lived decay product ^{233}Pa ($T_{1/2}$ = 26.98(2) d) at 86.595(5) keV with an intensity of 1.95(11) [82, 86] per 100 decay events contribute to this peak. The correction is made using the decay measurements. It adds up to a contribution of 76 % in the BRR measurement of sample 8, to a contribution of 85 % in the sample 9 measurement with lower neutron flux, and to a contribution of only 23 % at the FRM II measurement of sample 8, with the higher neutron flux. Thus, the energy measured at FRM II is given here. In the BRR measurements an additional small interference due to Bi K_β X-rays from the BGO was observed in the blank sample irradiation and subtracted

accordingly. This contribution is about 0.3 %. The resulting relative intensities are still in fair agreement with the values being 0.2254(53), 0.2387(285) and 0.2186(113) for the measurements of samples 8 and 9 at BRR and of sample 8 at FRM II.

Prompt γ-ray line at 92.59(22) keV
In both measurements at BRR this peak is dominated by an interference of over 95 % from a K_α X-ray of ^{233}Pa at 92.288 keV. In the FRM II measurement this interference is reduced, but still 67 %, so the energy measured at this facility is arbitrarily given here as a best guess. The corrections were made using the respective decay measurements. Due to the high contribution the value of the intensity is quite uncertain, measured as 0.0043(114) and 0.0125(134) at the BRR and 0.0051(34) at the FRM II. In all three measurements a small background contribution was observed in the blank irradiation, which is due to the decay of the naturally occurring ^{234}Th. This was also corrected for.

Prompt γ-ray line at 96.94(10) keV
This peak is dominated by a K_α X-ray of Np at 97.069 keV [103]. The X-ray is mainly produced in the sample material by photo-absorption effects on the ^{237}Np atoms, and to less extent in internal conversion processes during the decay, it dominates in all three measurements with a contribution of over 90 %, explaining the high uncertainties of the measured data. The measured relative intensities are 0.052(44), 0.058(44) and 0.010(30), which are in good agreement given the uncertainties. Due to the X-ray contribution the fits in this region, however, exhibit reduced χ^2 values of over 60. Thus, the prompt γ-line at 96.94(10) keV might be considered unreliable and is given in parentheses.

Prompt γ-ray line at 99.01(17) keV
As a strong contribution from a U K_α X-ray at 98.434 keV [82, 86], emitted after the ^{233}Pa decay, contributed to the peak in the BRR measurements by over 90 %, but by only 53 % in the FRM II measurement, the energy determined in the FRM II experiment is given. The measured intensity values of 0.022(43), 0.049(35) and 0.055(6) are in good agreement given the high uncertainties in the two BRR measurements.

Prompt γ-ray line at 117.86(10) keV
The energy of this peak is determined to be 118.20(32) keV in the irradiation of sample 8 at the BRR, as 117.58(10) keV in the irradiation of sample 9 and as 118.52(17) keV at the FRM II. The respective relative intensities are 0.0515(464), 0.0346(255) and 0.0250(90). The differences can be explained by the X-ray background in this region, which in all measurements causes reduced χ^2 values of over 60 rendering the fits rather unreliable. This γ-line is therefore given in parentheses and may be considered doubtful, as the energy of the γ-line is not reproduced too well in the different measurements.

Prompt γ-ray line at 233.72(10) keV
A contribution of 1.8 % due to X-ray escape from the prompt γ-ray peak at 243.95(9) keV was corrected for using Geant4 simulations of the BRR PGAA facility. This contribution was found to be 2.3 % for the FRM II PGAA facility. From the simulations the

ratio between the areas of the 243.95(9) keV full energy peak and the X-ray escape peak was calculated. Using this ratio and the measured peak area of the 243.95(9) keV, the respective escape peak contribution was subtracted.

Prompt γ-ray line at 648.28(7) keV
This peak is rather broad in all measurements and might well be a doublet of two peaks close to each other. However, a consistent fit of a doublet was not possible with HYPERMET-PC.

Prompt γ-rays at 4687.37(26) keV and at 4690.75(15) keV
These peaks form a doublet, which in the FRM II measurement is not well resolved due to the distorted peak shape. Thus, the total intensity of both peaks in the FRM II measurement was divided by the intensity ration determined with the BRR measurements.

Table 4.2: List of the weighted averages of prompt γ-ray energies and relative intensities of $^{237}\mathrm{Np(n,\gamma)}^{238}\mathrm{Np}$ from the measurements at BRR and FRM II. The smaller of the uncertainties is given as the uncertainty of the weighted average. Values given in parentheses are derived from fits in energy regimes with strong X-ray interferences, where the reduced χ^2 had very high values of over 60.

E_γ [keV]	I_γ [†]	E_γ [keV]	I_γ [†]	E_γ [keV]	I_γ [†]
49.32(10)	0.6569(190)	351.48(10)	0.0049(7)	4156.00(13)	0.0054(2)
60.30(10)	0.0388(43)*	369.02(10)	0.0049(3)	4174.40(14)	0.0062(4)
66.76(10)	0.0036(9)*	380.14(10)	0.0021(4)*	4196.81(14)	0.0052(3)
72.83(10)[♯]	0.0395(13)*	382.74(22)	0.0027(4)	4212.34(20)	0.0033(4)*
73.14(10)[♯]	0.0370(11)	383.99(10)	0.0119(5)	4228.50(42)	0.0025(2)
75.01(10)	0.0452(25)*	391.26(9)	0.0190(8)	4232.09(13)	0.0109(4)
76.91(12)	0.0104(12)*	405.21(10)	0.0194(16)	4312.88(19)	0.0029(2)
79.55(13)	0.0073(15)	410.56(24)	0.0023(5)*	4324.60(12)	0.0072(2)
82.21(10)	0.0358(16)	417.78(16)	0.0036(6)	4345.39(14)	0.0043(3)
86.64(17)	0.2245(53)*	430.88(9)	0.0432(19)	4368.60(14)	0.0029(3)
(92.59(22)	0.0053(34))*	432.28(21)	0.0016(6)	4381.94(14)	0.0037(2)*
(96.94(10)	0.0245(302))*	442.04(15)	0.0059(5)	4400.20(30)	0.0014(2)
(98.50(10)	0.0548(64))*	461.45(9)	0.0262(6)	4441.36(21)	0.0023(2)
(107.51(11)	0.0332(107))*	496.43(9)	0.0323(8)	4454.52(33)	0.0011(2)
(109.55(12)	0.1013(70))*	497.98(9)	0.0112(5)	4460.84(21)	0.0019(2)
(117.86(71)	0.0265(90))*	530.62(10)	0.0216(18)	4501.63(13)	0.0055(2)*
(121.31(27)	0.0087(27))*	538.36(9)	0.0363(19)	4516.75(24)	0.0020(2)
129.51(11)	0.0031(2)	541.26(9)	0.0307(20)	4539.85(18)	0.0033(2)*
133.16(10)	0.0055(2)*	550.94(10)	0.0062(4)	4557.35(17)	0.0024(2)*
135.92(10)	0.0516(19)	552.13(9)	0.0111(5)	4570.72(22)	0.0019(3)
144.26(11)	0.0069(2)	555.24(9)	0.0215(5)	4584.72(14)	0.0052(2)

Continued on the next page

E_γ [keV]	I_γ [†]	E_γ [keV]	I_γ [†]	E_γ [keV]	I_γ [†]
156.36(10)	0.3457(65)*	557.34(9)	0.0122(4)	4619.19(14)	0.0048(2)
160.55(10)	0.0276(7)*	565.32(9)	0.0262(17)*	4654.86(31)	0.0026(2)
162.92(10)	0.0022(4)*	571.34(12)	0.0089(16)	4673.47(28)	0.0015(2)
175.50(28)	0.0011(2)*	584.45(9)	0.0332(7)	4678.21(13)	0.0140(4)*
176.50(10)	0.0046(2)*	588.04(9)	0.0147(18)	4687.37(26)♯	0.0035(2)*
179.51(10)	0.0027(2)	603.10(9)	0.0230(22)*	4690.75(15)♯	0.0063(7)*
182.82(10)	1.0000(131)	606.76(10)	0.0221(18)*	4705.57(21)	0.0021(2)
184.78(16)	0.0006(2)*	610.72(25)	0.0051(8)*	4723.76(29)	0.0021(2)
189.06(10)	0.0364(7)	612.60(12)	0.0231(19)	4764.79(18)	0.0028(2)
196.54(10)	0.0078(4)	614.58(26)	0.0027(6)	4779.06(13)	0.0136(3)
215.50(9)	0.0540(10)*	620.38(9)	0.0429(9)	4794.97(22)	0.0014(1)*
223.49(10)	0.0040(2)	625.51(13)	0.0063(5)	4814.02(16)	0.0077(2)
232.42(9)	0.0450(8)	631.17(10)	0.0115(6)	4868.92(13)	0.0105(3)
233.72(10)	0.0121(3)*	633.50(10)	0.0126(5)	4887.20(21)	0.0018(2)
236.02(9)	0.0514(10)	648.28(7)	0.0754(15)*	4903.80(14)	0.0060(3)
243.95(9)	0.2589(48)	3379.26(22)	0.0062(5)*	4921.15(20)	0.0026(2)
250.38(9)	0.0235(6)	3385.61(27)	0.0035(3)	4960.45(19)	0.0015(1)*
262.04(18)	0.0004(2)*	3666.09(20)	0.0037(3)*	5030.28(14)	0.0116(6)
264.54(10)	0.0058(3)	3776.66(12)	0.0061(3)	5046.70(14)	0.0098(4)
271.81(10)	0.0323(14)*	3942.64(12)	0.0040(2)*	5101.54(19)	0.0043(3)
278.59(9)	0.0020(3)*	3978.83(14)	0.0034(2)	5114.22(34)	0.0021(2)
281.65(9)	0.0123(3)	3995.69(19)	0.0025(4)*	5118.98(24)	0.0064(4)
289.05(9)	0.0121(4)*	4002.61(14)	0.0027(2)	5140.60(16)	0.0034(2)
294.24(9)	0.0216(4)*	4039.86(24)	0.0026(2)	5154.88(41)	0.0008(1)*
302.68(14)	0.0012(3)*	4080.42(19)	0.0037(3)	5229.36(15)	0.0027(1)
314.36(9)	0.0037(2)	4094.99(14)	0.0041(4)*	5238.15(14)	0.0097(2)
329.96(23)	0.0019(3)	4103.36(11)	0.0097(3)	5305.04(21)	0.0017(1)
332.22(9)	0.0705(14)	4112.47(13)	0.0061(4)*	5352.04(14)	0.0244(5)
334.04(18)	0.0039(3)	4117.64(22)	0.0033(3)*	5488.20(21)	0.0010(1)
346.82(10)	0.0095(3)	4124.90(15)	0.0042(4)		

† : Multiply by 22.06(39) b to get σ_γ (see Table 4.3),
or with 0.125(4) for the emission probability per neutron capture event p_γ (see text).
* : Interferences from other peaks (see section 4.1.1 for additional information).
♯ : Doublet of two peaks.

A comparison of the obtained data with those tabulated in ENSDF [105] is shown in Figure 4.6 in form of pull plots for both the energies and the relative intensities. The evaluated data are based on two datasets measured with different detectors, different samples, and in different energy regimes. The secondary prompt γ-radiation was measured by Hoff *et al.* [106] with curved crystal spectrometers at Institut Laue-Langevin (ILL) in

Grenoble, France, in 1990. A target of 3 mg $^{237}NpO_2$ embedded in 77 mg aluminum powder was irradiated with thermal neutrons. One of the curved crystal spectrometers measured in the energy range from 30 to 500 keV, while the other covered the energy range from 150 to 1200 keV. A very good energy resolution of 40 eV at 100 keV was thus achieved, with which the HPGe measurements performed in this work cannot compete. All of the secondary γ-ray lines listed in Table 4.2, however, have a counterpart in the measurement of Hoff *et al.* In 19 cases the γ-rays reported in this thesis are in fact tabulated as doublets of prompt γ-rays that cannot be resolved with the HPGe detector. For the comparison the intensities of these tabulated peaks were summed and the energy was averaged.
It should be noted that several prompt γ-rays listed in the ENSDF especially in the low energy regime could not be observed although they would be expected to show e.g. the tabulated γ-ray line at 373.03(5) keV with a relative intensity of 6.12(74) % [107]. Given these difficulties the large RMS of 3.34 ± 0.25 of the energy pull plot and the RMS of 2.33 ± 0.18 of the intensity pull plot for the low energetic γ-rays can be understood. The mean value of the energy pull plot is compatible with 0 being 0.22 ± 0.36, but the mean value of the relative intensities is systematically shifted by 1.20 ± 0.25 standard deviations. It should be noted that the uncertainties of the intensities obtained within the scope of this thesis are typically lower than the uncertainties of the tabulated intensities.

The second experiment on which the tabulated data are based was performed by Ionescu *et al.* [89] in 1979. In this experiment a target of 600 mg $^{237}NpO_2$ powder obtained from Oak Ridge with a purity of 99.52 % was irradiated with thermal neutrons at the SAPHIR reactor in Würenlingen. The prompt γ-ray spectra were recorded with a Li-doped germanium (Ge(Li)) detector in the energy range from 2600 to 5500 keV, a region completely distinct from the energy region where the secondary γ-radiation was measured by Hoff *et al.* The authors claim that the normalization they give for their relative intensities is only a rough estimate. The lines they observed are basically reproduced in the present experiments. The energies are reproduced well, with the mean of the pull plot for high energies being -0.07 ± 0.17 and a reasonable RMS of 1.34 ± 0.12. However, the mean of the intensity pull plot is systematically shifted to 2.94 ± 0.13 standard deviations, which can be explained by the rough normalization performed by Ionescu *et al.* The RMS of this pull plot is 1.07 ± 0.09.

In summary, no agreement of data from the present experiment with the tabulated secondary γ-rays could be observed. A basic agreement with the tabulated primary γ-rays is shown. A systematic shift in the intensity normalization of primary to secondary radiation in the ENSDF database is demonstrated.

Normalization

The thermal partial radiative neutron capture cross sections were derived from activity measurements of the irradiated gold foil after the PGAA measurements of samples 6 and

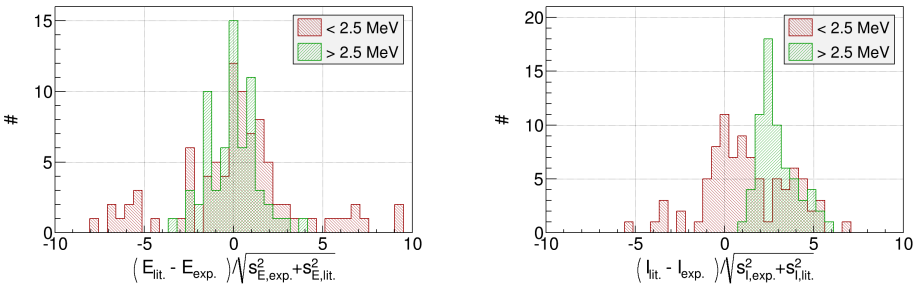

(a) (b)

Figure 4.6: Comparison of the data of ^{237}Np prompt γ-radiation obtained in this work with data tabulated in ENSDF for both secondary (red) and primary (green) prompt γ-rays. (a) Pull plot of the energies and (b) pull plot of the relative intensities. Data in the tabulation are derived from separate experiments in the low and high energy regime.

7. From the activity of ^{198}Au in the irradiated gold foil the average thermal equivalent neutron flux during irradiation was determined using equation 2.75. Then, employing equation 2.76 the partial cross section value for the most intense prompt γ-ray of ^{237}Np (182.82(10) keV) was calculated and used to normalize the relative intensities presented in Table 4.2. In principle, this is a normalization of the ^{237}Np partial capture cross sections with respect to the partial capture cross section of ^{197}Au. ^{197}Au is a cross-section standard for these kind of measurements, as both the thermal capture cross section and the emission probability of the most intense decay γ-ray of ^{198}Au are very precisely known from a great variety of different measurements.

The capture cross section of ^{197}Au is given as $\sigma^0_{c,\mathrm{Au}} = 98.66(14)$ b and was evaluated by the IAEA in the international evaluation of neutron cross section standards [108], adopted in ENDF/B-VII.1. The emission probability of the intense 411.8 keV decay γ-ray of ^{198}Au, created by neutron capture during irradiation, is $p_{\gamma,412} = 0.9562(6)$ per decay event tabulated, as by DDEP [82, 109] and ENSDF [80]. In total, this yields a partial capture cross section for the 411.8 keV decay γ-ray of $\sigma_{\gamma,412} = 94.34(15)$ b. This value is also in excellent agreement with the value of 94.30(15) b given in the PGAA Decay Gamma Data file provided by the IAEA [110]. The calculated value of $\sigma_{\gamma,412} = 94.34(15)$ b was used for the subsequent calculations. The half-life of ^{198}Au is given as 2.6943(3) d in DDEP [82, 109], as 2.6947(3) d in ENSDF and recommended as 2.6950(7) d by the IAEA [111, 112]. By arbitrarily increasing the uncertainty so that all values for the half-life are in agreement, a half-life of 2.6943(7) d was assumed for the decay correction of ^{198}Au in this work.

From the decay measurement of sample 6 at BRR an average thermal equivalent neu-

tron flux of $\Phi_0 = 9.73(11) \cdot 10^7\,\mathrm{cm^{-2}\,s^{-1}}$ was determined based on the 411.8 keV γ-ray line. From the PGAA measurement the flux was determined as $\Phi_0 = 9.45(24) \cdot 10^7\,\mathrm{cm^{-2}\,s^{-1}}$, in good agreement with the decay measurement. Using the prompt capture γ-ray of ^{197}Au at 6252.11(6) keV with a partial capture cross section of 4.82(7) b [2, 3] the flux was determined as $\Phi_0 = 9.98(31) \cdot 10^7\,\mathrm{cm^{-2}\,s^{-1}}$, which is also in good agreement with the flux determined solely from the decay measurement. For the further calculations, the weighted average from these measurements of $\Phi_0 = 9.71(11) \cdot 10^7\,\mathrm{cm^{-2}\,s^{-1}}$ was hence used. The partial capture cross section of the 182.82(10) keV prompt γ-ray of ^{237}Np was determined to be $\sigma_\gamma = 21.89 \pm 0.39$ b, with a relative uncertainty of 1.8 %. This value was deduced using the reaction rate correction η_1 (see equation 2.70), as calculated using the ENDF database (see section 3.4.1). The total uncertainty of the obtained partial capture cross section is dominated by the 1 % uncertainty on the measured peak area, 1 % uncertainty of the efficiency and 1.1 % uncertainty on the measured neutron flux. The reaction rate and photon absorption correction factors contribute 0.4 % and 0.2 % while the uncertainty contribution from the number of atoms is below 0.1 % and thus negligible.

For the measurement of sample 6 at FRM II with the self-made collimator an average thermal neutron flux of $\Phi_0 = 1.14(2) \cdot 10^9\,\mathrm{cm^{-2}\,s^{-1}}$ was determined from the decay measurement. From the PGAA measurement the flux was calculated to be $\Phi_0 = 1.18(4) \cdot 10^9\,\mathrm{cm^{-2}\,s^{-1}}$ from the 411.8 keV decay γ-ray line and $\Phi_0 = 1.06(3) \cdot 10^9\,\mathrm{cm^{-2}\,s^{-1}}$ from the 6252.11(6) keV capture γ-ray line.
The weighted average of the three values was calculated, yielding to a thermal equivalent neutron flux of $\Phi_0 = 1.15(2) \cdot 10^9\,\mathrm{cm^{-2}\,s^{-1}}$. Based on this value the partial capture cross section of the most intense capture γ-ray was deduced as $\sigma_\gamma = 21.98 \pm 0.59$ b, in good agreement with the BRR measurement.

Prior to the irradiation of sample 7 at FRM II the self-made collimator was removed to ensure the sample being homogeneously irradiated. The thermal equivalent neutron flux was determined as $\Phi_0 = 1.41(2) \cdot 10^9\,\mathrm{cm^{-2}\,s^{-1}}$ from the decay measurement, as $\Phi_0 = 1.47(5) \cdot 10^9\,\mathrm{cm^{-2}\,s^{-1}}$ and as $\Phi_0 = 1.45(4) \cdot 10^9\,\mathrm{cm^{-2}\,s^{-1}}$ from the PGAA spectrum. The weighted average of $\Phi_0 = 1.43(2) \cdot 10^9\,\mathrm{cm^{-2}\,s^{-1}}$ used for the following calculations, is somewhat higher than the flux in the measurement with the self-made collimator. This is due to the divergent part of the neutron beam being absorbed in the smaller collimator and thus not reaching the sample position. With the average Φ_0 the partial capture cross section of the 182.82(10) keV γ-ray was determined as $\sigma_\gamma = 22.32 \pm 0.48$ b.

These partial capture cross section values and related values which were calculated based on different assumptions for the reaction rate corrections can be found in Table 4.3. The values are in agreement regardless to the reaction rate correction employed and also agree with each other across the different measurements.
The measurements of sample 7 at FRM II and sample 6 at BRR are mostly uncorrelated, as both the samples and the detector systems differ but only mostly because the calibration methods, used software and the sample materials are the same. Also, as for the irradiation

of sample 7 the self-made collimator was not used, it can be assumed that the whole sample was irradiated. The weighted average of these two measurements $\sigma_\gamma = 22.06 \pm 0.39\,\mathrm{b}$ was therefore used for normalizing the relative intensities to partial capture cross sections. This weighted value is in agreement with the value of $20.83 \pm 0.84\,\mathrm{b}$ published in [92], based on measurements with samples of the second sample generation (see section 3.3.3).

Table 4.3: Partial radiative neutron capture cross sections of ^{237}Np measured for the most intense line at 182.82(10) keV at the BRR ($^{\mathrm{b}}$) and FRM II ($^{\mathrm{f}}$) PGAA facilities. Different reaction rate correction factors η_1 from Table 3.6 are applied. The weighted mean of the uncorrelated measurements 6^{b} and 7^{f} is given.

Sample No.	σ_γ [b] η_1 (ENDF)	η_1 (JEFF)	η_1 ($1/\sqrt{E_\mathrm{n}}$)
6^{b}	21.89(39)	22.23(40)	22.76(41)
6^{f}	21.98(59)	22.42(60)	23.15(62)
7^{f}	22.32(48)	22.77(49)	23.51(51)
$\bar{\sigma_\gamma}$	22.06(39)	22.44(40)	23.06(41)

4.1.2 Neutron Separation Energy

The nucleus ^{237}Np has a ground state spin and parity of $I_{^{237}\mathrm{Np}} = 5/2^+$ [39]. Thus, the compound nucleus is formed with a capture state spin and parity of $J_{\mathrm{c.s.}} = 2^+$ or $J_{\mathrm{c.s.}} = 3^+$ (see equation 2.27), as in the experiments with cold neutrons s-wave neutron capture is dominant due to the centrifugal barrier. The ground state of ^{238}Np has a spin and parity of $I_{^{238}\mathrm{Np}} = 2^+$ [80]. Thus, a direct M1 transition from the capture state to the ground state is possible. The highest energetic prompt capture γ-ray observed for ^{237}Np from the three previously described experiments found to be 5488.20(21) keV very likely corresponds to this ground state transition. After applying the correction for the nuclear recoil, the transition energy and thus the neutron separation energy was calculated as 5488.27(21) keV. From the long irradiation of sample 8 at BRR the best single measurement value was obtained as $S_\mathrm{n} = 5488.08(21)$ keV.
The most intense primary transition is the E1 transition from the capture state to a level with a spin and parity of 3^- [80]. This level in turn de-excites directly with an E1 transition to the ground state. Both the corresponding γ-rays are observed with γ-ray energies of 135.92(10) keV and 5352.04(14) keV. The sum of the transition energies, after correcting for the nuclear recoil, also corresponds to the capture state energy and hence to the neutron separation energy (see equation 2.26). In this way it was calculated as $S_\mathrm{n} = 5488.02(17)$ keV. The obtained values are in agreement with the value of $S_\mathrm{n} = 5488.09(20)$ keV tabulated in ENSDF. Also, the value obtained using the well-determined E1 transitions has a slightly smaller uncertainty than the tabulated value.

4.1.3 Thermal Neutron Capture Cross Section of ^{237}Np

The thermal radiative neutron capture cross section of ^{237}Np was derived from the intense decay γ-radiation of ^{238}Np ($T_{1/2} = 2.10(2)$ d) created by the neutron capture of ^{237}Np. The corresponding decay γ-rays are tabulated in DDEP [82, 85] or ENSDF [80]. The tabulated values are in good agreement between the two databases. Here the DDEP tabulated values were employed.

For the calculation of the thermal neutron capture cross section of ^{237}Np the four most intense lines were used. These are the decay γ-rays with, first an energy of 923.99(2) keV and emission probability of 2.604(20) per 100 decay events, second with an energy of 984.45(2) keV and emission probability of 25.18(13), and third and fourth the γ-rays creating a peak doublet at 1025.87(2) keV and 1028.54(2) keV with respective emission probabilities of 8.76(6) and 18.25(13) per 100 decay events [82, 85].

According to DDEP and ENSDF, a ^{238}Np decay γ-ray of 983.00(30) keV should be present next to the peak created by the 984.45(2) keV γ-ray in the measured gamma spectrum. However, the emission probability of the 983.00(30) keV γ-ray is only 0.27 % of the emission probability of the 984.45(2) keV γ-ray and thus the created additional peak has a very low count rate. Due to the rather small expected peak area compared to the 984.45(2) keV peak, the small peak cannot consistently be fitted with HYPERMET-PC. Therefore, the total peak area from both peaks was summed and divided between the two γ-rays according to the ratio of their emission probabilities from DDEP.

In the decay measurement of sample 6 at BRR, the peak doublet created by the 1025.87(2) keV and 1028.54(2) keV decay γ-rays was fitted well with HYPERMET-PC. Due to the distorted peak shape no consistent fit was possible for the two decay measurements performed at FRM II. At least one additional peak had to be included to describe the peak shape correctly. Thus, for these measurements, too, the peak areas of the fitted peaks were summed and divided according to the ratio of the emission probabilities from DDEP.

The calculated partial thermal neutron capture cross sections corresponding to the four most intense decay γ-rays of ^{238}Np are tabulated in Table 4.4 using reaction rate correction from Table 3.6 based on ENDF. The values obtained from the measurement of sample 6 at FRM II are systematically lower than the values from the other two measurements. This could be an indication that the irradiation of the sample was not completely homogeneous, probably due to the self-made neutron collimator. The average values derived from the mostly uncorrelated measurements of sample 6 at BRR and sample 7 at FRM II are also given in Table 4.4.

From these measured σ_γ values the thermal radiative capture cross section of ^{237}Np (that is for the ^{237}Np$(n,\gamma)^{238}$Np reaction) was determined based on the emission probabilities from the DDEP tabulation. The results are listed in table 4.5 for each γ-ray line.

Table 4.4: Partial radiative neutron capture cross sections for ^{238}Np measured for different intense lines at the BRR ([b]) and FRM II ([f]). The reaction rate correction from Table 3.6 with ENDF data is applied. The weighted mean of the uncorrelated measurements of 6^{b} and 7^{f} is given as $\bar{\sigma_\gamma}$ with the smaller of the two uncertainties. In the measurement of sample 6 at FRM II the self-made collimator was used, so a completely homogeneous irradiation is not ensured. For the FRM II measurements the 1025.872 keV and 1028.54(2) keV doublet was resolved by dividing the total measured peak area according to the tabulated intensities.

Sample No.	σ_γ [b]			
	923.99 keV	984.45 keV	1025.87 keV	1028.54(2) keV
6^{b}	4.60(12)	44.26(119)	15.32(45)	32.35(82)
6^{f}	4.53(14)	43.67(211)	15.22(48)	31.74(99)
7^{f}	4.57(13)	44.36(158)	15.50(44)	32.32(91)
$\bar{\sigma_\gamma}$	4.59(12)	44.29(119)	15.41(44)	32.34(81)

The weighted average of the averages of the two experiments is $\sigma_c^0 = 176.3 \pm 4.7$ b. It is associated with the smaller of the two uncertainties, as some correlations, e.g. due to the material used still exist (the uncertainty of the weighted average would be 3.4 b).
(By using the reaction rate correction based on the JEFF database instead of the ENDF database, the ^{237}Np(n, γ)^{238}Np radiative capture cross section was calculated as $\sigma_c^0 = 178.3 \pm 4.7$ b. This value is in very good agreement with the value obtained based on the ENDF database.)

The obtained value agrees well with the value of 175.9 ± 2.9 b recommended by the IAEA [113, 114] and tabulated in the Atlas of Neutron Resonances [39]. In Figure 4.7 a comparison of the obtained thermal cross section value with a number of published experimental values is shown. The values published most recently are 169 ± 4 b [115], 177 ± 5 b [116] and 182.2 ± 4.5 b [117]. They all agree with the value obtained in this work and have comparable uncertainties. However, a significant disagreement of almost five standard deviations is observed for the value of 141.7 ± 5.4 b [118]. Note that some experimentalists have suggested corrections on the values obtained by other experimentalists in previous experiments. Such corrected values are not included in the plot.

Both Harada *et al.* [115] and later Letourneau *et al.* [117] have suggested alternative values for the ^{233}Pa emission probabilities employed for determining the number of ^{237}Np atoms in previous (as well as their own) experiments. However, both have suggested different values, with Letourneau *et al.* also altering the value calculated by Harada *et al.* The changed values are in agreement with the value obtained in this thesis. It should be noted, that in this work the measured cross section value does not depend on the said emission probabilities.

Table 4.5: Thermal radiative neutron capture cross section σ_c^0 of ^{237}Np deduced from ^{238}Np decay γ-rays with different energies listed in the left most column. The measurements with sample 6 and sample 7 were carried out at the BRR ([b]) and FRM II ([f]). The emission probabilities per decay event are taken from the DDEP evaluation and are given in the text. The reaction rate corrections with ENDF data from Table 3.6 were used. All σ_c^0 values in the table are given in b.

Used Line	σ_c^0 [b] from 6[b]	7[f]
923.99 keV	176.7(50)	175.6(52)
984.45 keV	175.8(48)	176.2(63)
1025.87 keV	174.9(53)	176.9(51)
1028.54 keV	177.2(47)	177.1(52)
Averages	176.2(47)	176.5(51)
Total Average	176.3(47)	

Based on the determined thermal neutron capture cross section the emission probability of the 182.82(10) keV γ-ray was determined by $p_\gamma = \sigma_\gamma/\sigma_c^0$. This value can be used for normalizing the relative intensities given in Table 4.2. From the measurement of sample 6 at BRR it was calculated as $p_\gamma = 0.124(4)$ and from the measurement of sample 7 at FRM II as $p_\gamma = 0.127(4)$. The weighted average was derived as $p_\gamma = 0.125(4)$. This value is in agreement with the tabulated value of 0.139(16) [80] based on the measurement of Hoff *et al* [106]. The uncertainty achieved in this thesis, however, is a factor of four lower than the literature value.

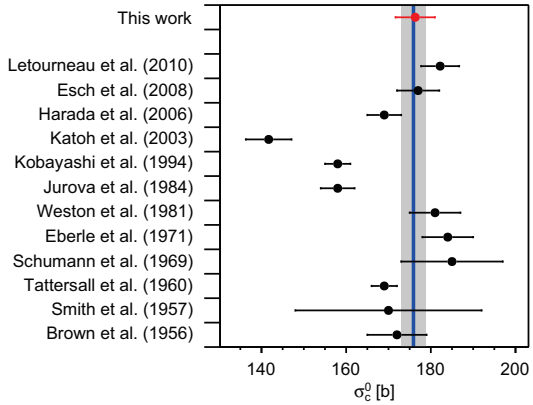

Figure 4.7: Thermal radiative neutron capture cross section of ^{237}Np as calculated from the measurements described in this work along with values taken from literature [119, 120, 121, 122, 123, 124, 125, 126, 118, 115, 116, 117]. The value recommended by the IAEA is indicated by the blue line and its uncertainty by the gray area [113, 114].

4.2 Americium-241

The samples manufactured by PTB from the obtained ^{241}Am-nitrate solution were transported to FRM II and irradiated at the external cold neutron beam of the PGAA-facility. Sample 1503 was irradiated for about 35 h using the self-made collimator, so that a spectrum with minimum interference could be obtained. The samples 1506 and 1507 which included a gold foil as a comparator where irradiated using the elliptical beam guide extension, without additional collimation. This ensured a maximum activation of the small amount of ^{241}Am which is important for the cross section measurements. All PGAA measurements during irradiation and decay measurements were performed in 45° tilting. The gold foil faced the neutron beam during irradiation. Sample 1506 was turned around after irradiation, so that the ^{241}Am layer was facing the detector during the decay counting. The second decay measurement of sample 1506 was performed 14 d after the irradiation. This corresponds to 21 times the half-life of the ^{242g}Am created during the irradiation. This activation product had therefore basically decayed completely by the time of the measurement. Timing details of the measurements can be found in Table 4.6.

As discussed in section 3.4.1 ^{241}Am has two comparably low energetic resonances at 0.307 eV and at 0.574 eV [39]. The created divergence from the $1/\sqrt{E_n}$ dependence is in the order of 6 % or 14 % at 0.0253 eV, depending on the chosen database. As already shown in Figure 3.30 the progression of the capture cross section is very different in the

Table 4.6: Details on measurements of the samples made by PTB using dissolved ^{241}Am. The samples were irradiated and measured at the FRM II PGAA facility. The front of the samples (e.g. defined by the gold foil) was facing the detector except for the decay measurement of sample 1506, where the ^{241}Am layer was facing the detector. The type of measurement is indicated as (p)rompt (during irradiation) and (d)elayed (after irradiation). For the PGAA measurements of the samples containing gold the elliptical beam extension was used to increase the neutron flux.

Sample No.	t_{real} [s]	t_{live} [s]	Rate [cps]	type
1503	127 534.9	126 694.7	276.90	p
1506	56 981.9	42 587.6	8930.35	p
1506	3626.0	3600.0	350.87	d
1506	5387.9	5358.3	252.83	d
1507	19 230.9	14 371.0	8902.92	p
1507	15 083.9	15 000.0	277.90	d
Blank	27 190.6	27 000.0	177.25	p

two evaluations, so that the derived reaction rate correction factors, also accounting for the divergence from $1/\sqrt{E_{\mathrm{n}}}$ are not compatible. This is a major source of uncertainty. It should be noted that using the cold neutron beam at FRM II the uncertain deviation from the $1/\sqrt{E_{\mathrm{n}}}$ dependence can be mostly omitted (for illustration see Figure 4.8).

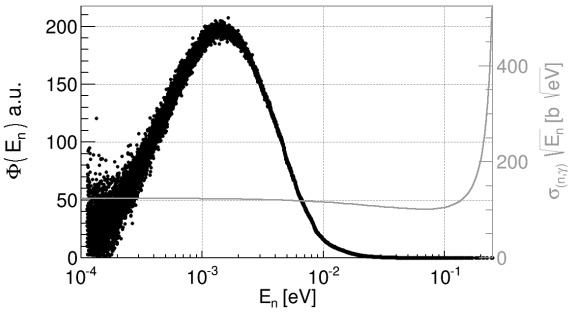

Figure 4.8: Plot of the neutron capture cross section of ^{241}Am (gray line) as given in the ENDFVII/I and weighted by $\sqrt{E_{\mathrm{n}}}$ for convenience, and of the energy distribution of the cold neutron beam at the PGAA facility at FRM II (black points).

4.2.1 Partial Neutron Capture Cross Sections σ_γ of ^{241}Am

The prompt γ-ray lines of ^{241}Am were identified in the spectrum obtained during the irradiation of sample 1503. Even though the amount of ^{241}Am in sample 1503 is more

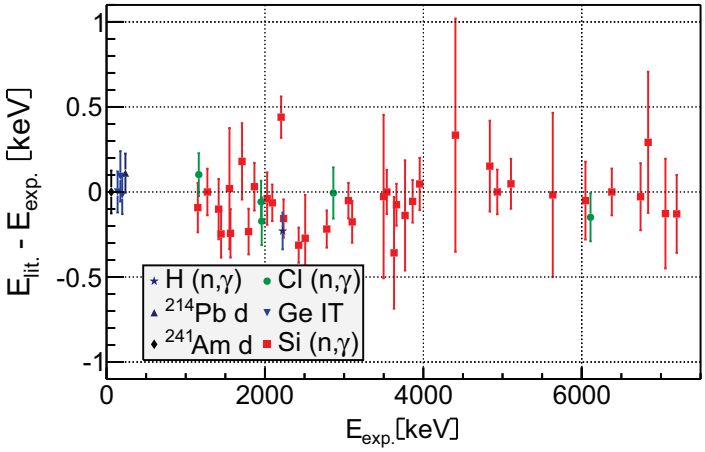

Figure 4.9: Comparison of the energies of identified background lines measured during the irradiation of sample 1503 at FRM II with tabulated values.

than a factor of 100 lower than in the samples created from actinide-containing pellets, 19 prompt γ-rays of ^{241}Am could be identified. These include 7 primary γ-rays with high energies. 2 of the secondary prompt γ-ray intensities had to be corrected for small interferences from background lines, which were identified using the blank sample irradiation and decay measurements. The identified prompt γ-ray lines and the calculated intensities relative to the strongest identified prompt γ-ray line at 154.72(7) keV are listed in Table 4.7.

The energy calibration was made piecewise using the ^{241}Am decay line at 59.54 keV [82, 86] and the prompt lines of ^{28}Si at 1273.35 keV, 3538.97 keV, 4933.89 keV and 6379.80 keV [101]. The corresponding non-linearity correction functions were applied for the different energy regions. The validity of both the energy calibration and the determined energy uncertainties over the whole measurement range is demonstrated in Figure 4.9.

Normalization

The partial radiative neutron capture cross sections of ^{241}Am were deduced from the PGAA and decay measurements of samples 1506 and 1507. The average thermal equivalent neutron flux Φ_0 during irradiation was determined from the activity of the gold foil. Subsequently, the partial capture cross section of the most intense prompt γ-line at 154.72(7) keV was calculated according to equation 2.76. The characteristics of ^{198}Au used for the flux determination are given in section 4.1.1, where a similar normalization procedure is discussed for ^{237}Np.

Table 4.7: Energies and relative intensities of prompt γ-rays of ^{241}Am measured at FRM II, along with the corresponding photon-absorption correction factors η_0. The normalization to σ_γ is given using the reaction rate correction factor derived with the JEFF evaluation (others are listed in Table 4.8).

E_γ [keV]	I_γ †	η_0	E_γ [keV]	I_γ †	η_0
132.57(12)	0.1803(82)	1.0113(23)	382.46(14)	0.0198(21)	1.0069(15)
154.72(10)	1.0000(350)	1.0103(21)	435.03(10)	0.0876(35)	1.0066(15)
186.44(11)	0.8552(443)*	1.0094(20)	4714.02(50)	0.0071(17)	1.0021(5)
191.71(11)	0.1543(63)	1.0093(20)	4719.35(61)	0.0059(17)	1.0021(5)
194.51(11)	0.2422(93)	1.0092(20)	4822.06(38)	0.0081(17)	1.0020(5)
195.84(11)	0.1668(67)	1.0092(20)	4855.56(41)	0.0070(16)	1.0020(5)
230.45(11)	0.1702(64)	1.0086(19)	5160.87(28)	0.0083(10)	1.0020(4)
274.48(11)	0.3693(137)	1.0079(17)	5167.03(74)	0.0023(9)	1.0020(4)
296.56(12)	0.0556(47)*	1.0077(17)	5174.59(21)	0.0156(13)	1.0020(4)
316.28(16)	0.0124(26)	1.0075(17)			

† : Multiply by 72.80(252) b to calculate σ_γ (see table 4.8),
or with 0.109(6) to calculate p_γ (see text) per neutron capture event.
* : Interferences from other peaks, see section 4.2.1 for additional information.

For the irradiation of sample 1506 an average thermal equivalent neutron flux of $\Phi_0 = 2.76(1) \cdot 10^{10}\,\mathrm{cm^{-2}\,s^{-1}}$ was calculated using the peak area created by the 411.8 keV decay γ-ray of ^{198}Au. Additionally, using the intense prompt capture γ-ray of ^{197}Au at 6252.11(6) keV a thermal equivalent flux of $\Phi_0 = 2.77(8) \cdot 10^{10}\,\mathrm{cm^{-2}\,s^{-1}}$ was determined, confirming the above result.
For sample 1507 the flux was calculated as $\Phi_0 = 2.58(5) \cdot 10^{10}\,\mathrm{cm^{-2}\,s^{-1}}$ from the decay γ-ray of ^{198}Au and as $\Phi_0 = 2.47(7) \cdot 10^{10}\,\mathrm{cm^{-2}\,s^{-1}}$ from the prompt γ-ray of ^{197}Au. These values are also in good agreement with each other.
For both samples the weighted average of the two flux determinations together with the smaller of the uncertainties was applied to calculate the partial capture cross section normalizations for the most intense prompt γ-ray line at 154.72(7) keV as listed in Table 4.8.

Even though the shape of the capture cross sections tabulated in ENDF and JEFF differ substantially, and consequently the corresponding reaction rate corrections differ, the derived partial capture cross section values are in agreement with a difference of 1.3 times the combined standard deviation.
The value of 72.80(252) b determined with the reaction rate correction based on the JEFF evaluated database seems to be more reliable, as it is based on recent measurements performed by Lampoudis *et al.* [127] specifically for the JEFF evaluation. In the calculation of $p_\gamma = \sigma_\gamma/\sigma_c^0$ the reaction rate correction factor cancels out, so the normalization to

emission probabilities given in Table 4.7 is independent of the data set chosen for the correction.

Table 4.8: Partial radiative neutron capture cross sections of ^{241}Am measured for the most intense line at 154.72(7) keV at the FRM II (^{f}) PGAA facility. Different reaction rate correction factors η_1 from Table 3.6 are applied. The weighted average of the measurements is given.

Sample No.	σ_γ [b] η_1 (ENDF)	η_1 (JEFF)	η_1 ($1/\sqrt{E_n}$)
1506	67.34(236)	71.89(252)	76.13(267)
1507	69.48(289)	74.16(309)	78.54(327)
$\bar{\sigma_\gamma}$	68.20(236)	72.80(252)	77.09(267)

The ENSDF evaluation of ^{241}Am [128] secondary and primary prompt γ-radiation is based on a publication of Salicio *et at.* [129]. The situation is the same as in the case of ^{237}Np. Primary and secondary γ-rays were measured separately with different detectors and samples. The secondary γ-radiation was measured at ILL with two curved crystal spectrometers, one operating in the energy region from 30 to 400 keV and one from 200 to 1200 keV. For this irradiation a target of 0.4(1) mg AmO_2 wrapped in an aluminum casing with a total target thickness of 0.5 mm was provided by ORNL [129]. In the publication and in the ENSDF file only relative intensities are reported.
The primary prompt γ-radiation was measured using a target of about 1.1 g Am_2O_3 encapsulated in a thin-walled box made of aluminum. The measurement in the energy range from 2 to 6 MeV was carried out at the SAPHIR reactor in Würenlingen with a Ge(Li) detector, as in the case of the measurement of the primary prompt γ-radiation of ^{237}Np. Only a rough estimate on the emission probabilities per neutron capture event is provided with an estimated uncertainty of 50 %. No normalization of the intensities between the low and high energetic measurements is provided.
Due to these obstacles and the relatively small number of lines identified in this work, a comparison of the evaluated data and the data measured here by means of a pull plot is not sensible. It should be mentioned, however, that for all of the prompt γ-lines measured in this thesis counterparts in the evaluation exist. As in this work both the higher and lower energetic parts of the prompt γ-ray spectrum were measured simultaneously and also the normalization was determined these results, in principle, could be used to normalize the ENSDF tabulated data.

4.2.2 Thermal Neutron Capture Cross Section of ^{241}Am

The thermal radiative neutron capture cross section of ^{241}Am was determined from the decay measurements of samples 1506 and 1507.

After neutron capture ^{242}Am is created in two different isomers. The ground state ^{242g}Am with a half-life of 16.01(2) h [82, 86] is formed with an isomeric production ratio of 0.914(70) [130], measured by Fioni *et al.* at thermal neutron energies. This is basically the same as the isomeric production ratio given as 0.91(10) in the evaluation of Bernard and Bouland of the Commissariat à l'Energie Atomique et aux Energies Alternatives, France [131]. Besides the ground state ^{242g}Am, also the metastable ^{242m}Am with a half-life of 143(2) yr [82, 104] is produced.

In the decay of ^{242g}Am only two known γ-rays with energies of 42.13 keV and 44.54 keV are emitted with rather low and uncertain emission probabilities of below 0.0004 per decay event. As the emission probabilities are so low and the γ-rays have energies in the region dominated by the very intense decay peak of ^{241}Am at 59.54 keV as well as its X-ray escape peaks, the γ-rays of ^{242g}Am could not be observed in the decay measurements in this work. Neither could the even less intense γ-rays from the decay of ^{242m}Am be observed. Thus, the K_α and K_β X-rays following the electron capture decay of ^{242g}Am to ^{242}Pu were utilized for the thermal capture cross section determination. The emission probability of the $K_{\alpha,1}$ X-ray at 103.734 keV is given as 0.056(3) per decay event in the DDEP data base. The emission probability of the $K_{\alpha,2}$ X-ray at 99.525 keV is given as 0.0355(17) per decay event. However, two decay γ-rays of ^{241}Am with energies of 98.97 keV and 102.98 keV produce peaks very close to the X-ray peaks, which also have a larger width than the γ-ray peaks. Further these peak doublets are close to each other with regard to the detector resolution. Therefore, the whole region was integrated in HYPERMET-PC using a linear description of the background. The measurement that was taken 14 d after the irradiation, when basically all of the ^{242g}Am had decayed, was integrated in the same manner. The resulting area corresponds to the background from the decay γ-rays of ^{241}Am and hence was subtracted from the previous area. For sample 1507 no decay measurement long after the irradiation could be performed, thus the area obtained in the decay spectrum of sample 1506 – 14 d after the irradiation – was weighted by the corresponding certified activities. This weighted result was regarded as the background from the decay γ-rays of ^{241}Am and subtracted from the area resulting from the integration in the decay spectrum of sample 1507. The resulting areas of both X-ray peaks were hence used to determine the thermal capture cross section for the production of ^{242g}Am.

Due to a high neutron flux during irradiation, the X-ray activities of the created ^{242g}Am showed to be dominant in this region. The ^{241}Am background contribution in this area was found to be only about 12 % of the integration result.
In addition, the thermal capture cross section was also determined using the $K_{\beta,1}$ and $K_{\beta,2}$ X-rays following the electron capture decay of ^{242g}Am to ^{242}Pu. These X-rays have energies of 117 keV and 120 keV with emission probabilities of 0.0206(110) and 0.0072(4) per decay event [82, 86]. All the results are listed in Table 4.9.
All obtained values are in good agreement with each other. This is also true of the values calculated with the different reaction rate corrections based on the ENDF or the JEFF database.

Table 4.9: Thermal neutron capture cross section $\sigma^0_{c,\mathrm{g.s.}}$ of the reaction $^{241}\mathrm{Am}(\mathrm{n},\gamma)^{242\mathrm{g}}\mathrm{Am}$. The values are calculated using different X-ray lines following the decay of $^{242\mathrm{g}}$Am, which are listed in the first column. The measurements were carried out at the FRM II. The emission probabilities per decay event are taken from the DDEP evaluation and are given in the text. The reaction rate corrections with ENDF and JEFF data from Table 3.6 are used.

Used Line	$\sigma^0_{c,\mathrm{g.s.}}$ [b] (ENDF) from 1506	1507	$\sigma^0_{c,\mathrm{g.s.}}$ [b] (JEFF) from 1506	1507
K_α	571.5(268)	579.4(263)	610.1(285)	618.4(281)
$K_{\beta,1}$	567.9(351)	583.1(537)	606.2(375)	622.4(573)
$K_{\beta,2}$	568.3(422)	552.2(425)	606.7(450)	589.5(454)
Averages	569.8(268)	573.5(263)	608.2(285)	612.2(281)
Total Average	571.7(263)		610.3(281)	

The major contribution to the uncertainty on the thermal $^{241}\mathrm{Am}(\mathrm{n},\gamma)^{242\mathrm{g}}\mathrm{Am}$ capture cross section values arises from a 5 % uncertainty of the tabulated X-ray emission probabilities. The determination of the neutron flux contributed about 2 % to the overall uncertainty, while the efficiency and the number of ^{241}Am nuclei calculated from the certified activity contributed below 1 %. For the K_α X-rays the total integrated peak area could be determined with 1 % uncertainty. For the K_β X-rays this uncertainty was calculated as 4 – 7 %.

The obtained thermal $^{241}\mathrm{Am}(\mathrm{n},\gamma)^{242\mathrm{g}}\mathrm{Am}$ capture cross section regards the production of the ground state ^{242}Am, only. It hence does not equal the thermal radiative neutron capture cross section of ^{241}Am, that is the thermal cross section for the reaction $^{241}\mathrm{Am}(\mathrm{n},\gamma)^{242}\mathrm{Am}$. To obtain the thermal radiative neutron capture cross section of ^{241}Am the thermal $^{241}\mathrm{Am}(\mathrm{n},\gamma)^{242\mathrm{g}}\mathrm{Am}$ capture cross section was divided by the above stated isomeric production ratio of 0.914(70).
Using the reaction rate correction based on ENDF a thermal capture cross section of $\sigma^0_c = 625.5 \pm 29.2$ b was derived. The same cross section calculated with reaction rate correction based on JEFF has a value of 667.7 ± 31.2 b.
These two values agree with each other. For the same reason as in the case of the partial capture cross sections, the value obtained using the JEFF-based reaction rate correction seems to be more reliable. The weighted averages calculated with the different reaction rate correction factors are shown in Figure 4.10 together with other published values for the thermal capture cross section of ^{241}Am.

The ENDF-based value of 625.5 ± 29.2 b for the thermal neutron capture cross section value is in good agreement with the value of 585 ± 12 b evaluated in the Atlas of Neutron Resonances [39] and recommended by the IAEA. The JEFF-based value (667.7 ± 31.2 b),

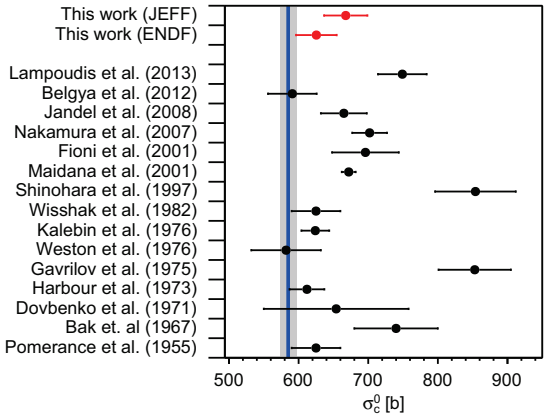

Figure 4.10: Thermal radiative neutron capture cross section of ^{241}Am as calculated from the measurements described in this work using reaction rate correction factors calculated with the ENDF and JEFF evaluated databases. For comparison values taken from other publications are given [132, 133, 134, 135, 136, 137, 138, 139, 140, 141, 130, 142, 143, 144, 127]. When only a capture cross section for the production of ^{242g}Am ($\sigma^0_{c,\mathrm{g.s.}}$) was given, the capture cross section for the ground and metastable state was calculated using the isomeric production ratio of Fioni *et al.* [130]. The value of Harbour *et al.* [135] was taken from the evaluation by Lynn *et al.* [145]. The IAEA-recommended value is indicated by the blue line and its uncertainty by the gray area.

by contrast, is higher than the IAEA-recommended thermal capture cross section value by 2.5 times the combined uncertainty.
The measured JEFF-based value, however, is in good agreement with the ENDF/B-VII.I evaluated value of 684 b. The agreement of the ENDF/B-VII.I evaluated thermal capture cross section with the measured ENDF-based thermal capture cross section is less good. Both the measured ENDF-based and the measured JEFF-based thermal capture cross section values are lower than the JEFF 3.2 evaluated value of 748 b.
From Figure 4.10 it can be seen that the different published values of the capture cross section scatter in a wide range between 580 and 890 b, which at least partly can be explained by the uncertain progression of the capture cross section at higher neutron energies. However, an agreement of both the ENDF-based and the JEFF-based thermal capture cross section values obtained in this work with the majority of the published data is observed.

Preliminary capture cross section values obtained within the scope of this thesis were published in [146, 147]. However, with new insights gained in the meantime and updated data in databases the values presented here are lower than those presented earlier. There

are two reasons for this. First and primarily, this difference is based on the reaction rate correction. In the earlier publication a $1/\sqrt{E_\mathrm{n}}$ dependence of the capture cross section was assumed in the energy region from 0.0001 to 0.0253 eV. As can be seen in Table 3.6 the reaction rate correction factors calculated based on JEFF and ENDF are significantly lower than the negligible correction factor corresponding to the $1/\sqrt{E_\mathrm{n}}$ assumption.
Second, in the publication a value of $\sigma_{\gamma,412} = 95.58(12)$ b for the 411.8 keV decay γ-ray of ^{198}Au was used (taken from measurement [2]). However, in section 4.1.1 the $\sigma_{\gamma,412}$ was calculated consistently from different evaluated data sets as 94.34(15) b, which is 1.3 % lower.

Finally, the emission probability $p_\gamma = \sigma_\gamma/\sigma_c^0$ was calculated as $p_\gamma = 0.109(6)$. To cross check this value, the calculation was made using both the ENDF-based and the JEFF-based partial capture cross sections of the line and the corresponding thermal capture cross section value. As it was expected, both calculations yielded the same value for p_γ.

4.3 Plutonium-242

Samples containing the $^{242}PuO_2$ pellets and a blank sample casing were irradiated and counted at the PGAA facilities at the BRR and FRM II sites. Prior to irradiation the pellets' integrity was visually checked. It turned out that the lightest pellet contained in sample 1 had not been stable enough and had split into two pieces during transport. Due to the limited neutron beam time not all of the intact samples could be irradiated at both facilities. All irradiations were carried out at very low count rates; usually below 1 % to decrease the probability of coincidence events and to keep the dead time to a minimum. The information on the measurement times is tabulated in Table 4.10. The spectrum measured during the irradiation of sample 2 at BRR is shown in the appendix Figure E.1 and that of the measurement at FRM II in Figure E.2.

Table 4.10: Details on measurements of samples containing pellets with ^{242}Pu at the different sites. The front of the samples (e.g. defined by the gold foil) was facing the detector except for the 6 h measurement of sample 3 on the LEGe, where the pellet was facing the detector. The type of measurement is indicated as (p)rompt (during irradiation) and (d)elayed (without irradiation) and the type of detector used is specified (LEGe or coaxial HPGe)

	Sample No.	t_{real} [s]	t_{live} [s]	Rate [cps]	type
BRR	2	82 881.7	82 136.6	230.18	p, HPGe
	2	4299.1	4287.4	99.04	d, HPGe
	3	51 756.2	51 386.7	170.01	p, HPGe
	3	21 610.0	21 590.5	200.69	d, LEGe
	3	61 234.0	61 176.2	161.64	d, LEGe
	3	65 343.9	65 290.0	317.81	d, HPGe
	Blank	20 280.5	20 216.4	44.21	p, HPGe
FRM II	2	97 139.5	96 300.5	258.10	p, HPGe
	2	450.4	450.0	25.92	d, HPGe
	3	23 485.5	23 333.2	190.9	p, HPGe
	3	13 897.0	13 888.4	15.02	d, HPGe
	10	43 669.0	42 315.6	757.04	p, HPGe
	10	6188.5	6183.5	23.85	d, HPGe
	Blank	36 000.0	35 947.4	25.52	p, HPGe

At the PGAA station of the BRR the samples were tilted by 30° against the neutron beam axis. For the PGAA measurements a circular collimator of ^{6}Li-enriched plastic with a diameter of 5.5 mm was placed in the mounts at the sample chamber opening to decrease the irradiation of the quartz glass, thus reducing unnecessary background radiation. At the FRM II the samples were placed at an angle of 45° in front of the detector. The self-made collimator of 5 mm diameter described in section 3.1.2 was placed at the end of

the neutron beam guide. The position of the resulting beam spot was determined with a sheet of the special Li-containing film fitted into the sample holder. This image was used to check the positioning of the samples prior to and after irradiation.

Sample 2 was irradiated at both facilities to measure spectra with as few background lines as possible to identify prompt γ-ray lines of ^{242}Pu neutron capture and to calculate their relative intensities. The samples containing gold foil were used to measure the partial capture cross section of the most intense prompt γ-ray line and then normalize the relative intensities. Thus, sample 2 was irradiated longer than the samples containing gold foil as a flux monitor. The samples with the gold foil were irradiated with the foil facing the neutron beam and the detector.

After irradiation the samples containing gold foil were counted for decay radiation. At the BRR sample 3 was irradiated and afterwards counted in the "DÖME" low-background counting chamber using both a LEGe and a coaxial HPGe detector, successively. The LEGe spectra were acquired in a one hour batch mode, meaning that each hour one spectrum was automatically collected, so that the decrease in the count rate from the ^{243}Pu could be measured. The spectra of one such batch were added up to get an integral spectrum, in which the peak areas could be determined with small uncertainties. Between stopping one measurement, saving of the spectrum and starting the next measurement only a few seconds passed, so that in the integral spectrum the dead time was increased only marginally compared to directly measuring the spectrum over the whole time period. For the first batch consisting of six one-hour measurements the pellet was facing the detector, so that the low energetic γ-rays of the ^{243}Pu decay could be measured without the photon absorption in the gold foil. As the half-life of ^{243}Pu (5 h) is much shorter compared to the half-life of ^{198}Au (2.7 d), the determination of the ^{198}Au activity of the gold foil was later done separately.
Then the sample was turned around and another batch of 17 one-hour measurements was taken with the gold foil facing the detector. After that, the detector was changed for a coaxial HPGe detector with 13 % relative efficiency. This detector had a four times higher efficiency at 411.8 keV, the energy of the strongest decay γ-ray line of ^{198}Au used for the determination of average thermal equivalent neutron flux.

At the FRM II site samples 3 and 10 were irradiated and counted for determining the partial capture cross sections. The decay counting was performed directly with the detector of the PGAA station with closed beam shutter. Sample 10 was irradiated in the fully opened beam without the self-made collimator to ensure a homogeneous irradiation.

4.3.1 Partial Neutron Capture Cross Sections σ_γ of ^{242}Pu

From the spectra taken during the irradiation of sample 2 at the BRR and FRM II PGAA facilities, energies and intensities relative to the strongest prompt γ-ray line found were

determined. Using the background spectra collected from the irradiation of the blank sample, interferences from prompt γ-radiation caused by the irradiation of the sample casing or from the usual beam background were identified. It was thoroughly checked for the presence of prompt γ-lines from any stable element using EGAF [4] and from any actinide using ENSDF [80] libraries. Using the ENSDF [80], DDEP [82] and NuDat [102] databases, as well as the Table of Isotopes [103] it was checked for any radioisotope and corresponding decay- and X-radiation. The prompt γ-ray lines of ^{242}Pu neutron capture were identified using the adopted level scheme tabulated in ENSDF [80]. In total 127 prompt γ-ray lines of ^{242}Pu were observed consistently in the two measurements.

Background lines clearly identified in the PGAA spectra were used for the absolute energy calibration of the spectra. These were background lines originating from the irradiation of the sample casing or of the measurement environment, as well as the strongest line from the ^{241}Am activity in the sample (see section 3.3.1).
The energy calibration for the BRR PGAA measurement was based on the ^{241}Am decay γ-ray line at 59.54 keV [82, 86] and the prompt γ-ray line of ^{28}Si at 4933.89 keV [101] combined with the pre-determined non-linearity correction. As it was necessary to use two non-linearity functions for the FRM II measurement the energy calibration was made piecewise using the ^{241}Am line at 59.54 keV [82, 86], the line at 351.93 keV [82, 148] from the β-decay of ^{214}Pb, the prompt line of ^{28}Si at 1273.35 keV [101], the decay line of ^{20}F at 1633.5 keV [2] (from the FEP foil), the prompt line of ^{1}H at 2223.25 keV [149] and the prompt lines of ^{28}Si at 3538.97 keV, 4933.89 keV, 6379.80 keV and, 8472.22 keV [101].
The validity of both the energy calibration and the determined energy uncertainties is demonstrated in Figure 4.11, where the energy residuals from the measured and the tabulated data of clearly identified peaks from different isotopes are plotted as a function of the measured energy. No systematic effects are observed and the uncertainties given seem to be reasonable, as the residuals generally scatter around 0 within just 2 standard deviations. The average residual for the BRR measurement is 0.024(28) keV and for the FRM II measurement 0.005 ± 0.037 keV, both perfectly compatible with 0.

127 prompt γ-ray lines were identified in the BRR and the FRM II, PGAA measurements of sample 2. In Figure 4.12 the energies of the identified prompt γ-rays as measured at the BRR are compared with the corresponding ones measured at the FRM II. The mean of the pull plot in Figure 4.12(a) is -0.019 ± 0.078 and thus perfectly compatible with 0, whereas the RMS is 0.88 ± 0.06. This might indicate an overestimation of the given uncertainties. No systematic deviations are observed in the plot of the residuals against the measured energies in Figure 4.12(b). Both plots demonstrate a very good agreement of the measured prompt γ-ray energies.

The pull plot for the relative intensities in Figure 4.13(a) with a mean of 0.026 ± 0.102 and an RMS of 1.150 ± 0.072 shows that the two measurements are in good statistical agreement. The graph of the residuals of the relative intensities as a function of the measured energy in Figure 4.13(b) shows that no visible systematic energy-dependent

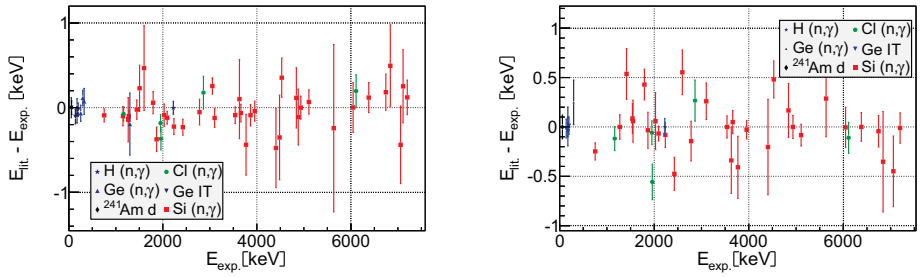

(a) (b)

Figure 4.11: Comparison of the energies of identified background lines measured during the irradiation of sample 2 at (a) BRR and (b) FRM II with tabulated values.

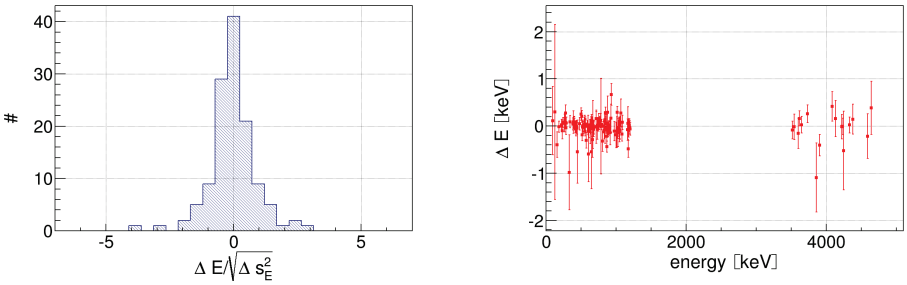

(a) (b)

Figure 4.12: Comparison of the ^{242}Pu prompt γ-ray energies measured at BRR with those measured at FRM II. (a) Pull plot of the measured energies. (b) Graph showing the residuals as a function of the measured γ-ray energy.

effects seem to occur. Thus, it can be concluded that the two measurements of the relative intensities are in very good agreement over the whole measured energy-range.

A set of 81 γ-ray lines observed in both the BRR and the FRM II PGAA measurements, that could not be assigned yet and that thus could be additional prompt γ-rays of the ^{242}Pu neutron capture reaction, is listed in the appendix in Table A.3. The relative intensities are calculated with respect to the 287.69(8) keV γ-ray line. Neither the relative intensities nor the energies of these unassigned lines differ by more than 1.6 standard deviations between the two measurements, so they are in excellent agreement. However, as they have not yet been placed in the level scheme, their assignment is uncertain.

The intensities relative to the strongest line were derived from the measured peak areas after applying the appropriate corrections, such as the efficiency or $\eta_0(E_\gamma)$. Most of the

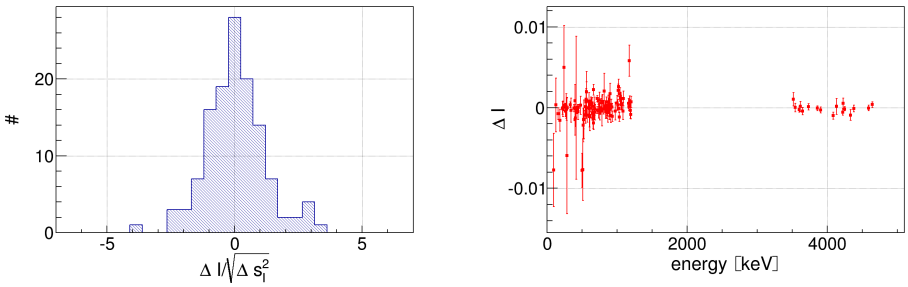

(a) (b)

Figure 4.13: Comparison of ^{242}Pu prompt γ-ray relative intensities measured at BRR with those measured at FRM II. (a) Pull plot of the measured relative intensities. (b) Graph showing the residuals as a function of the measured γ-ray energy.

lines were clearly identified and fitted well, with no necessary corrections for background contributions. The uncertainties of the measured peak areas are typically higher for the FRM II than for the BRR PGAA measurement. This is due to the distorted peak shapes in the FRM II PGAA spectrum, which is especially true for the strongest line. As all intensities were calculated relative to the intensity of the strongest line this uncertainty propagates accordingly.
All the measured energies and relative intensities of 127 prompt γ-ray lines derived from the BRR PGAA measurement are given in the appendix in Table A.1. Those from the measurement at FRM II are given in Table A.2 along with the photon absorption correction factors $\eta_0(E_\gamma)$ applied. The weighted averages of both the energies and the relative intensities I_γ from the two measurements are given in Table 4.11 together with the smaller of both uncertainties. Intensities derived from peak areas that were corrected for interferences with other peaks seen in the blank sample irradiation or the decay counting are marked with asterisks. These corrections are basically the same for both measurements. Corrections were applied by weighting the peak area measured in the blank sample irradiation or the decay counting with the corresponding live times and subtracting that value from the investigated peak area. These corrections were generally relatively small, in or below the percent range. In the following some special cases will be discussed.

Prompt γ-ray line at 96.06(10) keV
A weak interference from the 96.4(4) keV γ-ray from the β-decay of ^{243}Pu was corrected for using the tabulated relative intensity of 0.06(1) [93] and the measured ^{243}Pu decay γ-ray line at 84.14(5) keV, which is the strongest of the decay γ-ray lines of ^{243}Pu. All in all the interference correction was smaller than the uncertainty of the measured peak areas.

Prompt γ-ray line at 125.47(71) keV
An interference from a decay γ-ray line of ^{241}Am at 125.30(2) keV with an intensity of 0.0041(20) per 100 α-decays was corrected for using the measured peak are of the strongest ^{241}Am line at 59.54 keV with an intensity of 35.92(17) per 100 α-decays. The values are taken from DDEP [82, 86]. As the intensity of the prompt γ-ray line of ^{242}Pu is rather weak the correction turned out to be almost one half of the total peak area for the BRR measurement, but only 4 % of the peak area for the FRM II measurement, due to the higher neutron flux and thus the higher reaction rate. The resulting relative intensities of 0.0010(3) and 0.0013(33) nevertheless agree very well within their uncertainties.

Prompt γ-ray line at 159.47(10) keV
Interferences at this energy are due to an activation of the HPGe crystal. A decay γ-line from the metastable state in ^{77m}Ge at 159.7(1) keV [150] and a weaker prompt γ-ray peak from ^{73}Ge at 159.27(2) keV [151] are present. As these interferences stem from the normal background and do not depend on the actual sample, the subtraction was made using the peak area measured in the irradiation of the blank sample weighted by the live times. The correction was 34 % of the peak area for the BRR measurement, but only 14 % of the peak area for the FRM II measurement. This implies that the increased distance between the detector and the neutron beam and the thicker neutron shielding overcome the higher neutron flux and thus the higher flux of scattered neutrons in comparison to the BRR PGAA detector. Still the resulting relative intensities 0.0025(4) and 0.0018(6) are in good agreement for the two measurements.

Prompt γ-ray line at 241.93(7) keV
A 1.9 % contribution from a 241.997(3) keV γ-ray originating from the β-decay of ^{214}Pb in the lead shielding was corrected for in the FRM II measurement using the blank sample spectrum. No such contribution was found in the BRR measurement. The resulting relative intensities are in agreement being 0.0807(15) and 0.0857(49).

Prompt γ-ray line at 277.98(9) keV
One of the strongest decay γ-ray lines of the ^{239}Np contaminant in the sample material at 277.599(1) keV contributed massively to the relatively small measured peak area of the 277.98(9) keV prompt γ-ray. The decay line has an intensity of 14.4(1) per 100 decay events. Its contribution was corrected for by using the equally strong decay γ-line at 228.183(1) keV with an emission probability of 11.32(22) per 100 decay events seen in the same measurement. Decay data are taken from DDEP [82, 85]. In the case of the BRR measurement this contribution is 52 % of the measured peak area, whereas it is 20 % in the case of the FRM II measurement.
An additional small interference with a Ge X-ray escape peak from the strongest prompt γ-ray of ^{242}Pu at 287.69(8) keV was also corrected for. The correction was performed based on the ratio between the X-ray escape peak and the full energy peak determined with Geant4 simulations for the respective detectors. The contribution to the measured peak area was calculated to 9 % for the BRR measurement and as 23 % for the FRM II

measurement.
Another 6 % contribution seen in the blank sample measurement at the BRR, but not at the FRM II was also corrected for. It probably originates from the activation of the copper cooling finger in the HPGe crystal, as it corresponds to the strongest prompt γ-ray line of ^{63}Cu. All in all the resulting relative intensities of 0.0031(8) and 0.0029(11) agree very well within their uncertainties.

Prompt γ-ray line at 333.37(35) keV
In the BRR measurement this peak is dominated by a decay γ-line of ^{239}Np at 334.310(3) keV with an intensity of 2.04(2) per 100 decays [82, 85], contributing 72 % to the measured peak area. In the FRM II measurement this contribution is only 19 %. Thus, the energy determination of this prompt γ-ray at the BRR cannot be deemed reliable and the energy determined at FRM II is given. The corrections were calculated using the 228.183(1) keV decay γ-ray line. The resulting relative intensities are 0.0003(2) and 0.0006(3), which are in agreement.

Prompt γ-ray line at 480.63(9) keV
This peak is situated on top of the Doppler-broadened 477.6 keV γ-ray peak from the ^{10}B(n, α)^{7}Li reaction. Approximating the shape at the top of the Doppler-broadened peak a small region around the peak at 480.63(9) keV was regarded as flat . The resulting relative intensities of 0.0139(6) and 0.0142(10) agree well within their uncertainties.

Prompt γ-ray line at 516.61(9) keV
A 31 % contribution from the prompt γ-ray of ^{36}Cl at 517.077(8) keV with a partial capture cross section of 7.58(5) b [152] was corrected for in the BRR measurement using the blank sample irradiation. The same contribution was only 15 % in the FRM II measurement.
Additionally, a contribution of 0.8 % was determined resulting from the chlorine contaminant in the sample material. This was done using the undisturbed prompt γ-ray line of ^{36}Cl at 1164.87 keV with a partial capture cross section of 8.91(4) b [152] after the correction of the background. The resulting relative intensities, 0.0165(16) and 0.0144(13), are in agreement.

Prompt γ-ray line at 787.17(72) keV
This prompt γ-ray peak is in between the two stronger prompt γ-ray peaks of ^{36}Cl at 786.3 keV and at 788.4 keV with partial capture cross sections of 3.419(3) b [152] and 5.42(5) b [152]. The intensity was determined by subtracting the contributions of chlorine as explained in the previous paragraph. The energy of this γ-ray was assumed to be the energy tabulated in ENSDF [93] with an estimated uncertainty of one channel.

Prompt γ-ray line at 3519.06(11) keV
The peak appears to be broader than usual for the FRM II measurement and could, instead of being one peak, be a doublet of two peaks with similar intensities. In the BRR measurement no evidence was found for this, but that might be due to the smaller peak

area.

Table 4.11: List of the weighted means of the prompt γ-ray line energies and relative intensities from the ^{242}Pu(n, γ)^{243}Pu reaction from the measurements at BRR and FRM II. The smaller of the two uncertainties is given as the uncertainty of the weighted average.

E_γ [keV]	I_γ [†]	E_γ [keV]	I_γ [†]	E_γ [keV]	I_γ [†]
96.06(10)	0.0789(21)*	607.32(18)	0.0014(2)	924.98(18)	0.0019(3)
125.47(71)	0.0010(3)*	609.80(9)	0.0104(8)*	931.69(12)	0.0040(4)
159.47(10)	0.0023(4)*	625.24(8)	0.0135(5)	975.93(13)	0.0068(6)
184.21(8)	0.0243(5)	633.14(16)	0.0058(6)	999.68(15)	0.0039(5)*
219.49(8)	0.0138(3)	637.87(10)	0.0068(4)	1008.66(14)	0.0032(3)
229.15(8)	0.0136(5)	644.10(12)	0.0055(5)	1015.58(9)	0.0072(5)*
233.65(10)	0.0024(2)	647.09(33)	0.0024(6)	1022.36(9)	0.0098(6)
241.93(7)	0.0811(15)*	656.21(8)	0.0118(8)*	1028.19(12)	0.0014(2)
261.58(8)	0.0103(4)	662.42(10)♯	0.0099(5)	1031.34(10)	0.0027(2)
263.24(11)	0.0015(1)	663.98(12)♯	0.0060(4)*	1042.37(8)	0.0074(3)
275.28(8)	0.0236(6)	666.55(30)	0.0008(3)	1045.89(17)	0.0017(4)*
277.98(9)	0.0030(8)*	675.78(8)	0.0140(8)	1050.37(10)	0.0040(4)
284.32(8)	0.0202(6)	679.13(11)	0.0055(5)	1054.23(13)	0.0038(4)
287.69(8)	1.0000(129)	683.13(10)	0.0092(7)	1056.30(12)	0.0047(4)*
333.37(35)	0.0004(2)*	714.77(15)	0.0020(2)	1070.46(18)	0.0027(4)
343.80(8)	0.0270(5)*	716.78(10)	0.0049(3)	1087.12(11)	0.0058(7)*
385.84(8)	0.0071(2)*	729.86(13)	0.0019(3)	1091.49(10)	0.0060(6)
388.07(14)	0.0013(1)	738.14(8)	0.0124(4)	1162.40(15)	0.0046(4)*
400.81(8)	0.0350(7)*	746.36(7)	0.0139(5)	1170.34(24)	0.0017(3)
402.52(8)	0.0353(7)	752.37(7)	0.0050(5)*	1176.43(12)	0.0119(13)*
407.32(8)	0.0183(4)	757.17(10)	0.0049(5)	1180.27(14)	0.0028(3)*
416.50(8)	0.1361(53)*	780.92(9)	0.0035(3)	1190.57(7)	0.0175(5)
426.06(10)	0.0040(3)	787.17(72)	0.0044(13)*	1196.70(8)	0.0080(4)
439.39(9)	0.0055(3)	791.36(8)	0.0142(4)	1201.11(8)	0.0103(4)*
444.67(8)	0.0163(4)	805.20(15)	0.0037(4)	3519.06(11)	0.0052(4)*
447.54(42)	0.0004(2)	813.84(7)	0.0376(8)	3544.47(18)	0.0041(4)
480.63(9)	0.0140(6)*	831.12(10)	0.0041(4)*	3598.68(19)	0.0022(2)
501.14(9)	0.0276(14)	838.45(10)	0.0065(6)	3615.28(11)	0.0089(4)
513.78(8)	0.0543(27)*	841.55(15)	0.0027(4)	3648.64(12)	0.0058(3)
516.61(9)	0.0153(13)*	844.52(9)	0.0073(5)	3734.99(11)	0.0043(3)
522.25(7)	0.0215(5)	847.61(8)	0.0128(7)*	3859.57(15)	0.0014(1)
526.27(7)	0.0448(8)	850.25(9)	0.0147(6)	3906.50(11)	0.0036(2)
534.06(8)	0.0091(3)	862.35(14)	0.0053(6)	4087.19(14)	0.0029(2)
546.91(10)	0.0089(7)	867.60(8)	0.0140(8)*	4130.59(10)	0.0047(3)

Continued on the next page

E_γ [keV]	I_γ †	E_γ [keV]	I_γ †	E_γ [keV]	I_γ †
551.60(12)	0.0040(6)	870.98(14)	0.0047(6)*	4222.36(12)	0.0036(2)
555.89(9)	0.0185(7)	874.15(9)	0.0099(5)	4226.59(10)	0.0082(4)
558.05(9)	0.0197(8)	880.38(23)	0.0026(5)	4246.21(51)	0.0003(1)
560.16(14)	0.0063(6)	887.43(9)	0.0129(5)	4332.10(9)	0.0087(5)
564.73(8)	0.0393(11)*	889.30(8)	0.0272(6)	4382.74(12)	0.0026(2)*
566.34(8)	0.0350(10)*	893.58(10)	0.0063(4)	4589.23(16)	0.0015(1)
573.24(11)	0.0061(5)	902.91(7)	0.0202(5)	4644.39(17)	0.0014(1)
589.15(8)	0.0112(5)	913.36(8)	0.0138(5)		
600.54(10)	0.0033(5)*	918.43(14)	0.0042(3)		

† : Multiply by 7.07(12) b to calculate σ_γ (see Table 4.12),
or with 0.332(13) to calculate p_γ per neutron capture event (see Table 4.18).
* : Interferences from other peaks, see text for additional information.
♯ : Doublet of two peaks.

In Figure 4.14 the obtained data are compared with data tabulated in the ENSDF [93]. Within the stated uncertainties the values tabulated in ENSDF [93] are, generally, in agreement with the data measured in this work, as shown by the pull plots. At high energies, however, a systematic deviation from the tabulated γ-ray energies is observed, as the mean of the corresponding pull plot is -2.22 ± 0.20. On an absolute scale this corresponds to an average deviation of -1.7 keV between the γ-ray energies measured in this work compared to those in the tabulated data set. These deviations are, however, within the reported systematic uncertainty of up to 3 keV. The pull plot of the relative intensities for the lower energetic secondary γ-rays has a mean of 0.03 ± 0.10 and an RMS of 1.00 ± 0.07, whereas the higher energetic primary γ-rays scatter more with an RMS of 1.90 ± 0.33.

The ENSDF data are based on a work of Casten *et al.* [153] published in 1976. In that work, the primary and secondary prompt γ-radiation was studied at the Brookhaven Reactor using 2.66 eV neutrons, so that the primary neutron capture mechanism was resonance capture. A massive target of 288 mg Pu with a 98.26 % ^{242}Pu enrichment embedded in a sulfur matrix was used the whole target weighting 2.72 g. The spectra of primary and secondary γ-rays were obtained separately with two Ge(Li) detectors one operating in the energy range from 0 to 1.5 MeV and a second operating from 0 to 6 MeV. By using two detectors, γ-γ-coincidence data could be measured, so that individual γ-ray cascades could be determined from the capture state to the ground state. To reduce coincidence events a 1.5 mm lead absorber was introduced between sample and detector. The γ-ray energies in the lower energetic regime (secondary γ-rays) are claimed to have an uncertainty of 0.2 to 0.6 keV, whereas for higher energies an uncertainty of 1 keV and a systematic accuracy of ± 3 keV is estimated. Relative intensities are said to have uncertainties in the order of 15 %. All in all the uncertainties of both the γ-ray energies

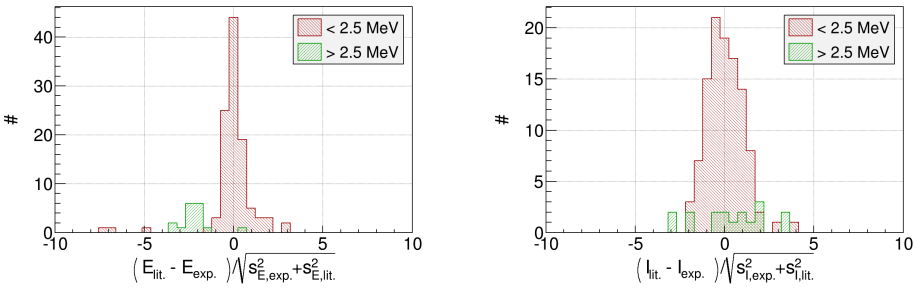

(a) (b)

Figure 4.14: Comparison of the ^{242}Pu prompt γ-ray data deduced in this work with data tabulated in ENSDF. (a) Pull plots of the energies. The lower energetic pull plot has a mean of 0.07 ± 0.12 and an RMS of 1.28 ± 0.09 and the higher energetic one has a mean of -2.22 ± 0.20 and an RMS of 0.83 ± 0.14. (b) Pull plots of the relative intensities. The lower energetic pull plot has a mean of 0.03 ± 0.10 and an RMS of 1.00 ± 0.07 and the higher energetic one has a mean of 0.38 ± 0.46 and an RMS of 1.90 ± 0.33.

and the relative intensities determined in this thesis have a much lower uncertainty.

Normalization

The thermal partial radiative neutron capture cross sections were calculated for the most intense prompt γ-line of ^{242}Pu according to the procedure described in section 4.1.1 for ^{237}Np.

Both the decay spectra taken at the BRR measurement facility with the LEGe and the coaxial HPGe detectors were used to determine the neutron flux, employing equation 2.75. From the LEGe measurement a thermal equivalent neutron flux of $\Phi_0 = 8.08(10) \cdot 10^7\,\mathrm{cm}^{-2}\,\mathrm{s}^{-1}$ and from the HPGe measurement one of $\Phi_0 = 8.07(9) \cdot 10^7\,\mathrm{cm}^{-2}\,\mathrm{s}^{-1}$ were determined with very good agreement. To cross check Φ_0 was also determined from the 411.8 keV peak in the PGAA measurement and from several strong prompt γ-ray peaks of the ^{197}Au neutron capture using the EGAF-tabulated partial cross section values [2, 3, 154]. The resulting values of Φ_0 were all in agreement with the values obtained with the decay measurements. For the further analysis the thermal equivalent neutron flux was defined as the weighted average of all the obtained Φ_0 values, as $\Phi_0 = 8.08(9) \cdot 10^7\,\mathrm{cm}^{-2}\,\mathrm{s}^{-1}$. Using equation 2.76 the partial capture cross section of the 287.69(8) keV was determined as 7.05 ± 0.12 b, using the reaction rate correction η_1 calculated with the ENDF database. The uncertainty of 1.7 % is dominated by a 1 % uncertainty of the fitted peak area, a 1.2 % uncertainty of Φ_0 and 1 % uncertainty of the efficiency. The photon absorption and reaction rate correction factors contribute only

about 0.1 % each.

For the FRM II measurements the thermal equivalent neutron flux was determined in the same way as for the BRR measurements. As at the BRR the values obtained from the decay counting are much more precise than the values from the PGAA measurement. For sample 3 a thermal equivalent neutron flux of $\Phi_0 = 9.09(24) \cdot 10^8\,\mathrm{cm^{-2}\,s^{-1}}$ was determined from the 411.8 keV decay γ-ray line of ^{198}Au. The weighted average of all values $\Phi_0 = 9.17(24) \cdot 10^8\,\mathrm{cm^{-2}\,s^{-1}}$ was used for further calculations. The partial radiative capture cross section of the prompt γ-ray line at 287.69(8) keV was calculated as 6.87(19) b. For sample 10, where the neutron beam was fully opened, the average neutron flux was determined accordingly as $\Phi_0 = 1.42(2) \cdot 10^9\,\mathrm{cm^{-2}\,s^{-1}}$. This results in a partial radiative capture cross section of 7.09 ± 0.14 b.
Although all three values are in good agreement with each other, the value derived from the measurement of sample 3 at FRM II was somewhat lower than those values obtained from the measurements of samples 10 at FRM II and 3 at BRR. This implies that the self-made collimator might have cut off a small part of the divergent beam, resulting in a slightly inhomogeneous irradiation of the sample. For this reason, and as the measurement of sample 10 at the FRM II is practically uncorrelated with the measurement of sample 3 at BRR, because the neutron beam, the detector system and the sample differ, the sample 3 measurement at FRM II was omitted for the weighted average which was then used to normalize the relative intensities to the partial cross sections in Table 4.11.

The determined partial cross section values calculated with different reaction rate correction factors η_1 and the weighted averages are tabulated in Table 4.12. The weighted average of 7.07 ± 0.12 b is in fair agreement with the value of 7.67(31) b published in [92], which was obtained with the samples of the second generation prepared according to the procedure described in section 3.3.3.

Table 4.12: Partial radiative neutron capture cross sections of ^{242}Pu measured for the most intense line at 287.69(8) keV at the BRR ($^{\mathrm{b}}$) and FRM II ($^{\mathrm{f}}$) PGAA facilities. Different reaction rate correction factors η_1 from Table 3.6 were applied. The weighted average of the uncorrelated measurements ($\bar{\sigma_\gamma}$) of 3^{b} and 10^{f} is given.

Sample No.	σ_γ [b] η_1 (ENDF)	η_1 (JEFF)	η_1 ($1/\sqrt{E_\mathrm{n}}$)
3^{b}	7.05(12)	7.07(12)	7.03(12)
3^{f}	6.87(19)	6.88(19)	6.84(19)
10^{f}	7.10(14)	7.11(14)	7.06(14)
$\bar{\sigma_\gamma}$	7.07(12)	7.08(12)	7.05(12)

4.3.2 ^{243}Pu Decay Radiation and Half-Life

Based on the LEGe measurement directly following the irradiation where the pellet instead of the gold foil was facing the detector, the relative intensities of the decay γ-rays of ^{243}Pu were determined. A comparison of the observed lines with the data tabulated in ENSDF can be found in Table 4.13. The peaks are all very well fitted without overlapping peaks with the exception of the 25.62(11) keV peak, which is in the tail of the intense ^{241}Am decay peak at 26.34(6) keV (the tabulated value of this peaks energy is 26.344 60(24) keV [82, 86]) and the fitting of this relatively small peak might thus be unreliable. The energy calibration was made using the pre-determined non-linearity function of the LEGe detector, and the ^{241}Am decay γ-ray peak at 59.54 keV as well as the ^{198}Au decay γ-ray peak at 411.80 keV for the normalization of the calibration. The measured γ-ray energies have a much smaller uncertainty than the tabulated values. The relative intensities have similar uncertainties. The values are generally in agreement.

In the tabulation only an approximate normalization of $p_\gamma \approx 0.23$ per decay event is given for the 84.14(5) keV γ-ray. Based on the determined thermal equivalent neutron flux and a half-life value for the decay of 4.956(3) h [93] for ^{243}Pu the partial radiative capture cross section of this line was determined. From the LEGe measurement of sample 3 it was deduced as $\sigma_\gamma = 3.11(6)$ b and from the HPGe measurement as $\sigma_\gamma = 3.60(11)$ b. From the decay measurement of sample 3 at FRM II a value of $\sigma_\gamma = 3.36(11)$ b was obtained and a value of $\sigma_\gamma = 3.51(11)$ b of the decay measurement of sample 10. The differences are quite high, especially given that the direct decay measurement with the LEGe and later with the HPGe of sample 3 at the BRR. This is especially interesting as the deduced neutron fluxes are in very good agreement. A half-life of ^{243}Pu higher than the one tabulated, however, might account for that phenomenon.

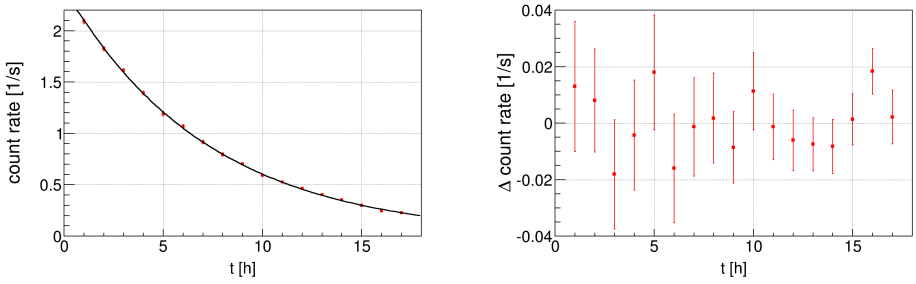

(a) (b)

Figure 4.15: Fit of an exponential function to the measured count rates of the 84.14(5) keV γ-ray peak. (a) The fit results and (b) the corresponding residuals.

From the 17 one-hour measurements taken with the gold foil facing the detector, the

Table 4.13: Measured γ-rays of ^{243}Pu β^--decay to ^{243}Am and corresponding data taken from ENSDF [93] for comparison.

E_γ [keV]	I_γ	$E_{\gamma,\text{Lit.}}$ [keV]	$I_{\gamma,\text{Lit.}}$
25.62(11)	0.0060(31)	(25.2(3))†	($\approx$0.003)†
35.04(9)	0.0024(9)	$\approx$34	>0.003
41.87(5)	0.0423(21)	41.8(2)	0.0365(30)‡
67.03(5)	0.0131(7)	67(1)	0.010(5)
84.14(5)*	1.0000(112)	84.0(2)	1.0
109.39(5)	0.0069(5)	109.2(2)	0.0070(7)
356.51(5)	0.0064(10)	356.4(2)	0.0058(3)
381.80(5)	0.0288(20)	381.6(2)	0.025(1)

† : γ-ray not observed, but from level balance calculation.
‡ : Intensities combined from two tabulated adjacent peaks, unresolvable in this measurement.
* : Weighted average of decay measurements with HPGe13 (84.11(7) keV) and LEGe (84.16(5) keV) in the "DÖME" chamber at the BRR site. PGAA measurements: 84.12(8) keV (BRR) and 84.21(11) keV (FRM II).

half-life of ^{243}Pu β^--decay to ^{243}Am was obtained. A least-squares fit of an exponential function of the form $A \cdot \exp(-\lambda \cdot x)$ to the count rates measured for the 84.14(5) keV peak was performed. The result is shown in Figure 4.15. The fit is very good with a reduced χ^2 of only 0.74. The residuals shown in Figure 4.15(b) show no systematic deviations. The resulting half-life of ^{243}Pu is 4.996(35) h which is higher than but still in fair agreement with the ENSDF-tabulated value of 4.956(3) h. The tabulated value is based on two measurements [155, 156]. The value obtained in this work is in excellent agreement with one of these measurements, which yielded a value of 4.98(2) h [155]. Using the measured half-life for further calculations changes the partial cross section values to $\sigma_\gamma = 3.08(7)$ b in the case of the LEGe measurement and to $\sigma_\gamma = 3.47(15)$ b in the case of the HPGe measurement.

4.3.3 Neutron Separation Energy

Due to the ^{242}Pu nucleus having a spin of $I_{^{242}\text{Pu}} = 0$ the capture state has a spin of $J_{\text{c.s.}} = 1/2^+$. The ground state of ^{243}Pu has $J_{\text{g.s.}} = 7/2^+$. A direct ground state transition would, thus, be at least an $M3$ transition. The latter is unlikely to occur, as the capture state can de-excite through other levels with $E1$ and $M1$ transitions. No indication of such an $M3$ transition was observed in the measurements.

The transition energies in a single γ-ray cascade add up to the neutron separation energy (see equation 2.40). Thus, in order to determine the neutron separation energy a least-squares fit of the measured γ-ray energies, corrected for the nuclear recoil, was performed using gtol [157]. The resulting neutron separation energy was found to be $S_n = 5036.33(59)$ keV, where the fitted uncertainty of 0.07 keV was multiplied by the reduced χ^2 of the fit to estimate an unbiased uncertainty. The calculated S_n is in good agreement with the value of 5034.2(26) keV tabulated in ENSDF [93], within the high uncertainty of the tabulated value.
The calculated value of S_n is higher by 2.14 keV than the tabulated value, which was deduced using the measurement by Casten *et al.* [153] having the above mentioned γ-ray energy deviations at high energies.

4.3.4 Nuclear Structure Calculations

Using nuclear structure Monte-Carlo simulations the thermal radiative neutron capture cross section of ^{242}Pu can be obtained directly from the measured partial capture cross sections of the prompt γ-radiation. Such simulations also indicate whether new prompt γ-rays could be assigned to known levels of the nucleus. Nuclear structure simulations of ^{243}Pu will be described in the following. For these simulations the DICEBOX statistical decay simulation code [59] was used (see section 2.8.2). In each simulation run 100 separate realizations of the level scheme were created in order to minimize biasing of the results from singular realizations. The differences between the realizations are reflected in the uncertainty given in the DICEBOX output. In each realizations 200 000 decay γ-ray cascades from the capture state were simulated to yield optimal statistical variation in the simulated level populations.

4.3.4.1 PSF and LD Models

As different models all show agreement with current measurements, by choosing combinations of different models provided by DICEBOX the impact of the models on the resulting capture cross section was studied. The parameters for the ^{243}Pu level density (LD) and photon strength function (PSF) models were taken from the Reference Input Parameter Library (RIPL) [158, 159]. As no parameterization of the ^{243}Pu giant dipole electric resonance (GDER) and giant quadrupole electric resonance (GQER) are provided, the ones given for the neighboring nuclide ^{239}Pu were assumed. As ^{239}Pu has the same mass number and also an odd nucleon number the parameterization is expected to be very similar for ^{243}Pu [158, 159]. The PSF models used according to the RIPL parameterization are plotted in Figure 4.16 together with measured photo-absorption cross sections taken from [160] and converted by equation 2.42. The experimental data is reproduced well by both models in the low energetic regime, which is important to this work. This assumption is supported by measurements on other actinides such as ^{237}Np or ^{238}U based on which

similar parameterizations were derived [158, 159].

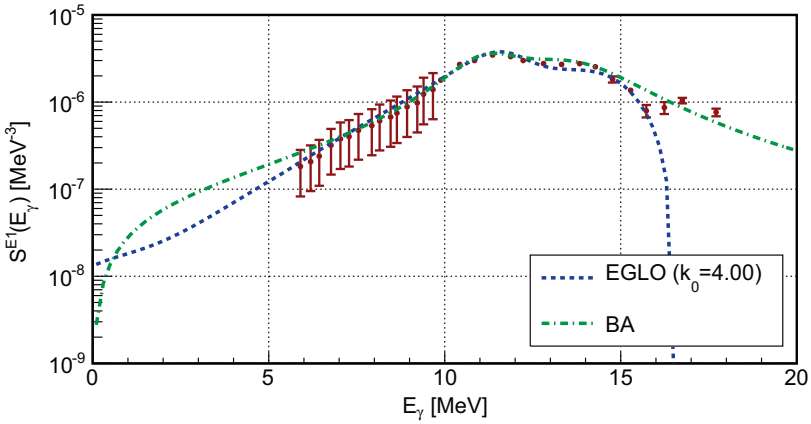

Figure 4.16: The PSF models used in this work (color-coded lines) based on the RIPL parameterization compared to experimental data reported in reference [160].

The GDER parameters are based on measurements, whereas the parameters of the GQER stem from a theoretical parametrization. For the giant dipole magnetic resonance (GDMR) a single particle strength of $1 \cdot 10^{-8}$ was assumed, but adjusting this value by an order of magnitude in both directions did not significantly alter the resulting capture cross sections. In addition, a model based on the recent parameterization of the GDMR of ^{239}U [48], which has an even mass number and an odd nucleon number like ^{243}Pu, was used for comparison. This parameterization was derived from measurements. The much weaker contribution due to $E2$ transitions is modeled according to the theoretical isoscalar-isovector model of the GQER. The parameters used for the level density models are listed in Table 4.14, while the resonance parameters are listed in Table 4.15. In addition, the parities of the levels are modeled based on a Fermi-Dirac distribution according to the semi-empirical nuclear mass model (see section 2.2.1).

Table 4.14: Level density parameters and pairing energy Π used in the DICEBOX calculations. The notation of the listed parameters is in accordance with the parameters given in equation 2.21 for the BSFG LD and in equation 2.25 for the CTF LD models. See sections 2.2.1 and 2.2.2 for details on these parameters.

θ [MeV]	E_0 [MeV]	E_1 [MeV]	a [MeV^{-1}]	Π [MeV]
0.41	−0.74	−0.19	27.2	0

Table 4.15: Parameters of the GDER, GDMR and GQER used in the DICEBOX simulations of ^{243}Pu. The GDER parameterization from the RIPL files [158, 159] of the closest even-odd nucleus ^{239}Pu, for which measured data exist was used. GDMR parameters for ^{239}U are used [48]. The GQER is described by a single Lorentzian and derived from a theoretical parametrization. The notation of the listed parameters is in accordance with the parameters given in equation 2.43 for the BA PSF and equation 2.44 for the EGLO PSF with $k_0 = 4.0$. See section 2.4.5 for details on these parameters.

Resonance	$E_{GR,1}$ [MeV]	$\Gamma_{GR,1}$ [MeV]	$\sigma_{GR,1}$ [mb]	$E_{GR,2}$ [MeV]	$\Gamma_{GR,2}$ [MeV]	$\sigma_{GR,2}$ [mb]
GDER	11.28	2.48	325.0	13.73	4.25	384.0
GDMR	2.00	0.30	0.80	2.80	0.30	1.20
GQER	10.10	3.19	6.78	-	-	-

4.3.4.2 The Level Scheme of ^{243}Pu

For ^{243}Pu the critical energy $E_{\text{crit.}}$ up to which the level scheme is assumed to be complete, was established as 450 keV, because above this value several levels without assigned de-excitation γ-rays exist even though they are likely to be de-excited to lower energetic existing levels due to their spin and parity. Levels and assigned γ-rays were adopted from the ENSDF [93] database, where the level energies were determined from a least-squares fit of the level energies to the measured transition energies, as described above. There are 13 known levels below $E_{\text{crit.}}$ according to ENSDF. 11 measured secondary prompt γ-rays corresponding to transitions between levels below $E_{\text{crit.}}$ and the 16 measured primary prompt γ-rays (de-exciting the capture state) were included within this level scheme. Three measured γ-rays newly identified in this work were assigned to levels based on the energy differences between the levels and on the multipolarities of the transitions. The lowest possible multipolarities allowed by the angular momentum selection rules were chosen (equation 2.37), as such transitions are the most likely (see section 2.4.3). In principle, only measured γ-ray transitions were used. These newly assigned prompt γ-rays were already listed in Table 4.11.
Three levels below $E_{\text{crit.}}$ reported in ENSDF with high spins ($13/2^+$, $15/2^+$ and $17/2^+$) have no observed de-excitation γ-rays, however, these would not be expected taking the capture state spin of $J^P = 1/2^+$ into account. As expected these levels did not influence the DICEBOX simulation results as the simulated populations of these levels were negligible.
Tentative multipolarity and J^P assignments reported in ENSDF were confirmed with the simulations carried out in this work. As some levels were not depopulated completely six weak but likely transitions were postulated. The transitions' intensities were assumed based on the level balance (the ratio of measured population to measured depopulation). Missing depopulation intensity was assumed to be caused by the postulated transitions. This intensity was increased if indicated by the simulation results, independent of the underlying models.

The conversion coefficients corresponding to the transitions were calculated with the BRICC code [41, 161]. The fully built-up level scheme is presented in the appendix in ENSDF format, see section B. Improvements made to the original levels adopted from ENSDF aside from the level energies will be given in the following in order of the levels starting from the ground state.

A ground state transition was assigned to the level at 58.28(8) keV, as the level was populated under emission of measured γ-rays but not depopulated. The postulated $M1$ transition of energy 58.28 keV is predicted to have a relative intensity of 0.0059, as it exhibits high internal conversion. Thus, it would produce a small peak in the spectrum, which, however, is not observed due to the strong background in that region created particularly by the ^{241}Am decay peak at 59.54 keV.
The measured 125.47(71) keV γ-ray was assigned to the level at 124.65(10) keV corresponding to an $E2$ transition to the ground state. In addition, the more likely $M1$ transition to the level at 58.28(8) keV is postulated, which would have a relative intensity of 0.000 31. Again, this would only create a small peak in the spectrum and might thus not be observable, as the decay of ^{243}Pu produces a relatively strong peak at 67.03(5) keV.
A 45.87 keV $M1$ transition was postulated for the level at 333.43(7) keV. The corresponding prompt γ-ray would de-excite this level to the level at 287.56(6) keV. This prompt γ-ray was predicted to have a relative intensity of 0.0019. It was not observed, as it would be right below the cut-off energy of the PGAA measurement taken at the FRM II and slightly above this energy in the measurement at BRR.
The measured 96.06(11) keV γ-ray was assigned to the level at 383.64(7) keV as an $M1$ transition. This $J^P = 1/2^+$ level is not depopulated in the ENSDF, but the placement of the γ-ray shows very good consistency with the nuclear model simulations.
An $M1$ transition with an energy of 54.48 keV and an relative intensity of 0.000 45 was postulated for the level at 387.95(11) keV. This transition would also result in a very small peak in a region dominated by background, especially due to ^{241}Am decay.
For the level at 392.32(7) keV an 8.66 keV $M1$ transition was postulated with a relative intensity of 0.0007. The corresponding γ-ray would be clearly below the detection threshold of common HPGe detectors and undergoes strong internal conversion. However, its inclusion is crucial for the level balances of both the 392.32(7) keV and the 387.95(11) keV levels.
The weakest of the three de-excitation γ-rays of the level at 402.57(8) keV with 344.5 keV was not observed in the PGAA measurements in this work, as it is too close to the strong prompt γ-ray peak at 343.80(8) keV. Based on the ENSDF branching ratio a relative intensity of 0.0006 was calculated.
The level at 447.57(8) keV has no de-excitation γ-rays assigned to it in ENSDF. The measured 447.57(42) keV γ-ray was assigned to this level as an $M1$ transition to the ground state. Additionally, a 54.82 keV $M1$ transition to the level at 392.32(7) keV was postulated with a predicted relative intensity of 0.0092.
All results obtained are thus primarily based on directly measured data on prompt γ-ray partial radiative capture cross sections. This includes the 287.69(8) keV prompt γ-ray,

which has the highest measured partial capture cross section of all the measured prompt γ-rays of the ^{242}Pu(n, γ)^{243}Pu reaction. This prompt γ-ray corresponds to an $M1$ transition from the level at 287.56(6) keV to the ground state.

4.3.4.3 Thermal Neutron Capture Cross Section of ^{242}Pu

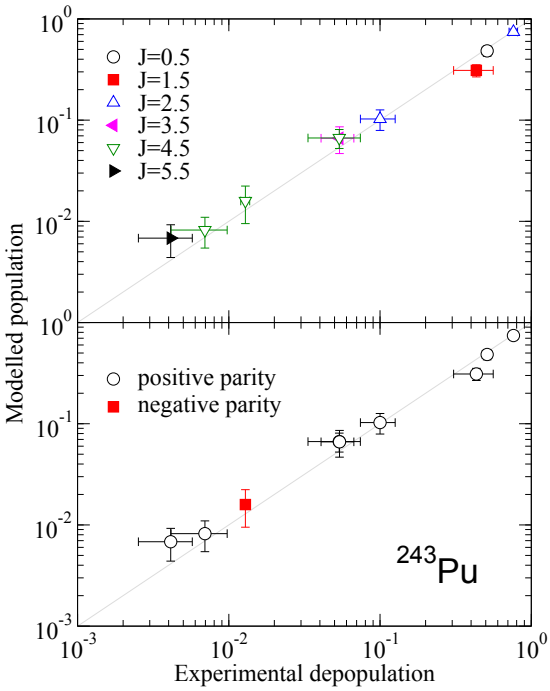

Figure 4.17: DICEBOX simulated population (P_i^{sim}) against experimentally determined depopulation (P_i^{exp}) of levels in ^{243}Pu using the BSFG level density model, an EGLO PSF and a single particle strength of $1 \cdot 10^{-8}$ for the $M1$ PSF. The same plot is shown twice in this figure, in the top one the levels are color-coded to visualize the spins whereas in the lower one the levels parities are visualized by the color-code.

The agreement between the chosen models and the measured partial capture cross section data can be studied in population-depopulation level balance plots, in which the simulated population of the levels is plotted against the measured depopulation (see section 2.8.2 for details). Perfect agreement between model and measurement is given, if all levels are populated and depopulated equally (that means no γ-ray cascade ends in a level above the ground state). In Figure 4.17 the population-depopulation plot is shown

resulting from a simulation using the enhanced generalized Lorentzian (EGLO) $E1$ photon strength function (PSF) and the Backshifted Fermi-gas (BSFG) level density (LD) together with a $1 \cdot 10^{-8}$ single particle strength for the $M1$ PSF. This choice corresponds to the best agreement between simulated population and measured depopulation. No deviation of the simulated level population from the experimental depopulation by more than one standard deviation is observed, as demonstrated by the corresponding plot of the pulls (residuals divided by the corresponding uncertainty, see Equation 4.1) in Figure 4.18. However, other model combinations did mostly influence the weaker populated high spin levels ($J = 9/2$ and $J = 11/2$) and thus the general appearance of the population-depopulation plots was not affected much, nor did the corresponding simulations yield a significantly different result for the thermal radiative neutron capture cross section. The thermal neutron capture cross section values resulting from the investigated model combinations are tabulated in Table 4.16 and the corresponding simulated total radiative widths are tabulated in Table 4.17. All corresponding population-depopulation plots can be found in the appendix C.

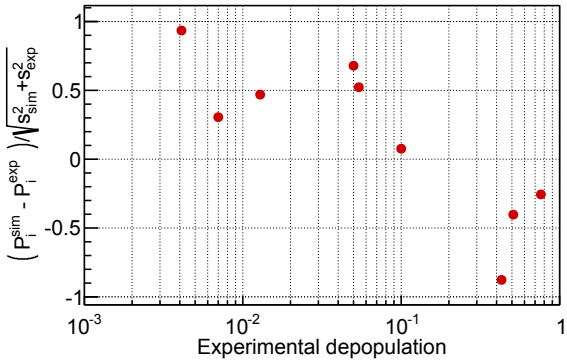

Figure 4.18: Pulls of the simulated population ($P_i^{\mathrm{sim}} \pm s_{\mathrm{sim}}$) with experimentally determined depopulation ($P_i^{\mathrm{exp}} \pm s_{\mathrm{exp}}$) of levels i in ^{243}Pu using the BSFG level density model, an EGLO PSF and a single particle strength of $1 \cdot 10^{-8}$ for the $M1$ PSF. A "1" (or "-1") on the y-axis corresponds to a difference of one standard deviation between P_i^{sim} and P_i^{exp}. This plot corresponds to the population-depopulation plot shown in Figure 4.17.

All the results are in very good statistical agreement, although the use of the alternative parameterization of the GDMR resonance yielded systematically higher values. So the average of 22.40 ± 1.46 b is relatively independent of the particular theoretical models employed for the PSF and the level density. As the model combinations are correlated, however, a choice was made based on the agreement of the combinations with measured data. From the simulated total radiative widths in Table 4.17 it can be seen that the combinations of a Brink-Axel model (BA) PSF with a constant temperature formula (CTF)

Table 4.16: Resulting σ_c^0 values for different combinations of PSF and LD models in DICEBOX, with a single-particle strength model (SPS) of the GDMR and alternativly a GDMR model adopted from a recent publication (Scissors). The weighted averages are given together with the smallest of the associated uncertainties and a total average over all models is given.

	SPS		Scissors	
	CTF	BSFG	CTF	BSFG
BA	21.78(153)	21.99(153)	23.41(223)	23.48(223)
EGLO	21.85(160)	21.92(146)	23.26(188)	22.42(202)
Average	21.89(146)		23.32(188)	
Total Av.	22.40(146)			

Table 4.17: The simulated total radiative widths to be compared with a tabulated value of 22(1) meV [39]. All radiative width values are given in units of mb.

	SPS		Scissors	
	CTF	BSFG	CTF	BSFG
BA	28(1)	53(2)	27(1)	52(2)
EGLO	15(1)	28(1)	14(1)	28(1)

LD model ($\Sigma_0 = 28(1)$ meV) and a EGLO PSF with a BSFG LD model ($\Sigma_0 = 28(1)$ meV) reproduce the adopted value of $\Sigma_0 = 22(1)$ meV best, regardless of the chosen GDMR model. However, as from these combinations only the EGLO PSF ($k_0 = 4.0$) and a BSFG LD model together with a single-particle strength of $1 \cdot 10^{-8}$ show a perfect agreement between the simulated level population and the measured level depopulation, this combination was selected, yielding a thermal neutron capture cross section of 21.92 ± 1.46 b for the ^{242}Pu(n, γ)^{243}Pu reaction.

In Figure 4.19 a comparison of this result with data from other experiments [162, 163, 164, 165, 166] is shown, including the current evaluated thermal neutron capture cross section of 21.28 ± 0.77 b adopted in ENDF. The thermal radiative neutron capture cross section obtained in this work is in very good agreement with the ENDF value.
The obtained result also agrees very well with the most recent measurement of 22.5 ± 1.1 b reported by Marie *et al.* [166]. To obtain this result Marie *et al.* used a sample of only 10.5 µg ^{242}Pu. This sample was irradiated and after the produced ^{243}Pu had completely decayed the α-activity of its decay product ^{243}Am was measured. The resulting cross section has an uncertainty of similar magnitude as the one calculated in this thesis.
The 16 % difference between the cross section values determined in this work and those determined in the three older works with very low uncertainties and results close to 18.5 b might be explained by absorption effects. Neutron absorption causes an inhomogeneous

irradiation, so that the inner parts of the samples get irradiated less. Marie *et al.* argue that the difference can be explained by less well characterized neutron beams and the divergence from $1/\sqrt{E_n}$ of the capture cross section of ^{242}Pu at thermal energies.

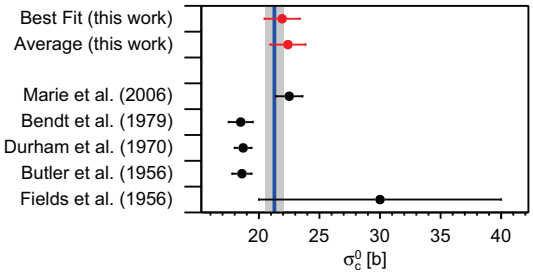

Figure 4.19: Thermal radiative neutron capture cross sections of ^{242}Pu, as calculated from the measurements described in this work along with values taken from literature [162, 163, 164, 165, 166]. The average value of all simulated model combinations is given together with the value from the model combination that best fitted the measured data. The ENDF/B-VII.1 evaluated value is indicated by the blue line and its uncertainty by the gray area.

Based on the obtained thermal capture cross section the emission probability per neutron capture event $p_\gamma = \sigma_\gamma/\sigma_c^0$ was calculated for the most intense prompt γ-ray of ^{242}Pu. This value was than used to normalize the relative intensities listed in Table 4.11. The values calculated from the measurement of sample 3 at BRR and of sample 10 at FRM II are listed in Table 4.18. The average value is $p_\gamma = 0.322(20)$ per neutron capture event, which is significantly lower than the value of 0.41(7) reported by Casten *et al.* [153]. Similarly, the intensity per beta decay event of ^{243}Pu was calculated. The resulting values of p_γ are listed in Table 4.19. In ENSDF only an approximate value of $p_\gamma \approx 0.23$ is tabulated, which is significantly lower than the value determined in this work. The differences between the p_γ values found in this work and the tabulated data are probably a result of the lower thermal neutron capture cross section assumed in the older works. The values obtained in this work, however, exhibit significantly decreased uncertainties.

Table 4.18: Emission probability per neutron capture p_γ for the most intense line at 287.69(8) keV of ^{242}Pu measured at the BRR ([b]) and FRM II ([f]) PGAA facilities. Calculations were performed using the evaluated capture cross section of 21.28(77) b tabulated in ENDF and the average and selected value determined with DICEBOX based on the PGAA measurements carried out in this work together with the partial capture cross section determined using a reaction rate correction with ENDF data.

Sample No.	p_γ (ENDF)	p_γ (Average DICEBOX)	p_γ (Best Fit DICEBOX)
3[b]	0.332(13)	0.315(21)	0.322(22)
10[f]	0.333(14)	0.317(22)	0.324(22)
$\bar{p_\gamma}$	0.332(13)	0.316(21)	0.322(22)

Table 4.19: Emission probability per β-decay event of ^{243}Pu for the 84.14(5) keV line measured at the BRR ([b]) and FRM II ([f]) PGAA-facilities with LEGe ([l]) and coaxial HPGe ([h]) detectors. Calculations were performed using the evaluated capture cross section of 21.28(77) b tabulated in ENDF and the average and selected value determined with DICEBOX based on the PGAA measurements carried out in this work together with the partial capture cross section determined using a reaction rate correction with ENDF data.

Sample No.	p_γ (ENDF)	p_γ (Average DICEBOX)	p_γ (Best Fit DICEBOX)
3[b,l]	0.146(6)	0.139(9)	0.142(10)
3[b,h]	0.169(8)	0.161(12)	0.164(12)
10[f,h]	0.165(8)	0.157(11)	0.160(12)
$\bar{p_\gamma}$	0.157(6)	0.146(9)	0.154(10)

4.4 Detection Limits

Up to this point the basic nuclear data have been obtained which are required in PGAA for the identification and quantification of ^{237}Np, ^{241}Am, and ^{242}Pu in a given matrix. This section will take one step back and focus on the applicability of PGAA for qualification and quantification of the investigated actinides, by calculating general limits of detection for the investigated actinides. This will give a sense of the minimum quantities of these actinides that could, in principle, be detected using PGAA at the BRR and FRM II facilities.

The minimum quantity of a nuclide that can be detected inside a given matrix depends on several parameters, the central of these being the γ-ray energies, as they define the

penetrability of the radiation in the material and the location of the corresponding peak in a measured spectrum (e.g. the background of the measurement). For quantification the corresponding partial neutron capture cross sections, which define the probability with which the γ-rays are emitted when the nuclei are exposed to a neutron beam are crucial. Both of these parameters have been investigated in this thesis. A further factor strongly influencing the detection limits is the assay used for detection. The parameters relevant for the detection limits are the detector efficiency and the provided neutron flux. A higher neutron flux, a higher detector efficiency or a longer measuring time will, generally, decrease the detection limits, so that smaller quantities of a nuclide can be detected. For the measurement time a compromise has to be found between long measurement times favorable because more counts can be collected within a γ-ray peak in a spectrum and times short enough to be practical for routine measurements.

Considering that, the detection limits usually have to be calculated for a given facility and matrix in which the investigated nuclide is embedded, i.e. for any future assay for the characterization of actinide residues in complex matrices using PGAA this limit has to be calculated separately. As the development of such an assay is beyond the scope of this work, a more general detection limit will be discussed here, to get a sense of the potential of PGAA for the identification and quantification at the PGAA facilities used in the work. The absolute detection limit (DL) given in units of g can be defined as

$$\mathrm{DL} = \frac{P_{A,\min} M}{N_A \sigma_\gamma \Phi_0 \epsilon(E_\gamma) t_m}, \tag{4.2}$$

with the Avogadro constant $N_A \approx 6.022 \cdot 10^{23}\,\mathrm{mol}^{-1}$, the measurement time t_m, the average thermal equivalent neutron flux Φ_0, the detector efficiency $\epsilon(E_\gamma)$ and the partial radiative neutron capture cross section σ_γ of a prompt γ-ray of energy E_γ of the nuclide investigated with molar mass M [2]. $P_{A,\min}$ is the minimal detectable peak area. This quantity depends on the given background and thus on the matrix in which a containing nuclide is to be detected. If the background radiation (e.g. produced by the activation of the matrix components) causes no interfering peaks, 100 counts usually suffice to identify a peak and to give a rough quantification. In the higher energetic regime which typically has a low background 10 counts can already suffice to identify a peak. These estimates are taken from the Handbook of Prompt Gamma Activation Analysis [2] and seem very reasonable in view of the blank measurements performed in this work.
For practical reasons a measurement time of $t_m = 10\,000\,\mathrm{s} \approx 3\,\mathrm{h}$ is assumed for this discussion. Based on the measurements performed in this thesis, thermal equivalent neutron fluxes of $1 \cdot 10^8\,\mathrm{cm}^{-2}\,\mathrm{s}^{-1}$ at the BRR PGAA facility, of $1.5 \cdot 10^9\,\mathrm{cm}^{-2}\,\mathrm{s}^{-1}$ at the FRM II PGAA facility and of $2.5 \cdot 10^{10}\,\mathrm{cm}^{-2}\,\mathrm{s}^{-1}$ at the FRM II PGAA facility using the elliptical beam extension can realistically be deemed achievable.

Based on these assumptions detection limits were calculated for the most intense lines

of the investigated actinides and additionally for the most intense primary γ-rays. The latter might be of interest when determining the actinide contents in dense matrices, as these prompt γ-rays have high energies and hence high penetration power. The results are listed in Table 4.20.
At the investigated PGAA facilities the size of samples that can be probed are limited by the dimensions of the sample chambers and neutron beam profiles. Thus, the given detection limits apply for the characterization of actinide residues in small samples (e.g. IAEA swipe samples or scratch samples from dismantling activities).

For comparison, the absolute limits for clearance according to Strahlenschutzverordnung Anlage III [167] are 1 kBq of ^{237}Np, 10 kBq of ^{241}Am and 10 kBq of ^{242}Pu corresponding to 38 µg of ^{237}Np, 0.08 µg of ^{241}Am and 69 µg of ^{242}Pu. The detection limits for ^{237}Np and ^{242}Pu are thus both almost an order of magnitude lower than the limits for clearance, even with the lower flux at the BRR PGAA facility. For the determination of ^{241}Am content at the clearance level PGAA proves rather limited, as the detection limit is only below the clearance level with the maximum neutron flux at FRM II. This could, however, to some extent, be compensated by a longer measurement time.

Concluding, the calculated detection limits show that PGAA has a great potential to be utilized for the non-destructive identification and quantification of actinide residues in complex matrices.

Table 4.20: Detection limits for ^{237}Np, ^{241}Am and ^{242}Pu derived for the PGAA facilities at BRR and FRM II. Calculated according to equation 4.2 with $t_m = 10\,000$ s and assumed values of $\Phi_0 = 1 \cdot 10^8\,\mathrm{cm^{-2}\,s^{-1}}$ (BRR), $\Phi_0 = 1.5 \cdot 10^9\,\mathrm{cm^{-2}\,s^{-1}}$ (FRM II) and $\Phi_0 = 2.5 \cdot 10^{10}\,\mathrm{cm^{-2}\,s^{-1}}$ (FRM II with elliptical beam extension marked by * in the last column). The calculations are performed using the measured detector efficiencies for the γ-ray lines of energies E_γ and partial capture cross sections σ_γ.

Isotope	E_γ [keV]	σ_γ [b]	DL [µg]		
			BRR	FRM II	FRM II*
^{237}Np	182.82(10)	22.06(39)	1.8	0.93	0.056
	5352.04(14)	0.538(15)	92.8	23.0	1.4
^{241}Am	154.72(7)	72.80(252)	0.53	0.28	0.017
	5174.59(21)	1.14(10)	42.8	10.7	0.64
^{242}Pu	287.69(8)	7.07(12)	7.3	3.38	0.20
	4332.10(9)	0.0615(37)	637.5	167.1	10.0

CHAPTER V

Conclusion

In this thesis the potential of Prompt Gamma Neutron Activation Analysis (PGAA) for non-destructive analysis of actinides, such as ^{237}Np, ^{241}Am and ^{242}Pu was investigated. For this purpose the fundamental nuclear data necessary for identification and quantification (namely prompt γ-ray energies and partial neutron capture cross sections) of ^{237}Np, ^{241}Am and ^{242}Pu via PGAA were studied.

A sample design was developed encasing actinide containing samples between 0.2 mm thick Suprasil® quartz glass sheets. Oxidic actinide powder was pressed into pellets of mg masses and placed into a sandwich of three of these quartz sheets, the middle one of them having a suitable hole in the center. Another sample type was prepared by drying µl-droplets of solutions with actinide content on the surface of one glass sheet and covering it with another glass sheet. In order to measure the neutron flux during irradiation samples containing a 3 µm thick gold foil on top of the actinide pellets/droplets were prepared. All samples were packed inside bags of 0.025 mm thick FEP foil. This quartz glass casing allows a safe handling during the measurements, offers a means of optically checking for the samples integrity and provides a well-defined geometry during the measurement. The well-defined geometry allows for an accurate calculation of corrections for the neutron and photon self-absorption effects within the samples. These corrections were calculated via Monte-Carlo simulations with MCNP5 and Geant4 representations of the measurement setups. It was demonstrated that the effect of neutron absorption, causing a non-homogeneous distribution of photon sources within the sample, creates a small energy dependent systematic shift of the photon absorption correction compared to direct calculations assuming a homogeneous source distribution. This effect however is insignificant for photon energies above 400 keV. During irradiation the Suprasil® creates well-defined background prompt γ-rays, which can easily be identified and also used for the energy calibration of the detector.

In this work 152 prompt γ-rays of $^{237}\mathrm{Np}(\mathrm{n},\gamma)^{238}\mathrm{Np}$ were consistently measured in two separate experiments using external cold neutron beams at BRR and FRM II. 125 of these prompt γ-rays were consistently observed in the irradiation of another sample at BRR. 65 of the identified prompt γ-rays have an energy exceeding 2.5 MeV and are most likely primary prompt γ-rays. The irradiation of 36.80(28) µg ^{241}Am at the cold neutron beam at FRM II yielded 19 prompt γ-rays of $^{241}\mathrm{Am}(\mathrm{n},\gamma)^{242}\mathrm{Am}$. These include 7 primary prompt γ-rays with energy > 2.5 MeV. In two PGAA measurements using the guided cold neutron beams at BRR and FRM II 127 prompt γ-rays of $^{242}\mathrm{Pu}(\mathrm{n},\gamma)^{243}\mathrm{Pu}$ were identi-

fied, 17 of which are primary γ-rays with energies exceeding 2.5 MeV. The intensities of the identified prompt γ-ray lines were determined relative to the respective most intense prompt γ-ray line.
The current datasets found in the ENSDF tabulation on prompt γ-radiation from the examined reactions are based on separate measurements of the lower energetic secondary and higher energetic primary radiation. In this thesis measurements covering both secondary and primary γ-radiation over an energy range from 45 keV to 12 MeV were performed. Thus, systematic shifts arising from an erroneous normalization between the separate measurements in the current tabulation could be avoided.

The partial radiative capture cross sections of the prompt γ-ray lines identified were determined separately, using samples containing gold foils for the *in-situ* measurement of the neutron flux. In these measurements the partial capture cross section of the most intense prompt γ-ray of each respective nuclide was determined and was used to normalize the measured relative intensities. Also, the respective emission probabilities per neutron capture were determined.
The most intense prompt γ-ray of $^{237}\mathrm{Np}(\mathrm{n},\gamma)^{238}\mathrm{Np}$ with a measured energy of $E_\gamma = 182.82(10)$ keV was found to have a partial capture cross section of $\sigma_\gamma = 22.06(39)$ b and an emission probability of $p_\gamma = 0.125(4)$ per neutron capture event. This value was validated by two independent measurements at BRR and at FRM II.
From the PGAA measurements at FRM II the partial capture cross section of the most intense prompt γ-ray of $^{241}\mathrm{Am}(\mathrm{n},\gamma)^{242}\mathrm{Am}$ with $E_\gamma = 154.72(7)$ keV was consistently calculated as $\sigma_\gamma = 72.80(252)$ b. The corresponding emission probability for this prompt γ-ray line was calculated as 0.109(6).
For the $^{242}\mathrm{Pu}(\mathrm{n},\gamma)^{243}\mathrm{Pu}$ reaction the most intense prompt capture γ-ray line was found to have an energy of $E_\gamma = 287.69(8)$ keV. Its partial capture cross section of 7.07(12) b was consistently determined in two independent PGAA measurements and the corresponding emission probability per neutron capture event was calculated as $p_\gamma = 0.332(13)$.
None of the most intense prompt γ-ray lines had to be corrected for background interference, which demonstrates that the chosen sample design is well suited for these measurements. The partial radiative capture cross sections reported within this thesis are the first measurements on this quantity determined from the simultaneous measurement of both primary and secondary prompt γ-radiation. The accuracy of the ENSDF tabulated emission probabilities could be increased by a factor of 4 for ^{237}Np and ^{242}Pu. For ^{241}Am up to now no values are listed in ENSDF.
The most intense primary and secondary prompt γ-ray lines are listed in Table 5.1. These lines might be the most interesting ones for the identification and quantification of ^{237}Np, ^{241}Am or ^{242}Pu content with PGAA.

Additionally to these data, the neutron separation energies for ^{238}Np and ^{243}Pu were determined from the measured prompt γ-ray energies. The calculations are based on the assumption that the neutron separation energy is equal to the sum of the transition energies in a γ-ray cascade from the capture to the ground state, as the kinetic energy

Table 5.1: The most intense primary and secondary prompt capture γ-rays emitted in the reactions ^{237}Np$(n,\gamma)^{238}$Np, ^{241}Am$(n,\gamma)^{242}$Am and ^{242}Pu$(n,\gamma)^{243}$Pu. The listed absolute detection limits (DL) are calculated for the FRM II PGAA station using the elliptical neutron beam extension, which provides a thermal equivalent neutron flux of $2.5 \cdot 10^{10}\,\mathrm{cm^{-2}\,s^{-1}}$, and assuming a practicable measurement time of 10 000 s.

Isotope	E_γ [keV]	σ_γ [b]	p_γ [per capture event]	DL [µg]
^{237}Np	182.82(10)	22.06(39)	0.125(4)	0.056
	5352.04(14)	0.538(15)	0.0030(1)	1.4
^{241}Am	154.72(7)	72.80(252)	0.109(6)	0.017
	5174.59(21)	1.14(10)	0.0017(2)	0.64
^{242}Pu	287.69(8)	7.07(12)	0.332(13)	0.20
	4332.10(9)	0.0615(37)	0.0029(2)	10.0

of cold neutrons is negligible. The transition energies equal the measured prompt γ-ray energies after applying a correction for nuclear recoil.
In this way the neutron separation energy of ^{238}Np was calculated as $S_\mathrm{n} = 5488.02(17)$ keV and of ^{243}Pu as $S_\mathrm{n} = 5036.33(59)$ keV. While the accuracy of the neutron separation energy of ^{238}Np was slightly improved compared to the value given in the ENSDF evaluation, it was improved by almost a factor of 6 for ^{243}Pu.

In addition, the thermal radiative neutron capture cross sections of ^{237}Np and ^{241}Am were calculated from the spectra of the decay radiation emitted after the neutron irradiation. For ^{237}Np $\sigma_c^0 = 176.3(47)$ b was determined consistently from mostly uncorrelated measurements of two different samples at BRR and at FRM II. For each measurement the cross section value was determined using the four most intense decay γ-rays of ^{238}Np with energies of 923.99, 984.45, 1025.87, and 1028.54 keV.
For ^{241}Am the thermal cross section for the formation of ^{242g}Am was calculated as $\sigma_{c,\mathrm{g.s.}}^0 = 610.3(281)$ b using the K_α and K_β X-radiation following the electron capture decay of ^{242g}Am to ^{242}Pu. From this the thermal radiative neutron capture cross section of ^{241}Am for the formation of both the ground and meta-stable isomers was calculated as $\sigma_c^0 = 667.7(312)$ b by applying the isomeric production ratio of 0.914(70) measured by Fioni *et al.* [130].

The thermal radiative neutron capture cross section of ^{242}Pu$(n,\gamma)^{243}$Pu was determined from nuclear structure simulations performed with DICEBOX. These simulations were constrained by the measured σ_γ and S_n values. Different combinations of photon strength function (PSF) and level density models were investigated. The simulated total radiative widths of the capture state were found to be strongly model-dependent and was used to determine σ_c^0 by comparing it with the total radiative width tabulated in the Atlas of Neutron Resonances [39]. The best agreement between the simulated and the

tabulated total radiative widths as well as between the simulated level population and measured level depopulation was found using an EGLO PSF and a BSFG level density model together with a single-particle strength of $1 \cdot 10^{-8}$ for the GDMR. In this simulation $\sigma_c^0 = 21.92(146)\,\mathrm{b}$ was determined. However, all values of σ_c^0 deduced using the different model combinations are in agreement with each other. Thus, the given thermal capture cross section is almost independent of the chosen model combination.
From the simulation a critical energy $E_{\mathrm{crit.}} = 450\,\mathrm{keV}$ was established below which the level scheme can be regarded as complete.

It can be concluded that the sample design developed within the scope of this work is suitable for the measurement of basic nuclear data, particularly needed for PGAA. The energies and the partial radiative neutron capture cross sections determined in separate experiments were all in agreement with each other, demonstrating that the used methods and materials were reliable. The measured data provide a reliable foundation for the identification and quantification of ^{237}Np, ^{241}Am and ^{242}Pu via PGAA or INAA. The detection limits calculated for the investigated actinides demonstrate that PGAA has great potential for the non-destructive analysis of actinide inventories in complex matrices.

List of References

[1] E. Mauerhofer and R. Odoj. Messmethoden zur Charakterisierung radioaktiver Abfälle und zur Freimessung von Reststoffen aus der Stilllegung kerntechnischer Anlagen (MESRAB), Fachlicher Schlussbericht. Technical report, 2006.

[2] Zs. Révay, T. Belgya, R. M. Lindstrom, et al. *Handbook of Prompt Gamma Activation Analysis with Neutron Beams*. Kluwer Academic Publishers, Dordrecht, Bosten, London, 2004.

[3] International Atomic Energy Agency. *Database of Prompt Gamma Rays from Slow Neutron Capture for Elemental Analysis*, volume STI/PUB/12. IAEA, Vienna, 2007.

[4] R. Firestone. Database of Prompt Gamma Rays from Slow Neutron Capture for Elemental Analysis (International Atomic Energy Agency, Vienna, 2006), [Online] Available at: https://www-nds.iaea.org/pgaa/egaf.html, 2006.

[5] M. Chadwick, M. Herman, P. Obložinský, et al. ENDF/B-VII.1 Nuclear Data for Science and Technology: Cross Sections, Covariances, Fission Product Yields and Decay Data. *Nuclear Data Sheets*, 112(12):2887–2996, December 2011.

[6] A. Santamarina, D. Bernard, P. Blaise, et al. The JEFF-3.1.1 Nuclear Data Library, JEFF Report 22. Technical report, Nuclear Energy Agency, Organisation for Economic Co-operation and Development, 2009.

[7] K. Shibata, O. Iwamoto, N. Tsuneo, et al. JENDL-4.0: A New Library for Nuclear Science and Engineering. *Journal of Nuclear Science and Technology*, 48(1):1–30, January 2011.

[8] K. Debertin and R. G. Helmer. *Gamma- and X-Ray Spectrometry with Semiconductor Detectors*. North Holland, Amsterdam, New York, 1988.

[9] G. F. Knoll. *Radiation Detection and Measurement*. John Wiley & Sons, New York, 4 edition, 2010.

[10] K. S. Krane. *Introductory Nuclear Physics*. John Wiley & Sons, New York, 3 edition, 1987.

[11] *International System of Units (SI)*. Bureau international des poids et mesures, 8 edition, December 2006.

[12] A. Einstein. Ist die Trägheit eines Körpers von seinem Energieinhalt abhängig? *Annalen der Physik*, 323(13):639–641, 1905.

[13] W. K. Heisenberg. Über den anschaulichen Inhalt der quantentheoretischen Kinematik und Mechanik. *Zeitschrift für Physik*, 43(3-4):172–198, March 1927.

[14] W. K. Heisenberg. Die physikalischen Prinzipien der Quantentheorie. *Zeitschrift für Angewandte Chemie*, 43(41):914–914, October 1930.

[15] J. Beringer, J. F. Arguin, R. M. Barnett, et al. Review of Particle Physics. *Physical Review D*, 86(1):010001, July 2012.

[16] L. de Broglie. Ondes et Quanta. *Comptes rendus de l'Académie des Sciences*, 177:507–510, 1923.

[17] E. Rutherford. The scattering of α and β particles by matter and the structure of the atom. *Philosophical Magazine Series 6*, 21(125):669–688, May 1911.

[18] N. Bohr. On the Constitution of Atoms and Molecules. *Philosophical Magazine*, 26:1–25, 1913.

[19] E. Schrödinger. Quantisierung als Eigenwertproblem (Erste Mitteilung). *Annalen der Physik*, 79(4):361–376, 1926.

[20] E. Schrödinger. Quantisierung als Eigenwertproblem (Zweite Mitteilung). *Annalen der Physik*, 79(4):489–527, 1926.

[21] W. Demtröder. *Experimentalphysik 3: Atome, Moleküle und Festkörper*. Springer, 4 edition, 2010.

[22] C. J. Foot. *Atomic Physics*. Oxford University Press, 2005.

[23] W. Pauli. Über den Zusammenhang des Abschlusses der Elektronengruppen im Atom mit der Komplexstruktur der Spektren. *Zeitschrift für Physik*, 31(1):765–783, February 1925.

[24] E. Fermi. Zur Quantelung des idealen einatomigen Gases. *Zeitschrift für Physik*, 36(11-12):902–912, November 1926.

[25] P. A. M. Dirac. On the Theory of Quantum Mechanics. *Proceedings of the Royal Society A: Mathematical, Physical and Engineering Sciences*, 112(762):661–677, October 1926.

[26] R. Woods and D. Saxon. Diffuse Surface Optical Model for Nucleon-Nuclei Scattering. *Physical Review*, 95(2):577–578, July 1954.

[27] N. Schwierz, I. Wiedenhover, and A. Volya. Parameterization of the Woods-Saxon Potential for Shell-Model Calculations. *ArXiv e-prints*, arXiv:0709.3525v1, September 2007.

[28] H. Bethe. Nuclear Physics B. Nuclear Dynamics, Theoretical. *Reviews of Modern Physics*, 9(2):69–244, April 1937.

[29] H. Vonach and M. Hille. Die Energieabhängigkeit der Niveaudichte im Bereich der Kernmassen A = 30–65. *Nuclear Physics A*, 127(2):289–304, April 1969.

[30] J. Huizenga, H. Vonach, A. Katsanos, A. Gorski, and C. Stephan. Level Densities from Excitation Functions of Isolated Levels. *Physical Review*, 182(4):1149–1164, June 1969.

[31] E. Gadioli and L. Zetta. Level Density of Light Nuclei. *Physical Review*, 167(4):1016–1026, March 1968.

[32] W. Dilg, W. Schantl, H. Vonach, and M. Uhl. Level density parameters for the back-shifted fermi gas model in the mass range $40 < A < 250$. *Nuclear Physics A*, 217(2):269–298, December 1973.

[33] J. Dobaczewski, P. Magierski, W. Nazarewicz, W. Satula, and Z. Szymanski. Odd-even staggering of binding energies as a consequence of pairing and mean-field effects. *Physical Review C*, 63(2):024308, January 2001.

[34] T. von Egidy and D. Bucurescu. Systematics of nuclear level density parameters. *Physical Review C*, 72(4):044311, October 2005.

[35] S. Al-Quraishi, S. Grimes, T. Massey, and D. Resler. Level densities for $20 \leq A \leq 110$. *Physical Review C*, 67(1):015803, January 2003.

[36] T. von Egidy, H.-F. Wirth, and D. Bucurescu. Level density parameters. In *Proceedings of Science: Workshop on Photon Strength Functions and Related Topics*, PoS(PSF07)005 , SISSA (International School for Advanced Studies), Trieste, [Online] Available: http://pos.sissa.it/archive/conferences/044/005/PSF07_005.pdf, Prague, 2007.

[37] G. Zhigang, Y. Hongwei, Z. Youxiang, et al. The updated version of the Chinese Evaluated Nuclear Data Library (CENDL-3.1) and China nuclear data evaluation activities. In O. Bersillon, F. Gunsing, E. Bauge, R. Jacqmin, and S. Leray, editors, *ND2007*, pages 753–757, Les Ulis, France, May 2008. EDP Sciences, [Online] Available at: http://dx.doi.org/10.1051/ndata:07570.

[38] G. Breit and E. Wigner. Capture of Slow Neutrons. *Physical Review*, 49(7):519–531, April 1936.

[39] S. F. Mughabghab. *Atlas of Neutron Resonances: Resonance Parameters and Thermal Cross Sections Z=1-100: Resonance Parameters and Thermal Cross Sections. Z=1-100.* Elsevier Science & Technology, New York, Amsterdam, 5 edition, 2006.

[40] A. T. Yue, M. S. Dewey, D. M. Gilliam, et al. Improved Determination of the Neutron Lifetime. *Physical Review Letters*, 111(22):222501, November 2013.

[41] T. Kibédi, T. Burrows, M. Trzhaskovskaya, P. Davidson, and C. Nestor. Evaluation of theoretical conversion coefficients using BrIcc. *Nuclear Instruments and Methods in Physics Research Section A: Accelerators, Spectrometers, Detectors and Associated Equipment*, 589(2):202–229, May 2008.

[42] D. M. Brink. PhD thesis, Oxford University, 1955.

[43] P. Axel. Electric Dipole Ground-State Transition Width Strength Function and 7-Mev Photon Interactions. *Physical Review*, 126(2):671–683, April 1962.

[44] J. Kopecky and R. Chrien. Observation of the M1 giant resonance by resonance averaging in 106Pd. *Nuclear Physics A*, 468(2):285–300, June 1987.

[45] H. Feshbach, D. Peaslee, and V. Weisskopf. Erratum: On the Scattering and Absorption of Particles by Atomic Nuclei [Phys. Rev. 71, 145 (1947)]. *Physical Review*, 71(8):564–564, April 1947.

[46] A. M. Hurst, R. B. Firestone, B. W. Sleaford, et al. Investigation of the tungsten isotopes via thermal neutron capture. *Physical Review C*, 89(1):014606, January 2014.

[47] S. G. Kadmenski, V. P. Markushev, and V. I. Furman. Radiative widths of neutron resonances. Giant dipole resonances. *Yadernaya fizika (Soviet Journal of Nuclear Physics)*, 37(2):277–283 (165–168), 1983.

[48] M. Guttormsen, L. A. Bernstein, A. Görgen, et al. Scissors resonance in the quasicontinuum of Th, Pa, and U isotopes. *Physical Review C*, 89(1):014302, January 2014.

[49] C. Porter and R. Thomas. Fluctuations of Nuclear Reaction Widths. *Physical Review*, 104(2):483–491, October 1956.

[50] O. Klein and Y. Nishina. Über die Streuung von Strahlung durch freie Elektronen nach der neuen relativistischen Quantendynamik von Dirac. *Zeitschrift für Physik*, 52(11-12):853–868, July 1929.

[51] H. Bethe and W. Heitler. On the Stopping of Fast Particles and on the Creation of Positive Electrons. *Proceedings of the Royal Society A: Mathematical, Physical and Engineering Sciences*, 146(856):83–112, August 1934.

[52] M. Berger, J. Hubbell, S. Seltzer, et al. XCOM: Photon Cross Section Database (version 1.5) [Online] Available at: http://physics.nist.gov/xcom, 2010.

[53] H. Koch, H. Börner, J. Pinston, et al. The curved crystal gamma ray spectrometers "GAMS 1, GAMS 2, GAMS 3" for high resolution (n, γ) measurements at the high flux reactor in Grenoble. *Nuclear Instruments and Methods*, 175(2-3):401–423, September 1980.

[54] X-5 Monte Carlo Team. MCNP – A General N-Particle Transport Code, Version 5. Technical report, Los Alamos National Laboratoy, 2003.

[55] S. Agostinelli, J. Allison, K. Amako, et al. Geant4 – a simulation toolkit. *Nuclear Instruments and Methods in Physics Research Section A: Accelerators, Spectrometers, Detectors and Associated Equipment*, 506(3):250–303, July 2003.

[56] J. Allison, K. Amako, J. Apostolakis, et al. Geant4 developments and applications. *IEEE Transactions on Nuclear Science*, 53(1):270–278, February 2006.

[57] D. E. Cullen, J. H. Hubbel, and L. Kissel. EPDL97: the Evaluated Photon Data Library, '97 Version. Technical report, Faculty of Engineering and Physical Sciences, School of Physics and Astronomy, 1997.

[58] G. Cirrone, G. Cuttone, F. Di Rosa, et al. Validation of the Geant4 electromagnetic photon cross-sections for elements and compounds. *Nuclear Instruments and Methods in Physics Research Section A: Accelerators, Spectrometers, Detectors and Associated Equipment*, 618(1-3):315–322, June 2010.

[59] F. Bečvár. Simulation of γ cascades in complex nuclei with emphasis on assessment of uncertainties of cascade-related quantities. *Nuclear Instruments and Methods in Physics Research Section A: Accelerators, Spectrometers, Detectors and Associated Equipment*, 417(2-3):434–449, November 1998.

[60] N. Bohr. Neutron Capture and Nuclear Constitution. *Nature*, 137(3461):344–348, February 1936.

[61] E. Mauerhofer and A. Havenith. The MEDINA facility for the assay of the chemotoxic inventory of radioactive waste packages. *Journal of Radioanalytical and Nuclear Chemistry*, in print, June 2014.

[62] Budapest Neutron Centre Office. [Online] Available at: http://www.bnc.hu/?q=node/6, 2014.

[63] Zs. Révay, T. Belgya, Z. Kasztovszky, J. Weil, and G. Molnár. Cold neutron PGAA facility at Budapest. *Nuclear Instruments and Methods in Physics Research Section B: Beam Interactions with Materials and Atoms*, 213:385–388, January 2004.

[64] Zs. Révay, T. Belgya, L. Szentmiklósi, and Z. Kis. Recent developments of prompt gamma activation analysis at Budapest. *Journal of Radioanalytical and Nuclear Chemistry*, 278(3):643–646, November 2008.

[65] L. Szentmiklósi, T. Belgya, Zs. Révay, and Z. Kis. Upgrade of the prompt gamma activation analysis and the neutron-induced prompt gamma spectroscopy facilities at the Budapest research reactor. *Journal of Radioanalytical and Nuclear Chemistry*, 286(2):501–505, August 2010.

[66] T. Belgya. Prompt Gamma Activation Analysis at the Budapest Research Reactor. *Physics Procedia*, 31:99–109, January 2012.

[67] T. Belgya, Zs. Revay, B. Fazekas, et al. The new Budapest capture gamma-ray facility. In G. Molnar, T. Belgya, and Z. Revay, editors, *Proceedings of the 9th International Symposium on Capture gamma-ray spectroscopy and related topics*, pages 826–837. Springer Verlag, Budapest, Hungary, 1997.

[68] T. Belgya. Private Communication.

[69] P. Kudejova, G. Meierhofer, K. Zeitelhack, et al. The new PGAA and PGAI facility at the research reactor FRM II in Garching near Munich. *Journal of Radioanalytical and Nuclear Chemistry*, 278(3):691–695, November 2008.

[70] Zs. Révay. Private Communication.

[71] B. Fazekas, G. Molnár, T. Belgya, L. Dabolczi, and A. Simonits. Introducing HYPERMET-PC for automatic analysis of complex gamma-ray spectra. *Journal of Radioanalytical and Nuclear Chemistry*, 215(2):271–277, January 1997.

[72] Zs. Révay, T. Belgya, P. P. Ember, and G. Molnár. Recent developments in HYPERMET PC. *Journal of Radioanalytical and Nuclear Chemistry*, 248(2):401–405, 2001.

[73] G. W. Phillips and K. W. Marlow. Automatic analysis of gamma-ray spectra from germanium detectors. *Nuclear Instruments and Methods*, 137(3):525–536, September 1976.

[74] Z. Révay, T. Belgya, and G. L. Molnár. Application of Hypermet-PC in PGAA. *Journal of Radioanalytical and Nuclear Chemistry*, 265(2):261–265, July 2005.

[75] B. Fazekas, J. Östör, Z. Kiss, A. Simonits, and G. L. Molnár. Quality assurance features of "HYPERMET-PC". *Journal of Radioanalytical and Nuclear Chemistry*, 233(1-2):101–103, July 1998.

[76] B. Fazekas, Zs. Révay, J. Östör, et al. A new method for determination of gamma-ray spectrometer non-linearity. *Nuclear Instruments and Methods in Physics Research Section A: Accelerators, Spectrometers, Detectors and Associated Equipment*, 422(1-3):469–473, February 1999.

[77] Z. Kis, B. Fazekas, J. Östör, et al. Comparison of efficiency functions for Ge gamma-ray detectors in a wide energy range. *Nuclear Instruments and Methods in Physics Research Section A: Accelerators, Spectrometers, Detectors and Associated Equipment*, 418(2-3):374–386, December 1998.

[78] G. Molnár, Zs. Révay, and T. Belgya. Wide energy range efficiency calibration method for Ge detectors. *Nuclear Instruments and Methods in Physics Research Section A: Accelerators, Spectrometers, Detectors and Associated Equipment*, 489(1-3):140–159, August 2002.

[79] R. Firestone, G. Molnar, Zs. Revay, et al. The evaluated gamma-ray activation file (EGAF). *Lawrence Berkeley National Laboratory*, page http://escholarship.org/uc/item/5pv6c5m8.pdf, 2004.

[80] Brookhaven National Laboratory. Evaluated Nuclear Structure Data File (ENSDF), an electronic database of evaluated experimental nuclear structure data maintained by the National Nuclear Data Center, [Online] Available at: http://www.nndc.bnl.gov/ensdf/.

[81] M. Bhat. Evaluated Nuclear Structure Data File (ENSDF). In S. M. Qaim (editor) *Nuclear Data for Science and Technology, Research Reports in Physics*, pages 817–821. Springer Berlin Heidelberg, 1992.

[82] Laboratoire National Henri Becquerel. Decay Data Evaluation Project Recommended data [Online] Available at: http://www.nucleide.org/DDEP_WG/DDEPdata.htm, 2014.

[83] R. Brun and F. Rademakers. ROOT – An object oriented data analysis framework. *Nuclear Instruments and Methods in Physics Research Section A: Accelerators, Spectrometers, Detectors and Associated Equipment*, 389(1-2):81–86, April 1997.

[84] E. Jones, T. Oliphant, P. Peterson, and Others. SciPy: Open source scientific tools for Python.

[85] M.-M. Bé, V. Chisté, C. Dulieu, et al. *Table of Radionuclides, Volume 4*, volume 4 of *Monographie BIPM-5*. Bureau International des Poids et Mesures, Pavillon de Breteuil, F-92310 Sèvres, France, 2008.

[86] M.-M. Bé, V. Chisté, C. Dulieu, et al. *Table of Radionuclides, Volume 5*, volume 5 of *Monographie BIPM-5*. Bureau International des Poids et Mesures, Pavillon de Breteuil, F-92310 Sèvres, France, 2010.

[87] P. Feldhaus. *Valenzstabilisierung von Neptunium in salpetersauren Medien bei der Wiederaufarbeitung abgebrannter Brennelemente*. Phd thesis, RWTH Aachen, 1996.

[88] T. Reich. Private communication, 2014.

[89] V. Ionescu, J. Kern, R. Casten, et al. Nuclear levels in 238Np. *Nuclear Physics A*, 313(3):283–306, January 1979.

[90] W. M. Haynes. *CRC Handbook of Chemistry and Physics*. Taylor & Francis Ltd., 94 edition, 2013.

[91] C. Genreith, M. Rossbach, E. Mauerhofer, T. Belgya, and G. Caspary. First results of the prompt gamma characterization of 237Np. *Nukleonika*, 57(4):443–446, 2012.

[92] C. Genreith, M. Rossbach, E. Mauerhofer, T. Belgya, and G. Caspary. Measurement of thermal neutron capture cross sections of 237Np and 242Pu using prompt gamma neutron activation. *Journal of Radioanalytical and Nuclear Chemistry*, 296(2):699–703, August 2012.

[93] Y. Akovali. Nuclear Data Sheets for A = 243. *Nuclear Data Sheets*, 103(3):515–564, November 2004 and interim evaluation by C.D. Nesaraja, E.A. Mccutchan, revision of 30-Sep-2013, to be published in *Nuclear Data Sheets*, 121:695, 2014. Data extracted from the ENSDF database (May 2014).

[94] Heraeus Quarzglas GmbH & Co. KG Suprasil Data Sheet [Online] Available at: http://heraeus-quarzglas.de/media/webmedia_local/downloads/broschren_mo/Suprasil_CG_synthetischesQuarzglas.pdf, 2014.

[95] C. Velten. *Experimente zur Validierung der Bestimmung von thermischen Wirkungsquerschnitten für Neutroneneinfang mittels PGAA*. Bachelorarbeit in Physik, RWTH Aachen, 2013.

[96] Geant4 Collaboration. Geant4 Material Database [Online] Available at: http://geant4.cern.ch/UserDocumentation/UsersGuides/ForApplicationDeveloper/html/apas08.html, 2014.

[97] Goodfellow. Fluorinated Ethylene Propylene Copolymer (FEP) Material Information [Online] Available at: http://www.goodfellow.com/E/Fluorinated-Ethylene-Propylene-Copolymer.html, 2014.

[98] Nuclear Energy Agency (Agency of Organisation for Economic Co-operation and Development). Development. The JEFF-3.2 Nuclear Data Library [Online] Available at: https://www.oecd-nea.org/dbforms/data/eva/evatapes/jeff_32/ and https://www-nds.iaea.org/exfor/endf.htm, 2014.

[99] C. T. Chantler. Theoretical Form Factor, Attenuation, and Scattering Tabulation for Z=1–92 from E=1–10 eV to E=0.4–1.0 MeV. *Journal of Physical and Chemical Reference Data*, 24(1):71, 1995.

[100] National Institute of Standards and Technology. Uncertainties Near Soft X-Ray LII, LIII, MIV, MV Edges, and the Reason for the New Tabulation [Online] Available at: http://physics.nist.gov/PhysRefData/FFast/Text2000/sec06.html#tab2, 2014.

[101] R. B. Firestone. EGAF (International Atomic Energy Agency, Vienna, 2006), [Online] Available at: https://www-nds.iaea.org/pgaa/EGAF/29SI_EGAF.ens, 2006.

[102] Brookhaven National Laboratory. NuDat 2.6 [Online] Available at: http://www.nndc.bnl.gov/nudat2/, 2014.

[103] R. Firestone and L. Ekström. LBNL Isotopes Project - LUNDS Universitet WWW Table of Radioactive Isotopes, database version 2/28/99 [Online] Available at: http://ie.lbl.gov/toi/, 2014.

[104] M.-M. Bé, V. Chisté, C. Dulieu, et al. *Table of Radionuclides, Volume 6*, volume 6 of *Monographie BIPM-5*. Bureau International des Poids et Mesures, Pavillon de Breteuil, F-92310 Sèvres, France, 2011.

[105] F. Chukreev, V. Makarenko, and M. Martin. Nuclear Data Sheets for A = 238. *Nuclear Data Sheets*, 97(1):129–240, September 2002. Data extracted from the ENSDF database (May 2014).

[106] R. Hoff, S. Drissi, J. Kern, et al. Nuclear structure of Np238 from neutron-capture and α-decay measurements. *Physical Review C*, 41(2):484–512, February 1990.

[107] J. K. Tuli and B. Pritychenko. Thermal Neutron Capture γ's (CapGam), Website of the National Nuclear Data Center, [Online] Available at: http://www.nndc.bnl.gov/capgam/, 2014.

[108] A. Carlson, V. Pronyaev, D. Smith, et al. International Evaluation of Neutron Cross Section Standards. *Nuclear Data Sheets*, 110(12):3215–3324, December 2009.

[109] M.-M. Bé, V. Chisté, C. Dulieu, et al. *Table of Radionuclides, Volume 8*, volume 8 of *Monographie BIPM-5*. Bureau International des Poids et Mesures, Pavillon de Breteuil, F-92310 Sèvres, France, 2015.

[110] International Atomic Energy Agency and R. Paviotti-Corcuera. PGAA Database Files [Online] Available at: https://www-nds.iaea.org/pgaa/databases.htm, 2014.

[111] International Atomic Energy Agency. Update of X ray and gamma ray decay data standards for detector calibration and other applications, Volume 1: Recommended decay data, high energy gamma ray standards and angular correlation coefficients. Technical report, IAEA, Vienna, 2007.

[112] A. L. Nichols. IAEA Co-ordinated Research Project: update of X-ray and gamma-ray decay data standards for detector calibration and other applications. *Applied radiation and isotopes : including data, instrumentation and methods for use in agriculture, industry and medicine*, 60(2-4):247–256, 2004.

[113] International Atomic Energy Agency Nuclear Data Section. Actinide data: Thermal neutron cross sections, resonance integrals, and Westcott factors [Online] Available at: https://www-nds.iaea.org/sgnucdat/a5.htm, 2014.

[114] A. L. Nichols, D. L. Aldama, and M. Verpelli. Handbook of nuclear data for safeguards: database extensions, August 2008. Technical report, Nuclear Data Section Division of Physical an d Chemical Sciences Department of Nuclear Sc iences and Applications International Atomic Energy Agency, Vienna, 2008.

[115] H. Harada, S. Nakamura, M. Ohta, T. Fujuii, and H. Yamana. Emission Probabilities of Gamma Rays from the Decay of 233 Pa and 238 Np, and the Thermal Neutron Capture Cross Section of 237 Np. *Journal of Nuclear Science and Technology*, 43(11):1289–1297, November 2006.

[116] E.-I. Esch, R. Reifarth, E. Bond, et al. Measurement of the Np237(n,γ) cross section from 20 meV to 500 keV with a high efficiency, highly segmented 4π BaF2 detector. *Physical Review C*, 77(3):034309, March 2008.

[117] A. Letourneau, F. Marie, P. Mutti, and I. Almahamid. Emission probabilities of gamma-rays from 238Np and their use for determination of the thermal neutron capture cross section of 237Np. *Applied radiation and isotopes : including data, instrumentation and methods for use in agriculture, industry and medicine*, 68(3):432–438, March 2010.

[118] T. Katoh, S. Nakamura, K. Furutaka, et al. Measurement of Thermal Neutron Capture Cross Section and Resonance Integral of the 237 Np(n , γ) 238 Np Reaction. *Journal of Nuclear Science and Technology*, 40(8):559–568, August 2003.

[119] F. Brown and G. Hall. The thermal neutron capture cross-section of Np237. *Journal of Inorganic and Nuclear Chemistry*, 2(4):205–208, April 1956.

[120] M. Smith, R. Smith, E. Joki, and J. Evans. Neutron Total Cross Section of Np237 from 0.02 to 2.8 ev. *Physical Review*, 107(2):525–527, July 1957.

[121] R. Tattersall, H. Rose, S. Pattenden, and D. Jowitt. Pile oscillator measurements of resonance absorption integrals. *Journal of Nuclear Energy. Part A. Reactor Science*, 12(1-2):32–46, May 1960.

[122] R. Schuman and J. Berreth. Resonance Integral Measurement (Reference and Data taken from Letourneau2010). *Progress Report of Idaho Nuclear Corporation*, IN-1296, 1969.

[123] S. Eberle, H. Bleyl, E. Gantner, J. Reinhardt, and C. Krueckeberg. Wirkungsquerschnitte. *Gesellschaft für Kernforschung (Karlsruhe). Projekt Actiniden: Halbjahresbericht*, 1456:51–61, 1971.

[124] L. Weston and J. Todd. Neutron Capture Cross Section of Neptunium-237. *Nuclear Science and Engineering*, 79(2):184–196, 1981.

[125] L. Jurova, V. Poljakov, and V. Rukhlo. Yadernye Konstanty (Reference and Data taken from Letourneau2010). *Vop At. Nauki i Tekhn. Ser.*, 55(1):3, 1984.

[126] K. Kobayashi, A. Yamanaka, and I. Kimura. Measurements of Thermal Neutron Cross Section and Resonance Integral for 237 Np(n, γ) 238 Np Reaction. *Journal of Nuclear Science and Technology*, 31(12):1239–1247, December 1994.

[127] C. Lampoudis, S. Kopecky, O. Bouland, et al. Neutron transmission and capture cross section measurements for 241Am at the GELINA facility. *The European Physical Journal Plus*, 128(8):86, August 2013.

[128] Y. Akovali. Nuclear Data Sheets for A = 242. *Nuclear Data Sheets*, 96(1):177–239, May 2002. Data extracted from the ENSDF database (May 2014).

[129] J.-L. Salicio, S. Drissi, M. Gasser, et al. Level structure of the doubly-odd Am242 nucleus. *Physical Review C*, 37(6):2371–2390, June 1988.

[130] G. Fioni, M. Cribier, F. Marie, et al. Incineration of 241Am induced by thermal neutrons. *Nuclear Physics A*, 693(3-4):546–564, October 2001.

[131] D. Bernard and O. Bouland. Americium-241 phase I: reevaluation for JEFF-3.1.1 and a step forward. *Journal of Nuclear Science and Technology*, 49(1):132–166, January 2012.

[132] H. Pomerance. Oak Ridge National Laboratory Physics Division Semiannual Progress Report ORNL-1879: Absorption Cross Sections For Long-Lived Fission-Product Zr93, Am241, And Enriched Stable Platinum Isotopes. Technical report, Oak Ridge National Laboratory Physics Division, 1955.

[133] M. A. Bak, A. S. Krivokhatskii, K. A. Petrzhak, et al. Cross Sections and Resonance Integrals for Capture and Fission in Long-lived Americium Isotopes. *Atomnaya Énergiya*, 23(4):316–319, 1967. Translated from Russian in *Soviet Atomic Energy*, 23(4):1059–1063, October 1967.

[134] A. G. Dovbenko, V. A. Ivanov, V. E. Kolesov, and V. A. Tolstikov. Report Obninsk Russia, Translated by H. Dahlby Los Alamos Scientific Laboratory. Technical report, Los Alamos Scientific Laboratory, 1971.

[135] R. M. Harbour, K. W. MacMurdo, and F. J. McCrosson. Thermal-Neutron Capture Cross Sections and Capture Resonance Integrals of Americium-241. *Nuclear Science and Engineering*, 50(4):364–369, 1973.

[136] V. D. Gavrilov, V. A. Goncharov, V. V. Ivanenko, V. N. Kustov, and V. P. Smirnov. Thermal cross sections and resonance integrals of fission and capture of 241Am, 243Am, 245Cm, 249Bk, and 249Cf. *Soviet Atomic Energy*, 41(3):808–812, September 1976.

[137] L. W. Weston and J. H. Todd. Neutron Absorption Cross Section of Americium-241. *Nuclear Science and Engineering*, 61(3):356–365, 1976.

[138] S. M. Kalebin, V. S. Artamonov, R. N. Ivanov, et al. Total neutron cross section and neutron resonance parameters of 241Am in the energy range 0.004–30 eV. *Soviet Atomic Energy*, 40(4):373–377, April 1976.

[139] K. Wisshak, J. Wickenhauser, F. Käppeler, G. Reffo, and F. Fabbri. The Isomeric Ratio in Thermal and Fast Neutron Capture of Americium-241. *Nuclear Science and Engineering*, 81(3):396–417, 1982.

[140] N. Shinohara, Y. Hatsukawa, K. Hata, and N. Kohno. Radiochemical Determination of Neutron Capture Cross Sections of 241 Am. *Journal of Nuclear Science and Technology*, 34(7):613–621, July 1997.

[141] N. L. Maidana, M. S. Dias, and M. F. Koskinas. Measurement of the thermal neutron capture cross section and resonance integral of Am-241. *Radiochimica Acta*, 89(7/2001), January 2001.

[142] S. Nakamura, M. Ohta, H. Harada, T. Fujii, and H. Yamana. Thermal-Neutron Capture Cross Section and Resonance Integral of Americium-241. *Journal of Nuclear Science and Technology*, 44(12):1500–1508, December 2007.

[143] M. Jandel, T. Bredeweg, E. Bond, et al. Neutron capture cross section of Am241. *Physical Review C*, 78(3):034609, September 2008.

[144] T. Belgya, L. Szentmiklosi, and Z. Kis. Measurement of 241Am Ground State Radiative Neutron Capture Cross Section with Cold Neutron Beam. Progress Report on Research Contract HUN14318 for the CRP on Minor Actinide Neutron Reaction Data (MANREAD). *INIS*, 43(13):INDC(HUN)–0037, 2012.

[145] J. Lynn, B. Patrick, M. Sowerby, and E. Bowey. Evaluation of differential nuclear data for americium isotopes part I: 241Am. *Progress in Nuclear Energy*, 5(3):255–282, January 1980.

[146] C. Genreith, M. Rossbach, Zs. Révay, and P. Kudejova. Determination of (n,γ) Cross Sections of 241Am by Cold Neutron Activation. *Nuclear Data Sheets*, 119:69–71, May 2014.

[147] M. Rossbach and C. Genreith. 241Am: a difficult actinide for (n,gamma) cross section measurement. In E. Chiaveri (editor) *Proceedings of the ERINDA workshop*, volume CERN-Proce, pages 157–163. CERN, Geneva, Switzerland, 2013.

[148] M.-M. Bé, V. Chisté, C. Dulieu, et al. *Table of Radionuclides, Volume 2*, volume 2 of *Monographie BIPM-5*. Bureau International des Poids et Mesures, Pavillon de Breteuil, F-92310 Sèvres, France, 2004.

[149] R. Firestone. EGAF (International Atomic Energy Agency, Vienna, 2006), [Online] Available at: https://www-nds.iaea.org/pgaa/EGAF/2H_EGAF.ens, 2006.

[150] B. Singh and N. Nica. Nuclear Data Sheets for A = 77. *Nuclear Data Sheets*, 113(5):1115–1314, May 2012. Data extracted from the ENSDF database (May 2014).

[151] R. Firestone. EGAF (International Atomic Energy Agency, Vienna, 2006), [Online] Available at: https://www-nds.iaea.org/pgaa/EGAF/71GE_EGAF.ens, 2006.

[152] R. Firestone. EGAF (International Atomic Energy Agency, Vienna, 2006), [Online] Available at: https://www-nds.iaea.org/pgaa/EGAF/36CL_EGAF.ens, 2006.

[153] R. Casten, W. Kane, J. Erskine, A. Friedman, and D. Gale. States in 243Pu from the (n ,γ), (d , p), and (d , t) reactions. *Physical Review C*, 14(3):912–932, September 1976.

[154] R. Firestone. EGAF (International Atomic Energy Agency, Vienna, 2006), [Online] Available at: https://www-nds.iaea.org/pgaa/EGAF/198AU_EGAF.ens, 2006.

[155] D. Engelkemeir, P. Fields, and J. Huizenga. Radiations of Pu243. *Physical Review*, 90(1):6–10, April 1953.

[156] D. Hoffman, F. Lawrence, and W. Daniels. Decay of 243Pu. *Nuclear Physics A*, 131(3):551–560, July 1969.

[157] T. W. Burrows, B. Barton, L. Ekstrom, and P. Andersson. GTOL Version 6.4b [December 3,2003], [Online] Available at: https://www-nds.iaea.org/workshops/ictp2005/Codes/ENSDF_Codes/mswindows/gtol/readgtol.htm, 2003.

[158] R. Capote, M. Herman, P. Obložinský, et al. RIPL – Reference Input Parameter Library for Calculation of Nuclear Reactions and Nuclear Data Evaluations. *Nuclear Data Sheets*, 110(12):3107–3214, December 2009.

[159] International Atomic Energy Agency. Reference Input Parameter Library (RIPL-3), [Online] Available at: http://www-nds.iaea.org/RIPL-3/, 2009.

[160] B. Berman, J. Caldwell, E. Dowdy, et al. Photofission and photoneutron cross sections and photofission neutron multiplicities for U233, U234, Np237, and Pu239. *Physical Review C*, 34(6):2201–2214, December 1986. Data taken from the EXFOR database, retrieved from http://cdfe.sinp.msu.ru/cgi-bin/exf2htm?LINK=m0722018. Dataset evaluated in V. V. Varlamov and

N .N. Peskov. Evaluation of (γ,xn), (γ,sn), (γ,n),(γ,2n), and (γ,f) reactions cross sections for actinides nuclei 232Th, 238U, 237Np, and 239Pu: consistency between data obtained using quasimonoenergetic annihilation and bremsstrahlung photons. MSU-INP-2007-8/829, 2007

[161] International Network of Nuclear Structure and Decay Data Evaluators and D. D. (NSDD). BrIcc v2.3S Conversion Coefficient Calculator, [Online] Available at: http://bricc.anu.edu.au/, 2011.

[162] P. R. Fields, G. L. Pyle, M. G. Inghram, et al. Pile Neutron Cross Sections of the Heavier Plutonium Isotopes. *Nuclear Science and Engineering*, 1(1):62–67, 1956.

[163] J. P. Butler, M. Lounsbury, and J. S. Merritt. The neutron capture cross sections of Pu238, Pu242, and Am243 in the thermal and epicadmium regions. *Canadian Journal of Physics*, 35(2):147–154, 1957.

[164] R. W. Durham and F. Molson. Capture cross section of 242Pu. *Canadian Journal of Physics*, 48(6):716–724, March 1970.

[165] P. J. Bendt and E. T. Jurney. Thermal-Neutron Capture-Gamma Spectrum of 242Pu. *Los Alamos Scientific Laboratory Report*, LA-7853-MS, 1979.

[166] F. Marie, A. Letourneau, G. Fioni, et al. Thermal neutron capture cross-section measurements of 243Am and 242Pu using the new mini-INCA - and -spectroscopy station. *Nuclear Instruments and Methods in Physics Research Section A: Accelerators, Spectrometers, Detectors and Associated Equipment*, 556(2):547–555, January 2006.

[167] Verordnung über den Schutz vor Schäden durch ionisierende Strahlen vom 20. Juli 2001 (BGBl. I S. 1714; 2002 I S. 1459), die zuletzt durch Artikel 5 Absatz 7 des Gesetzes vom 24. Februar 2012 (BGBl. I S. 212) geändert worden ist, Anlage III: Freigrenzen, F.

[168] NIST. NIST: Atomic Weights and Isotopic Compositions for All Elements [Online] Available at: http://physics.nist.gov/cgi-bin/Compositions/stand_alone.pl, 2014.

List of Abbreviations

BA Brink-Axel model 26

BGO Bismuth germanium oxide 34

BRR Budapest Research Reactor vi

BSFG Backshifted Fermi-gas 17

CTF constant temperature formula 16

DDEP Decay Data Evaluation Project 67

EGAF Evaluated Gamma-ray Activation File 1

EGLO enhanced generalized Lorentzian 27

ENDF Evaluated Nuclear Data File 2

ENSDF Evaluated Nuclear Structure Data File 67

FRM II Forschungs-Neutronenquelle Heinz Maier-Leibnitz 55

FZJ Forschunsgzentrum Jülich GmbH 69

Ge(Li) Li-doped germanium 103

GDER giant dipole electric resonance 132

GDMR giant dipole magnetic resonance 133

Geant4 Geometry And Tracking 4 46

GQER giant quadrupole electric resonance 27

HPGe High-Purity-Germanium 2

IAEA International Atomic Energy Agency 1

IEK-6 Institut für Energie und Klimaforschung: Nukleare Entsorgung und Reaktorsicherheit (Institute for Energy and Climate Research: Nuclear Waste Management and Reactor Safety) 69

ILL Institut Laue-Langevin 102

INAA instrumental neutron activation analysis 43

JEFF Joint Evaluated Fission and Fusion File 2

JENDL Japanese Evaluated Nuclear Data Library 2

LD level density 17

LEGe Low Energy Germanium Detector 54

MCA multi-channel analyzer 34

MCNP5 Monte-Carlo N-Particle code version 5 46

NAA neutron activation analysis 39

NIST National Institute for Science and Technology 90

ORNL Oak Ridge National Laboratory 69

PGAA Prompt Gamma Neutron Activation Analysis 1

PSF photon strength function 26

PTB Physikalisch-Technische Bundesanstalt 70

RIPL Reference Input Parameter Library 132

RMS root-mean-square 96

SI International System of Units 5

TUM Technische Universität München 69

List of Figures

2.1 Bohr/Rutherford model of the atom 8

2.2 Schematic illustrations of electron orbitals. 11

2.3 Meson Exchange Model 14

2.4 Effective Nucleon Potential 16

2.5 Differential Cross Section 20

2.6 Cross Section ^{241}Am 21

2.7 Neutron Decay 22

2.8 Photoeffect 28

2.9 Compton Scattering 30

2.10 Photo-effect 31

2.11 Mass attenuation coefficients for germanium. 32

2.12 Band structure of a Ge crystal 36

2.13 Detector Response Function 37

2.14 n-type coaxial HPGe detector 39

2.15 Radiative neutron capture 40

2.16 Build-up and Decay Function 44

2.17 Sketch of the PGAA principle 44

3.1 Cold neutron Spectrum BRR 52

3.2 Budapest PGAA station 53

3.3 Geant4 simulation representation of Budapest detector system 54

3.4 Budapest PGAA station 55

3.5 Cold neutron Spectrum FRM II 56

3.6 Garching PGAA station 57

3.7 Geant4 simulation representation of Garching detector system 58

3.8 Optimizing of HPGe detector positioning at FRM II. 59

3.9 PGAA spectrum 60

3.10 Hypermet-PC peak fit 62

3.11 Non-linearity function of the PGAA facility in Budapest 64

3.12 Non-linearity function of the PGAA facility in Budapest 65

3.13 Efficiency functions of the PGAA facilities 66

3.14 Detection efficiency functions of the detectors at the PGAA stations at the BRR and the FRM II 67

3.15 Preparation of aluminum encapsulated samples 71

3.16 CAD drawing of the aluminum sample casing 72

3.17 Sketch illustrating the self-absorption correction 73

3.18 Reopening of aluminum encapsulated samples 74

3.19 Images of samples in quartz vials 75

3.20 Neutron radiographic images of the actinide samples encapsulated in quartz glass vials. 76

3.21 Geant4 Simulation of the Quartz vial samples 76

3.23 Mini-Pellet Press 79

3.24 Glove box setup 80

3.25 Assembly of a quartz glass sheet encapsulated sample. 81

3.27 Picture of sample preparation with ^{241}Am-nitrate solution and a neutron radiographic image of sample 6. 85

3.28 Simulated neutron propagation through samples. 87

3.29 Deviations from $1/\sqrt{E_n}$ of the capture cross sections at thermal neutron energy (^{237}Np,^{242}Pu) 89

3.30 Deviations of the capture cross sections at thermal neutron energy in different evaluated data libraries (ENDF/B-VII.1,JEFF-3.2) 90

3.31 Geant4 Attenuation Correction factor simulation 92

4.1 Pictures of sample 6 in the sample holder frames at BRR and FRM II . . . 95

4.2 Comparison of the energies of identified background lines measured at BRR/FRM II to tabulated values. 96

4.3 Pull plots of ^{237}Np prompt γ-ray energies. 97

4.4 Pull plots of ^{237}Np prompt γ-ray intensities. 97

4.5 Comparison of the relative intensities of ^{237}Np prompt γ-rays measured at BRR and at FRM II 98

4.6 Comparison of the data of ^{237}Np prompt γ-radiation obtained in this work to data tabulated in ENSDF. 104

4.7 Thermal neutron capture cross sections of ^{237}Np as calculated from the measurements described in this work along with values taken from literature. 110

4.8 Neutron capture cross section of ^{241}Am and energy distribution of the cold neutron beam at FRM II. 111

4.9 Comparison of the energies of identified background lines measured at FRM II to tabulated values. 112

4.10 Thermal neutron capture cross sections of ^{241}Am, using reaction rate correction factors calculated with the ENDF and JEFF evaluated databases. . 117

4.11 Comparison of the energies of identified background lines measured during the irradiation of sample 2 at BRR/FRM II with tabulated values 122

4.12 Comparison of the ^{242}Pu prompt γ-ray energies measured at BRR with those measured at FRM II 122

4.13 Comparison of ^{242}Pu prompt γ-ray relative intensities measured at BRR with those measured at FRM II 123

4.14 Comparison of the ^{242}Pu prompt γ-ray data deduced in this work with data tabulated in ENSDF. 128

4.15 Fit of the half-life of ^{243}Pu. 130

4.16 Experimental photon strength functions. 133

4.17 Simulated population against experimentally determined depopulation of levels in ^{243}Pu. 136

4.18 Pulls of the simulated level population with the experimental depopulation. 137

4.19 Thermal neutron capture cross sections of ^{242}Pu, as calculated from the measurements described in this work along with values taken from literature. 139

C.1 Simulated population against experimentally determined depopulation of levels in ^{243}Pu. XXI

C.2 Simulated population against experimentally determined depopulation of levels in ^{243}Pu. XXII

C.3 Simulated population against experimentally determined depopulation of levels in ^{243}Pu. XXIII

C.4 Simulated population against experimentally determined depopulation of levels in ^{243}Pu. XXIV

D.1 Comparison of the energies of identified background lines measured at BRR with tabulated values. XXV

D.2 Comparison of ^{237}Np prompt γ-ray intensities measured at BRR. XXVI

D.3 Comparison of ^{237}Np prompt γ-ray intensities measured at BRR. XXVI

E.1 Spectrum of the irradiation of sample 2 measured at BRR. XXVIII

E.2 Spectrum of the irradiation of sample 2 measured at FRM II. XXIX

E.3 Spectrum of the irradiation of sample 9 measured at BRR. XXX

E.4 Spectrum of the irradiation of sample 8 measured at BRR. XXXI

E.5 Spectrum of the irradiation of sample 8 measured at FRM II. XXXII

APPENDIX A

Data from Measurements

A.1 Data sets from ^{242}Pu neutron irradiations

Table A.1: Energies and relative intensities of prompt γ-rays from the reaction $^{242}\mathrm{Pu}(\mathrm{n},\gamma)^{243}\mathrm{Pu}$ measured at BRR with sample 2.

E_γ [keV]	rel. Intensity	η_0	E_γ [keV]	rel. Intensity	η_0
95.95(72)	0.0806(21)	1.1851(75)	757.14(10)	0.0049(5)	1.0135(4)
125.43(71)	0.0010(3)	1.3467(754)	780.85(12)	0.0032(4)	1.0130(4)
148.28(24)	0.0004(2)	1.2260(87)	787.17(72)	0.0046(13)	1.0128(4)
159.52(10)	0.0025(4)	1.1887(71)	791.35(8)	0.0141(4)	1.0128(4)
184.21(8)	0.0246(5)	1.1330(49)	805.35(15)	0.0037(4)	1.0125(4)
219.48(8)	0.0138(3)	1.0900(33)	813.84(7)	0.0374(8)	1.0124(3)
229.15(8)	0.0136(5)	1.0807(29)	831.18(10)	0.0040(5)	1.0122(3)
233.68(10)	0.0024(2)	1.0779(28)	838.40(10)	0.0068(7)	1.0121(3)
241.89(8)	0.0807(15)	1.0726(25)	841.61(24)	0.0026(5)	1.0120(3)
261.56(8)	0.0105(4)	1.0616(22)	844.45(11)	0.0076(5)	1.0120(3)
263.20(15)	0.0013(1)	1.0594(21)	847.47(8)	0.0127(7)	1.0120(3)
275.22(8)	0.0236(6)	1.0553(20)	850.23(9)	0.0148(6)	1.0119(3)
277.90(9)	0.0031(8)	1.0544(19)	862.33(14)	0.0053(6)	1.0118(3)
284.34(8)	0.0203(6)	1.0509(18)	867.78(8)	0.0143(8)	1.0117(3)
287.67(8)	1.0000(129)	1.0501(18)	871.09(15)	0.0049(6)	1.0117(3)
334.17(72)	0.0003(2)	1.0381(13)	874.17(9)	0.0097(5)	1.0116(3)
343.77(8)	0.0270(5)	1.0372(13)	880.25(23)	0.0025(6)	1.0116(3)
385.82(8)	0.0071(2)	1.0301(11)	887.48(9)	0.0128(5)	1.0115(3)
388.04(14)	0.0013(1)	1.0291(11)	889.32(8)	0.0272(6)	1.0114(3)
400.78(8)	0.0349(7)	1.0286(9)	893.60(10)	0.0064(5)	1.0114(3)
402.49(8)	0.0355(7)	1.0284(9)	902.94(7)	0.0199(5)	1.0113(3)
407.31(8)	0.0186(4)	1.0279(9)	913.37(8)	0.0141(5)	1.0112(3)
416.51(8)	0.1361(53)	1.0270(8)	918.53(22)	0.0039(5)	1.0111(3)
426.08(10)	0.0041(3)	1.0263(8)	924.87(24)	0.0018(4)	1.0111(3)
439.40(9)	0.0055(3)	1.0253(8)	931.51(12)	0.0045(4)	1.0110(3)
444.69(8)	0.0164(4)	1.0249(8)	976.00(16)	0.0071(9)	1.0106(3)
447.87(52)	0.0004(3)	1.0247(8)	999.81(23)	0.0035(8)	1.0104(3)

Continued on the next page

E_γ [keV]	rel. Intensity	η_0	E_γ [keV]	rel. Intensity	η_0
480.61(9)	0.0139(6)	1.0223(7)	1008.76(29)	0.0029(6)	1.0103(3)
501.02(9)	0.0321(16)	1.0209(6)	1015.45(9)	0.0059(6)	1.0103(3)
513.69(8)	0.0582(27)	1.0202(6)	1022.43(9)	0.0088(6)	1.0102(3)
516.69(9)	0.0165(16)	1.0201(6)	1028.30(28)	0.0014(5)	1.0102(3)
522.25(7)	0.0217(5)	1.0198(6)	1031.37(14)	0.0037(5)	1.0101(3)
526.27(7)	0.0449(8)	1.0196(6)	1042.34(8)	0.0070(3)	1.0101(3)
534.07(8)	0.0094(3)	1.0193(6)	1045.94(20)	0.0011(4)	1.0100(3)
546.90(10)	0.0094(7)	1.0188(5)	1050.43(10)	0.0036(4)	1.0100(3)
551.59(12)	0.0039(6)	1.0186(5)	1054.28(13)	0.0034(4)	1.0100(3)
555.89(9)	0.0182(7)	1.0184(5)	1056.28(12)	0.0045(5)	1.0100(3)
558.04(9)	0.0195(8)	1.0183(5)	1070.37(18)	0.0025(4)	1.0099(3)
560.16(14)	0.0058(6)	1.0183(5)	1087.20(11)	0.0060(8)	1.0098(3)
564.73(8)	0.0389(11)	1.0181(5)	1091.45(10)	0.0054(6)	1.0098(3)
566.32(8)	0.0348(10)	1.0180(5)	1162.44(17)	0.0044(4)	1.0093(3)
573.40(12)	0.0068(7)	1.0177(5)	1170.31(25)	0.0017(3)	1.0092(3)
589.15(8)	0.0112(5)	1.0171(5)	1176.71(14)	0.0091(13)	1.0092(3)
600.52(18)	0.0027(9)	1.0168(5)	1180.29(14)	0.0025(3)	1.0092(3)
607.86(56)	0.0025(13)	1.0166(5)	1190.57(7)	0.0176(5)	1.0091(3)
609.87(11)	0.0112(17)	1.0166(5)	1196.71(8)	0.0083(4)	1.0091(2)
625.24(8)	0.0134(5)	1.0163(5)	1201.13(8)	0.0101(4)	1.0090(2)
633.22(21)	0.0059(10)	1.0161(5)	3519.11(15)	0.0050(4)	1.0057(2)
637.89(10)	0.0066(4)	1.0160(5)	3544.48(20)	0.0041(4)	1.0057(2)
644.09(12)	0.0051(5)	1.0159(5)	3598.77(26)	0.0023(3)	1.0057(2)
647.54(72)	0.0028(7)	1.0158(5)	3615.20(11)	0.0088(4)	1.0057(2)
656.18(8)	0.0124(8)	1.0156(4)	3648.63(12)	0.0060(3)	1.0057(2)
662.45(12)	0.0111(7)	1.0155(4)	3734.81(15)	0.0043(3)	1.0057(2)
664.24(36)	0.0046(5)	1.0154(4)	3860.62(72)	0.0015(3)	1.0056(2)
666.53(41)	0.0013(3)	1.0154(4)	3906.81(20)	0.0038(3)	1.0056(2)
675.78(8)	0.0139(8)	1.0152(4)	4086.86(28)	0.0037(4)	1.0056(2)
679.17(11)	0.0055(6)	1.0151(4)	4130.44(37)	0.0045(9)	1.0056(2)
683.14(10)	0.0095(7)	1.0150(4)	4222.37(23)	0.0040(3)	1.0055(2)
714.77(32)	0.0013(3)	1.0144(4)	4226.59(14)	0.0079(4)	1.0055(2)
716.70(10)	0.0050(3)	1.0143(4)	4246.53(66)	0.0004(2)	1.0055(2)
729.91(18)	0.0015(3)	1.0141(4)	4332.08(14)	0.0092(5)	1.0055(2)
738.13(8)	0.0125(4)	1.0139(4)	4382.61(30)	0.0027(4)	1.0055(2)
746.36(7)	0.0136(5)	1.0137(4)	4589.42(44)	0.0015(3)	1.0055(2)
752.31(7)	0.0055(7)	1.0136(4)	4644.04(54)	0.0011(3)	1.0055(2)

Table A.2: Energies and relative intensities of prompt γ-rays from the reaction ^{242}Pu(n, γ)^{243}Pu measured at FRM II using sample 2.

E_γ [keV]	rel. Intensity	η_0	E_γ [keV]	rel. Intensity	η_0
96.06(10)	0.0728(40)	1.2258(82)	780.97(9)	0.0038(3)	1.0159(4)
125.72(171)	0.0013(33)	1.4203(957)	787.17(72)	0.0042(14)	1.0158(4)
159.13(25)	0.0018(6)	1.2318(90)	791.38(8)	0.0148(8)	1.0156(4)
184.20(8)	0.0230(12)	1.1619(61)	805.03(16)	0.0036(5)	1.0153(4)
219.50(8)	0.0138(8)	1.1072(41)	813.83(8)	0.0394(20)	1.0152(4)
229.15(8)	0.0135(9)	1.0990(37)	831.06(11)	0.0042(4)	1.0149(4)
233.58(14)	0.0024(3)	1.0934(35)	838.50(11)	0.0063(6)	1.0148(4)
241.97(7)	0.0857(49)	1.0865(32)	841.52(15)	0.0027(4)	1.0148(4)
261.61(8)	0.0101(5)	1.0722(28)	844.58(9)	0.0070(5)	1.0147(4)
263.26(11)	0.0017(1)	1.0725(28)	847.76(9)	0.0129(7)	1.0147(4)
275.35(9)	0.0237(14)	1.0662(25)	850.28(9)	0.0144(8)	1.0146(4)
278.18(15)	0.0029(11)	1.0656(25)	862.38(15)	0.0052(6)	1.0145(4)
284.30(11)	0.0143(72)	1.0624(24)	867.34(9)	0.0137(8)	1.0144(4)
287.73(10)	1.0000(505)	1.0586(23)	870.87(14)	0.0046(6)	1.0143(4)
333.19(35)	0.0006(3)	1.0474(18)	874.13(10)	0.0104(7)	1.0143(4)
343.86(10)	0.0267(14)	1.0444(17)	880.53(26)	0.0027(5)	1.0142(4)
345.44(29)	0.0011(3)	1.0442(17)	887.38(9)	0.0131(7)	1.0141(4)
385.86(10)	0.0071(4)	1.0362(15)	889.29(9)	0.0273(14)	1.0140(4)
388.13(19)	0.0013(2)	1.0374(15)	893.56(11)	0.0062(4)	1.0140(4)
400.86(10)	0.0358(19)	1.0334(15)	902.88(9)	0.0216(11)	1.0139(4)
402.56(10)	0.0340(18)	1.0334(15)	913.35(9)	0.0131(7)	1.0137(4)
407.35(10)	0.0173(10)	1.0343(11)	918.39(14)	0.0043(3)	1.0137(4)
416.50(10)	0.1361(71)	1.0331(10)	925.03(18)	0.0019(3)	1.0136(4)
426.03(12)	0.0038(4)	1.0323(10)	932.18(20)	0.0034(5)	1.0135(4)
439.38(10)	0.0054(3)	1.0311(9)	975.89(13)	0.0066(6)	1.0130(4)
444.64(10)	0.0159(8)	1.0306(9)	999.62(15)	0.0041(5)	1.0127(4)
447.32(42)	0.0005(2)	1.0304(9)	1008.63(14)	0.0032(3)	1.0127(4)
480.66(10)	0.0142(10)	1.0274(8)	1015.74(9)	0.0080(5)	1.0126(3)
501.27(10)	0.0244(14)	1.0256(8)	1022.29(9)	0.0114(7)	1.0125(3)
513.90(9)	0.0505(27)	1.0248(7)	1028.17(12)	0.0013(2)	1.0125(3)
516.50(10)	0.0144(13)	1.0247(7)	1031.32(10)	0.0026(2)	1.0124(3)
522.24(9)	0.0202(11)	1.0243(7)	1042.40(10)	0.0087(7)	1.0123(3)
526.27(9)	0.0435(23)	1.0241(7)	1045.86(17)	0.0024(4)	1.0123(3)
534.04(10)	0.0085(5)	1.0236(7)	1050.31(11)	0.0048(6)	1.0123(3)
546.93(12)	0.0085(7)	1.0230(7)	1054.18(14)	0.0043(4)	1.0123(3)
551.63(14)	0.0040(7)	1.0228(7)	1056.32(13)	0.0049(4)	1.0122(3)
555.89(10)	0.0192(12)	1.0226(7)	1070.64(24)	0.0030(5)	1.0121(3)

Continued on the next page

E_γ [keV]	rel. Intensity	η_0	E_γ [keV]	rel. Intensity	η_0
558.07(10)	0.0202(12)	1.0225(7)	1087.03(11)	0.0056(7)	1.0120(3)
560.16(15)	0.0069(6)	1.0224(7)	1091.53(11)	0.0066(7)	1.0120(3)
564.74(10)	0.0408(23)	1.0222(6)	1162.36(15)	0.0049(5)	1.0114(3)
566.36(10)	0.0357(20)	1.0221(6)	1170.37(24)	0.0018(4)	1.0113(3)
573.10(11)	0.0058(5)	1.0218(6)	1176.22(12)	0.0149(14)	1.0113(3)
589.15(10)	0.0112(6)	1.0210(6)	1180.25(14)	0.0034(5)	1.0112(3)
600.54(10)	0.0035(5)	1.0206(6)	1190.58(11)	0.0172(9)	1.0112(3)
607.26(18)	0.0014(2)	1.0204(6)	1196.68(11)	0.0075(4)	1.0111(3)
609.76(9)	0.0103(8)	1.0204(6)	1201.07(11)	0.0108(6)	1.0111(3)
625.24(9)	0.0138(8)	1.0200(6)	3519.03(11)	0.0060(7)	1.0070(2)
633.10(16)	0.0058(6)	1.0197(6)	3544.46(18)	0.0041(4)	1.0070(2)
637.85(10)	0.0071(5)	1.0196(6)	3598.62(19)	0.0021(2)	1.0070(2)
644.12(12)	0.0057(5)	1.0195(6)	3615.36(11)	0.0090(5)	1.0070(2)
646.99(33)	0.0021(6)	1.0194(6)	3648.66(12)	0.0056(3)	1.0070(2)
656.25(9)	0.0110(9)	1.0191(6)	3735.08(11)	0.0044(3)	1.0069(2)
662.40(10)	0.0092(5)	1.0190(5)	3859.53(15)	0.0014(1)	1.0069(2)
663.95(12)	0.0069(4)	1.0189(5)	3906.40(11)	0.0035(2)	1.0069(2)
666.56(30)	0.0003(3)	1.0189(5)	4087.27(14)	0.0027(2)	1.0068(2)
675.78(9)	0.0141(8)	1.0186(5)	4130.60(10)	0.0047(3)	1.0068(2)
679.10(11)	0.0054(5)	1.0186(5)	4222.35(12)	0.0034(2)	1.0068(2)
683.11(10)	0.0089(7)	1.0185(5)	4226.59(10)	0.0085(5)	1.0068(2)
714.76(15)	0.0024(2)	1.0176(5)	4246.01(51)	0.0003(1)	1.0068(2)
716.85(10)	0.0047(3)	1.0176(5)	4332.10(9)	0.0083(5)	1.0068(2)
729.84(13)	0.0023(3)	1.0172(5)	4359.60(79)	0.0003(1)	1.0068(2)
738.15(8)	0.0120(8)	1.0170(5)	4382.76(12)	0.0025(2)	1.0068(2)
746.36(8)	0.0146(8)	1.0168(5)	4589.21(16)	0.0015(1)	1.0067(2)
752.46(8)	0.0048(5)	1.0167(5)	4644.43(17)	0.0015(1)	1.0067(2)
757.21(10)	0.0049(5)	1.0165(5)			

Table A.3: Energies and relative intensities of γ-rays measured at both FRM II and BRR in excellent agreement, that are thus possibly prompt γ-rays of ^{242}Pu neutron capture.

E_γ [keV]	rel. Intensity	E_γ [keV]	rel. Intensity
137.57(10)	0.0048(3)	1350.77(16)	0.0049(4)
156.34(9)	0.0277(17)	1494.48(16)	0.0042(4)
162.03(9)	0.0038(4)	1682.43(10)	0.0118(5)
165.46(8)	0.0400(8)	1863.28(21)	0.0033(4)
171.55(22)	0.0008(2)	1907.69(20)	0.0025(3)
212.42(16)	0.0007(2)	1947.51(16)	0.0052(5)
257.69(22)	0.0004(1)	2051.33(14)	0.0039(5)
266.65(11)	0.0017(2)	2055.69(17)	0.0039(4)
269.90(10)	0.0018(2)	2238.36(23)	0.0032(4)
307.15(13)	0.0011(1)	2324.97(12)	0.0056(4)
309.04(9)	0.0033(2)	2454.75(39)	0.0017(4)
320.68(17)	0.0013(2)	2488.69(30)	0.0017(3)
331.53(8)	0.0193(4)	2534.79(30)	0.0027(4)
376.62(14)	0.0007(1)	2670.06(8)	0.0093(5)
405.54(33)	0.0010(3)	2680.80(12)	0.0027(3)
417.80(12)	0.0089(14)	2773.90(36)	0.0014(3)
434.60(19)	0.0011(2)	2777.77(18)	0.0052(4)
490.75(7)	0.0008(1)	2783.42(56)	0.0021(5)
503.30(16)	0.0049(5)	2856.94(16)	0.0038(4)
536.00(15)	0.0019(2)	2867.35(21)	0.0048(5)
542.32(28)	0.0018(6)	2873.90(12)	0.0062(5)
622.26(17)	0.0028(4)	2877.45(17)	0.0044(4)
630.77(26)	0.0012(3)	2918.42(9)	0.0047(3)
656.21(8)	0.0118(8)	2938.74(24)	0.0017(2)
659.94(32)	0.0009(2)	2948.22(12)	0.0073(4)
668.95(31)	0.0010(3)	3001.57(13)	0.0027(4)
724.37(22)	0.0011(2)	3012.42(10)	0.0055(3)
743.58(19)	0.0012(3)	3095.71(9)	0.0056(3)
749.51(23)	0.0009(3)	3214.39(15)	0.0028(2)
759.27(18)	0.0017(3)	3226.29(12)	0.0038(3)
761.58(20)	0.0014(3)	3233.83(13)	0.0032(2)
831.12(10)	0.0041(4)	3239.14(15)	0.0030(2)
884.78(27)	0.0012(5)	3280.77(17)	0.0020(2)
916.70(28)	0.0018(4)	3343.15(23)	0.0009(1)
947.19(9)	0.0101(6)	3454.43(19)	0.0015(1)
987.86(9)	0.0070(4)	3478.88(12)	0.0051(3)
991.38(10)	0.0064(4)	3492.44(14)	0.0032(2)

Continued on the next page

E_γ [keV]	rel. Intensity	E_γ [keV]	rel. Intensity
997.97(39)	0.0015(4)	3602.19(13)	0.0045(3)
1006.41(34)	0.0009(2)	3835.26(35)	0.0004(1)
1084.13(38)	0.0009(3)	3845.49(16)	0.0013(1)
1206.92(25)	0.0012(2)		

A.2 Data sets from ^{237}Np neutron irradiations

Table A.4: Energies and relative intensities of prompt γ-rays from the reaction $^{237}\mathrm{Np}(\mathrm{n},\gamma)^{238}\mathrm{Np}$ measured at BRR using sample 8.

E_γ [keV]	rel. Intensity	η_0	E_γ [keV]	rel. Intensity	η_0
49.32(10)	0.6670(199)	1.5897(241)	557.42(9)	0.0126(4)	1.0123(3)
54.31(21)	0.0279(135)	1.4481(188)	565.34(9)	0.0260(17)	1.0121(3)
60.16(12)	0.0464(43)	1.3372(129)	571.53(12)	0.0083(16)	1.0119(3)
66.65(10)	0.0035(9)	1.2558(97)	581.78(12)	0.0085(14)	1.0117(3)
72.72(11)	0.0403(13)	1.2022(74)	584.46(9)	0.0332(7)	1.0116(3)
73.63(17)	0.0376(11)	1.1971(73)	588.04(9)	0.0146(18)	1.0116(3)
75.03(10)	0.0495(132)	1.1875(69)	603.14(9)	0.0212(41)	1.0113(3)
76.94(12)	0.0107(12)	1.1759(64)	606.77(10)	0.0201(59)	1.0113(3)
79.48(13)	0.0091(20)	1.1621(57)	609.88(47)	0.0071(28)	1.0112(3)
82.16(10)	0.0381(22)	1.1486(52)	612.90(22)	0.0156(50)	1.0112(3)
86.44(10)	0.2254(53)	1.1324(45)	614.80(37)	0.0020(20)	1.0112(3)
92.28(14)	0.0043(114)	1.1113(38)	620.38(9)	0.0464(22)	1.0111(3)
96.87(10)	0.0520(444)	1.0993(33)	625.70(15)	0.0065(9)	1.0110(3)
98.33(10)	0.0222(434)	1.0957(32)	631.20(11)	0.0119(9)	1.0109(3)
107.53(11)	0.0242(107)	1.0777(101)	633.55(10)	0.0134(9)	1.0109(3)
109.53(12)	0.1183(245)	1.0740(129)	648.28(7)	0.0748(15)	1.0107(3)
118.20(32)	0.0515(464)	1.0630(107)	2629.70(25)	0.0021(4)	1.0045(1)
121.29(27)	0.0081(29)	1.2015(418)	3378.61(27)	0.0056(8)	1.0041(1)
129.53(11)	0.0030(2)	1.1707(349)	3385.82(28)	0.0033(5)	1.0041(1)
133.16(10)	0.0055(2)	1.1597(253)	3666.12(20)	0.0032(3)	1.0040(1)
135.92(10)	0.0495(22)	1.1521(172)	3776.66(12)	0.0064(3)	1.0040(1)
139.75(10)	0.0028(4)	1.1418(60)	3942.71(12)	0.0037(2)	1.0039(1)
141.43(16)	0.0019(2)	1.1381(51)	3978.96(14)	0.0034(2)	1.0039(1)
144.20(11)	0.0071(2)	1.1318(49)	3995.80(19)	0.0026(5)	1.0039(1)
152.85(10)	0.0427(17)	1.1142(42)	4002.65(14)	0.0030(2)	1.0039(1)
153.74(10)	0.0336(12)	1.1130(41)	4039.99(24)	0.0023(2)	1.0039(1)
156.35(10)	0.3474(109)	1.1089(39)	4080.50(19)	0.0037(3)	1.0039(1)
160.54(10)	0.0279(7)	1.1013(37)	4095.01(14)	0.0040(4)	1.0039(1)
162.91(10)	0.0016(4)	1.0984(36)	4103.35(11)	0.0097(3)	1.0039(1)
175.13(71)	0.0012(2)	1.0828(32)	4112.40(13)	0.0064(4)	1.0039(1)
176.45(10)	0.0047(2)	1.0817(29)	4117.44(25)	0.0032(3)	1.0039(1)
179.44(10)	0.0026(2)	1.0795(28)	4124.90(15)	0.0044(4)	1.0039(1)
182.81(10)	1.0000(132)	1.0766(27)	4156.08(13)	0.0057(2)	1.0039(1)
185.63(71)	0.0005(2)	1.0733(26)	4174.36(14)	0.0066(5)	1.0039(1)
189.05(10)	0.0371(7)	1.0703(25)	4196.86(14)	0.0051(4)	1.0039(1)

Continued on the next page

E_γ [keV]	rel. Intensity	η_0	E_γ [keV]	rel. Intensity	η_0
196.54(10)	0.0078(4)	1.0648(23)	4212.32(20)	0.0034(4)	1.0039(1)
198.34(10)	0.0021(4)	1.0629(22)	4228.54(42)	0.0025(2)	1.0039(1)
215.49(9)	0.0542(10)	1.0534(19)	4232.20(13)	0.0106(4)	1.0039(1)
217.66(10)	0.0217(27)	1.0522(18)	4312.96(19)	0.0030(3)	1.0039(1)
218.44(17)	0.0049(12)	1.0518(18)	4324.62(12)	0.0072(2)	1.0039(1)
223.45(10)	0.0043(2)	1.0489(17)	4345.40(14)	0.0045(5)	1.0039(1)
232.40(9)	0.0454(8)	1.0459(16)	4368.64(14)	0.0033(5)	1.0039(1)
233.67(10)	0.0121(3)	1.0454(16)	4381.74(14)	0.0039(2)	1.0039(1)
236.00(9)	0.0519(10)	1.0443(15)	4400.34(30)	0.0013(2)	1.0039(1)
243.93(9)	0.2626(48)	1.0420(15)	4441.21(21)	0.0024(2)	1.0038(1)
250.34(9)	0.0245(6)	1.0397(14)	4454.49(33)	0.0012(2)	1.0038(1)
261.96(18)	0.0004(2)	1.0361(13)	4461.01(21)	0.0020(2)	1.0038(1)
264.52(10)	0.0060(3)	1.0350(12)	4501.63(13)	0.0056(2)	1.0038(1)
271.72(10)	0.0312(14)	1.0327(12)	4516.68(24)	0.0020(2)	1.0038(1)
278.53(9)	0.0019(3)	1.0318(11)	4540.06(18)	0.0031(2)	1.0038(1)
281.63(9)	0.0122(3)	1.0308(11)	4557.36(17)	0.0026(2)	1.0038(1)
289.03(9)	0.0117(4)	1.0300(10)	4570.61(22)	0.0021(3)	1.0038(1)
294.21(9)	0.0213(4)	1.0295(10)	4584.73(14)	0.0051(2)	1.0038(1)
297.66(9)	0.0584(13)	1.0288(10)	4619.24(14)	0.0049(2)	1.0038(1)
298.98(26)	0.0061(23)	1.0285(10)	4655.06(31)	0.0027(2)	1.0038(1)
302.75(14)	0.0011(3)	1.0275(10)	4673.61(28)	0.0019(2)	1.0038(1)
314.31(9)	0.0039(2)	1.0258(10)	4678.23(13)	0.0143(4)	1.0038(1)
329.61(25)	0.0014(5)	1.0242(9)	4687.39(26)	0.0036(2)	1.0038(1)
332.21(9)	0.0708(64)	1.0234(9)	4690.76(15)	0.0064(7)	1.0038(1)
334.18(20)	0.0028(5)	1.0228(9)	4705.56(21)	0.0022(2)	1.0038(1)
346.82(10)	0.0095(3)	1.0226(8)	4723.90(29)	0.0021(2)	1.0038(1)
351.45(10)	0.0050(7)	1.0224(9)	4764.69(18)	0.0029(2)	1.0038(1)
367.60(12)	0.0030(2)	1.0192(8)	4779.04(13)	0.0136(3)	1.0038(1)
369.01(10)	0.0050(3)	1.0208(8)	4794.88(22)	0.0014(1)	1.0038(1)
374.20(17)	0.0031(5)	1.0187(8)	4813.98(16)	0.0076(2)	1.0038(1)
375.36(9)	0.0071(29)	1.0190(8)	4840.45(15)	0.0012(4)	1.0038(1)
380.21(10)	0.0030(5)	1.0192(8)	4868.93(13)	0.0104(3)	1.0038(1)
382.72(22)	0.0028(4)	1.0195(8)	4887.22(21)	0.0018(2)	1.0038(1)
384.05(10)	0.0120(19)	1.0199(8)	4903.70(14)	0.0062(4)	1.0038(1)
391.26(9)	0.0188(8)	1.0188(8)	4921.22(20)	0.0025(2)	1.0038(1)
405.29(10)	0.0180(16)	1.0179(5)	4960.50(19)	0.0014(1)	1.0038(1)
410.47(24)	0.0024(5)	1.0176(5)	5030.19(14)	0.0110(6)	1.0038(1)
417.80(16)	0.0034(6)	1.0172(5)	5046.59(14)	0.0100(4)	1.0038(1)
430.91(9)	0.0428(19)	1.0166(5)	5101.51(19)	0.0046(4)	1.0038(1)
432.20(21)	0.0016(6)	1.0166(5)	5114.61(34)	0.0019(2)	1.0038(1)

Continued on the next page

E_γ [keV]	rel. Intensity	η_0	E_γ [keV]	rel. Intensity	η_0
442.03(17)	0.0058(17)	1.0162(5)	5119.05(26)	0.0056(4)	1.0038(1)
461.51(9)	0.0264(6)	1.0154(4)	5140.52(16)	0.0034(2)	1.0038(1)
496.50(9)	0.0333(8)	1.0139(4)	5155.00(43)	0.0007(1)	1.0038(1)
498.07(9)	0.0102(6)	1.0138(4)	5229.35(15)	0.0027(1)	1.0037(1)
530.63(13)	0.0213(62)	1.0129(4)	5238.16(14)	0.0098(2)	1.0037(1)
538.38(12)	0.0363(123)	1.0127(3)	5271.76(18)	0.0027(3)	1.0037(1)
541.26(13)	0.0301(97)	1.0126(3)	5305.07(21)	0.0018(1)	1.0037(1)
550.95(10)	0.0064(4)	1.0124(3)	5352.09(14)	0.0251(5)	1.0037(1)
552.14(9)	0.0111(5)	1.0124(3)	5488.01(21)	0.0009(1)	1.0037(1)
555.29(9)	0.0217(5)	1.0123(3)			

Table A.5: Energies and relative intensities of prompt γ-rays from the reaction $^{237}\mathrm{Np}(\mathrm{n},\gamma)^{238}\mathrm{Np}$ measured at BRR using sample 9.

E_γ [keV]	rel. Intensity	η_0	E_γ [keV]	rel. Intensity	η_0
49.34(10)	0.6481(190)	1.5545(224)	530.63(10)	0.0216(18)	1.0123(3)
60.43(10)	0.0346(77)	1.3156(119)	538.35(9)	0.0354(19)	1.0121(3)
72.95(10)	0.0345(95)	1.1902(69)	541.32(9)	0.0312(21)	1.0121(3)
75.05(10)	0.0533(61)	1.1771(65)	552.08(15)	0.0103(23)	1.0118(3)
76.93(17)	0.0070(28)	1.1667(61)	555.21(9)	0.0213(6)	1.0118(3)
79.50(14)	0.0070(15)	1.1534(54)	557.26(10)	0.0116(5)	1.0117(3)
82.22(10)	0.0370(16)	1.1412(49)	620.38(9)	0.0422(9)	1.0106(3)
86.48(10)	0.2387(285)	1.1240(42)	625.44(13)	0.0059(5)	1.0105(3)
92.31(12)	0.0125(134)	1.1059(36)	631.15(10)	0.0119(6)	1.0105(3)
96.83(10)	0.0577(438)	1.0943(31)	633.47(10)	0.0125(5)	1.0104(3)
98.35(10)	0.0492(354)	1.0911(30)	648.27(8)	0.0763(18)	1.0103(3)
107.60(12)	0.0150(129)	1.0737(96)	3379.49(22)	0.0065(5)	1.0039(1)
109.27(19)	0.0947(146)	1.0714(120)	3665.44(25)	0.0039(5)	1.0039(1)
110.96(10)	0.0207(421)	1.0681(118)	3776.56(19)	0.0052(5)	1.0038(1)
117.58(10)	0.0346(255)	1.0601(102)	3942.66(21)	0.0043(5)	1.0038(1)
121.27(27)	0.0092(27)	1.1902(399)	3979.02(27)	0.0043(6)	1.0038(1)
129.43(13)	0.0031(4)	1.1617(330)	3995.25(30)	0.0036(5)	1.0038(1)
133.10(13)	0.0056(5)	1.1510(240)	4002.94(41)	0.0029(4)	1.0038(1)
135.93(10)	0.0526(19)	1.1445(162)	4043.54(31)	0.0033(4)	1.0038(1)
141.38(19)	0.0024(3)	1.1315(49)	4094.88(23)	0.0049(9)	1.0037(1)
144.41(14)	0.0057(6)	1.1250(46)	4103.42(12)	0.0098(5)	1.0037(1)
152.98(13)	0.0463(43)	1.1085(39)	4112.66(18)	0.0056(5)	1.0037(1)
153.89(14)	0.0306(63)	1.1073(39)	4117.97(22)	0.0035(4)	1.0037(1)
156.40(10)	0.3468(65)	1.1032(37)	4125.10(22)	0.0034(5)	1.0037(1)

Continued on the next page

E_γ [keV]	rel. Intensity	η_0	E_γ [keV]	rel. Intensity	η_0
160.60(10)	0.0281(10)	1.0970(35)	4156.01(20)	0.0050(3)	1.0037(1)
162.88(12)	0.0035(7)	1.0937(34)	4174.50(17)	0.0064(5)	1.0037(1)
176.66(18)	0.0047(7)	1.0784(28)	4196.66(18)	0.0048(4)	1.0037(1)
179.82(21)	0.0032(9)	1.0749(26)	4232.01(14)	0.0115(5)	1.0037(1)
182.85(10)	1.0000(131)	1.0722(25)	4312.01(29)	0.0039(7)	1.0037(1)
189.07(10)	0.0369(7)	1.0670(23)	4324.66(19)	0.0072(6)	1.0037(1)
196.55(10)	0.0073(7)	1.0614(21)	4345.52(19)	0.0049(4)	1.0037(1)
215.50(10)	0.0545(10)	1.0513(18)	4368.83(23)	0.0028(4)	1.0037(1)
217.75(10)	0.0238(12)	1.0501(17)	4381.88(24)	0.0035(4)	1.0037(1)
218.98(26)	0.0025(6)	1.0492(17)	4399.14(69)	0.0012(4)	1.0037(1)
223.56(11)	0.0040(3)	1.0465(16)	4441.49(33)	0.0029(5)	1.0037(1)
232.40(10)	0.0449(8)	1.0439(15)	4501.58(19)	0.0053(4)	1.0037(1)
233.62(11)	0.0119(4)	1.0428(15)	4516.89(57)	0.0022(4)	1.0037(1)
236.01(9)	0.0517(10)	1.0416(14)	4539.38(36)	0.0029(4)	1.0037(1)
243.93(9)	0.2637(49)	1.0386(14)	4584.71(19)	0.0057(5)	1.0037(1)
250.32(10)	0.0237(6)	1.0385(16)	4619.14(22)	0.0045(4)	1.0037(1)
264.50(10)	0.0061(4)	1.0338(12)	4678.25(15)	0.0140(6)	1.0036(1)
271.74(10)	0.0390(57)	1.0318(11)	4705.95(37)	0.0019(3)	1.0036(1)
281.59(10)	0.0129(3)	1.0295(10)	4724.16(51)	0.0021(4)	1.0036(1)
289.00(9)	0.0136(5)	1.0277(11)	4765.10(24)	0.0034(3)	1.0036(1)
294.21(10)	0.0223(7)	1.0282(10)	4779.06(14)	0.0135(6)	1.0036(1)
297.66(9)	0.0592(12)	1.0273(10)	4794.68(51)	0.0012(3)	1.0036(1)
302.68(27)	0.0005(5)	1.0264(10)	4814.19(16)	0.0086(5)	1.0036(1)
332.20(9)	0.0709(14)	1.0223(8)	4840.82(22)	0.0012(4)	1.0036(1)
346.80(10)	0.0094(9)	1.0216(8)	4868.82(15)	0.0109(5)	1.0036(1)
351.43(11)	0.0050(7)	1.0214(9)	4887.15(29)	0.0023(3)	1.0036(1)
356.34(23)	0.0008(4)	1.0203(8)	4921.04(31)	0.0023(3)	1.0036(1)
367.68(25)	0.0027(8)	1.0193(8)	5030.16(19)	0.0111(9)	1.0036(1)
368.90(18)	0.0047(8)	1.0192(8)	5046.75(15)	0.0101(5)	1.0036(1)
375.33(9)	0.0104(11)	1.0185(8)	5101.70(25)	0.0045(3)	1.0036(1)
380.01(17)	0.0017(4)	1.0185(7)	5114.44(40)	0.0025(4)	1.0036(1)
383.88(10)	0.0124(5)	1.0183(7)	5118.96(24)	0.0066(4)	1.0036(1)
391.25(9)	0.0197(8)	1.0179(9)	5140.83(28)	0.0032(8)	1.0036(1)
405.16(11)	0.0185(16)	1.0171(5)	5154.27(68)	0.0009(4)	1.0036(1)
417.77(25)	0.0036(11)	1.0164(5)	5229.44(25)	0.0022(3)	1.0036(1)
430.86(10)	0.0423(45)	1.0159(4)	5238.10(16)	0.0100(5)	1.0036(1)
442.06(15)	0.0054(5)	1.0154(4)	5305.10(42)	0.0019(3)	1.0036(1)
461.43(10)	0.0261(9)	1.0147(4)	5352.07(15)	0.0238(8)	1.0036(1)
496.44(10)	0.0336(15)	1.0133(4)	5487.90(55)	0.0012(2)	1.0036(1)
497.98(13)	0.0111(5)	1.0132(4)			

Table A.6: Energies and relative intensities of prompt γ-rays from the reaction ^{237}Np(n, γ)^{238}Np measured at FRM II using sample 8.

E_γ [keV]	rel. Intensity	η_0	E_γ [keV]	rel. Intensity	η_0
49.27(17)	0.6530(896)	1.7261(315)	571.10(14)	0.0096(16)	1.0147(4)
60.24(18)	0.0333(47)	1.4088(168)	584.45(12)	0.0364(68)	1.0143(4)
67.22(20)	0.0037(13)	1.3039(120)	588.05(22)	0.0169(89)	1.0142(4)
72.46(71)	0.0307(48)	1.2507(120)	603.05(11)	0.0235(22)	1.0139(4)
73.42(71)	0.0283(45)	1.2407(114)	606.75(11)	0.0223(18)	1.0138(4)
74.93(18)	0.0440(25)	1.2275(87)	610.96(25)	0.0050(8)	1.0137(4)
76.85(18)	0.0107(12)	1.2135(80)	612.51(12)	0.0242(19)	1.0137(4)
79.67(19)	0.0068(15)	1.1929(73)	614.47(26)	0.0028(6)	1.0137(4)
82.28(18)	0.0326(24)	1.1791(66)	620.38(12)	0.0435(22)	1.0136(4)
86.64(17)	0.2186(113)	1.1565(59)	625.46(16)	0.0067(6)	1.0135(4)
92.59(22)	0.0051(34)	1.1329(48)	631.16(13)	0.0108(7)	1.0134(4)
97.19(17)	0.0100(302)	1.1196(42)	633.50(12)	0.0124(8)	1.0134(4)
99.01(17)	0.0553(64)	1.1153(40)	648.29(8)	0.0755(50)	1.0132(4)
107.33(20)	0.0499(122)	1.0941(120)	3379.39(23)	0.0061(5)	1.0050(1)
109.78(18)	0.1014(70)	1.0888(159)	3385.41(27)	0.0035(3)	1.0050(1)
118.52(17)	0.0250(90)	1.0746(131)	3666.57(29)	0.0044(4)	1.0049(1)
121.36(42)	0.0087(41)	1.2435(522)	3776.73(19)	0.0061(4)	1.0049(1)
129.62(24)	0.0033(7)	1.2068(434)	3942.47(22)	0.0045(3)	1.0048(1)
133.24(19)	0.0054(5)	1.1956(313)	3978.41(24)	0.0032(4)	1.0048(1)
135.90(17)	0.0524(27)	1.1839(215)	3995.88(40)	0.0020(4)	1.0048(1)
144.19(19)	0.0049(15)	1.1599(61)	4002.43(24)	0.0025(2)	1.0048(1)
156.34(16)	0.3238(275)	1.1313(51)	4039.50(40)	0.0031(3)	1.0048(1)
160.51(16)	0.0253(17)	1.1236(46)	4080.16(34)	0.0038(6)	1.0048(1)
162.98(19)	0.0026(6)	1.1197(45)	4095.05(23)	0.0042(9)	1.0048(1)
175.56(28)	0.0008(4)	1.1023(39)	4103.31(17)	0.0093(6)	1.0048(1)
176.52(17)	0.0044(10)	1.0995(37)	4112.44(19)	0.0061(4)	1.0048(1)
179.49(17)	0.0031(4)	1.0944(36)	4117.40(35)	0.0033(3)	1.0048(1)
182.80(14)	1.0000(450)	1.0900(38)	4124.73(24)	0.0043(4)	1.0048(1)
184.74(16)	0.0054(14)	1.0900(33)	4155.83(22)	0.0054(3)	1.0048(1)
189.04(16)	0.0334(16)	1.0846(31)	4174.38(21)	0.0060(4)	1.0048(1)
196.53(17)	0.0080(6)	1.0771(29)	4196.85(19)	0.0053(3)	1.0048(1)
215.51(15)	0.0523(25)	1.0642(24)	4212.41(36)	0.0033(5)	1.0048(1)
223.46(17)	0.0037(3)	1.0595(23)	4228.45(42)	0.0023(4)	1.0048(1)
232.48(15)	0.0442(21)	1.0542(21)	4232.04(19)	0.0106(7)	1.0048(1)
233.90(16)	0.0125(7)	1.0549(20)	4313.58(36)	0.0027(2)	1.0047(1)
236.05(15)	0.0487(23)	1.0527(22)	4324.50(20)	0.0073(4)	1.0047(1)
243.98(15)	0.2356(114)	1.0488(22)	4345.29(20)	0.0042(3)	1.0047(1)

Continued on the next page

E_γ [keV]	rel. Intensity	η_0	E_γ [keV]	rel. Intensity	η_0
250.48(15)	0.0214(11)	1.0466(18)	4368.35(23)	0.0029(3)	1.0047(1)
262.28(33)	0.0004(2)	1.0436(18)	4382.38(23)	0.0034(2)	1.0047(1)
264.61(15)	0.0055(4)	1.0427(23)	4400.32(45)	0.0015(2)	1.0047(1)
272.00(15)	0.0336(21)	1.0418(17)	4441.48(28)	0.0022(2)	1.0047(1)
278.75(14)	0.0027(8)	1.0398(16)	4454.57(43)	0.0011(2)	1.0047(1)
281.75(15)	0.0111(6)	1.0377(16)	4460.43(33)	0.0018(2)	1.0047(1)
289.15(15)	0.0114(7)	1.0362(16)	4501.65(20)	0.0056(3)	1.0047(1)
294.29(14)	0.0213(16)	1.0341(15)	4516.80(31)	0.0020(2)	1.0047(1)
295.90(37)	0.0001(6)	1.0359(15)	4539.68(26)	0.0038(3)	1.0047(1)
302.53(22)	0.0017(4)	1.0337(15)	4557.29(36)	0.0021(2)	1.0047(1)
314.54(16)	0.0033(3)	1.0311(14)	4570.94(31)	0.0017(3)	1.0047(1)
330.25(23)	0.0021(3)	1.0281(14)	4584.72(23)	0.0053(4)	1.0047(1)
332.25(14)	0.0680(32)	1.0299(20)	4619.13(21)	0.0048(3)	1.0047(1)
333.92(18)	0.0045(3)	1.0264(13)	4654.29(53)	0.0024(3)	1.0047(1)
340.49(14)	0.0015(9)	1.0276(13)	4672.89(58)	0.0012(2)	1.0047(1)
346.85(14)	0.0095(10)	1.0272(15)	4678.15(20)	0.0132(7)	1.0047(1)
351.56(15)	0.0043(14)	1.0262(14)	4687.29(53)	0.0035(4)	1.0047(1)
356.56(31)	0.0004(5)	1.0260(12)	4690.74(26)	0.0062(7)	1.0047(1)
369.15(19)	0.0048(6)	1.0249(12)	4705.41(30)	0.0021(2)	1.0047(1)
371.22(28)	0.0014(4)	1.0246(12)	4723.49(33)	0.0021(2)	1.0047(1)
380.05(22)	0.0016(5)	1.0235(12)	4764.68(29)	0.0026(2)	1.0047(1)
382.76(26)	0.0025(6)	1.0243(12)	4779.08(20)	0.0138(7)	1.0047(1)
384.05(14)	0.0109(9)	1.0235(14)	4795.31(36)	0.0014(2)	1.0046(1)
391.26(13)	0.0181(13)	1.0214(12)	4813.90(23)	0.0075(5)	1.0046(1)
405.16(13)	0.0208(17)	1.0219(6)	4869.00(21)	0.0101(5)	1.0046(1)
410.71(32)	0.0019(14)	1.0215(6)	4887.19(31)	0.0017(2)	1.0046(1)
417.77(23)	0.0046(13)	1.0211(6)	4904.05(22)	0.0060(3)	1.0046(1)
430.86(12)	0.0438(21)	1.0204(6)	4921.13(27)	0.0028(2)	1.0046(1)
432.56(39)	0.0015(6)	1.0203(6)	4960.36(24)	0.0016(1)	1.0046(1)
442.04(15)	0.0062(5)	1.0198(6)	5030.52(22)	0.0129(10)	1.0046(1)
461.40(12)	0.0257(12)	1.0188(5)	5046.76(21)	0.0095(5)	1.0046(1)
496.34(13)	0.0289(15)	1.0171(5)	5101.47(22)	0.0042(3)	1.0046(1)
497.75(17)	0.0123(8)	1.0170(5)	5113.82(38)	0.0021(2)	1.0046(1)
530.60(12)	0.0216(18)	1.0158(4)	5118.96(26)	0.0066(4)	1.0046(1)
538.36(12)	0.0372(19)	1.0156(4)	5140.60(23)	0.0034(2)	1.0046(1)
541.21(12)	0.0303(20)	1.0155(4)	5154.97(41)	0.0009(1)	1.0046(1)
550.90(18)	0.0056(7)	1.0152(4)	5229.35(21)	0.0028(2)	1.0046(1)
552.15(13)	0.0110(15)	1.0152(4)	5238.19(19)	0.0090(5)	1.0046(1)
555.21(12)	0.0213(12)	1.0151(4)	5304.98(28)	0.0015(1)	1.0046(1)
557.31(12)	0.0119(10)	1.0150(4)	5351.95(19)	0.0219(12)	1.0046(1)

Continued on the next page

E_γ [keV]	rel. Intensity	η_0	E_γ [keV]	rel. Intensity	η_0
565.27(12)	0.0268(29)	1.0148(4)	5488.64(31)	0.0011(1)	1.0046(1)

Table A.7: Energies and relative intensities of γ-rays measured at both FRM II and BRR in excellent agreement, that are thus possibly prompt γ-rays of ^{242}Pu neutron capture.

E_γ [keV]	rel. Intensity	E_γ [keV]	rel. Intensity
345.31(11)	0.0051(3)	723.57(12)	0.0090(6)
348.53(13)	0.0027(2)	755.97(23)	0.0129(22)
401.51(10)	0.0118(9)	758.04(20)	0.0174(23)
426.41(14)	0.0035(5)	777.26(15)	0.0168(15)
428.65(10)	0.0036(2)	783.11(10)	0.0096(8)
450.20(10)	0.0084(3)	891.15(15)	0.0037(5)
452.26(14)	0.0045(3)	900.38(12)	0.0051(5)
454.40(14)	0.0035(4)	913.99(9)	0.0072(5)
458.82(10)	0.0123(7)	922.08(9)	0.0150(4)
488.91(16)	0.0036(7)	929.36(10)	0.0086(4)
502.42(14)	0.0027(9)	955.12(11)	0.0045(4)
527.74(23)	0.0020(6)	1169.27(18)	0.0022(4)
532.63(16)	0.0041(8)	1231.67(12)	0.0041(3)
535.96(11)	0.0075(8)	1382.44(19)	0.0032(4)
544.85(10)	0.0166(15)	2978.72(38)	0.0018(3)
547.84(19)	0.0028(10)	3745.00(36)	0.0027(3)
651.36(10)	0.0081(6)	3919.61(23)	0.0015(2)
653.72(10)	0.0089(8)	3986.85(25)	0.0012(4)
678.04(13)	0.0040(6)	4090.05(23)	0.0015(3)
680.67(9)	0.0136(5)	4130.34(32)	0.0020(3)
682.88(9)	0.0122(4)	4242.15(23)	0.0016(2)
710.61(12)	0.0115(8)	4291.27(23)	0.0014(1)
713.96(16)	0.0057(7)	4487.02(13)	0.0069(2)
716.21(9)	0.0108(6)	4770.15(20)	0.0023(2)
717.96(10)	0.0227(7)	4853.65(28)	0.0012(1)
720.45(10)	0.0184(7)	5164.68(19)	0.0018(1)

APPENDIX B

Level Scheme of ^{243}Pu

The following level scheme of ^{243}Pu is presented in EGAF format, which is similar to the ENSDF format. Levels are denoted by an "L" and γ-ray transitions are denoted by a "G" in the sixth column. After that follows the level/transition energy and then the uncertainty of the energy. For levels the next parameter denotes the spin and parity related to that level. For transitions the emission intensity and associated uncertainty follows after the energy uncertainty. Then the multipolarity of the transition is denoted (In parentheses if tentative). The last two values are the internal conversion coefficient and its uncertainty. A "c" in the fifth column marks a commentary.

```
243PU    242Pu(N,G) E=THERMAL
243PU  N     4.54  28           1.0
243PU cN 243Pu adopted levels from Ca76
243PU2cN with PGAA rel. Int. data on 242Pu
243PU3cN normalize by 7.07(12)b
243PU  L   0.0        7/2+
243PU  L 58.28      8 9/2+
243PU  G 58.3      10 0.0059 22  [M1]                    27.2  4
243PU2cG Based on intensity balance
243PU3cG to close to Am241d so not observed
243PU  L 124.65    10 11/2+
243PU  G 66.37     71 0.0003125  [M1]                    18.61
243PU cG 66 possible transition but unobserved due to Pu243decay peak,
243PU2cG 66 gtol int balance and Dicebox indicate
243PU  G 125.47    71 0.0010  3  [E2]                    5.71  17
243PU  L 207.1     27 13/2+
243PU  L 287.56     6 5/2+
243PU  G 229.15     8 0.0136  5  [E2]                    0.52  1
243PU  G 287.69     8 1.000  12   M1                     1.34  2
243PU  L 299          15/2+
243PU  L 333.43     7  7/2+
243PU  G 45.87     71 0.0019  7  [M1]                    55.26
243PU cG 45.8 most likely transition
243PU2cG 45.8 not observed, though indication at energy cut-off at 45.57
243PU  G 275.28     8 0.0236  6  [M1]                    1.515 22
```

```
243PU  G 333.37    35 0.0004  2  [M1]                    0.889 13
243PU  L 383.64     7 (1/2+)            0.33 US
243PU  G 96.06     11 0.0789 21  [E2]                    19.04 30
243PU  L 387.95    11 (9/2+)
243PU  G  54.48    50 0.0004525  [M1]                    33.2  11
243PU cG  54.48 small and in Am241d thus not visible, but likely as in band transitior
243PU  G 263.24    11 0.0015  1  [M1]                    1.715 24
243PU  G 388.07    15 0.0013  1  [M1]                    0.588 9
243PU cG 387.90 spin assignment only tentative in ensdf
243PU  L 392.32     7 (3/2+)
243PU cG 8.66 to 386 not observed and highly converted but likely [M1] in band trans
243PU  G 8.66      50 0.0007  2  [M1]                    1916
243PU  L 402.57     8  9/2-
243PU  G 277.98     9 0.0030  8  [E1]                    0.0488 7
243PU  G 344.5      5 0.0006  6  [E1]                    0.0307 5
243PU cG not observed in tail of 343.9 keV transition
243PU2cG Intensity based on ENSDF Branching ratio and 402.35 keV peak
243PU  G 402.52     8 0.0353  7   E1                     0.0222 4
243PU cG A similar energy g-ray is assigned to L2030 but it has a 37/2+ spin
243PU2cG thus this should be a clean transition
243PU  L 404.0        17/2+
243PU  L 447.14     8 (5/2+)
243PU  G  54.82    30 0.0092 23  [M1]                    32.6   7
243PU cG  54.9 not observed/next to Am241d maybe there, est with dicebox
243PU  G 447.54    42 0.0004520  [M1]                    0.399  6
243PU  L 450.1        (7/2+)
243PU cG  2.56     90 0.00005 1  [M1]                    1903
243PU cG  2.56 added as in band transition
243PU cL 454        6 11/2-
243PU  L 454          11/2-
243PU cL 466.7     15(11/2+)
243PU  L 466.7       (11/2+)
243PU  L 519         19/2+
243PU cG 220.1
243PU cL 536.6     15(13/2+)
243PU  L 536.6       (13/2+)
243PU cL 564.5     15(9/2+)
243PU  L 564.5       (9/2+)
243PU cL 595.3     15(15/2-)
243PU  L 595.3       (15/2-)
243PU  L 625.64     8 (1/2+)
243PU  G 233.65    10 0.0024  2  [M1]                    2.392
```

```
243PU  G 241.93     7 0.0811 15  [M1]                    2.170
243PU cL 626        2 (9/2+)
243PU  L 626       14 (9/2+)
243PU  L 646.8        21/2+
243PU cG 242.8
243PU  L 653.90     8 (3/2+)
243PU  G 261.58     8 0.0103  4  [M1]                    1.745
243PU  L 677.26     8 (5/2+)
243PU  G 284.32     8 0.0202  6  [M1]                    1.385
243PU  G 343.80     8 0.0135  3  [M1]                    0.820
243PU cG 343.9keV placed two times in Levelscheme, therefore half intensity
243PU  L 704.16     7 (3/2-)
243PU  G 416.50     8 0.1361 53  [E1]                    0.021
243PU cL 734.1     20
243PU  L 734.1
243PU  L 741.8     15(7/2+)
243PU  L 784          23/2+
243PU cG 264.9
243PU  L 790.93     8 (3/2-)
243PU  G 343.80     8 0.0135  3  [E1]                    0.031
243PU cG 343.9keV placed two times in Levelscheme, therefore half intensity
243PU  G 407.32     8 0.0183  4  [E1]                    0.022
243PU  L 809.69     7 1/2+,3/2
243PU cL 809.5 assuming  1/2+ is correct the following multipolarities arise
243PU cG 426.06     7 0.0040  3  [M1]                    0.456
243PU  G 426.06    10 0.0020  2  [M1]                    0.456
243PU cG 426.07keV placed two times in Levelscheme, therefore half intensity
243PU  G 522.25     7 0.0215  5  [E2]                    0.047
243PU  L 813.81     6  3/2+
243PU cG 159.50     5 0.0030  4  [M1]                    7.008
243PU  G 159.47    10 0.0023  4  [M1]                    7.011
243PU cG 159.50 placed two times by me at otherwise not deexited L 446.8
243PU  G 480.63     9 0.0140  6  [E2]                    0.058
243PU  G 526.27     7 0.0448  8  [M1]                    0.257
243PU  G 813.84     7 0.0376  8 18 [E2]                 0.018
243PU  L 834.4     15 (7/2-)
243PU  L 845.61    11 (5/2+)
243PU  G 558.05     9 0.0197  8  [M1]                    0.220
243PU  G 787.17    72 0.0044 13  [E2]                    0.020
243PU cG adjacent Cl-peaks, this is the restpeak
243PU cG 788.45     6 0.0048  5  [E2]                    0.020
243PU cG 844.43    11 0.0064  5  [M1]                    0.072
```

```
243PU  G 845.66    52 0.0037  3  [M1]                    0.072
243PU  L 873.39    11 (1/2-)
243PU  G 219.49     8 0.0138  3  [E1]                    0.083
243PU  L 895.6     15(7/2+)
243PU  L 905.91     8 (1/2-)
243PU  G 513.78     8 0.0543 27  [E1]                    0.014
243PU  G 522.25     7 0.0215  5  [E1]                    0.013
243PU  L 920.6     15 (11/2-)
243PU  L 933.0        25/2+
243PU cG 286.2
243PU  L 948.34     8 (3/2-)
243PU  G 501.14     9 0.0276 14  [E1]                    0.014
243PU  G 555.89     9 0.0185  7  [E1]                    0.012
243PU  G 564.74     8 0.0393 11  [E1]                    0.011
243PU  L 954        2 (9/2+)
243PU  L 981.31     9 (5/2+)
243PU  G 534.06     8 0.0091  3  [M1]                    0.247
243PU  G 589.15     8 0.0112  5  [M1]                    0.190
243PU  G 647.09    33 0.0012  3  [M1]                    0.147
243PU cG 648.8keV placed two times in Levelscheme, therefore half intensity
243PU  G 693.5      7 0.0037 17  [M1]                    0.123
243PU cG 693.5 observed but on edge of Ge-triangle, used ENSDF branching
243PU  L 1044       2
243PU  L 1080       2 (9/2+)
243PU  L 1092         27/2+
243PU cG 307.5
243PU  L 1114       3
243PU cL 1130.1     4 (1/2+,3/2)
243PU  L 1130.17    8 (1/2+)
243PU cL 1130.1 assuming  1/2+ is correct the following multipolarities arise
243PU cG 426.07     6 0.0041  3  [E1]                    0.020
243PU  G 426.06    10 0.0020  2  [E1]                    0.020
243PU cG 426.07keV placed two times in Levelscheme, therefore half intensity
243PU  G 683.13    10 0.0046  4  [E2]                    0.026
243PU cG 683.13keV placed two times in Levelscheme, therefore half intensity
243PU  G 738.14     8 0.0124  4  [M1]                    0.104
243PU  G 746.36     8 0.0139  5  [M1]                    0.101
243PU  L 1145       3
243PU cL 1176.5     3  3/2+,5/2+
243PU cL 1176.5 assuming  3/2+ is correct the following multipolarities arise
243PU cG 385.83     2 0.0075  4  [E1]                    0.024
243PU cG 551.59    10 0.0038  6  [M1]                    0.575
```

```
243PU cG 730.1      7 0.0023  9  [M1]                    0.107
243PU cG 730.1 observed but not fitable, Ge-triangle and background,
243PU2cG ENSDF intensity used
243PU cL 1176.5 assuming  5/2+ is correct the following multipolarities arise
243PU  L 1176.83    7  5/2+
243PU  G 385.84     8 0.0071  2  [E1]                    0.024
243PU  G 551.60    12 0.0040  6  [M2]                    0.575
243PU  G 729.87    13 0.0019  3  [M1]                    0.107
243PU  G 843.40    52 0.0037  3  [M1]                    0.072
243PU  G 889.31     8 0.0272  6  [M1]                    0.063
243PU  G 1176.43   12 0.0119 13  [M1]                    0.030
243PU  L 1197       3
243PU  L 1213.02   16 (5/2-)
243PU  G 880.38    23 0.0026  5  [E1]                    0.0050
243PU  G 924.98    18 0.0019  3  [E1]                    0.0046
243PU  L 1233       3
243PU  L 1243       3
243PU  L 1261.1       29/2+
243PU  L 1265       3
243PU  L 1286       3
243PU cL 1301.26   11
243PU cL 1301.6     5 1/2,3/2
243PU  L 1301.47    9 (3/2+)
243PU cL 1301.6 assuming 3/2+ the following multipolarities arise
243PU cG 647.54    39 0.0028  7  [M1]                    0.147
243PU  G 647.09    33 0.0012  3  [M1]                    0.147
243PU cG 648.8keV placed two times in Levelscheme, therefore half intensity
243PU  G 675.78     8 0.0140  8  [M1]                    0.131
243PU  G 918.44    15 0.0042  3  [M1]                    0.058
243PU  L 1324       2
243PU  L 1354       2
243PU  L 1359       3
243PU cL 1367.8     6  1/2,3/2
243PU  L 1368.31   10  (1/2+)
243PU cL 1367.8 assuming positive parity, multipolarities arise
243PU  G 663.98    12 0.0060  4  [E1]                    0.008
243PU  G 714.77    15 0.0020  2  [M1]                    0.113
243PU  G 975.93    13 0.0068  6  [M1]                    0.049
243PU  L 1387.58    8  3/2+
243PU  G 439.39     9 0.0055  3  [E1]                    0.019
243PU  G 683.13    10 0.0046  4  [E1]                    0.0080
243PU cG 683.13keV placed two times in Levelscheme, therefore half intensity
```

```
243PU  G 1054.23   13 0.0038  4  [E2]                    0.011
243PU  L 1403       3
243PU  L 1420.77    8 (3/2+)
243PU  G 716.78    10 0.0049  3  [E1]                    0.0073
243PU  G 1028.19   12 0.0014  2  [M1]                    0.043
243PU  G 1087.12   11 0.0048  7  [E2]                    0.011
243PU  L 1434.78    8 1/2+,3/2
243PU  G 625.24     8 0.0135  5  [M1]                    0.162
243PU  G 644.10    12 0.0055  5  [E1]                    0.0089
243PU  G 757.18    10 0.0049  5  [M1]                    0.097
243PU  G 780.92     9 0.0035  3  [M1]                    0.089
243PU  G 1042.37    8 0.0074  3  [M1]                    0.041
243PU  L 1437.60   20 31/2+
243PU cG 347.5
243PU  L 1444       3
243PU  L 1465       3
243PU  L 1491.82   20  1/2-,3/2-
243PU  L 1516.39   10  (3/2-)
243PU  G 838.45    10 0.0065  6  [E1]                    0.0055
243PU  L 1627.6       33/2+
243PU cG 366.5
243PU  L 5036.33    7 1/2+
243PU  G 3519.08   11 0.0052  4  [E1]                    0.002
243PU  G 3544.50   18 0.0041  4
243PU  G 3598.70   19 0.0022  2
243PU  G 3615.31   11 0.0089  4
243PU  G 3648.67   12 0.0058  3
243PU  G 3735.02   11 0.0043  3
243PU  G 3859.61   15 0.0014  1
243PU  G 3906.53   11 0.0036  2
243PU  G 4087.22   14 0.0029  2
243PU  G 4130.63   10 0.0047  3
243PU  G 4222.40   12 0.0036  2  [M1]                    0.003
243PU  G 4226.63   10 0.0082  4  [M1]                    0.003
243PU  G 4332.14    9 0.0087  5  [E1]                    0.002
243PU  G 4382.78   12 0.0026  2  [M1]                    0.003
243PU  G 4589.28   16 0.0015  1  [E2]                    0.002
243PU  G 4644.44   17 0.0014  1  [M1]                    0.003
```

APPENDIX C

Population-Depopulation Plots

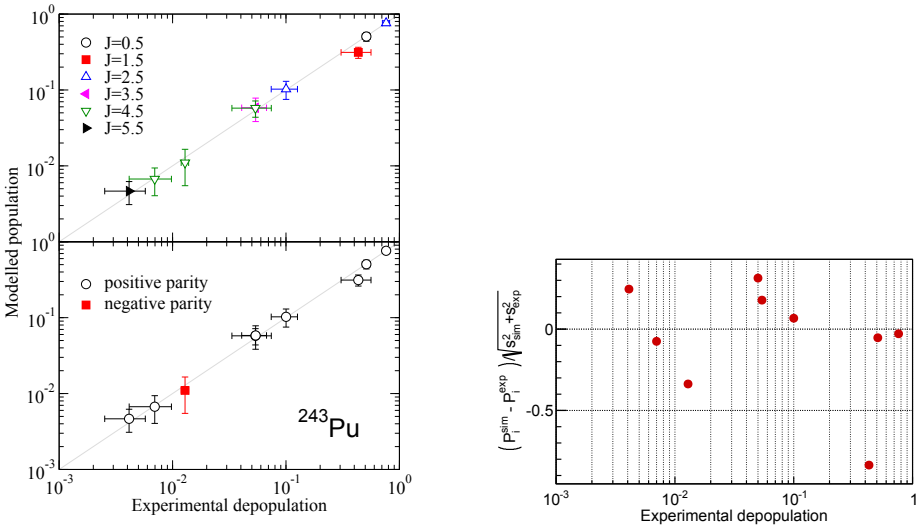

Figure C.1: (a) DICEBOX simulated population (P_i^{sim}) against experimentally determined depopulation (P_i^{exp}) of levels i in ^{243}Pu using the CTF level density model, an EGLO PSF and a single particle strength of $1 \cdot 10^{-8}$ for the $M1$ PSF. (a) Pulls corresponding to this population-depopulation plot. A "1" (or "-1") on the y-axis corresponds to a difference of one standard deviation between P_i^{sim} and P_i^{exp}, where s_{sim} denotes the uncertainty of the simulated population and s_{exp} to the uncertainty of the experimental depopulation.

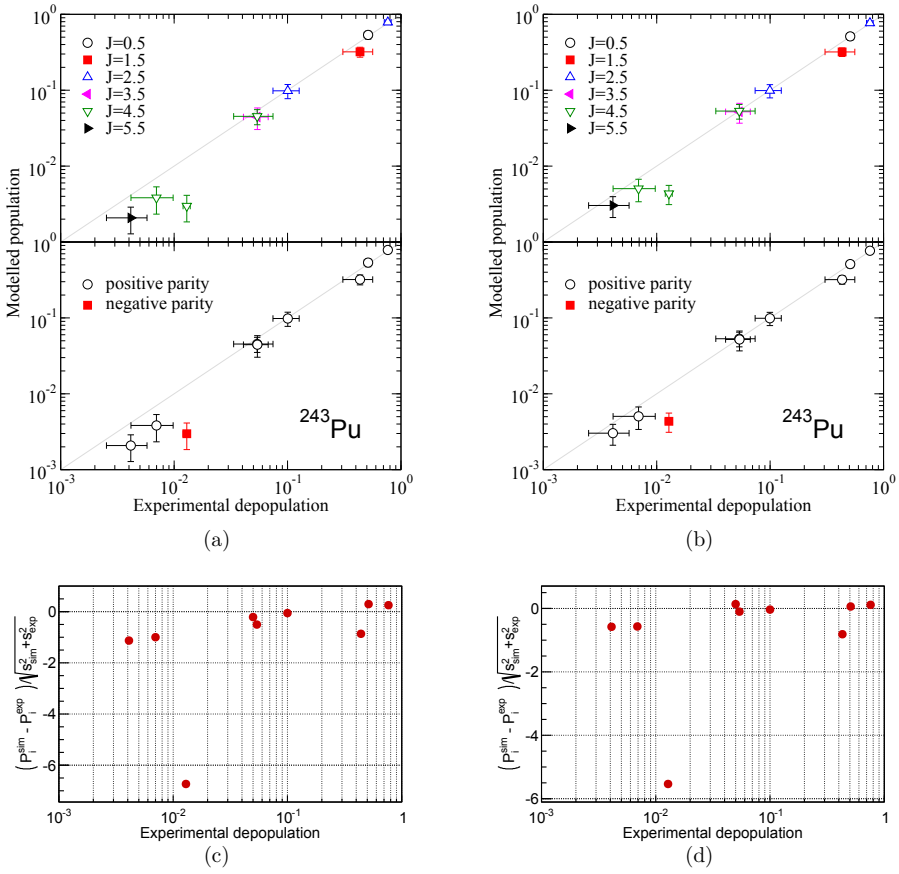

Figure C.2: DICEBOX simulated population (P_i^{sim}) against experimentally determined depopulation (P_i^{exp}) of levels i in ^{243}Pu using (a) the CTF and (b) the BSFG level density model, an BA PSF and a single particle strength (SPS) of $1 \cdot 10^{-8}$ for the $M1$ PSF. The pulls corresponding to the population-depopulation plots are given in (c) for the BA/CTF/SPS model combination shown in plot (a) and in (d) for the BA/BSFG/SPS model combination shown in plot (b). A "1" (or "-1") on the y-axis of these later plots corresponds to a difference of one standard deviation between P_i^{sim} and P_i^{exp}, where s_{sim} denotes the uncertainty of the simulated population and s_{exp} to the uncertainty of the experimental depopulation.

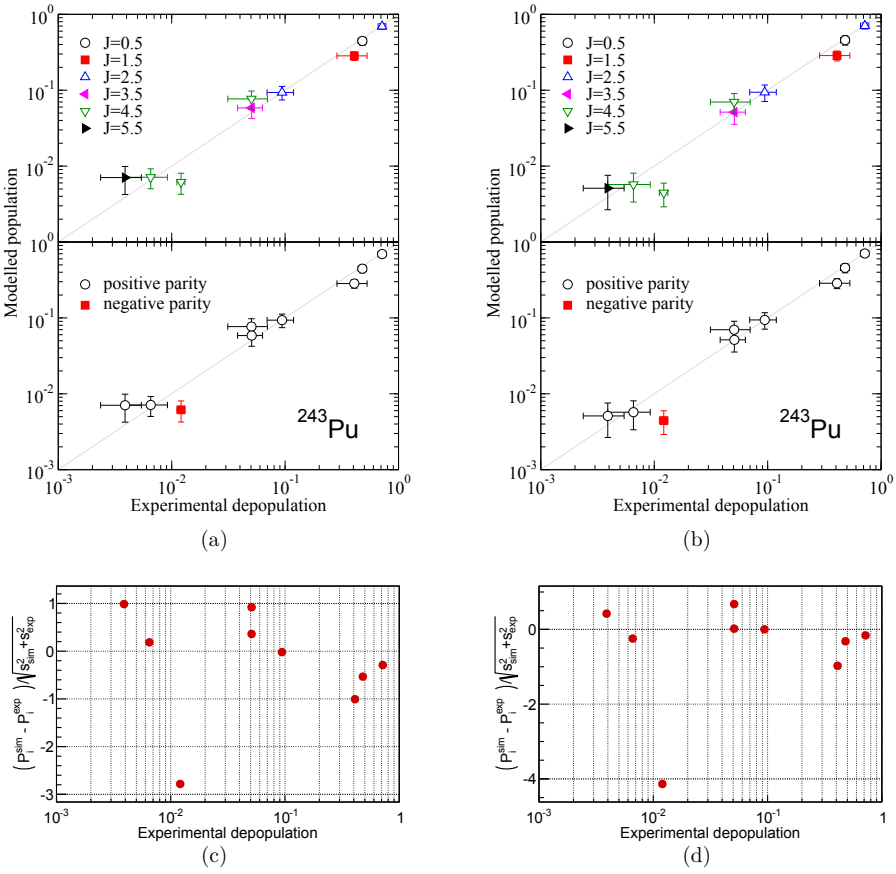

Figure C.3: DICEBOX simulated population (P_i^{sim}) against experimentally determined depopulation (P_i^{exp}) of levels i in ^{243}Pu using (a) the BSFG and (b) the CTF level density model, an EGLO PSF and a Lorentzian model of the GDMR (GLO) for the $M1$ PSF. The pulls corresponding to the population-depopulation plots are given in (c) for the EGLO/BSFG/GLO model combination shown in plot (a) and in (d) for the EGLO/CTF/GLO model combination shown in plot (b). A "1" (or "-1") on the y-axis of these later plots corresponds to a difference of one standard deviation between P_i^{sim} and P_i^{exp}, where s_{sim} denotes the uncertainty of the simulated population and s_{exp} to the uncertainty of the experimental depopulation.

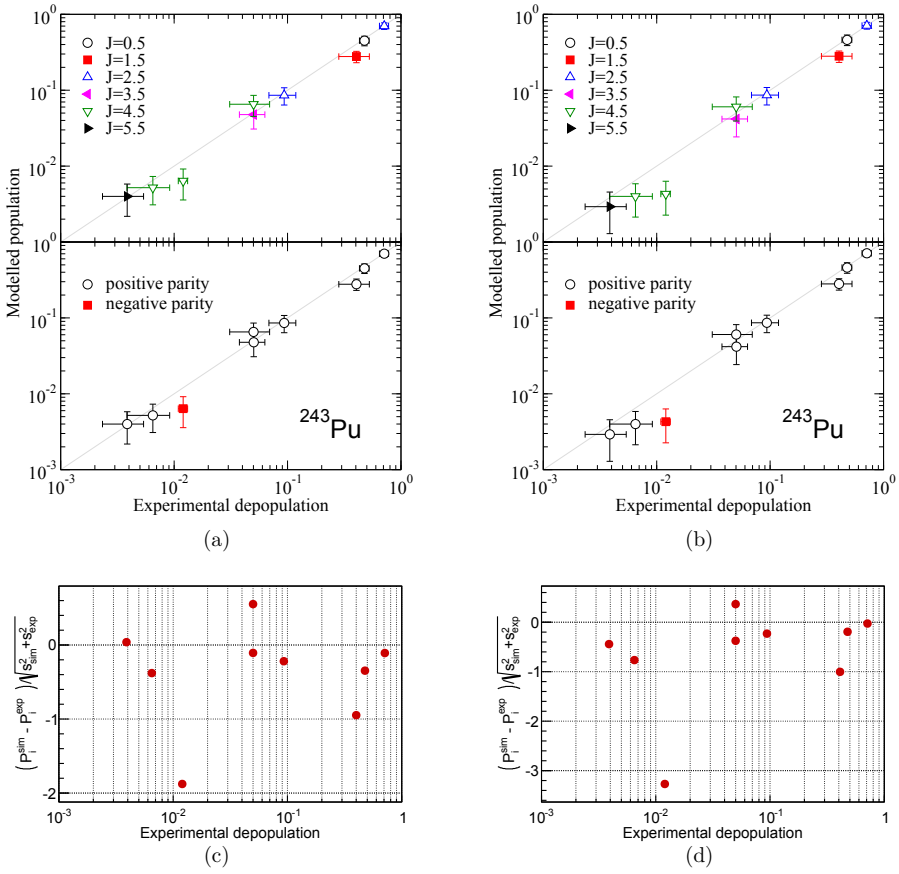

Figure C.4: DICEBOX simulated population (P_i^{sim}) against experimentally determined depopulation (P_i^{exp}) of levels i in ^{243}Pu using (a) the BSFG and (b) the CTF level density model, an BA PSF and a Lorentzian model of the GDMR (GLO) for the $M1$ PSF. The pulls corresponding to the population-depopulation plots are given in (c) for the BA/BSFG/GLO model combination shown in plot (a) and in (d) for the BA/CTF/GLO model combination shown in plot (b). A "1" (or "-1") on the y-axis of these later plots corresponds to a difference of one standard deviation between P_i^{sim} and P_i^{exp}, where s_{sim} denotes the uncertainty of the simulated population and s_{exp} to the uncertainty of the experimental depopulation.

APPENDIX D

Addtional Plots for the ^{237}Np Evaluation

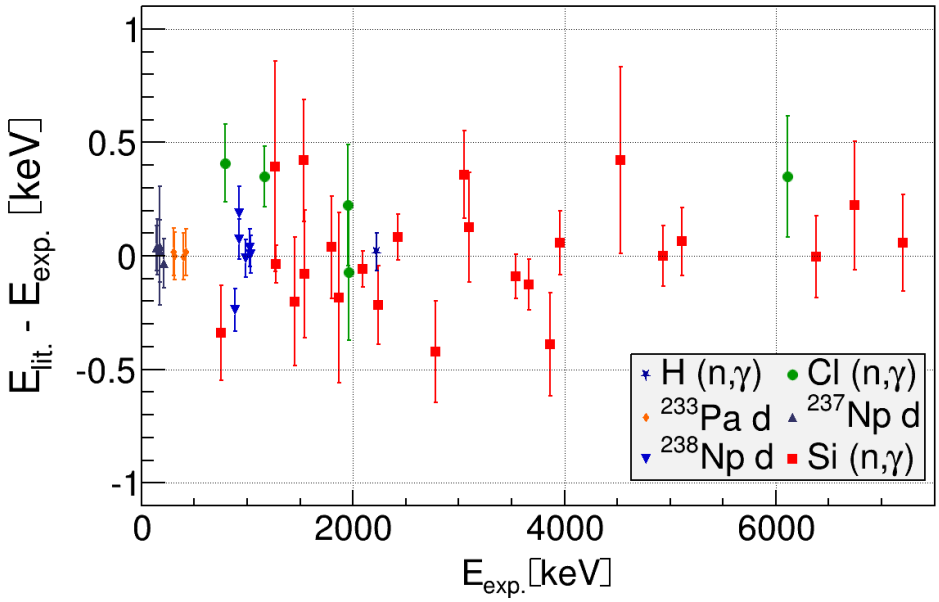

Figure D.1: Comparison of the energies of identified background lines measured during the irradiation of sample 9 at BRR with corresponding tabulated values.

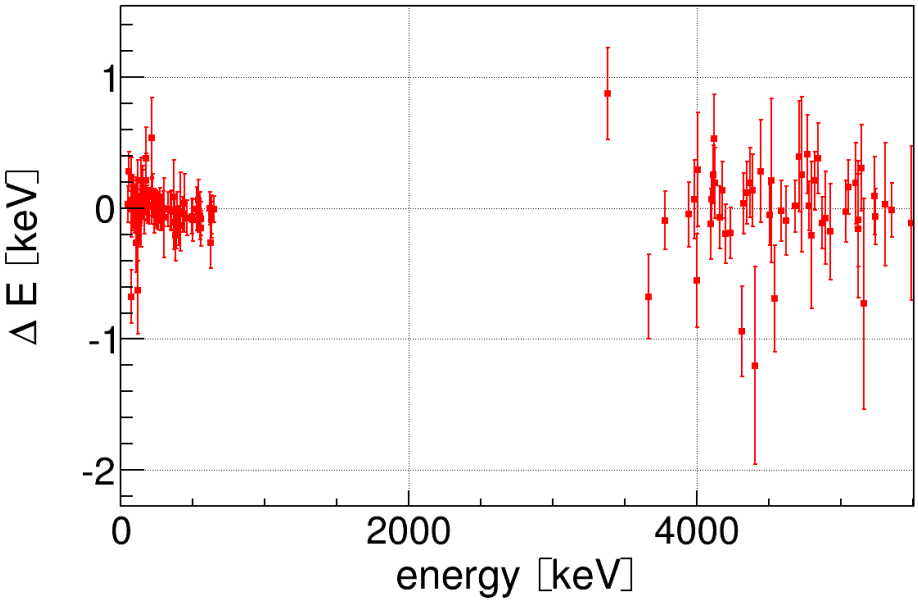

Figure D.2: Comparison of ^{237}Np energy measurements of prompt γ-rays at BRR with sample 8 and sample 9 as a function of the measured energy.

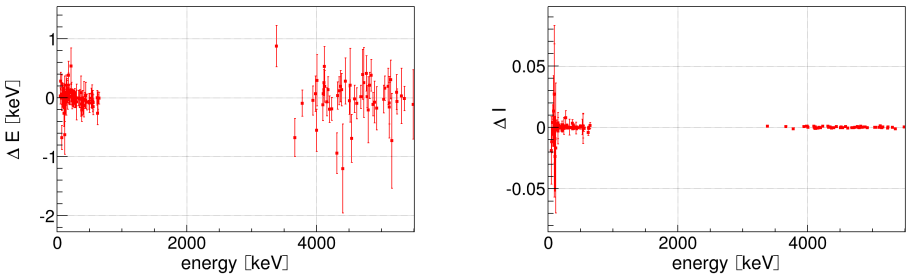

(a) (b)

Figure D.3: Comparison of ^{237}Np prompt γ-ray measurements at BRR with sample 8 and sample 9 as a function of the measured energy. Residuals of (a) γ-ray energies and (b) relative intensities.

APPENDIX E

Plots of Actinide Spectra

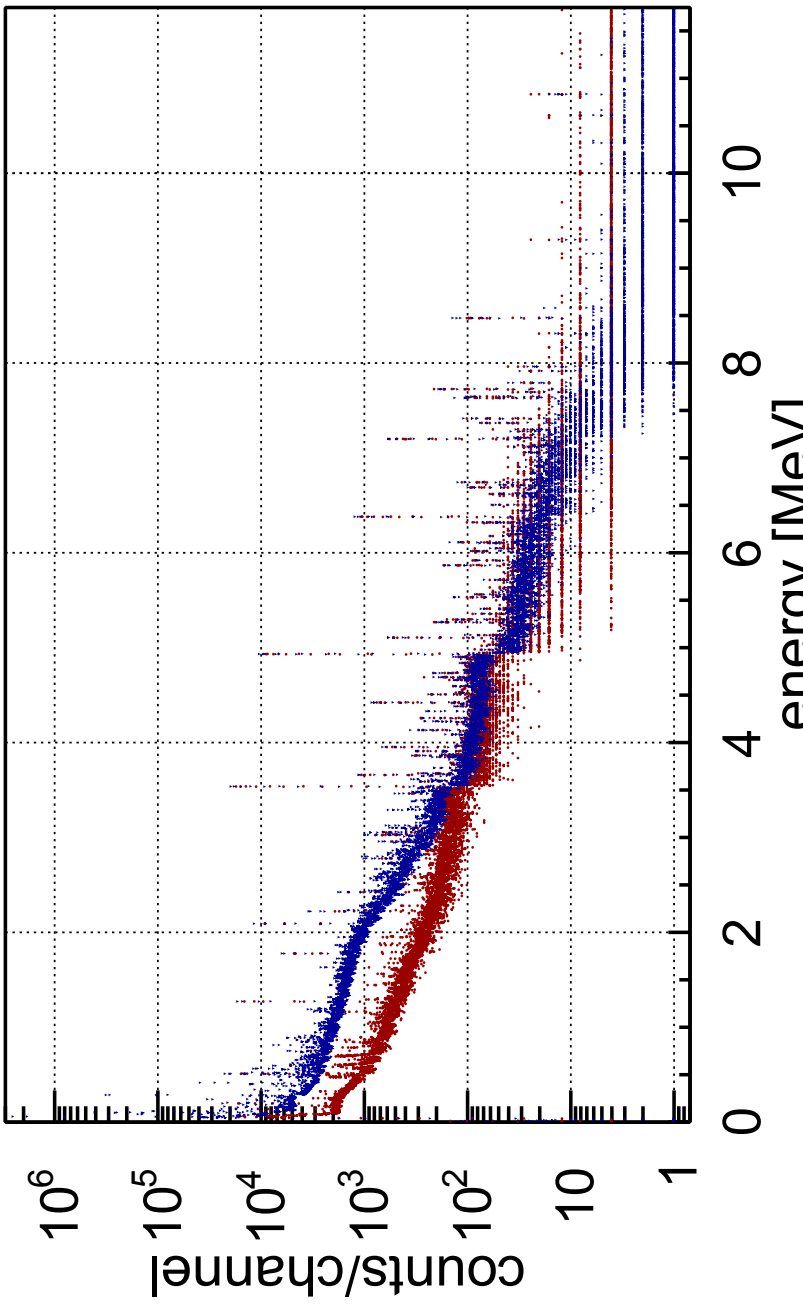

Figure E.1: Spectrum taken during the irradiation of sample 2 (blue triangles) and of the blank sample casing (red circles) at BRR. The blank sample spectrum was renormalized to the live time of the measurement of sample 2.

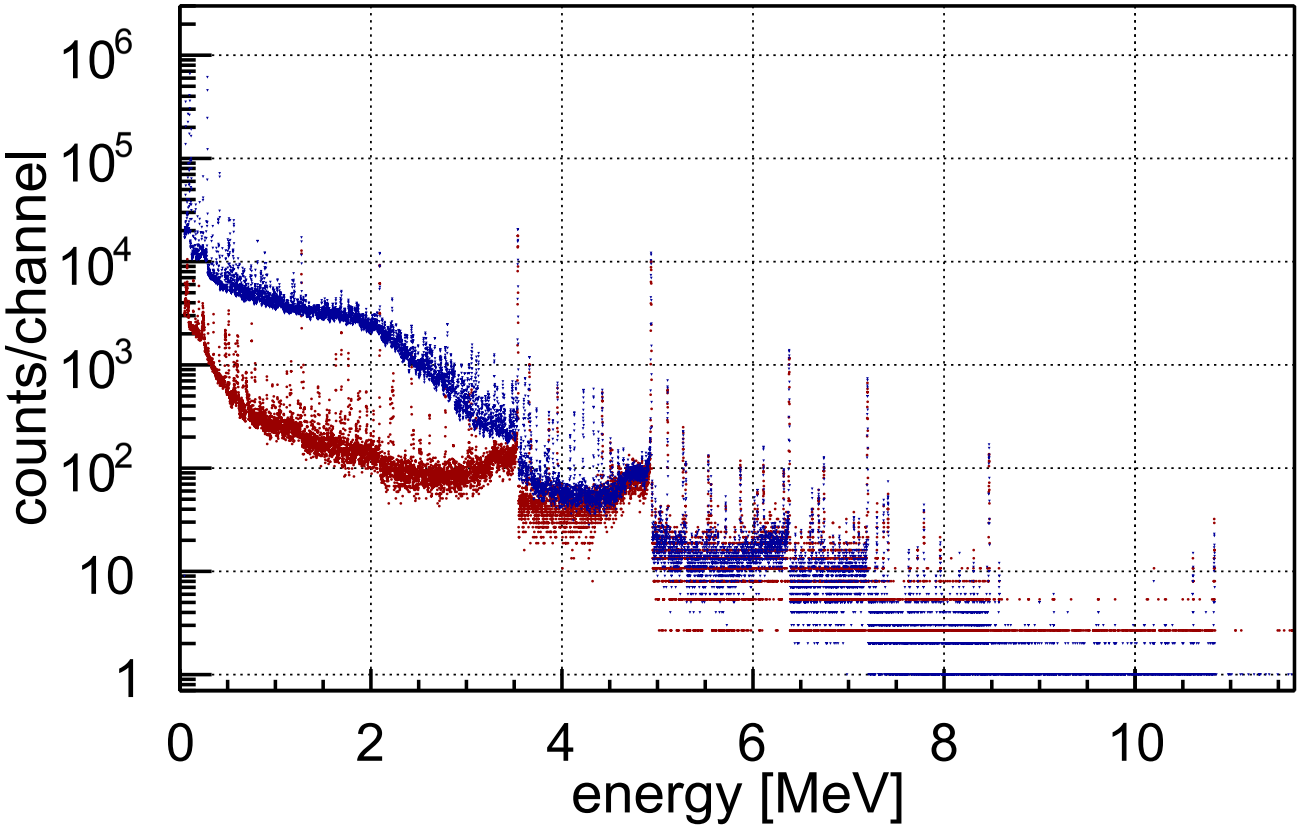

Figure E.2: Spectrum taken during the irradiation of sample 2 (blue triangles) and of the blank sample casing (red circles) at FRM II. The blank sample spectrum was renormalized to the live time of the measurement of sample 2.

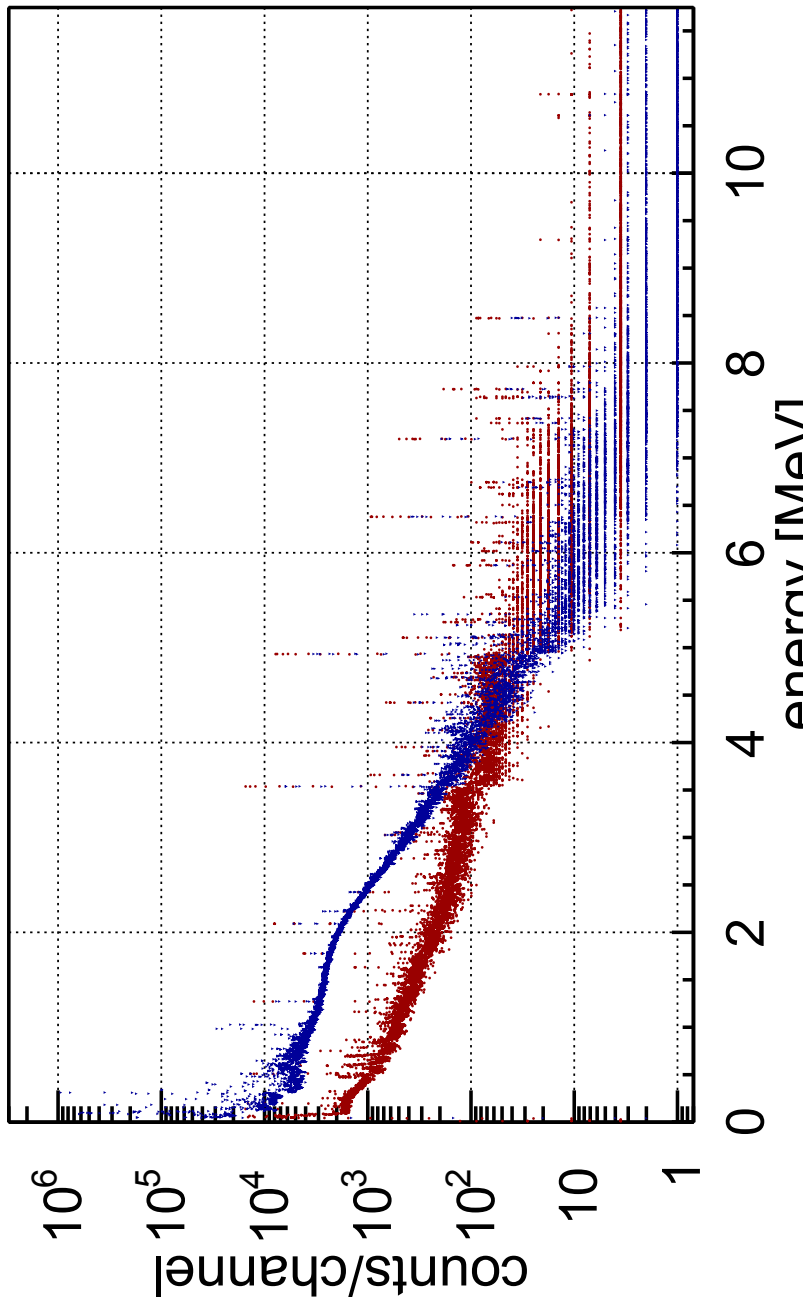

Figure E.3: Spectrum taken during the irradiation of sample 9 (blue triangles) and of the irradiation of the blank sample casing (red circles) at BRR. The blank sample spectrum was renormalized to the live time of the measurement of sample 9.

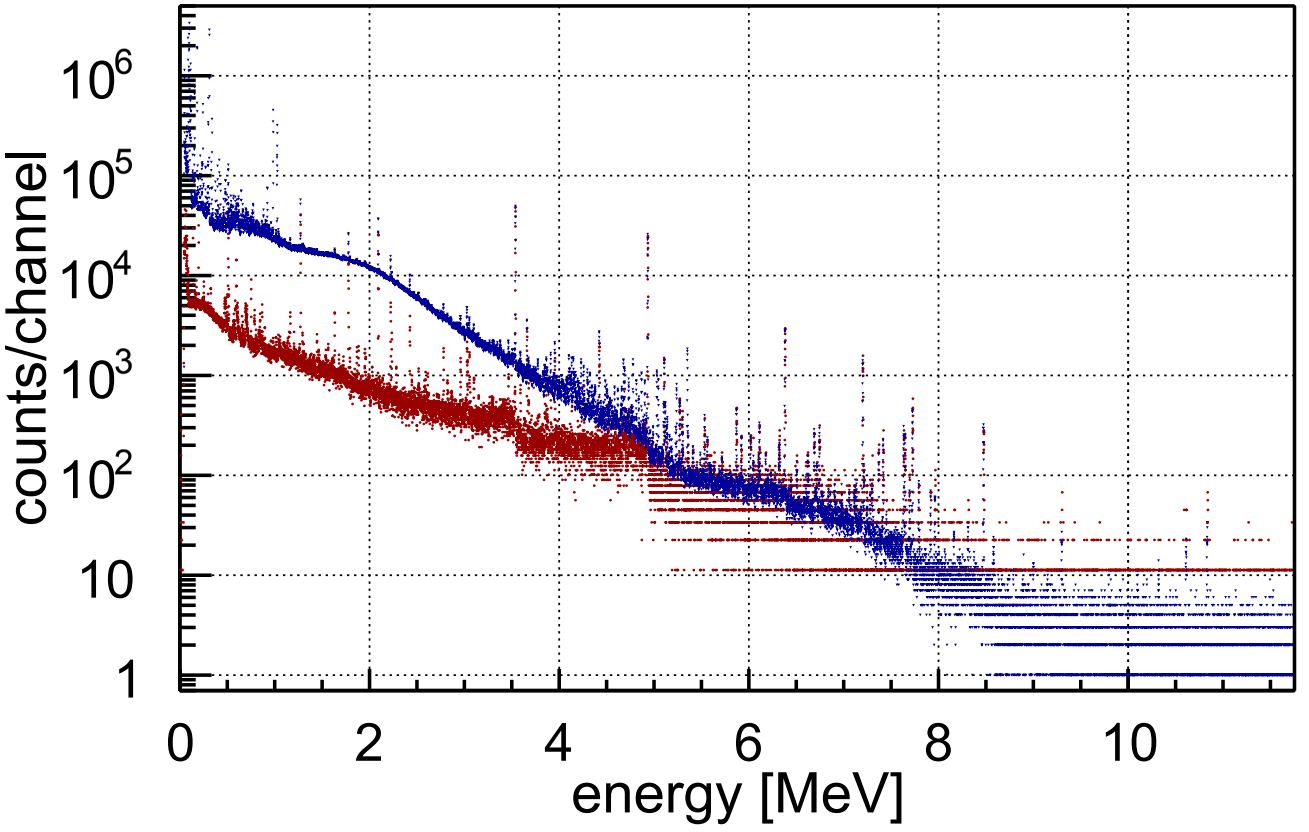

Figure E.4: Spectrum taken during the irradiation of sample 8 (blue triangles) and of the blank sample casing (red circles) at BRR. The blank sample spectrum was renormalized to the live time of the measurement of sample 8.

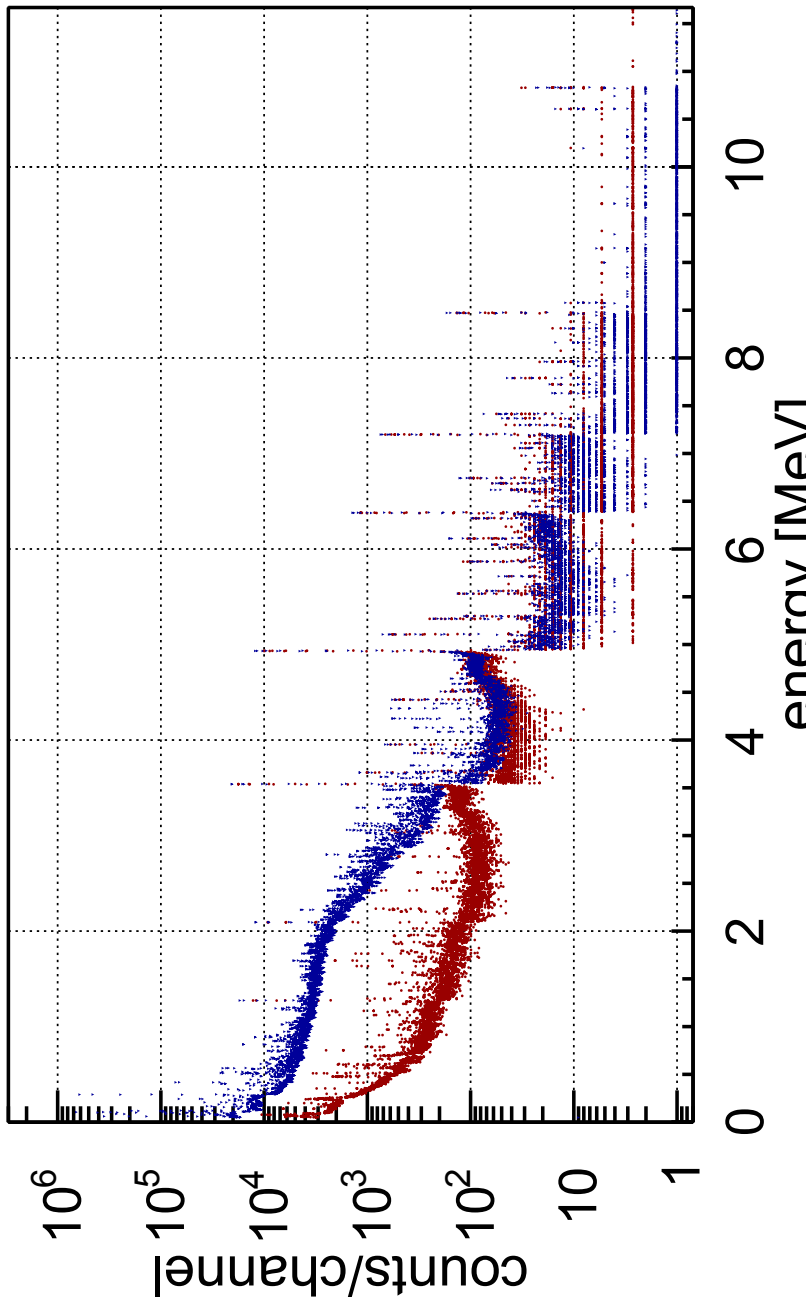

Figure E.5: Spectrum taken during the irradiation of sample 8 (blue triangles) and of the blank sample casing (red circles) at FRM II. The blank sample spectrum was renormalized to the live time of the measurement of sample 8.

APPENDIX F

Values of Physical Quantities used in this Work

Table F.1: Values of physical quantities used in this work. Unless otherwise stated in the text, data are taken from NIST [168], Geant4 material database [96], CRC Handbook of Chemistry and Physics [90], DDEP [82], ENDF [5] and EGAF [4].

Quantity	Value [unit]	Quantity	Value [unit]	Quantity	Value [unit]
$\rho(\mathrm{Au})$	$19.32\,\mathrm{g\,cm^{-3}}$	$m_a(^{241}\mathrm{Am})$	241.06 u	$T_{1/2}(^{242}\mathrm{Pu})$	$3.73(3)\cdot10^5$ yr
$\rho(\mathrm{SiO_2})$	$2.2\,\mathrm{g\,cm^{-3}}$	$m_a(^{242}\mathrm{Pu})$	242.06 u	$T_{1/2}(^{243}\mathrm{Pu})$	4.956(3) h
$\rho(\mathrm{FEP})$	$2.15\,\mathrm{g\,cm^{-3}}$	$T_{1/2}(^{198}\mathrm{Au})$	2.6943(7) d	$\sigma_c^0(^{197}\mathrm{Au})$	98.66(14) b
$\rho(\mathrm{NpO_2})$	$11.1\,\mathrm{g\,cm^{-3}}$	$T_{1/2}(^{237}\mathrm{Np})$	$2.144(7)\cdot10^6$ yr	$p_\gamma(^{198}\mathrm{Au}, 412\,\mathrm{keV})$	95.62(6) %
$\rho(\mathrm{PuO_2})$	$11.5\,\mathrm{g\,cm^{-3}}$	$T_{1/2}(^{238}\mathrm{Np})$	2.10(2) d	$p_\gamma(^{238}\mathrm{Np}, 924\,\mathrm{keV})$	2.604(2) %
$m_a(\mathrm{H_{nat}})$	1.0078 u	$T_{1/2}(^{239}\mathrm{Np})$	2.356(3) d	$p_\gamma(^{238}\mathrm{Np}, 984\,\mathrm{keV})$	25.18(13) %
$m_a(\mathrm{O_{nat}})$	15.999 u	$T_{1/2}(^{241}\mathrm{Am})$	432.6(6) yr	$p_\gamma(^{238}\mathrm{Np}, 1026\,\mathrm{keV})$	8.76(6) %
$m_a(\mathrm{Cl_{nat}})$	35.453 u	$T_{1/2}(^{242\mathrm{g}}\mathrm{Am})$	16.01(2) h	$p_\gamma(^{238}\mathrm{Np}, 1029\,\mathrm{keV})$	18.25(13) %
$m_a(\mathrm{Au_{nat}})$	196.97 u	$T_{1/2}(^{243}\mathrm{Am})$	7367(23) yr	$\sigma_\gamma(\mathrm{H_{nat}}, 2223\,\mathrm{keV})$	0.3326(7) b
$m_a(^{237}\mathrm{Np})$	237.05 u	$T_{1/2}(^{241}\mathrm{Pu})$	14.33(4) yr	$\sigma_\gamma(\mathrm{Cl_{nat}}, 1165\,\mathrm{keV})$	8.91(4) b

Acknowledgement

This work would not have been possible without the support of many people. My special thanks go to Prof. Dr. Bruno Thomauske for offering me this fascinating topic and for reviewing this thesis and to him and Prof. Dr. Dirk Bosbach for providing the working environment and means at the IEK-6. Furthermore, I deeply thank Prof. Dr. Syed M. Qaim who agreed to review this thesis and who has supported this work in many ways.
I severely thank Dr. Matthias Rossbach, who has supervised this work and who has contributed by countless fruitful discussions and invaluable advice. Also, I would like to thank Dr. Eric Mauerhofer and his group (especially Dr. Thomas Krings) for many interesting discussions in and beyond the scope of this work.
For giving me deeper insights into PGAA, I would especially like to thank Dr. Zsolt Révay of the FRM II for priceless discussions and for his willing support. In this context thank you to Dr. Tamás Belgya and Dr. Laszlo Szentmiklosi from the BRR PGAA team.
I am truly grateful to Dr. Richard Firestone for inviting me to visit the LBNL and for introducing me to the basics of nuclear structure calculations. A warm thank you to Dr. Aaron Hurst for introducing me to DICEBOX and very for interesting discussions as well as proofreading.
Further, I would like to thank the BRR and FRM II PGAA teams for their great support during the irradiation experiments and Dr. Peter Schillebeeckx and Dr. Bjorn Becker for helpful discussions. Experimental help by Prof. Dr. Tobias Reich, Dr. Giuseppe Modolo, Dr. Andreas Wilden, Fabian Sadowski, and Norman Lieck is gratefully acknowledged.
I also would like to thank the workshop team for manufacturing all the small utilities and the team from the FZJ library for their great support. This work was financed from the generous support of Dr. Guido Caspary, N-D of the FZJ. This work was supported by the European Commission within the Seventh Framework Programme through Fission-2010-ERINDA (project no.269499). Financial support by the Bundesministerium für Bildung und Forschung (BMBF) under grant 02S9052A is gratefully acknowledged.
Concluding, I specially thank Annalena Schriever for proofreading and her invaluable support during the writing phase. Also, I would like to thank my and her family for their permanent support. Last my apologies to all supporters I presumably forget to mention here. My thanks to you as well.

Band / Volume 237
Entwicklung von porösen Silica-Membranen zur CO_2-Abtrennung aus dem Rauchgas fossil befeuerter Kraftwerke
J. S. Eiberger (2014), II, 163 pp
ISBN: 978-3-95806-008-1

Band / Volume 238
Development of a highly sensitive and versatile mass spectrometer system for laboratory and atmospheric measurements
S. Albrecht (2014), iv, 171 pp
ISBN: 978-3-95806-009-8

Band / Volume 239
High Temperature Corrosion of Alloys and Coatings in Gas-Turbines Fired with Hydrogen-Rich Syngas Fuels
W. Nowak (2014), 201 pp
ISBN: 978-3-95806-012-8

Band / Volume 240
Einfluss neuer Membranmaterialien auf Herstellung und Betrieb von Direktmethanol-Brennstoffzellen
S. Hürter (2014), V, 164 pp
ISBN: 978-3-95806-013-5

Band / Volume 241
Spannungsinduziertes Versagen in Hochtemperaturschichtsystemen
C. Nordhorn (2014), v, 118 pp
ISBN: 978-3-95806-016-6

Band / Volume 242
Änderungsdetektion digitaler Fernerkundungsdaten mittels objekt-basierter Bildanalyse
C. Listner (2014), 176 pp
ISBN: 978-3-95806-017-3

Band / Volume 243
Räumlich hoch aufgelöste Modellierung des Spaltprodukt-verhaltens in einem HTR-Core mit kugelförmigen oder prismatischen Brennelementen
A. Xhonneux (2014), viii, 239 pp
ISBN: 978-3-95806-020-3

Band / Volume 244
Effects of Cercospora leaf spot disease on sugar beet genotypes with contrasting disease susceptibility
S. Schmittgen (2015), 121 pp
ISBN: 978-3-95806-021-0

Band / Volume 245
Light scattering and trapping in thin film silicon solar cells with an n-i-p configuration
W. Böttler (2015), 132 pp
ISBN: 978-3-95806-023-4

Band / Volume 246
Nanostructured Si-alloys for silicon solar cells
K. Ding (2015), 210 pp
ISBN: 978-3-95806-024-1

Band / Volume 247
Electrochemical Texturing and Deposition of Transparent Conductive Oxide Layers for the Application in Silicon Thin-Film Solar Cells
J.-P. Becker (2015), ix, 156, XXIV pp
ISBN: 978-3-95806-027-2

Band / Volume 248
Stoffliche Charakterisierung radioaktiver Abfallprodukte durch ein Multi-Element-Analyseverfahren basierend auf der instrumentellen Neutronen-Aktivierungs-Analyse – MEDINA –
A. W. Havenith (2015), 311 pp
ISBN: 978-3-95806-033-3

Band / Volume 249
Quantitative Two-Layer Inversion and Customizable Sensor-Array Instrument for Electromagnetic Induction based Soil Conductivity Estimation
A. T. Mester (2015), viii, 119 pp
ISBN: 978-3-95806-035-7

Band / Volume 250
Partial Neutron Capture Cross Sections of Actinides using Cold Neutron Prompt Gamma Activation Analysis
C. Genreith (2015), vii, 166, XXXII pp
ISBN: 978-3-95806-036-4

Energie & Umwelt /
Energy & Environment
Band / Volume 250
ISBN 978-3-95806-036-4

JÜLICH
FORSCHUNGSZENTRUM